Generation and Langmuir Probe Analysis of a DC Glow Discharge and the Deposition of Chromium from a Carbonyl Precursor

A Thesis submitted
for the degree of
Doctor of Philosophy

By

Lawrence Stuart Pilling

The University of Waikato
Te Whare Wānanga o Waikato

July 2003

Abstract

Experimental investigations detailed in this thesis fall into two distinct areas: Diagnostics of a nitrogen DC discharge with Langmuir probes and spectroscopy, and experiments designed to deposit chromium metal from a chromium hexacarbonyl precursor ($Cr(CO)_6$). New diagnostic equipment was designed, tested and implemented to record Langmuir probe data with high resolution and accuracy. A monochromator was employed to record the light emission from the plasma. This identified which ionized species were present as well as the ion temperature from the resulting band structures present. The monochromator analysis was necessary to validate the assumptions of the Langmuir probe theory and to allow a choice of which theories applied.

The Langmuir probe analysis of the recorded data for many plasmas have been well covered in the literature but few papers give a comprehensive coverage of the main probe theories using the one set of data and fewer still make use of double as well as single probes. The majority simply assume the particular theory used is relevant to the plasma conditions and the resulting temperatures and densities are correct.

During the experiments and subsequent analysis it was found, similar to other researchers, that the ion densities were consistently higher than the electron densities even though the theoretical analysis applied in the saturation regimes appeared to be valid. Rather than ignoring this issue, and assuming ion collisions or secondary electron emission were the cause, new methods were developed to analyse the data. By determining the gradient of the saturation regimes and comparing them to those expected experimentally, it was found that the ion saturation regime neither followed the orbital nor radial motion theories investigated. However, the electron current did follow the orbital motion theory and it is demonstrated that the densities obtained from the ion currents, using these theories, were incorrect. This had been previously shown to be true only with non-probe methods.

Using the same discharge configuration, impurity-free chromium films were deposited onto stainless steel substrates from a chromium hexacarbonyl precursor. This had been attempted by previous researchers, using a variety of discharge configurations, who invariably deposited similar metallic films with significant levels of oxygen and carbon impurities. The combination of the carbonyl precursor and the carrier gases (nitrogen and argon) with the discharge configuration resulted in these impurity-free films even when a negative bias of up to 50 V was applied to the sample.

Acknowledgements

I wish to thank those that helped.

Those that endured.

And those that believed.

Personally, I would like to thank the revolving circle that ended up with the unenviable task of supervising me, especially Dale Carnegie who chose the short straw and made this submission possible. I don't believe I can thank him enough. Thanks to Rainier Künnemeyer who helped in the interim and to Moira Steyn-Ross who has been an encouragement from the start of this project but ended up with it all in her lap.

I would also like to acknowledge Dr Evan Bydder, for without his knowledge and enthusiam this project would never have been started or finished.

Last, but by no means least, the second cog in my original supervisory panel, Professor Bruce Liley. Unfortunately you never saw the end of this work, but I hope you find peace since you, out of all of us, deserve it most.

I would like to thank the Foundation for Science and Technology who provided a scholarship for this research, and ECNZ my industry partner in this project. Without their support this project would have been impossible.

Dedication

I would like to dedicate this thesis to my parents, my sons and my partner. Some of the past has been rocky, but thank you for you patience and support.

Contents

List of Figures

List of Tables

Chapter 1 Introduction

1.1 Introduction

Plasmas are now more than brilliantly lit and fascinating objects to view and admire, they are fundamental tools in a wide variety of invaluable manufacturing methods over a broad spectrum of industry. However, they are still poorly understood even after centuries of investigation and most industrial methods, by necessity, are developed through trial and error rather than a theoretical approach. The ability to model and fully solve Boltzmann's equations, or even Grad's (1949) 13 moment approximation, over a myriad of different reactions, chemical and physical, for the astronomical number of particles present is the defining issue with the theoretical approach. Deposition and etching plasmas are fundamental tools on which modern technology is based. Miniaturisation, electronics and even the computer used to write this thesis are only possible through the use of plasma processing.

Even for the most simple of experimental measurements, the plasma equivalent of Ohms law, theory often does not match experiment. The first theoretical approach, experimental measurements, and even the name of the subject, "plasma", was determined, measured and coined by Irving Langmuir (1961) whose name now honours the probe technique. Langmuir formulated the orbital motion approach (OML), and with his colleagues manually integrated the plasma solution, which was fully solved numerically 30 years later by Allen, Boyd and Renyolds (1957) for ion collection. Many improvements to the theories were developed by authors such as Chen (1965) and Laframboise (1966). Even though it is now fifty years since the publication of these ion collection theories, they are still "state of the art" and large differences often occur between theory and experiment, Chen (2001).

1.2 Objectives

There were two main goals in this research project. The first was to definitively determine the plasma composition, temperature and density. For all plasma experiments this is a fundamental necessity, since without this knowledge, experiments are not repeatable by other researchers.

To determine the plasma parameters, Langmuir probes in conjunction with spectroscopic measurements of the plasma were necessary. Langmuir probes measure the raw data, while spectroscopy ensures that the base assumptions (such as the ion

species and ionisation states), of the Langmuir probe theories are fulfilled. To ensure the measurements were as accurate as possible, an original, automated Langmuir probe data acquisition system would be constructed for which the resolution of the data was expected to be uniform across seven orders of magnitude in the current domain, Pilling *et al.* (2003). Data recorded from this instrument would allow high accuracy recording of both the electron and ion currents simultaneously. Since the best mathematical constructs of the Langmuir probe behaviour occur for the ion currents, analyses of this region by previous researchers had been hampered by the low resolution enforced by the necessity to record the electron saturation current.

With this new tool, detailed analyses of the appropriate ion current theories, which were expected to be chosen from observation the spectroscopic data, would be investigated with a highly detailed data resolution. It was determined to resolve the issues surrounding which theory, if any, was applicable to plasmas within the range of the temperatures and densities of the system constructed in this research.

The second goal was to deposit coatings of chromium, as pure as possible, onto steel substrates from a chromium hexacarbonyl precursor. The motivation for this was two-fold. Firstly there is an increasing demand from environmentalists and governments to minimise the toxic waste and dangers inherent in the electrodeposition of chromium films.

Secondly, if deposition was successful and the quality of the films comparable to alternative methods, it would lead to a lost cost viable alternative to deposition methods with expensive tool such as ion beams.

1.3 Introduction to Deposition and Langmuir Probes

1.3.1 Brief History of Surface Modification

The early development of plasma discharges was not singular. Plasma discharges and their investigation evolved primarily in conjunction with better vacuum pumping systems and the development of electricity. The original glass tube DC discharges, such as those studied by Thompson (1913) who discovered the electron and Crookes (1891) who made the first systematic study on sputtering and deposition, were used since no other system was available. Alternate current (AC) was not widely available before 1900 and the pumping systems at this time were crude by today's standards. The measurements in the discharge tubes were plagued by contamination from the pumping systems and water vapour which was difficult to circumvent. Thus studies of the sputtering and deposition processes produced widely variable results until the early in the 20^{th} century.

In 1913 Langmuir started the first of his famous vacuum discharge experiments, solved the contamination problems and invented the mercury diffusion pump, Langmuir (1913). It was about this point in history that systematic investigations of plasmas, a term coined by Tonks and Langmuir (1929), could be achieved although sputter techniques were occasionally used before this time. It wasn't until the Second World War and beyond, that plasmas were viewed as more than a novelty by the wider scientific community. The advent of most techniques such as ion guns, radio frequency as a plasma generation method, and the replacement of vacuum tubes by plasma etched silicon devices occurred from 1930 - 1970. Substantial research funding was driven by U.S. government agencies, such as the Department of Energy and the National Aeronautics and Space Administration (NASA). Although systematic research on plasma coatings started in the 1930's it was boosted through the war era, for example, in developing the nuclear bomb and later to provide specialised materials and coatings for spacecraft and jet aeroplanes.

Surface modification by plasma treatment has come a long way since the filing of patents by Berghaus (1937) on the plasma processing of metals. This work led to the plasma assisted diffusion (PAD) and the physical vapour deposition methods (PVD) found today in ion plating. The PAD methods involve the transport of elements by the plasma capable of being incorporated in the target lattice as interstitials. PVD methods differ from the diffusion methods by transporting the interstitial forming elements as well as the required metal to the target surface. Interstitial forming elements are normally carbon and nitrogen while the metals used are usually titanium or chromium. Combinations of such elements form very hard and wear resistant films on the target surface. These methods of plasma surface engineering are termed "ion plating" or "ion coating" and involve the use of many plasma production methods and deposition assistance as each combination provides differing growth and stoichiometry of the films.

Surface modification can also be achieved by the use of ion beams and more recent techniques such as plasma source ion implantation (PSII). Ion beams consist of a stream of ions collimated in a narrow beam accelerated to high potentials. These beams, when impinging on the target surface, provide implantation of the ions into the target lattice. Applications of ion beams covers a more diverse range than any other plasma surface modification technique since there are fewer requirements on the target. Ion plating and coating methods also have minimal requirements on the target, but the difference between these methods and the use of ion beams is the surface modification provided by each process. In ion beams the ions are monoenergetic and have energies far greater than the energy necessary for penetration into the target lattice. In the ion plating methods, the energy distribution of the ions is low as the

energy range is controlled by the plasma parameters and the target bias (< 4 kV) so that minimal target lattice penetration occurs. The ion energies in ion plating are orders of magnitude below the ion beam ion energies. Thus surface treatment with ion beams is an implantation process while the ion plating methods only coat the target surface. Both techniques can be used in conjunction with one another to increase the quality of the films and the adhesion of the film to the substrate. Both methods allow the treatment of non-metals such as glass, ceramics, and plastics. Ion beams were designed for the implantation of dopants into semiconductors. This is an enormous area of research in industry with entire treatises, annual conferences as well as a great deal of money being devoted to this area. Ion beams created for the semiconductor industry have now been applied to surface engineering for ion implantation into metals.

Ion assisted coating (IAC) methods contain the best features of the ion PVD and beam implant methods. Ion beams can be used to improve film growth, adhesion, and to modify the initial surfaces formed by ion plating. The simplest form of IAC is ion beam mixing or recoil implantation. In this process, beams of ions, usually argon, are fired into film coatings and the subsequent recoil of atoms in the film, from atomic collisions, mixes the region between the film and the substrate. A further common use is beams of nitrogen fired into films such as titanium and other alloys containing transition metals. Another IAC process is radiation enhanced diffusion which occurs when the target temperature is allowed to rise during implantation. Simultaneous IAC and beam modification produce highly adherent thin films. This process is called ion beam enhanced deposition (IBED). IBED films can be deposited over a broad range of conditions. This occurs when, for example, ion beams of nitrogen are implanted into a titanium film which is being grown concurrently by ion plating methods.

1.3.2 Introduction to Langmuir Probes

Langmuir probes comprise of one or more small metallic electrodes immersed in a plasma to which a range of positive and negative voltages can be applied. A plot of current collected by the probe at the various voltages is called the "probe characteristic" which yields information on the charge carrier density, the plasma potential, and the velocity distribution of the electrons. In order to measure these parameters accurately it is necessary to minimise the disturbance of the plasma by the probe. The presence of a small conducting body immersed in a plasma invariably leads to perturbation of the plasma since it now contains another surface where ion recombination can occur. Langmuir probes can be applied to plasmas over a large

range of pressures, from 1×10^{-3} Pa to atmospheric pressure and over more than eight orders of magnitude in charge carrier concentration from 10^{6} cm^{-3} to 10^{14} cm^{-3}. Although the use of Langmuir probes increases the risk of incorrect measurements compared to some other diagnostic methods, they have the advantage of allowing direct local measurement of the plasma parameters.

The theory of electrical probes in plasmas was developed in the 1920s by Langmuir and his co-workers (Langmuir, 1961). They limited their analyses to the low pressure case where collisions between plasma particles can be neglected. The evaluation of plasma parameters from this situation is restricted to a Maxwellian velocity distribution of the charge carriers. However, the velocity of the electrons, particularly at low pressures, is commonly not Maxwellian and often is not isotropic, Swift and Schwar (1970). Irrespective of this, the actual distribution form can be determined from the form of the characteristic, Druyvesteyn, (1930).

Since the initial experiments of Langmuir, configurations of two or multiple probes have been used for the same purpose, namely the evaluation of the plasma parameters. The use of double probes arose particularly from the need to make measurements in afterglow and Radio Frequency (RF) generated plasmas. In these types of plasma, single probes can draw such a large current that the plasma is perturbed to the extent of yielding spurious data. Furthermore, the RF voltage fluctuations at the applied frequency need to be followed by a single probe since one side of the circuit is grounded. Double probes overcome this problem as they limit the current drawn to the ion saturation current and float at a voltage referenced to the plasma rather than to ground. Both single and double probes are used in the experiments described in this thesis, and so both types of probe configuration and the relevant theories are discussed. There are several different theories for the various types of plasma that can occur. Unfortunately it is unknown which theory should apply until the plasma properties are measured. A solution to this problem is to use a generalised theory such as the original Langmuir theory for the plasma analysis to provide rough values of the plasma parameters allowing more refined theories to be subsequently applied.

1.4 Thesis Structure

Chapter one has discussed and introduced the problems inherent in plasma diagnostics and proposed potential solutions, and new methods of data acquisition to better compare theory with experiment. Two sets of goals were discussed, one for determining the plasma parameters and the other to perform coating experiments with

a chromium carbonyl precursor. A general overview of the plasma deposition processes was presented.

Chapter two provides a literature review across relevant deposition systems described by researchers using the same, or a similar precursor to the one proposed in chapter one. Alternative deposition systems for generating chromium and its nitrides are examined for systems such as implantation, ion plating and ion beam methods. Nitrides of chromium are intricately linked to the deposition of chromium films and offer the possibility to replace chromium coatings in certain situations.

Chapter three provides the relevant theory of the discharge necessary to understand the conditions for plasma creation. This chapter contains theory for the classical mean free path as well as the excitation and ionisation cross-sections for electron impact from which the actual mean free paths can be calculated from the knowledge of the electron temperature and neutral pressure. Also detailed in this chapter is a comparison between nitrogen and carbon monoxide and their expected behaviour in a plasma.

In chapter four the theory for the measurement of the discharge using electrical probes is discussed. The common theories for single and double probes are examined. Also detailed are the more complex, and physically realistic, theories of current collection for low temperature ions. Where appropriate, the original solutions have been recalculated and analysed in terms of the gradients, or dependence the ion current theoretically has on the potential difference between the Langmuir probe and the plasma. Taking a different approach to conventional analysis, the theoretical calculations were directed so that the experimental data could be directly compared to the theoretical curves. Conventionally, a theoretical curve is generated from the experimental parameters and compared directly to the recorded Langmuir probe data.

Chapter five details the experimental equipment constructed, the measurement tools, and dimensions of the apparatus used to obtain data from the plasma system and to perform the coating experiments. Special attention is devoted to the Langmuir probe data acquisition system where a detailed comparison is made to previously published automated systems.

Chapter six details the complete spectroscopic investigations of the plasmas generated in this research. This includes discussions of the various theories and advances published in the literature. Although it is found that the measured plasma parameters invalidate the assumptions and conditions of all general theories, specific theoretical rotational temperature measurements appear to be valid even though the assumptions are invalid for the plasma conditions. A direct comparison between theoretically generated curves found in the published literature and the experimental band structures measured is presented.

Chapter seven presents the results of a detailed comparison of the experimental Langmuir probe data with the theories discussed in chapter four. The analysis procedures resulted in a contradiction between the density values obtained from the electron and ion saturation regimes. New methods of data analysis are applied to the raw data where it is shown that this conflict can be resolved and the issues creating this contradiction are discussed. A critical review of the results compared to previous published data from other researchers is also conducted.

Chapter eight details the experimental deposition experiments, where it is shown that films containing 97 atomic percent of chromium can be produced from the chromium hexacarbonyl precursor. The films deposited are free from carbon impurities, a problem that has been present in almost every published attempt. A variety of diagnostic tools are discussed and used to determine the structural and chemical composition of the films.

Chapter nine summarises the theoretical and experimental achievements, conclusions of these results, contributions to original research, and possible directions of future research.

1.5 References

Allen, J. E., R. L. F. Boyd, P. Renyolds, 1957, Proc. Phys. Soc. (London), **70**, p 297.

Berghaus, B., 1937, "*Improvements in and Relating to the Coating of Articles by Means of Thermally Vaporized Material*", British patent 510 933.

Chen, F. F., 1965, J. Nuc. Ener. C., **7**, p 47.

Chen, F., F., 2001, Phys. Plasmas, **8**, 6, p3029.

Crookes, W., 1891, Proc. Roy. Soc. (London), **50**, p 88.

Druyvesteyn, M. J., 1930, Z. Phys, **64**, p 781.

Grad, H., 1949, Commun. Pure Appl. Math., **2**, p 331.

Laframboise, J. G., 1966, *Fourth symposium on Rarefied Gas Dynamics*, edited by J. H. De Leeuw (Academic Press, New York), **Vol II**, p 22.

Langmuir, I., 1961, *Collected works of Irving Langmuir* (Permagon Press, New York) **Vol 4**.

Langmuir, I, 1913, Phys. Rev., **2**, p 450.

Pilling, L. S., E. L. Bydder, and D. A. Carnegie, 2003, Rev. Sci. Inst., **74**, 7, p 3341.

Swift, J. D., and M. J. R., Schwar, 1970, *Electrical Probes for Plasma Diagnostics* (Iliffe, London).

Thompson, J. J., 1913, *Rays of positive Electricity*, (Longmans, Greene and Co., London).

Tonks, L., and I. Langmuir, 1929, Phys. Rev., **34**, p 876.

Chapter 2 Summary of Plasma Processing

2.1 Introduction

A wide variety of methods, some of them not involving plasmas, have been used to coat thin films onto substrates using metal carbonyl precursors. Within this large range there have been relatively few papers published and surprisingly little research done in this field. Almost all the research has been covered by one particular group lead by H. Suhr. Many techniques using carbonyl precursors have been attempted, all of which contain undesirable oxygen or carbon contamination of the films. Chromium hexacarbonyl is a prime candidate for the plasma deposition of pure chromium films which are becoming more and more desirable to form due to the restrictive costs of disposing of electroplating waste products.

This chapter will present an overview of plasma processing covering the wide range of techniques available. A review of chromium films and their beneficial effects will be detailed along with the associated nitrides formed, as well as a comparison of experiments by other researchers using carbonyls in plasma systems to form thin films of chromium or its alloys. Implantation of nitrogen into chromium films by ion beams or plasma implantation methods will also be reviewed. The general formation of these and related compounds along with a discussion on the mechanisms behind the implantation processes detailing the physical processes that give rise to the beneficial effects found by many authors.

Reviews of Langmuir probe recording methods, data analysis, spectroscopic models and comparisons by other researchers will be conducted in the chapters that are appropriate for them.

2.2 Deposition and Etching Systems

Plasma deposition and etching processes cover a wide range of pressures, temperatures, and chemical activity. These methods are best presented in a graphical format split into two classes; by their specific plasma temperature and density, or alternatively by their physical nature. Additionally, different treatments can be differentiated by the operational pressure and hence the transport mechanisms dominant in the process. Generalised representations of these different plasma processes, including some from natural sources, are shown in figures 2.1 and 2.2 and

are taken from the papers of John (1993), Boulos (1991), Schram *et al.* (1987), Shohet (1991), and Hershkowitz (1998).

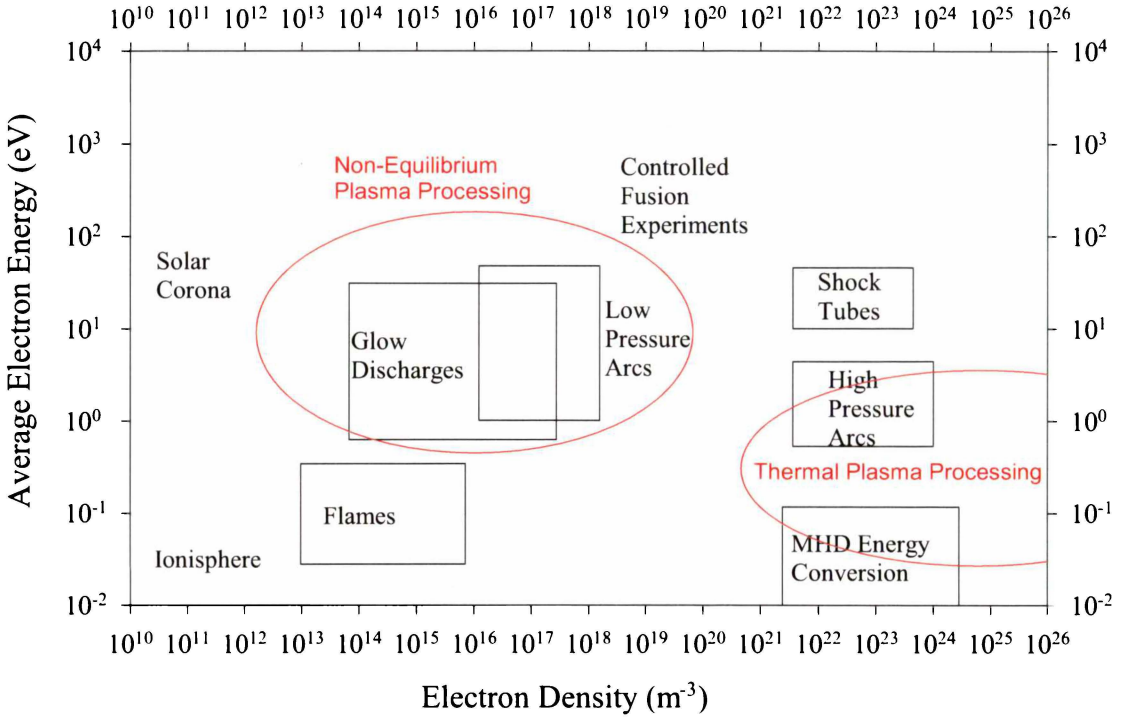

Figure 2.1 : A generalised representation of typical densities and temperatures where particular processes occur.

Each regime in these figures has different sub processes depending on the specific plasma generation process, configuration of the discharge system, and the particular external fields applied to the plasma. Each sub process is generally given its own acronym; some processes have had several acronyms over time, while others have different acronyms for the same process when only the plasma generation method has changed. For instance, early vacuum deposition from plasmas containing chemical precursors initially termed "glow discharge deposition" and changed with time to become "plasma deposition", "plasma enhanced chemical vapour deposition" (PECVD), or "plasma assisted chemical vapour deposition" (PACVD). In the second case, the process of "Plasma Source Ion Implantation" PSII, patented by Conrad (1988) and the paper, once the patent had been applied for, Conrad *et al.* (1987) for which the generation method was a DC plasma, was described as "Plasma Ion Immersion Implantation" (PIII) by Tendys *et al.* (1988) when a RF plasma was used as the source of the ions.

The use of acronyms in plasma processing is extensive and can be somewhat bewildering as, in many instances, the acronyms and processes overlap into common regions of physical, or plasma parameters (density and temperature).

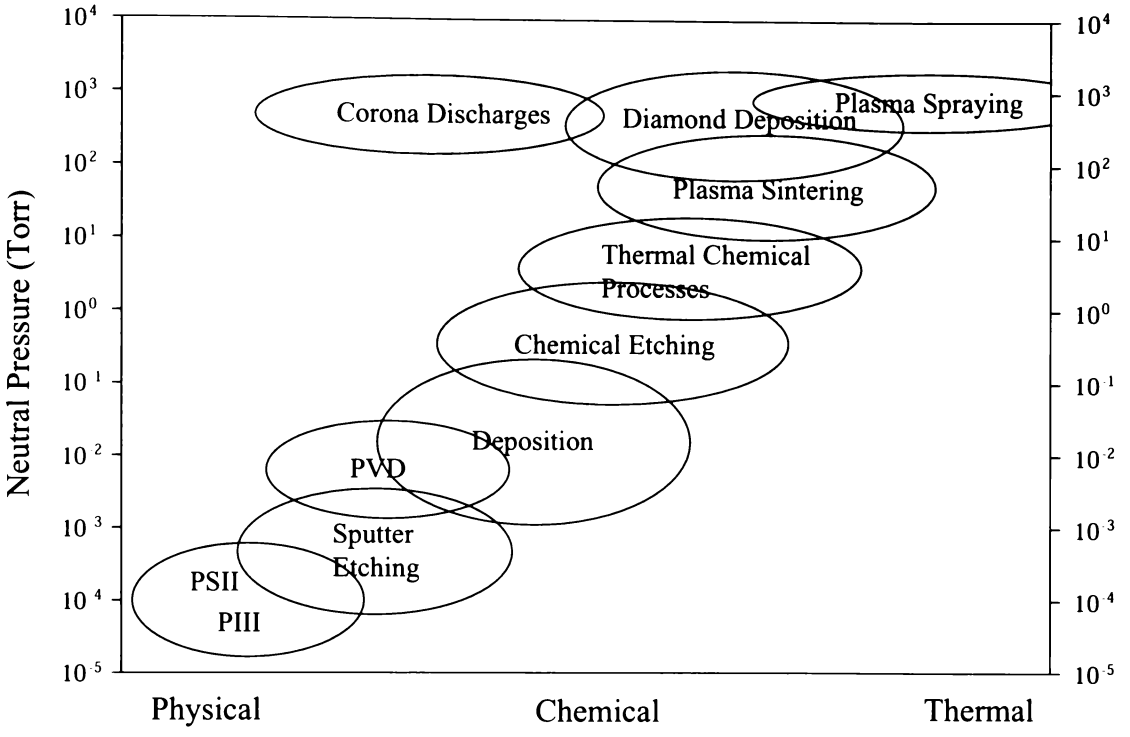

Figure 2.2 : A representation of various processes using plasmas separated by their characteristic operating pressure and the nature of the process itself.

An alternative method to defining processes by their temperature and density is the classification by neutral pressure. As shown in figure 2.2, if the neutral pressure rises, the processes in the plasma change from a simple statistical physical interaction, through the chemical phases such as adsorption into the thermal transport region which dominates at atmospheric pressure. This is not necessarily the case but it is the general trend. Each of these processes is important in its own right and provides coatings or etching which usually cannot be achieved by any other methods. However, we will not discuss each method with equal weighting as we are interested in areas and plasma generation methods which are close to the deposition regimes used in this thesis. This precludes processes such as plasma spraying and high pressure processes since the particulate material providing the coating is deposited in clusters of atoms, or blobs of molten metal rather than atom by atom.

It will be seen in later chapters that the characterisation of our process typically has a neutral pressure, electron temperatures and densities of 10^{-2} mbar, 5.75 eV and 2.45×10^{10} cm^{-3} respectively. Thus our DC plasma discharge falls into the boundary of DC discharges and low pressure arcs while the process is both chemical and physical in nature. Experimentally this is certainly the case, so we shall concentrate this review on processes similar to ours, but we will not neglect different processes that produce similar coatings to ours. We will start with the general history of plasmas and move into the specific areas of deposition.

2.3 Deposition Methods

2.3.1 Chemical Vapour Deposition

Chemical vapour deposition (CVD) covers a broad range of applications and methods across a wide pressure range and is applied to those processes which are dominantly chemical in nature as the name suggests. The conventional CVD process is the heating of the target in the presence of the gaseous species to be decomposed at atmospheric pressure or higher.

Research into CVD in vacuums started in the late 1800's primarily on the first generation of light bulbs. The plasma CVD process can be defined as the reaction of gaseous chemicals in the regions surrounding the target on which the reaction product is deposited. The subsets of the CVD process include APCVD (atmospheric pressure), LPCVD (low pressure), SACVD (sub atmospheric), PECVD (plasma enhanced) or PACVD (plasma assisted/activated), MOCVD (metal organic), and RPECVD (remote plasma enhanced). The prefixes that describe the particular processes are not mutually exclusive so that acronyms such as LP-PECVD (low pressure plasma enhanced chemical vapour deposition) are born. Each of these CVD processes can have different plasma generation methods such as DC, RF, ECR (electron cyclotron resonance) and laser deposition. However, the majority of low pressure plasma CVD processes use RF as the generation source.

The conventional CVD process requires the target to be heated, normally between 700 °C and 1500 °C to increase the chemical reaction rates so that the growth rate of the film becomes acceptable. This temperature requirement is also a limitation since the crystal structure of the film can only contain the phase(s) that are stable at this temperature. Certainly for the growth of semiconductor compounds this may not be the optimum sample temperature and only equilibrium products can be formed. The presence of a plasma enhances the thermal CVD process since the plasma, rather than the substrate temperature, provides the activation of the reaction and the final products which are deposited. The advantages are great. Firstly, the deposition rates and the species deposited are now almost independent of the sample temperature allowing almost any phase of the crystal structure to be grown since the temperature of the substrate can be significantly lowered. The plasma reaction, as well as allowing the deposition of non equilibrium species, is far more efficient than the thermal temperature at increasing the reaction rate leading to large rises in deposition rates. Deposition of structures generally unobtainable in thermal CVD such as boron nitride and diamond like coatings (DLC) are possible. Examples of these coatings can be found in the review by Sundgren and Hentzell (1986).

These facets of enhancing the CVD process with a plasma have spawned a new area of science; one that the silicon chip and electronics industry is now dependent on. Not only do plasma CVD systems allow new materials to be developed, but they can replace the older techniques such as wet chemical etching. To gain a view of the scope of this field, one simply needs to look at journals that were created for these new processes such as *Diamond and Related Materials* or those that predominantly contain CVD processes like *Thin Solid Films*, and *Surface and Coatings Technology*.

2.3.2 Physical Vapour Deposition

Physical vapour deposition (PVD) differs from CVD in that the term applies when the pressure is less than 10^{-2} mbar so that the neutral pressure and hence collisional effects play a lesser role in the deposition process. Generally PVD is split into evaporation, sputtering, and ion plating techniques while the average particle energy is 0.1 eV - 0.5 eV, 1 eV - 10 eV, and 10 eV - 100 eV respectively.

The three different methods are the processes by which the substrate is carried to the target sample. Evaporation is simply the thermal heating of the solid material to a temperature generally beyond its melting point so that the vapour pressure provides the working material. Sputtering is the deliberate bombardment of a solid surface by electrons or ions of sufficient energy to dislodge atoms from the surface. These liberated particles are the source of the coating material and generally provide an improved film quality and adhesion compared with the evaporated ones. Ion plating is the most actively investigated plasma PVD process at present. Although a deposition process similar to ion plating was first patented by Berghaus (1937) in the United Kingdom and then later in the United States by Berghaus and Burkhardt (1942), a patent for ion plating was granted to Mattox (1967). It was at this time that the benefits of ion plating were recognized and the system was used commercially. The ion plating process combines elements from the two previous PVD methods with a high energy bombardment of the growing film and hence the first ion plating methods used thermal vaporization or chemical precursors.

Again, there are many acronyms describing the variations in ion plating and the process itself is sometimes referred to as "ion assisted coating" IAC, "ion assisted deposition" IAD, or "ion vapour deposition" IVD or even "ionised physical vapour deposition" iPVD. However the process, bombarding the growing film, can lead to two competing processes, those of deposition and etching/sputtering. Which one of these processes dominates is dependent on the number and energy of the impacting

ions. Usually film growth is the desired goal and the deposition rate is far greater than the etching rate.

The ions impacting the film deposit energy into it. This provides a two fold benefit. Firstly, holes and dislocations in the growing film can be minimised by collisional impact which increases the density of the film and the uniformity of the crystal structure. Secondly, the energy deposited manifests itself as heat and thus gives the advantage that it is not necessary to heat the entire sample, since now the bombardment preferentially heats the film and the sample can be held at any desired temperature with cooling or heating systems. This allows particular or specific phases of a compound or element to be grown. An example of this is the well studied phases of iron nitride.

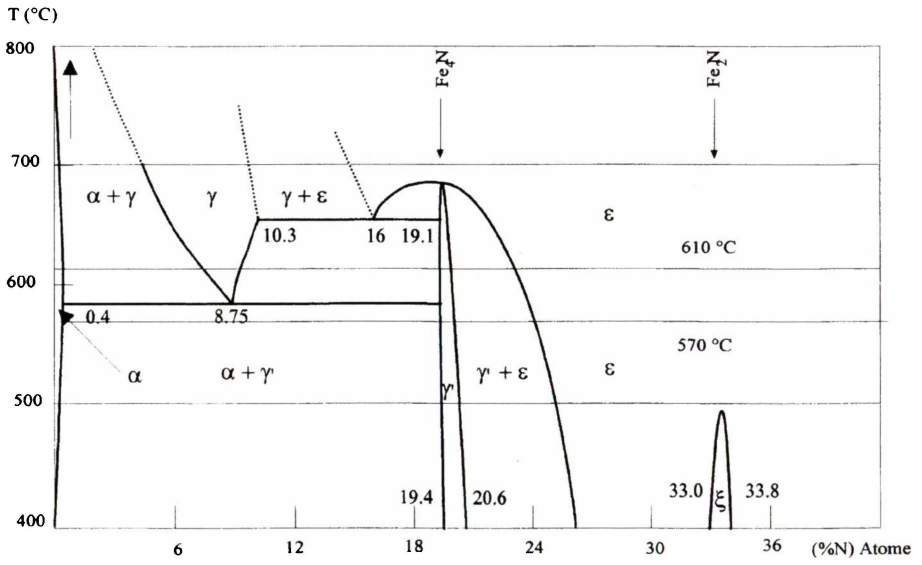

Figure 2.3 : The Fe - N phase diagram showing the relative phases vs. atomic composition, reproduced from the *Metals Handbook* (1982).

In the nitriding of iron, different phases that produce different beneficial effects occur at different temperature ranges although a sample temperature over 600 °C is needed to stabilize the nitride layers, Ricard (1997). The Fe - N phase diagram is reproduced in figure 2.3. The phases ε, γ, and γ' increase the wear and corrosion resistance while decreasing the friction coefficient of the implanted surface. The α layer increases the resistance of the target to deep wearing. The chromium nitride phase diagram is also reproduced in figure 2.4.

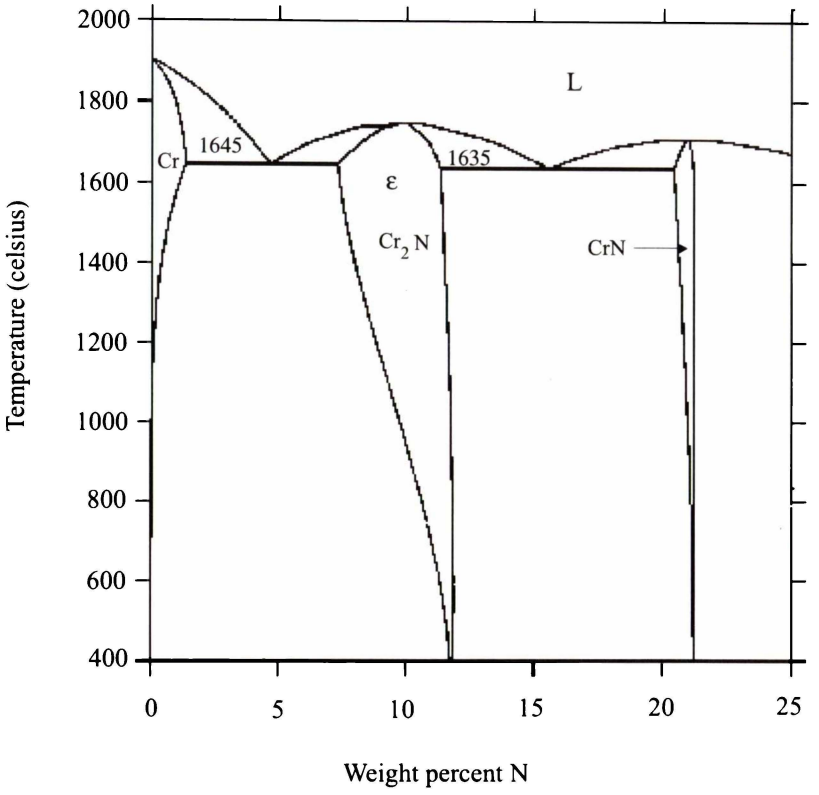

Figure 2.4 : The Cr - N phase diagram, reproduced from the *Metals Handbook* (1982).

2.4 Plasma Surface Modification

A diverse range of implantation and coating processes now exist so that films or implants can be optimised by the use of one or more methods, as well as the optimisation of the individual process parameters, as surface modification characteristics are strongly governed by partial pressures, growth rates and the final retained dose. Films can be implanted with interstitials which can have major beneficial effects, e.g. implantation of nitrogen into carbide layers and implantation into films grown by other methods such as electrodeposition.

2.4.1 Advantages of Surface Modification

Surface modification by plasmas is important because the implants and coatings obtained often cannot be produced by any other method, Holleck (1986). For those coatings that can be produced by conventional methods, such as electrodeposition, the properties of similar coatings from plasma treatment are often superior, as was found, for example, by Thoma (1986), Sliney (1986) and Qureshi *et al.* (1986). Advantages found include much better adhesion of the film to the

substrate, and more accurate control of the growth and stoichiometry of the films, with no thermal distortion, resulting in superior film properties.

In a plasma the electric field interacts with the gas molecules generating a wide variety of highly reactive species including electrons, positive and negative ions, neutral atoms and molecules in the ground and various excited states. The reactions that occur in a plasma are complex and differ from normal conditions since chemical equilibrium is not achieved. Solid surfaces can be sputtered away by various techniques and a fine line exists between plasma etching and coating since the rates can be similar. Plasma molecules also have the ability to react with the solid surface to produce new compounds.

Films of nitrides, borides and carbides are one of the most important applications of surface modification by plasmas. These films are now used extensively in industry as their properties include extreme microhardness, resistance to wear, friction, water corrosion, and oxidation up to 500 °C. Applications of these films include wear protection for cutting tools, sliding and rolling contacts for metals and alloys, decorative and protective coatings in the watch and jewellery industry, formation of resistors and diffusion barrier layers in microelectronics, solar cell technology, and superconductor applications. Transition metal nitrides, carbides, and borides have a metallic bonding structure with properties summarised in table 2.1. from Holleck *et al* (1986).

	Hardness	Brittleness	Melting Point	Stability - ΔG	Adherence	Interaction Tendency
High	b	n	c	n	b	b
	c	c	b	c	c	c
Low	n	b	n	b	n	n

Table 2.1 : Properties and schematic behaviour of transition metal carbides (c), nitrides (n), and borides (b).

Similar to film growth, implantation with elements listed in table 2.1 can also provide some of the qualities of the films without actually producing a film. This has the advantage over thin films in that there are no adhesion problems as there is no film. Dimensional changes of the substrate are not incurred since, most commonly, the nitrogen implanted is incorporated into the target lattice. No thermal distortion occurs since ion implantation is a low temperature process. Improvements in wear, corrosion, fatigue, friction properties, and micro hardness of various alloy steels as well as modification of optical and electrical properties of steels and silicon, have been reported. For transition metal alloys, reduction in orders of magnitude have been found for wear, corrosion, fatigue, and friction in laboratory and industrial tests

for standard dies, cutting tools, and steel hole punches. Of particular importance is the large reduction in wear and corrosion in medical implants such as artificial hips and knee femoral joints. Individual properties can be enhanced over others, or maximised for specific parameters, by control of deposition rates, implant doses, implant energies, and partial pressures of reactants as well as careful selection of alloys to be treated by a specific method. Many of the effects are dependent on the stoichiometry of the film, or the implanted layer, since this determines the compound formed and the crystallographic orientation of the film or implant. For example, titanium nitride forms many different phases depending on the gas composition, e.g. TiN, Ti_2N. Nitrogen implantation also has its limitations as beneficial wear, corrosion and friction properties are found only for substrates that contain transition metals such as Ti, V, Cr, Co, Ni for doses of 2×10^{17} - 1×10^{18} atoms cm^{-2}. This is the reason why austenitic stainless steels show the greatest improvements in these properties. References of these experiments can be found in Conrad *et al.* (1987).

Ion implantation is of enormous benefit in the semiconductor industry as the implant dose of any ion or ions to depths up to 10^{-5} m into any surface is possible depending on the ion energy, the total dose and ion species of the ion beam. The production of doped layers beneath the target surface, for use as optical waveguides, is one of the more recent applications to semiconductors. More efficient production of integrated circuits and etching procedures have been developed and applied in the past. A large number of applications and technology can be found in the books by Chernow *et al.* (1976), Kossowsky and Singhal (1984), Hollahan and Bell (1974), Perez and Coussement (1980), and Ziegler (1992).

The effects of surface modification hold enormous potential for the maximisation and efficient use of resources as well as reduced treatment times for production, less maintenance and machine down time, resulting in cost cutting for industry. These gains in the past have been offset by the large costs associated with plasma surface modification, especially with ion beams, so that industry acceptance has been slow and cautious. For this reason techniques such as PSII have been developed which reduce the costs, processing time, and the main problems associated with ion beams e.g. retained dose, sputtering rates, and target manipulation.

2.4.2 Chromium and Plasma Processing.

Chromium is one of 10 elements that comprise the first row transition elements in the periodic table. Its electron configuration is different from all other 3d transition elements apart from copper in that the 4s shell contains only one electron. In its metallic form, chromium takes a high polish and is well known for its shiny

lustrous finish. Its primary use is for the hardening of steels and the corrosion resistance it imbues to metals it is alloyed with. For these reasons it is an important metal in ion deposition processes. Compounds such as the nitrides, borides and carbides of chromium are some of the hardest, wear resistant, and corrosion resistant known. Similar to titanium, two forms of nitrides exist. The first is a physical structure of chromium bound to nitrogen in a regular crystal lattice resulting in the compounds CrN or Cr_2N. The second is the implantation or insertion of nitrogen molecules or atoms into the crystal structure of chromium metal (lattice structure bcc) itself. This second type is important process for ion implantation since the crystal structure can be strengthened without growth of a film. The rational is that since that nitrogen sits into the vacant spaces between the chromium atoms in its bcc lattice, it locks the crystal structure by making it more difficult for the chromium atoms to slide past each other. It is roughly equivalent to the hardening of iron by adding a small amount of carbon, which is also placed interstitially, resulting in the alloy steel.

Metallic chromium is normally deposited by chemical or electrochemical means. Two forms are deposited by these methods, either from the +3 or +6 oxidation states. All deposition processes, apart from those used in decorative coatings use the +6 oxidation state which produces superior coating properties. This oxidation state of chromium is highly toxic and is a carcinogen which requires its handling and disposal subject to many safety regulations. The main difficulty for industry is that safe disposal of the waste products after deposition are prohibitively expensive and have prompted the industry to search for alternative methods of depositing coatings equivalent to those produced chemically. Apart from the sputtering of chromium metal onto a target, or ion beam deposition, few plasma techniques exists to deposit chromium, or any other metal. Most plasma research on chromium deposition are either variants of ion plating, (in which the objective is to produce chromium nitrides or carbides), or implantation of nitrogen into existing chromium films (or films grown in conjunction with ion implantation techniques PSII, PIII, ion beams).

2.5 Physical State of the Implanted Solid

The types of defects directly generated by the incident ions are primarily vacancies and interstitials due to atom displacement and multiple vacancy centres in denser cascades. Large numbers of displacements are common, which can result in every atom being displaced many times during implantation. Some of the interesting physical states which can result include; homogenous layers (metastable or

equilibrium), new structures and amorphous phases, extremely fine dispersion of precipitates, high compressive stresses and dense defect microstructures.

In pure crystals, interstitials become mobile first. As the temperature is increased, vacancies become mobile, defect clusters become unstable, and at higher temperatures, extended defects anneal. At most implantation temperatures, some of the defects are mobile so that appreciable defect interaction and annealing occurs giving rise to secondary defect generation and the defect microstructure.

2.5.1 The Hardening of Metals by Implantation

Several mechanisms are believed to be important in the hardening of metals by ion implantation. Among these are compressive stress creation due to the injection of a large number of interstitial atoms, metal nitrides and related compound formation at high implantation doses, and dislocation pinning by mobile interstitials.

Interstitial atoms such as carbon and nitrogen interact strongly with the strain fields of the dislocations. The interstitial atoms are also surrounded by strain fields. When these atoms move within the dislocation strain field there is an overall reduction in the total strain energy. This energy reduction can cause interstitial atmospheres to condense in the vicinity of dislocations. In extreme cases, these concentrations can form lines of condensed atoms along the cores of the dislocation. The binding energy between a dislocation in steel and a interstitial carbon or nitrogen atom is ~ 0.5 eV. At low temperatures, dislocations can be held in position by strings of interstitials along the dislocation lines, increasing the stress needed to cause dislocation movement and hence increasing the wear and fatigue properties of the steel.

In order to form interstitial atmospheres at dislocations, diffusion of the solute from a random atmosphere must occur. This is possible in the 20 - 200°C temperature range due to the high diffusivity of carbon and nitrogen in steel. The interstitial concentration, c, in a dislocation strain field at a point where the binding energy is U is defined in equation 2.1

$$c = c_0 e^{-\left(\frac{U}{kT}\right)} \tag{2.1}$$

Normally a Maxwellian distribution of solute atoms around the dislocation would be expected. However the elastic interaction energy, U, between the solute and the dislocation interstitials in steel is so high that $U > kT$. This causes the atmosphere to condense. This condensed atmosphere has been confirmed experimentally by Longworth and Hartely (1978) using Mössbauer spectroscopy which is sensitive to the local environment of the iron nuclei.

Generally, an "as implanted" steel specimen contains impurity nitrides (Fe_4N, Fe_3N, Fe_2N, FeN, CrN, Cr_2N, TiN). After annealing at temperatures as low as 270 °C Burenkov and Komarov (1991) found that all the nitrogen can be dispersed in interstitial form.

From equation 2.2 there is a critical temperature below which condensation of the implanted random atmosphere will occur. This happens when c = 1 and U is maximised, giving

$$T_{crit} = \frac{U_{\max}}{k \ln\left(\frac{1}{c_0}\right)} \tag{2.2}$$

If $c_0 = 10^{-4}$ (1000 interstitials per dislocation line) and U_{max} = 0.5 eV, then T_{crit} = 630 K or 350 °C, which is in rough agreement with experimental results.

The temperatures found experimentally and theoretically are not very high and, in some cases, less than the sample temperatures during implantation. This means that transfer of implanted nitrogen into interstitial vacancies can occur immediately and accounts for many of the structural properties of nitrided steels. This effect is the reason why nitrogen implantation is so beneficial to wear resistance at depths far in excess of the implanted ion range. As wear proceeds, a dense network of dislocations propagates into the metal as the local subsurface stress increases past a critical point. Because of the strong attraction between interstitials and dislocations, transport of the impurities occurs by a process referred to as solute drag. Essentially the dislocations drag the interstitial atoms with them to deeper and deeper depths. Thus interstitial nitrogen is kept at a constant depth below the surface, neglecting nitrogen losses from the removal of wear volume, and disperses away from the wear region.

Metal	Phase in thermodynamic equilibrium at 300K	Observed phase	Comments
Cr (bcc)	Cr_2N (hcp)	Cr_2N, CrN (CrN is fcc)	Cr_2N and CrN form in sequence
Fe (bcc)	Fe_4N (fcc)	Fe_4N, Fe_3N (Fe_3N is hcp)	Fe_4N and Fe_3N form in sequence
Ti (hcp)	Ti_2N (~hcp)	TiN (fcc)	TiN seen as precipitates
V (bcc)	V_2N (hcp)	VN_x	x is significantly greater than zero

Table 2.2 : Comparison of the phases produced by N impact on metals with those expected for thermodynamic equilibrium, taken from Kelly (1982).

Diffusion of nitrogen into pure chromium is one hundred times higher than for diffusion into γ-Fe while α-Fe has the highest diffusion rate of any metal encountered so far, one hundred times the chromium diffusion rate. Another important point about nitrogen incorporation in this alloy is that both metals have the same crystal structure (bcc for Cr and α–Fe) while the nitrides of these elements are hcp and fcc respectively, as shown in table 2.2.

The diffusion lengths quoted in table 2.3 are likely to be lower limits of the true values. In general the mobility in bcc lattices is the highest, which is attributed to the open lattice structures.

Metal	Structure	$(Dt)^{1/2}$ for N (Å)
Cr	bcc	9
α-Fe	bcc	2000
γ-Fe	fcc	0.08
α-Ti	hcp	0.002
β-Ti	bcc	0.2
V	bcc	0.07

Table 2.3 : Volume diffusion length $(Dt)^{1/2}$ for N in various metals evaluated for T = 373K and t = 6000 s, reproduced from Kelly (1982).

2.5.2 Solid Solutions

One of the distinguishing features of ion implantation is that it randomly introduces a new chemical species into a solid in a dispersed fashion. This is an ideal process for forming solid solutions. Both equilibrium and metastable phases can be produced. The stability of the solution and the phase is determined by the radius ratio of the atomic species involved and the concentrations of the species.

Several classes of solid solutions exist.

A) Similar atoms.

Atoms of similar size with the same number of valence electrons and the same metal structure. These mixtures are stable over the entire composition range, (0 - 100 %).

B) Loves Phases.

These are formed when the size difference in the atoms is > 15%. Mixtures formed are approximately AB_2 where A is the large radii atom. Ideally $r_{large}/r_{small} = 1.225$ from geometric considerations. Experimentally, stable phases exist for ratios over the range 1.05 - 1.68. Other related phases are AB_3, AB_4 etc where high coordination numbers provide stability.

C) Electron Compounds (Hume - Rothery phases).

A series of phase changes occur, mainly for alloys of post transition metals. Boundaries are at particular electron/atom radii and occur for alloys such as brass.

The radii of various atomic species are presented in table 2.4 where the Muffin-Tin radii are equal to half the distance to the nearest atom in the appropriate crystal structure. From table 2.4 the atom radii vary considerable depending on the compound, or measurement technique. Experimentally, many phases are found for the borides, carbides, and nitrides so we expect class B to determine the lattice structure of the compound. Furthermore, the phases produced are often not those produced by thermodynamic equilibrium.

Element	Muffin-Tin radius	Radii from covalent molecules	Van der Waals radii
C	1.05	0.77	
N	2.01	0.70	1.57
O	1.47	0.66	1.40
Ti	1.37		
V	1.23		
Cr	1.18		
Fe	1.14		

Table 2.4 : Values of the Muffin-Tin radii from Ziegler *et al.* (1985) and other comparable radii from measurements on covalent molecules and Van der Waals solids.

2.5.3 Precipitate Formation And Evolution.

If the implanted atoms are mobile during implantation, then precipitation can occur when equilibrium solubilities are exceeded. The phases observed are those predicted by equilibrium phase diagrams. If the temperature during implantation is too high, the implanted atoms may diffuse out of the implanted layer as fast as they are introduced. Implanted atoms can also be immobilised before precipitation can occur, and a dispersed solution above equilibrium solubilities is maintained.

Precipitates may also occur by post implantation annealing. As the implant is heated, the atoms become mobile and the equilibrium phase predicted at that concentration can precipitate. The disorder produced by implantation can thus be annealed out. At higher temperatures diffusion into the bulk of the material can occur. In general, a very high density of small precipitates results due to the high

nucleation densities with typical precipitate sizes being 10 - 100 Å. Iron nitriding using glow discharges form such coatings as found in the papers by Bougdina *et al.* (1991) and Meletis and Yan (1993).

2.6 Review of Coating and Implantation Methods

Since plasma surface treatment is of great advantage in modifying surfaces, many processes have been developed to achieve this goal and other processes have been modified to achieve similar results. For comparison to work in this thesis we will narrow our focus in this area to deposition of chromium films, chromium nitrides and the implantation of nitrogen into chromium films.

2.6.1 Metallic Coatings from Plasma Deposition of Carbonyls

Many plasma sources and discharge configuration methods have been used to produce metallic films from metal carbonyl and metallorganic compounds. Most of these have been forms of chemical vapour deposition. Precursor compounds that are not carbonyls will in general be ignored, as most of these use complex organic molecules mainly used in CVD processes as opposed to the plasma processing that is considered in this thesis. Considering publications in the last 20 years where carbonyl precursors have been used, we start with Foord and Jackman (1984) who used pyrolytic, UV photolytic and electron beam deposition methods to form Fe films on silicon in ultra high vacuums. Considerable contamination by carbon and oxygen was found using Auger electron spectrometry. Gluck *et al.* (1987) used laser photolysis of carbonyls to form thin films of chromium, molybdenum and tungsten on silicon substrates. High levels of C and O impurities were found which required laser heating and annealing at temperatures up to 1200 K to reduce the impurity levels.

Feurer and Suhr (1988) used a commercial parallel RF reactor to deposit palladium films using an argon carrier gas. Some of their films were quoted as being 100% metallic. These films appear to have only been analysed for metal and carbon content by atomic absorption spectroscopy and a carbon analyser. The highest film conductivity reported was, however, half that of bulk palladium. Agarwal *et al.* (1988A) deposited chromium films by an evaporation method in an RF ammonia plasma. Using secondary ion mass spectrometry (SIMS) they found a variety of N, NH, C, and CH species deposited in the films. The concentrations of these impurities could be reduced by vacuum annealing at temperatures up to 773 K. Czekaj and Geoffroy (1988) used standard chemical vapour deposition methods to grow Fe and Co films. The temperature range for coherent film formation was a narrow band

between 573 K to 623 K. No composition analysis is given, only ratios of iron to cobalt in the film using atomic absorption analysis.

Turney *et al.* (1992) approached the problem of metallic film generation from carbonyls using a pulsed laser chemical vapour deposition method at two different wavelengths. The metallic content of the films ranged from 20% to 71% for tungsten, molybdenum and vanadium films measured by Auger electron spectroscopy. Suhr *et al.* (1992) also used a parallel plate reactor to deposit chromium, molybdenum and tungsten films from their carbonyls using carrier gas mixtures of Ar/O_2 and H_2S/H_2. The minimum temperature of the substrate to initiate film growth was 448 K while metal composition ranged from 25 wt% to 85 wt%, measured with atomic absorption spectroscopy.

Boyd *et al* (1997) used chemical vapour deposition without a carrier gas to deposit films of Co, Fe, Ru and Os at vacuum pressures of 1.3×10^{-3} Pa onto glass slides. These features make this approach different from normal chemical vapour deposition. High quality, low impurity films were reported. Typical carbon and oxygen impurities levels are quoted as 5 and 3 atomic percent respectively from X-ray photoelectron spectroscopy. Auger electron spectroscopy indicated consistent composition throughout the film depth. The film growth rates were between 73 and 240 angstroms per hour depending on the metal carbonyl being used. Slow oxidation of the film surface occurred in contact with air.

Carson and Chumbley (1997) used chromium metal powder and hexacarbonyl sublimination as precursors in an atmospheric RF torch to deposit thin chromium films onto steel and copper targets. A carrier gas of argon was used to transport the precursor. It was found that the hexacarbonyl produced superior films to the chromium powder but all had high levels of oxygen determined by Auger analysis, while the adhesion of the films overall was poor. No sample cleaning was performed and hence the oxide layer on the metal surface would have impeded the film bonding to the substrate. The films were thin with a maximum of 500 nm thickness, but no time of the experiments was given so the growth rates cannot be calculated.

These are the closest process used by other researchers to the work in this thesis. It reinforces the perception that RF plasmas are not the best choice for deposition of pure metallic films from carbonyl precursors. As speculated by Carson and Chumbley (1977), the oxygen levels for the carbonyl experiments probably originated from the dissociation of the liberated carbon monoxide while for the chromium powder the oxygen source was from the powder itself since it readily oxidises in air.

2.6.2 Ion Beams

Ion beams are the traditional method of implanting foreign atoms into surfaces. Originally they were developed for the semiconductor industry and have since been adapted for the implantation of nitrogen into films or substrates such as hard chromium layers, for example, to improve various properties such as wear or hardness as previously discussed.

Ion beams can be created from any element and provide ions of energies ranging from one keV to well into the MeV range, with beam currents from microamps to milliamps. In 1985 ten commercial ion implantation centres existed that use ion beams for nitrogen implantation into metals, Wittokwer and Hirvonen (1985). Ion beams have limitations as it is necessary to dissipate the power transferred to the target by the implantation process. If this energy is not dissipated, the target temperature can rise too high, causing diffusion of the implanted ions further into the target and beneficial effects may be lost. Temperature control is achieved by pulsing the ion beam to minimise diffusion. As detailed by Smidt and Sartwell (1985) and Smidt *et al.* (1987) surface temperature rises can be up to 800 °C for a 300 W/cm^2 beam over a 10 second duration.

During implantation with ion beams it is necessary to rotate or mask the target if the surface geometry of the target deviates away from planar geometry over the area of the beam. Masking is necessary to minimise sputtering effects at large incident angles, while manipulation of the target provides the most uniform implanted dose over the target area. In figure 2.5, reproduced from Smidt *et al.* (1987), it can be seen that the retained dose drops quickly with the beam angle regardless of the elements forming the beam.

Sputtering occurs in the first few atomic layers and results from energy deposition into nuclear collisions near the surface where some atoms receive a sufficiently negative component of momentum normal to the surface that they overcome the surface binding energy. This momentum transfer increases rapidly at increasing angles and the theory, compared by Dearnaley (1983), matched well with the experimental results. To minimise these effects, target masking is necessary which makes ion implantation with ion beams a time consuming process for spherical, cylindrical and any non planar target unless the beam can be well defined. It should also be noted that if the target is masked, then no target manipulation is possible.

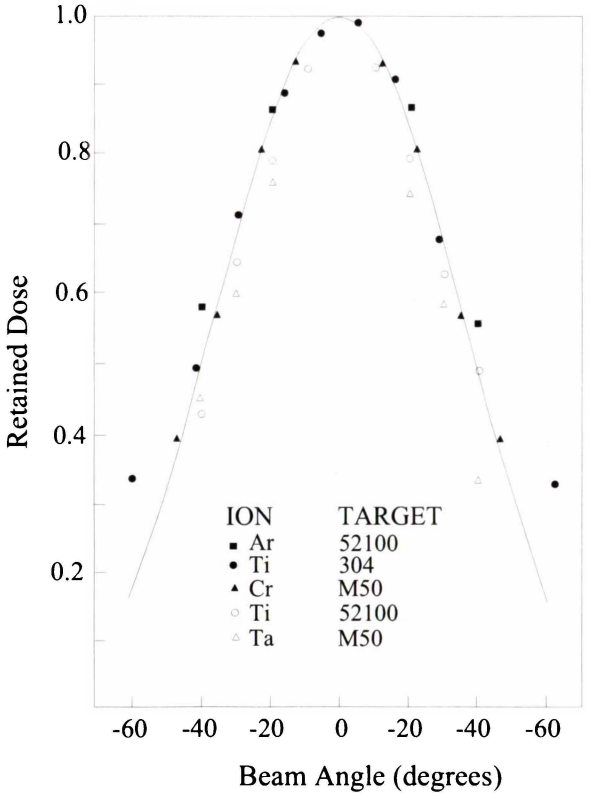

Figure 2.5 : Normalised retained dose (1 - 10 × 10^{17} atoms cm^{-2}) for a 150 keV ion energy.

The creation of ion beams involves careful design and beam control as the ions need to be accelerated to the required energy independent of the main implantation chamber and are usually confined to a narrow beam. The main advantage of ion beams is that they allow the depth and number of ions (of any atomic number) implanted into any material to be controlled independently. The dose is controlled by the beam current and implant time while the depth is controlled by the ion energy and the target temperature. Ion beams, of all the implantation or film modification methods, have no requirements on the target to be implanted, e.g. it is not necessary for the target to be conducting, so that a much broader range of applications is available for ion beams compared to other surface modification techniques such as PSII.

Specifically for chromium nitride formation, Demaree *et al.* (1996) used ion beams in the formation of Cr_xN_y films. The research motivation was to find a replacement for hard electroplated chromium due to the difficulties in disposal of the toxic byproducts. The films were produced by the thermal evaporation of chromium metal inside the vacuum chamber and simultaneous bombardment of the growing film with a 1200 eV nitrogen ion beam. The result always contained 3 - 5 atomic percent of oxygen impurities. Nitrogen contents of up to 45 atomic percent were also reported. The films were deposited on a range of substrates including silicon,

stainless steel, carbon foil, and glass slides and were less than 1 μm in thickness. The analyses completed included Rutherford back scattering (RBS), cohesive and adhesive strength measurements as well as examination of the surface in an scanning electron microscope (SEM).

Engel *et al.* (1998) used nitrogen ion beams and an electron beam evaporator to form Cr_2N and CrN films onto silicon and steel samples. The film composition was determined by Auger electron spectroscopy (AES), and x-ray diffraction studies (XRD) for which the nitrogen levels ranged from zero to 40 atomic percent. No impurity levels were presented. The films were tested for corrosion resistance as well as hardness. The experimental details of the sample conditions are not well defined and the authors only state that the beam energy ranged from 0.5 to 15 keV. Again no growth rates are given although it is stated that the films are less than 1 μm in thickness. In a later paper Engel, and the same co-authors (Engel *et al.* (1999)) extend their analysis of the films previously reported and include some details, such as the sample temperatures and the beam energies and the sample preparation techniques.

Volz *et al.* (1998) used electron beam evaporated chromium and a 30 keV nitrogen beam to deposit a mix of Cr, CrN, and Cr_2N onto silicon substrates. A variation of phase throughout the film and into the silicon substrate was observed via depth profiling using nuclear reaction analysis (NRA) and is unsurprising with a beam energy of this magnitude. The samples were polished, cleaned, and then etch bombarded before the coating experiments began. The cross-section and structure of the films were analysed with transmission electron microscopy (TEM) where it was found the films were 0.1 - 0.2 μm in thickness. No physical or mechanical analyses were performed.

Fu *et al.* (1999) used an argon beam to sputter deposit chromium films onto glass and steel which were simultaneously bombarded with a nitrogen beam of energy varying from 4 - 12 keV. Scanning electron microscopy (SEM) and AFM imaging showed that the films were finely grained with the particulate range size of 100 - 200 nm. The chemical composition determined from depth profiling is interesting and was achieved using x-ray photoelectron spectroscopy (XPS). The film shows significant mixing at the boundary layer which presumably comes from the high sample temperature indicated by the authors. The chromium and nitrogen contents are 50 and 40 atomic percent respectively with the remainder being mainly oxygen (~6 %) and a little silicon. Low angle XRD data is presented which confirms the film structure is CrN with the film thickness given as 1 μm.

2.6.3 Ion Plating and Ion Coating

These techniques can be distinguished from ion implantation in several ways although some features are common. In ion plating, the substrate bias is < 4 kV which is too low for substantial penetration of the ions into the target surface. Ion plating thus forms a coating on the target which is susceptible to scratching and delamination effects whereas implantation results in no film growth. The only possible exceptions for implantation are the change in the crystal structure lattice dimensions due to the volume increase needed to accommodate the implanted ions, and precipitation of the new compound.

It has been claimed by Kobayashi and Doi (1978) that a good coating layer with good cohesion can only be obtained at low temperatures by ion plating. Ion plating can occur by a variety of methods, e.g. evaporation methods, reactive ion sputtering. Most of these methods are summarised in a review by Spalvins (1980). Further reviews on ion coating and plating have been detailed by Sundgren (1985), Sundgren and Hentzell (1986), Harper *et al.* (1982), and more recently by Rossnagel *et al.* (1990), and Glocker and Shah (1994). The published literature on ion plating processes is vast so we will only review selected papers involving the generation of chromium nitride films. A wide variety of plasma processes, sources of chromium and nitrogen, pressure ranges and discharge configurations have been used to generate chromium nitride films. All of them make use of a plasma however. It will be seen in the review of the papers that follow that raising substrate temperature and/or bombardment of the growing film promotes the nitride growth, in accordance with the phase diagram in figure 2.4. This is a different process to the ion beam coating techniques where the beam current density to the chromium flux ratio plays a crucial role.

Agarwal *et al.* (1988B) used activated reactive evaporation (ARE) in a low pressure ammonia vapour (0.2 Pa) to deposit chromium nitride films onto silicon substrates. In this technique, the chromium is electroplated onto tungsten filaments which were subsequently heated until the required rate of evaporation occurred. By varying the temperature of the substrates, it was found that Cr, CrN, and Cr_2N could be deposited onto the silicon. The different films were identified by XRD analysis of the crystal structure while the N/Cr ratio increased with temperature using AES. At temperatures above 773 K, the films were found to exclusively possess the CrN morphology. It was further seen that as the temperature of the substrate rose, and hence the nitrogen levels increased, the films observed using a SEM had an increasing grain size from 50 nm at 303 K to 250 nm at 773 K.

Ehrlich *et al.* (1995) used a vacuum arc deposition process where the cathode was a chromium disc to produce chromium nitride films on steel and glass samples.

The sample could be held at a constant temperature while being independently biased. The sample temperature was held at 380 °C and the highest coating rate of 140 nm min^{-1} was observed when the sample was left at the floating potential. The nitrogen gas pressure was raised from zero to 1.5×10^{-2} mbar where the Cr/N ratio was the highest (0.5) and CrN was formed. Below this pressure, the ratio fell and at a pressure of 2×10^{-3} mbar, the composition was Cr_2N. The conclusion drawn by the authors was that with the sample floating, the lower ion energies reduced nitrogen resputtering from the film surface and thus promoted the growth of CrN over Cr_2N.

Baborowski *et al.* (1996) used a DC reactive magnetron discharge with argon gas to sputter a Cr target while nitrogen or ammonia were the reactive gases. Film compositions of CrN only were obtained at pressures of 5.3×10^{-4} mbar for sample temperatures ranging from room temperature to 400 °C. Deposition rates depended upon the power applied to the sample and growth rates up to 18 nm min^{-1} were obtained at 9 W cm^{-2} in a nitrogen atmosphere. When the bias on the sample was the floating potential (-20 V) the films were well crystallised and the XRD spectra had well defined peaks. When -155 V was applied to the samples a lesser quality of crystallisation occurred and the CrN peaks were broader and shifted.

Pakala and Lin (1996) used a RF magnetron sputtering deposition system to grown Cr_xN_y films on steel substrates. With substrate temperatures below 200 °C, a mix of Cr, CrN and Cr_2N films were found. Above this temperature, or with an increased nitrogen gas content, CrN films were formed. However, increasing the deposition temperature to 400 °C resulted in CrN films of poor quality since spalling of the films occurred readily due to the high thermal stress in the films.

Hurkmans *et al* (1996) used an unbalanced magnetron cathode arc discharge for film deposition. Similarly to Pakala and Lin (1996) they found that CrN was only formed at high nitrogen flow rates while they held the sample temperature constant at 250 °C. Films with the highest hardness had poor adhesion which the authors attribute to the high internal stress of the Cr_2N films. Grant *et al.* (1996) using a cathodic arc, also found that increasing nitrogen partial pressure increased the nitrogen content in the film until a Cr/N ratio of one was achieved at 5.3×10^{-4} mbar. The increase in the nitrogen content also lead to increased residual stress in the films. Again Hones *et al.* (1997) found that the nitrogen partial pressure and the sample temperature determined what phase of Cr_xN_y was deposited in a RF magnetron sputtering discharge. Confirming previous results, larger grain sizes were found for increasing substrate temperatures while the transition from Cr_2N to CrN occurred at 2×10^{-5} mbar.

He *et al.* (2000) used a DC magnetron sputtering process to deposit CrN films onto silicon substrates. Cr/N ratios ranging from 0.73 to 1.46 were found at sample

biases up to -600 V. It was found that increasing the sample bias or increasing the nitrogen partial pressure raised the nitrogen content in the films. Argon was used as a carrier gas and promoted the bombardment and resputtering of the films at higher substrate potentials. It was shown that an increased sample bias enhanced the sputtering of particular lattice planes and the crystal morphology could be adjusted by controlling the nitrogen partial pressure and the substrate bias.

Bertóti *et al.* (2002) deposited Cr_xN_y films using a DC magnetron discharge plasma onto molybdenum, stainless steel, and silicon substrates by sputtering a Cr target in an argon/nitrogen atmosphere at pressures of 4×10^{-5} mbar. The sample temperature was held constant at 300 °C. After deposition, the films were subjected to argon or nitrogen ion beam bombardment to remove surface oxygen and carbon contamination. Cr/N ratios of 2 - 0.83 were obtained via the incorporation of the ion beam particles into the film, analogous to implantation techniques.

2.6.4 Plasma Source Ion Implantation

This implant technology provides conditions where the target can be implanted uniformly by ions in the plasma irrespective of the target geometry. This method avoids complex target manipulation, and the retained dose problem found in ion implantation using ion beams, resulting in a superior implant (no sputtering at low beam angles) in a much reduced time (no need to mask target). In PSII this is achieved by biasing the target to large negative potentials, $\geq$ 25 kV, with low duty cycle pulses. This voltage pulse creates an ion sheath around the target so that ions are accelerated into the target uniformly and perpendicular to the target surface.

In the process a growing film, or a film previously grown, can be implanted analogous to the ion beam methods previously described. Almost all the papers published using these techniques are for the implantation of nitrogen into alloys of iron. Literature on implantation into metals such as chromium are not nearly as common as they are for steel substrates. The papers available for chromium will now be reviewed.

Chen *et al.* (1996) created implantation targets by depositing a 22 μm thickness hard electroplated chromium film onto a steel substrate. These targets were subsequently implanted at 60 keV with nitrogen ions to doses of 3 and 6×10^{17} atoms cm^{-2} after the chromium surface had been sputter cleaned with argon. Implantation depths of 0.2 and 0.3 μm were observed for these doses respectively with the maximum nitrogen content being 40 atomic percent. The presence of CrN as the main crystal structure was determined by electron spectroscopy. The chromium films also contained a consistent level of oxygen of 12 atomic percent which was

incorporated into the film from the electroplating process and surface contamination. Reduced wear and friction coefficients were observed for both doses.

Walter *et al.* (1996) also used an implantation method to modify 50 μm electrodeposited chromium films. Ammonia was used as the implantation gas primarily to try to obtain ionised nitrogen atoms rather than molecules. The implantation voltage was 60 keV. The composition of the implanted films was attributed to stoichiometric CrN which contained 12 atomic percent of hydrogen. The retained dose was found to be sputter limited at 2.2×10^{17} atoms cm^{-2} (nitrogen). Modest increases in hardness and good increases in wear resistance were observed.

Falkenstein *et al.* (1999) implanted nitrogen into pure aluminium sheets and electrodeposited chromium films 1 mm thick. The results were then compared the results to similarly implanted nitrogen using a 25 keV ion beam. The PSII voltage was 50 keV while the retained dose is given as $\sim 10^{18}$ atoms cm^{-2}. It was found that the nitrogen from the beam experiments penetrated to much greater depths due to diffusion since the samples reached a much higher temperature than they did in the PSII experiments.

Kuze *et al.* (2002) implanted nitrogen into a growing chromium film using a cathodic arc plasma where the metal source was a chromium disc. The chromium was deposited onto silicon substrates and were implanted by the application of 20 and 30 keV pulses. The films were determined to be CrN in composition by XRD.

2.7 References

Agarwal, V., V. D. Vankar, and K. L. Chopra, 1988A, J. Vac. Sci. Technol. A, **6**, 4, p 2341.

Agarwal, V., V. D. Vankar, and K. L. Chopra, 1988B, J. Vac. Sci. Technol. A, **6**, 4, p 2361.

Baborowski, J., M. Charbonnier, and M. Romand, 1996, Surf. Coat. Technol. **80**, p 190.

Berghaus, B., 1937, *"Improvements in and Relating to the Coating of Articles by Means of Thermally Vaporized Material"*, British patent 510 933.

Berghaus, B. and W. Burkhardt, 1942, *"Coating of Articles by Cathode Disintegration"*, U.S. patent 2,305,758.

Bertóti, I., M. Mohai, P. H. Mayrhofer, and C. Mitterer, 2002, Surf. Interface Anal., **34**, p 740.

Boulos, M. I., 1991, IEEE Trans. Plasma Sci., **19**, 6, p 1078.

Boyd, E. P., R. Ketchum., H. Deng, and S. G. Shore, 1997, Chem. Mater, 9, p 1544.

Bougdina, J., H. Henrion, M. Fabry, 1991, J. Appl. Phys. D, **24**, p 1076.

Burenkov, A. F., and F. F. Komarov, 1991, Vacuum, **42**, 1/2, p 13.

Carson, L., and L. S. Chumbley, 1997, Scripta Materialia, **37**, 10, p 1531.

Chen, A., X. Qiu, K. Sridharan, W. G. Horne, R. A. Dodd, A. H. Hamdi, A. A. Elmoursi, G. W. Malaczynski, and J. R. Conrad, 1996, Surf. Coat. Technol., **82**, p 305.

Chernow, F., J. A. Borders, D. K. Brice, 1976, Eds., *Ion Implantation in Semiconductors*, (Plenum Press, New York).

Conrad, J. R., R. L. Radtke, R. A. Dodd, F. J. Worzala, and N. C. Tran, 1987, J. Appl., Phys., **62**, 11, p 4591.

Conrad, J. R., 1988, "*Method and Apparatus for Plasma Source Ion Implantation*", U.S. patent 4,764,394.

Czekaj, C. L., and G. L. Geoffroy, 1998, Inorg. Chem, **27**, p 8.

Dearnaley, G., 1983, Thin Solid Films, **107**, p 315.

Demaree, J. D., C. G. Fountzolas, and J. K. Hirvonen, 1996, Surf. Coat. Technol., **86** - **87**, p 309.

Ehrlich, A., M. Kühn, F. Richter, and W. Hoyer, 1995, Surf. Coat. Technol. **76** - **77**, p 280.

Engel, P., G. Schwarz, and G. K. Wolf, 1998, Surf. Coat. Technol., **98**, p 1002.

Engel, P., G. Schwarz, and G. K. Wolf, 1999, Surf. Coat. Technol., **112**, p 286.

Falkenstein, Z., K. C. Walter, M. A. Nastasi, D. J. Rej, 1999, J. Mater. Res., **14**, 11, p 4351.

Feurer, E., and H. Suhr, 1988, Thin Solid Films, **15**, 157, p 81.

Foord, J. S., and R. B. Jackman, 1984, Chem. Phys. Lett., **112**, 2, p 190.

Fu, Y., X. Zhu, B. Tang, X. Hu, J. He, K. Xu, 1999, Mater. Lett., **40**, p 192.

Glocker, D. A., and S. I. Shah, 1994, Eds., *Handbook of Thin Film Process Technology*, (IOP Publishing, New York).

Gluck, N. S., G. J. Wolga, C. E. Bartosch, W. Ho, Z. Ying, 1987, J. Appl. Phys., **61**, 3, p 998.

Grant, W. K., C. Loomis, J. J. Moore, D. L. Olsen, B. Mishra, and A. J. Perry, 1996, Surf. Coat. Technol., **86** - **87**, p 788

Harper, J. M. E., J. J. Cuomo, and H. R. Kaufman, 1982, J. Vac. Sci. Technol., **21**, 3, p 737.

He, X.-M., N. Baker, B. A. Kehler, and M. Nastasi, 2000, J. Vac. Sci. Technol. A, **18**, 1, p 30

Hershkowitz, N, 1998, IEEE Trans. Plasma Sci., **26**, 6, p 1610.

Hollahan, J. R., and A. T. Bell, 1974, Eds., *Techniques and Applications of Plasma Chemistry*, (Wiley and Sons, New York).

Holleck, H., 1986, J. Vac. Sci. Technol. A, **4**, 6, p 2661.

Hones, P., R. Sanjines, F. Lévy, 1997, Surf. Coat. Technol., **94 - 95**, p 398.

Hurkmans, T., D. B. Lewis, J. S. Brooks, and W.-D. Münz, 1996, Surf. Coat. Technol., **86 - 87**, p 192

John, P. I., 1993, Current Science, **1**, 10, p48.

Kelly, R., 1982, J. Vac. Sci. Technol. A, **21**, 3, p 778.

Kobayashi, M., and Y. Doi, 1978, Thin Solid Films, **54**, p 67.

Kossowsky, R., S. C. Singhal, 1984, Eds., *Surface Engineering*, (Nato Series No. 85, Matrinus Nijhoff Publishers, Boston).

Kuze, E., T. Teramoto, K. Yukimura, and T. Maruyama, 2002, Surf. Coat. Technol., **158 - 159**, p 577.

Longworth, G., and N. E. W. Hartley, 1978, Thin Solid Films, **48**, p 95.

Mattox, D. M., 1967, "*Apparatus for Coating a Cathodically Biased Substrate from Plasma of Ionized Coating Material*", U.S.patent 3,329,601.

Meletis, E. I., and S. Yan, 1993, J. Vac. Sci. Technol. A, **11**, 1, p 25.

Metals Handbook, 1982, Vol 2, (ASM International, Metals Park, Ohio).

Pakala, M., and R. Y. Lin, 1996, Surf. Coat. Technol., **81**, p 233.

Perez, A., and R. Coussement, 1980, Eds., *Site characterization and Aggregation of Implanted Atoms in Materials*, (Plenum Press, London).

Qureshi J., A. Levy, and B. Wang, 1986, J. Vac. Sci. Technol. A, **4**, 6, p 2638.

Ricard, A., 1997, J. Phys. D: Appl. Phys., **30**, p 2261.

Rossnagel, S. M., J. J. Cuomo, W. D. Westwood, 1990, Eds. *Handbook of Plasma Processing Technology*, (William Andrew Publishing/Noyes Publications, New York).

Schram, D. C., Th. H. J. Bisschops, G. M. W. Kroesen, F. J. de Hogg, 1987, Plasma Phys. Controlled Fusion, **29**, 10A, p 1353.

Sliney H. E., 1986, J. Vac. Sci. Technol. A, **4**, 6, p 2629.

Shohet, J. L., 1991, IEEE Trans. Plasma Sci., **19**, 5, p 725.

Smidt, F. A., B. D. Sartwell, 1985, Nucl. Instrum. Methods Phys. Res., Sect. B, **6**, p 70.

Smidt, F. A., B. D. Sartwell, and S. N. Bunker, 1987, Mat. Sci. Eng., **90**, p 385.

Spalvins, T., 1980, J.Vac.Sci.Technol., **17**, 1, p 315.

Suhr, H., R. Schmid, and W. Stürmer, 1992, Plasma Chem. and Plasma Process., **12**, 2, p 147.

Sundgren, J. E., 1985, Thin Solid Films, **128**, p 21.

Sundgren, J. E., H. T. G. Hentzell, 1986, J. Vac. Sci. Technol. A, **4**, 5, p 2259.

Tendys, J., I. Donnelly, M. J. Kenny, J. T. A. Pollock, 1988, Appl. Phys. Lett, **53**, 22, p 2143.

Thoma M., J., 1986, J. Vac. Sci. Technol. A, **4**, 6, p 2633.

Turney, W., Hung, Y. M., Starcevich, S. G., Cardinahl, P. S., Grassian, V. H., and K. A. Singmaster., 1992, Chem. Mater., **4**, p 1192.

Volz, K., M. Kiuchi, and W. Ensinger, 1998, Surf. Coat. Technol., **108 - 109**, p 303.

Walter, K. C., J. T. Scheuer, P. C. McIntyre, P. Kodali, N. Yu, and M. Nastasi, 1996, Surf. Coat. Technol., **85**, p 1.

Wittokwer, A., and J. K. Hirvonen, 1985, Nucl. Instrum. Methods Phys. Res., Sect. B, **6**, p 78.

Ziegler, J. F., J. P. Biersack, U. Littmark, 1985, *The Stopping and Range of Ions in solids*, (Pergamon Press, New York), Vol 1.

Ziegler, J. F., 1992, Ed., *Handbook of Ion Implantation Technology*, (North Holland Publishing Company, Amsterdam).

Chapter 3 DC Discharge Theory

3.1 Introduction

The method employed to generate the plasma used for the experiments described in this thesis differs from a normal DC glow. Heated tungsten filaments are used to provide thermally emitted electrons which are then accelerated into the main chamber body. Furthermore, the negative glow of the discharge is confined to a small diameter Pyrex tube while the main positive column of the glow is allowed to fill the main chamber body to provide the working plasma. These conditions are optimised by the use of pressure adjustment. This setup allows stable operating conditions when the plasma discharge current is below 4 amps and the DC voltage drop is less than 400 V. A 50 Hz AC current is used to heat the filaments, but probe measurements taken throughout the main chamber show that none of this cyclic variation is found in the main plasma body. Due to the high temperatures and small temperature fluctuations of the filaments, little variation in electron emission is expected in the cooling and heating cycles of the AC current.

Glow discharges of this type are heavily dependent on collisional processes to provide the necessary ionisation and excitation to create a steady state plasma. The collisions range over a number of forms, for example, ionisation, excitation, charge transfer etc. The main equilibrium mechanisms maintaining the plasma are ionisation by electron collision and radiative recombination. The plasma is not in thermodynamic equilibrium and secondary effects such as charge transfer and collisions between ions and neutrals play a minimal role in the ionisation balance. This topic will be discussed in greater detail in chapter six.

While the positive column can be partially described by theory, the asymmetrical nature of the described discharge and the method used to provide additional electrons makes this task beyond the scope of the proposed research. The purpose of this thesis is to investigate Langmuir probe diagnostics and the coating of metals using carbonyl feeder gases and to build a plasma processing chamber suitable for this purpose.

3.2 Fundamental parameters and measures

3.2.1 Maxwell-Boltzmann Distribution Law

Molecules and atoms in a gas move with a generally random motion. Maxwell derived a function describing the velocity distribution of the particles, and Boltzmann proved that only one energy distribution could exist in equilibrium at a particular temperature. Both Maxwell and Boltzmann found that the equilibrium velocity distribution is given by

$$dN = 4\pi N\left(\frac{m}{2\pi kT}\right)^{3/2} v^2 e^{\frac{-mv}{2kT}}\, dv \tag{3.1}$$

for the fraction of particles dN within the velocity range $v + dv$, where N is the particle density, m is the particle mass, v is its velocity, and T is the temperature of the distribution. The most probable velocity corresponds to the maximum of the distribution and can be shown to be equal to $v_p = kT$. Similarly, the average velocity and the rms velocity can be shown to be, respectively

$$v_{ave} = \left(\frac{8kT}{\pi m}\right)^{1/2} = 1.13 v_p \tag{3.2}$$

$$v_{rms} = \left(\frac{3kT}{m}\right)^{1/2} = 1.22 v_p \tag{3.3}$$

These velocities and the form of the distribution are displayed in figure 3.1.

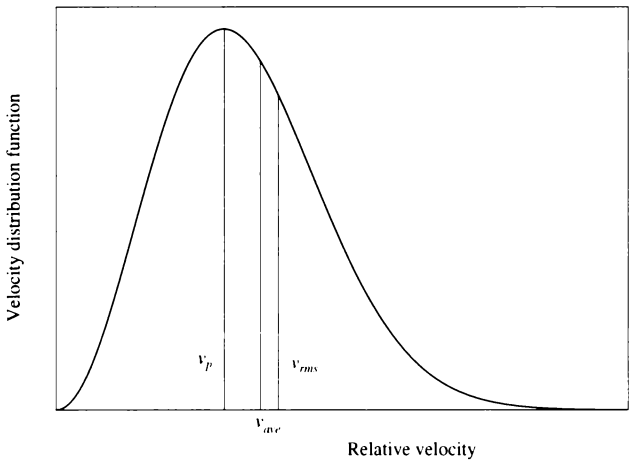

Figure 3.1 : The Maxwell-Boltzmann velocity distribution function

3.2.2 Mean Free path

The distance travelled by a particle between two successive collisions is called the free path. The mean free path (MFP) is the distance travelled between successive collisions averaged over all particles in the distribution. This value is a function of the density of the medium the particle is travelling through, the particle radii (or effective radii), and the gas it is traversing. The physical picture is of a fast moving particle suffering collisions travelling through a medium of a slow moving gas. Hence the mean free path can be written as

$$\lambda = \frac{1}{\pi(r_1 + r_2)^2 N} \tag{3.4}$$

for a fast travelling particle of type 2 moving through a slow moving gas of particle type 1 with respective radii of r_2 and r_1, where N is the density of the gas particles of r_1. This model is simplistic, treating the particles as solid spheres that have no interactions. Collisions are deemed to have taken place when the distance between the centre of the particles is less than the sum of their radii. For incident particles of the same type as the gas, equation 3.4 reduces to

$$\lambda = \frac{1}{4\pi r^2 N} \tag{3.5}$$

where r is the particle radius. However, if the impinging particles are much smaller, electrons for instance, then equation 3.5 reduces to

$$\lambda_e = \frac{1}{\pi r_1^2 N}. \tag{3.6}$$

When we consider a model in which the impinging particles have similar velocities to the colliding gas it can be shown that the mean relative velocity of the particles is

$$v = \sqrt{v_1^2 + v_2^2} \tag{3.7}$$

where v_1 and v_2 are the mean velocity of the respective species. We can also calculate the mean free path of the gas itself. If $v_1 = v_2$ then

$$\lambda_g = \frac{1}{4\sqrt{2}\pi r_1^2 N} \tag{3.8}$$

This allows an interesting comparison as we see that $\lambda_e = 5.66\lambda_g$. This fits the physical picture since small particles have a smaller cross-section and hence have a much longer mean free path.

The distribution function of the mean free paths can be derived by considering those particles which have collided and those that have not in a set period of time. The distribution is an exponential of the form

$$\frac{n}{n_0} = \mathrm{e}^{-\left(\frac{x}{\lambda}\right)} \tag{3.9}$$

where n is the collided particle number and n_0 is the total particle number after travelling distance x. This shows that 63% of the total particles will have collided after travelling the equivalent distance of one mean free path; obviously some will collide at a lesser distance and some at a greater distance.

3.2.3 Debye Length

The Debye length is a measure of the shielding distance between individual charges in the plasma on a microscopic basis. Due to the mass differential between the ions and the electrons, the electrons will have a much higher velocity than the ions and hence can respond more quickly than the ions to changing potentials and electric fields in the plasma. The application of external electric fields causes a plasma to shield itself and confine these fields in a thin sheath surrounding the main plasma body. This sheath is created by an excess or deficit of electrons with respect to the number of ions and is the plasma's method of minimizing these disturbances. This is highlighted by the dependence of the Debye length on the electron temperature and not the ion or gas temperature. The Debye length is effectively the distance up to which general quasi-neutrality is expected not to hold. It is the shielding distance, or the charge separation in a plasma, and it is of fundamental importance to calculate this parameter. The Debye length in SI units is given by equation 3.10 and is presented for several temperature and density combinations in table 3.1.

$$\lambda_d = \left(\frac{\varepsilon_0 k T_e}{N_0 e^2}\right)^{1/2} \tag{3.10}$$

where ε_0 is the vacuum permittivity, k is Boltzmann's constant, N_0 is the electron or plasma density, T_e is the electron temperature and e is the elementary charge of an electron.

Density (m^{-3})	Temperature (K)				
	23210 (2 eV)	46421 (4 eV)	69631 (6 eV)	92842 (8 eV)	116052 (10 eV)
10^{14}	1.05×10^{-3}	1.49×10^{-3}	1.82×10^{-3}	2.10×10^{-3}	2.53×10^{-3}
10^{16}	1.05×10^{-4}	1.49×10^{-4}	1.82×10^{-4}	2.10×10^{-4}	2.53×10^{-4}
10^{18}	1.05×10^{-5}	1.49×10^{-5}	1.82×10^{-5}	2.10×10^{-5}	2.53×10^{-5}
10^{20}	1.05×10^{-6}	1.49×10^{-6}	1.82×10^{-6}	2.10×10^{-6}	2.53×10^{-6}
10^{22}	1.05×10^{-7}	1.49×10^{-7}	1.82×10^{-7}	2.10×10^{-7}	2.53×10^{-7}

Table 3.1 : Debye lengths in metres.

3.2.4 Electron Production

For experiments reported in this thesis, a steady state plasma was created by the acceleration of thermally emitted electrons from heated tungsten filaments by an electric field into the main chamber body. The creation and support of the plasma was thus by collision of the accelerated electrons with the gas in the vacuum chamber. Thermal emission of electrons from a heated metal surface can be described using the Fermi-Dirac distribution law to calculate the number of electrons arriving at the metal surface with enough energy and a direction of motion sufficient to escape. The result is shown in equation 3.11 and is called the Richardson-Dushman equation

$$j = \frac{4\pi m_e}{h^3}(kT)^2 e^{\frac{-e\phi}{kT}} = AT^2 e^{\frac{-e\phi}{kT}} \qquad (3.11)$$

where j is the current density, A = 75 A cm^{-2} K^{-2} is the thermionic constant, and ϕ = 4.5 eV is the work function for tungsten. This equation is plotted in figure 3.2 against experimental data obtained from the CRC Handbook edited by Weast and Astle (1979).

Thermionic electron emission from tungsten filaments was used as the method of electron production for plasma generation in this thesis. These electrons were then accelerated into the main chamber body to create a plasma by collisional ionisation with the gas molecules already present. From figure 3.2, it can be seen that as the filament temperature increases, the rate of electron emission rises sharply. In general, if there are more electrons available for collision then there will be a greater number of ionising collisions per unit time and hence a higher plasma density. The cost of a higher filament temperature is the higher evaporation rate of tungsten from the filaments which can contaminate the plasma. These emitted tungsten atoms will provide an equilibrium number density and associated vapour pressure dependent on the temperature and surface area of the filaments. Figure 3.3 shows the evaporation

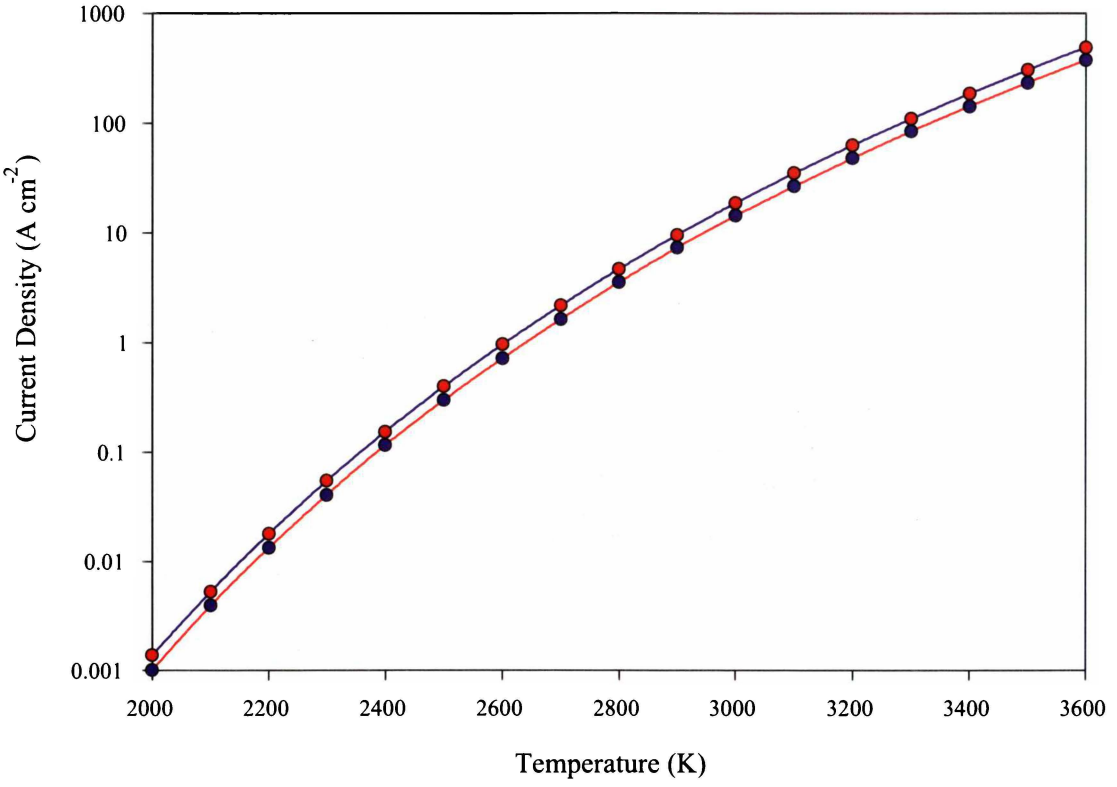

Figure 3.2 : A plot of electron emission from a heated tungsten filament. The blue line shows data from equation 3.11 while the red curve is data from the Handbook of Physics and Chemistry edited by Weast and Astle (1979).

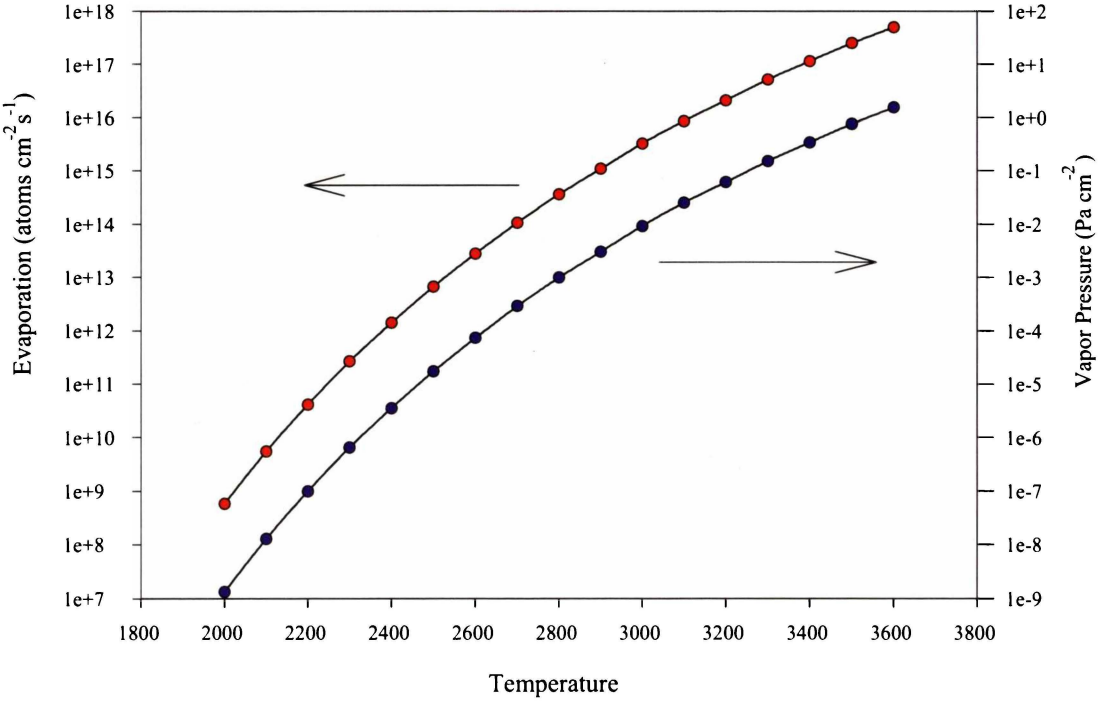

Figure 3.3 : Evaporation (red) and vapour pressure (blue) plotted against temperature for the emission of atomic material from heated tungsten in a vacuum from the Handbook of Physics and Chemistry edited by Weast and Astle (1979).

flux and the vapour pressure caused by these emitted atoms against the same temperature scale as figure 3.2. The temperature and surface area of the filaments were controlled experimentally to give a suitable plasma density (~10^{16} atoms m^{-3}) while minimising the emission of atoms from the filaments. The temperature range used was between 2700 K and 3000 K, a range chosen as a compromise between the plasma density and contamination by sputtered tungsten atoms.

3.3 The Glow Discharge

A glow discharge can be thought of as a closed system whereby electrons emitted from a cathode, typically as a result of collisions of ions with the surface of the cathode, are accelerated through a low pressure gas to an anode at the other end of the chamber. Similarly, ions created by the passage of the electrons causing collisional ionisation are accelerated towards the cathode. A voltage applied between the cathode and anode provides the driving force for this method of plasma formation. Glow discharges are complex phenomena with small changes in pressure and voltage being able to alter the discharge significantly. In general the discharge follows the form shown in figure 3.4.

The glow discharge is understood by considering emission of electrons from the cathode. The electrons are initially accelerated in the strong electric field at the cathode but complete few ionising collisions as their energy is below the ionisation potential. As the electrons travel further from the cathode, ionisation becomes more efficient and electron multiplication occurs in the negative glow region.

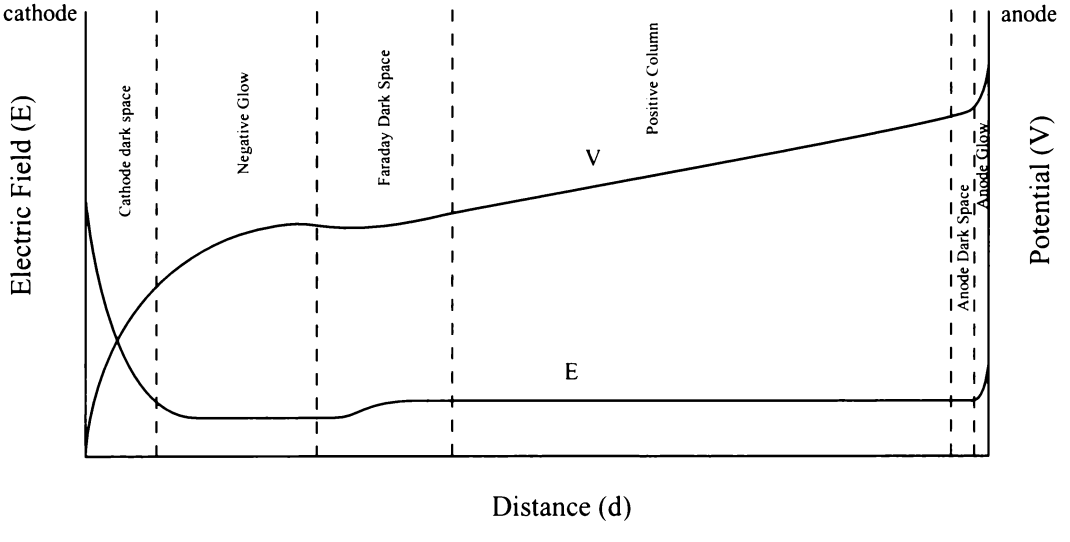

Figure 3.4 : The voltage and electric field across a DC discharge.

Due to this multiplication, the number of electrons with sufficient energy to cause ionisation increases between the cathode and the glow boundary, and a large number of positive ions are formed, providing a strong positive space charge. These ions are accelerated to the cathode. In the Faraday dark space, with increasing distance from the cathode, fewer fast electrons are found so the ionisation rate decreases. In the positive column there is effectively an equal number of electrons and ions. The ions are generally considered to be near to stationary so that the electrons virtually carry the entire current to the anode. Ionisation which occurs in the positive column results from the large random velocities acquired by the electrons due to elastic collisions. At pressures below 1 torr (132 Pa) the cathode region extends in length at the expense of the positive column, which shrinks. This tendency continues with pressure reduction until the positive column disappears entirely. At pressures above 1 torr the reverse occurs as the cathode sheath contracts and the positive column dominates the glow.

In the experiments, electrons are thermally emitted from the cathode, enhancing the discharge conditions and providing a larger number of energetic electrons than would otherwise be normally present. This modifies the standard DC glow discharge by reducing the need for elastic collisions to produce electrons energetic enough to ionise the carrier gas. This also affects the onset of the cathode space expansion with pressure as the emitted electrons are fast enough to ionise when they are emitted from the filaments. The cathode dark-space region was physically impossible to see due to the strong light emission from the heated filaments. However, this region can be absent when a heated cathode is used to provide a sufficient supply of fast electrons that can ionise directly from thermionic emission, Nasser (1971). The shrinking of the positive column is easily observable in nitrogen discharges since the negative glow is blue while the positive column is red. In these experiments, the positive column stayed reasonably constant in position and colour until the pressure was reduced to a threshold level, whereupon the positive column shrank quickly. The positive column was observable as a narrowing band which diminished in length as the pressure dropped. This constriction, was not one of those commonly observed for discharges in narrow glass tubes where the length is much greater than the radius, but rather an inability of the plasma to diffuse throughout the chamber. We chose to conduct experiments at a pressure just below the onset of this constriction in the positive column. This pressure was approximately 1×10^{-1} mbar and is much lower than that encountered in normal DC glow discharges. Pressures higher than that indicated above created a discharge that was concentrated closer to the filaments as the pressure rose. At lower pressures (1×10^{-3} mbar), the increase in the mean free paths reduced the plasma density below the desired threshold and the discharge became

tenuous. The colour at this point was pink corresponding to a balance of the emissions from the cathode and positive column regions.

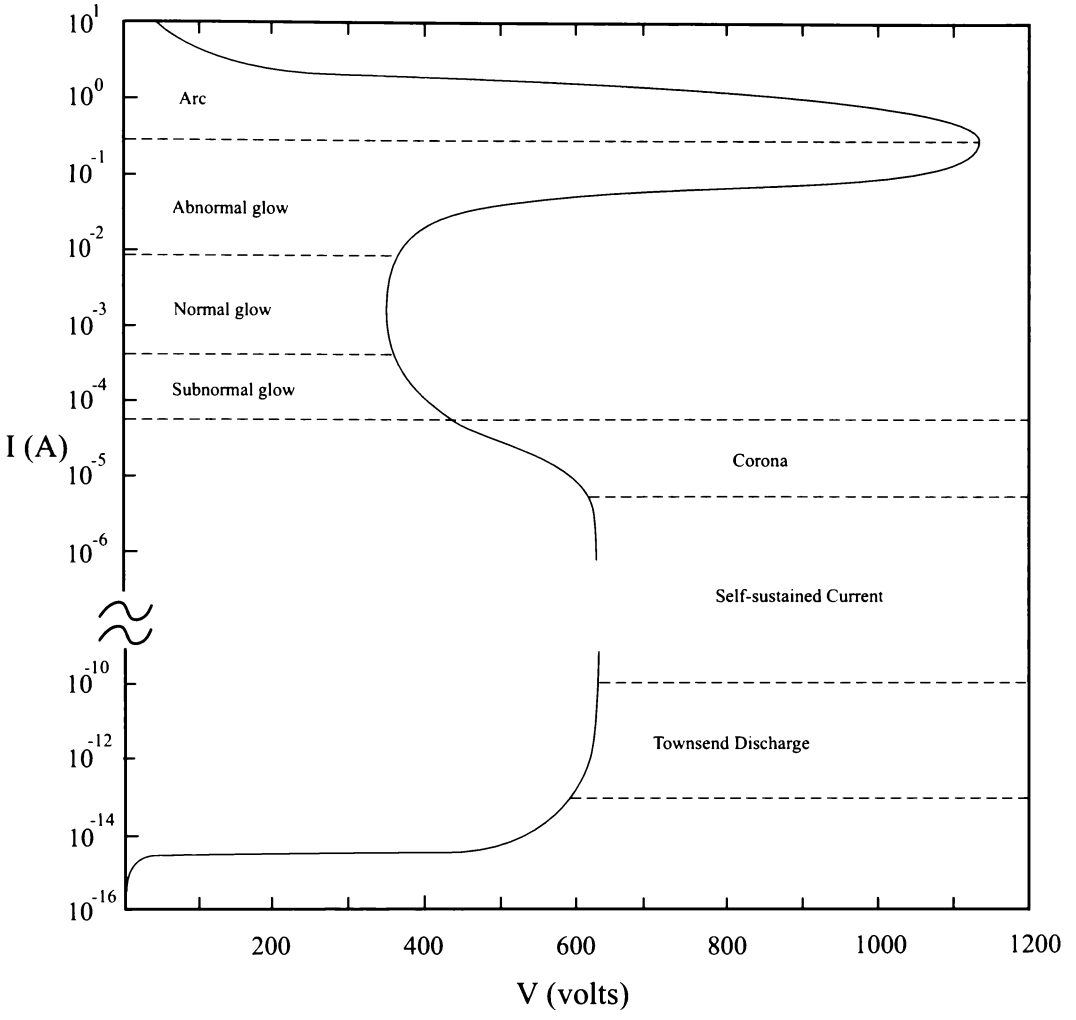

Figure 3.5 : Typical current voltage characteristic for a gaseous gap. This curve is for neon at 1 Torr (133 Pa) with 2 cm disc electrodes separated by 50 cm. This figure is taken from Nasser (1971).

The voltage-current relationship in a glow discharge generally follows a well known curve over the current range from 10^{-16} A to 10 A. The particular values for a given gas depend on pressure and the gap spacing of the electrodes, but the general shape is the same. The general form of the current, between two plane electrodes with changing voltage is shown in figure 3.5. The operating region for our experiments was in the abnormal glow region of figure 3.5. It was found that a plasma could be sustained with voltages as low as 80 V (DC) or discharge currents of 1 - 2 A with the assistance of thermionic emission. Using filaments as an electron source shifted the curve shown in figure 3.5 towards the *y* axis. Thus, the same discharge current could be obtained with a lower applied voltage by using an electron emission source. This discharge did have a tendency to "ride over" the peak shown in figure 3.5, that is, the

discharge would on occasions switch from an abnormal glow to an arc discharge. This caused no real problem since a true arc between the electrodes, or between the electrodes and the chamber wall, was never sustained because the power supplies were designed to limit the current drawn to prevent this. What actually occurred in practice was a large drop in voltage combined with a large increase in current which lasted for less than a second after which the discharge dropped back to its normal operating condition. When it occurred, this transition would disrupt the experiment in progress and the measurements being performed at that time. Most of the time this transition only occurred in the first few minutes of plasma generation and, in general, ceased to occur once the discharge had reached a stable state.

3.4 Collisional Processes

Collisional processes are the basis for the entire range of effects caused by interactions of particles in a plasma including the boundaries of the vacuum chamber. They include non-ionising processes such as charge transfer and elastic collisions, as well as excitation and ionisation which are needed to sustain the plasma. There are a many of types of collision, including multi-body collisions involving three or more particles. For the sake of simplicity, some of the more infrequent types of collisions will be omitted from consideration since their effects in our experimental plasma would be negligible.

3.4.1 The Collision Cross-Section

The true interaction between colliding particles is complex and requires the use of quantum theory to describe the interactive forces between the electrons during collision. The quantum theory is difficult for simple collisions with simple atoms such as hydrogen or helium, and for non-spherical particles with more than one nucleus very difficult indeed. Experimental results reported by various authors frequently do not match theoretical predictions. Since a quantum theory approach would not lead to further insights into the collisional process for molecules, we use simpler (if less accurate) classical models to describe the interaction processes. The collision cross-sections for the gases used in this thesis are all determined experimentally, so a rigorous theoretical treatment is not necessary.

The collision cross-section, σ, is proportional to the reciprocal of the mean free path and therefore has wide usage. Furthermore, σ is usually given subscripts to denote the nature or products of the collision. Examples of commonly used subscripts are *el*, *exc*, and *ion* which denote elastic, exciting and ionising collisions respectively.

Another outcome of electron-particle collisions is the capture of the electron by the particle to form a neutral or a negative particle (ion or molecule), for which an attachment cross-section may be defined.

The collision cross-section is the effective total target area of one particle and must be independent of pressure and temperature and hence independent of density. The product σN, where N is the number of particles per unit volume, is termed the total projected target area or total collision cross-section. The cross-sections presented in this thesis are the collision cross-sections, σ, rather than the total collision cross-section σN. As various density ranges have been investigated for the same collision processes we will define the total collision cross-section in equation 3.15. However, in some texts the "total collision cross-section", σN, is the reciprocal of the mean free path for that collision event, so in general

$$\lambda = \frac{1}{\sigma N} \tag{3.12}$$

represents the number of collisions per unit length per particle. The use of the collision cross-sections allows for the summation from various types of collisions and is the easiest method of determining a particular total cross-section. Thus

$$\sigma = \sigma_{el} + \sigma_{ex} + \sigma_{ion} + ... \tag{3.13}$$

The individual cross-sections can be further subdivided according to their formation, shown in equation 3.14, where cross-sections are defined for particular energy levels.

$$\sigma_{ex} = \sigma_{ex_1} + \sigma_{ex_2} + ... + \sigma_{ex_z} \tag{3.14}$$

Combining equations 3.13 and 3.14, the total collision cross-section can be written

$$\sigma = \sum_i \sigma_i \tag{3.15}$$

where i represents all possible types of collision a particle can experience.

The probability of ionisation, P_{ion}, is defined as the ratio of the ionisation cross-section to the collision cross-section which can be obtained from the total cross-section.

$$P_{ion} = \frac{\sigma_{ion}}{\sigma} \tag{3.16}$$

P_{ion} is also referred to as the ionisation function. Some authors use P_{ion} multiplied by σN which is a function of pressure and temperature having a representative value called the ionisation efficiency, η_{ion}, where

$$\eta_{ion} = P_{ion} \sigma N = \sigma_{ion} N \tag{3.17}$$

Finally, the collision frequency, f, is the number of collisions a particle undergoes per unit time, normally in one second, so that

$$f = v\sigma N \tag{3.18}$$

where v is the mean random velocity of the particle. Similar to the collision cross-section, the collision frequency can be subdivided according to the collision type

$$f = f_{el} + f_{ex} + \ldots \tag{3.19}$$

The subdivisions of the total collision cross-section and the collision frequency (equations 3.14 and 3.19) allow the calculation of the ratios of the number of excitation collisions to the ionisation collisions, for example. These ratios are important in understanding the relative contribution and frequency of each collision type to the plasma properties. The data presented in the next sections were obtained from a variety of sources and were originally presented as one of the above representations (λ, P_{ion}). These graphs and cross-sections have been converted, when needed, into collision cross-sections that are independent of variables such as temperature and pressure.

3.5 Ionisation

Direct collisional ionisation of atoms or molecules can occur only when the electron energy at impact exceeds the ionisation energy and enough energy is transferred to the particle for the ejection of a electron. If the electron has an energy below this minimum, collisional ionisation can only occur by indirect mechanisms. For ionisation by electrons to occur, the electrons need to transfer an energy $E_{ion} \geq eV_{ion}$, where V_{ion} is the ionisation potential. For ionisation by ions or fast neutrals in their own gas, the energy transfer needed is at least twice the ionisation energy since the maximum energy that can be transferred is half the energy of the impinging particle. For molecules, self ionisation requires molecular energies of at least 400 eV, Nasser (1971). This is the theoretical upper limit of molecular energies obtainable in the work of this thesis. Therefore we may expect that molecular collisions will produce very little, if any, ionisation and so can be safely ignored as an ionisation source.

3.5.1 Ionisation by collision

When a particle of mass m is moving with a velocity v and then collides with a particle of mass M, kinetic energy is exchanged. If no excitation or ionisation results,

the collision is said to be elastic. A collision is inelastic if the gas atom or molecule becomes excited or ionised by acquiring energy from the incident particle. If the collision is inelastic, some of the kinetic energy of the system prior to impact is converted to potential energy of one of the particles. For simplicity the results developed below are based on classical Newtonian mechanics. For a discussion of the theory based on a quantum mechanical approach the reader is referred to the work of Bates (1962) and Massey (1979). In the classical approach the particles will still be treated as rigid spheres although this assumption is certainly an oversimplification.

For the elastic collision of two particles of mass m and M, with particle M initially at rest, the final velocity of the particle of mass m is v_1 where

$$v_1 = \frac{m-M}{m+M} v \tag{3.20}$$

with v being the initial velocity of the particle of mass m. If the collision is inelastic, the energy, W_p, imparted to a gas atom of mass M, initially at rest, can be derived from the following energy balance,

$$\tfrac{1}{2} m v^2 = \tfrac{1}{2} m v_1^2 + \tfrac{1}{2} \frac{m^2}{M} (v - v_1)^2 + W_p \tag{3.21}$$

For maximum W_p,

$$\frac{v_1}{v} = \frac{m}{M+m} \tag{3.22}$$

Thus the maximum energy gained by M, for the case $m = M$, occurs when the final velocity of m is half the initial velocity, i.e.

$$v_1 = v/2 \tag{3.23}$$

If the collision is for electron impact, where m is the electron mass for which $m << M$, then the maximum energy transfer occurs when

$$v_1 \approx \frac{m}{M} v \tag{3.24}$$

Thus v_1 becomes only a small fraction of the initial velocity v with the incident electron losing most of its kinetic energy. If the particles have the same mass, the incident particle cannot lose more than three quarters of its initial kinetic energy. For $m = M$, and maximum W_p, if the struck particle was at rest before the collision both particles leave the collision with the same velocity. If the colliding particle is an electron, then virtually all the kinetic energy of the electron can be lost. Therefore, to attain direct ionisation of a particle by electron collision, the electron must have a kinetic energy equal to, or greater than, the ionisation energy of the ground state neutral atom or molecule. However, because ionisation of the particle can occur from

excited states, the electron energy needed to ionise a particle can be less than the ionisation energy of the ground state neutral atom or molecule. Collisions resulting in ionisation caused by the exchange of kinetic energy are called collisions of the first order. Collisions of the second order occur when a particle delivers part of its potential energy to cause ionisation by collision.

In second order collisions, metastable states are much more significant than normal excited states due to the former's longer lifetimes. It is also possible that an excited atom or molecule will de-excite, i.e. lose its potential energy after impact, rather than be ionised. In a mixture of two gases, A and B, the following processes may occur for fast (f) and slow (s) particles, where the superscript * denotes an excited state:

$$A^* + B_s = A + B_f \qquad \text{Inelastic de-excitation} \quad (3.25)$$

$$A^* + B = A + B^* \qquad \text{Excitation Transfer} \quad (3.26)$$

$$A^* + B^* = A + B_f^+ + e \qquad \text{Second Order Ionisation} \quad (3.27)$$

$$A^+ + B = A + B^+ \qquad \text{Charge Transfer} \quad (3.28)$$

$$A^* + B = A + B^+ + e \qquad \text{Penning Effect} \quad (3.29)$$

Molecular processes are frequently of great importance in collisional effects and can be associative or dissociative. Collisional molecular processes include reactions of the form

$$A^* + B_2 = A + B + B^+ + \mathrm{e} \qquad \text{Dissociative ionisation} \quad (3.30)$$

where B_2 is a diatomic molecule.

In general, the products of collisions involving excited states are such that the potential energy converted to kinetic energy is a minimum. The Penning effect described in the above reaction is known as seeding. This occurs when a small proportion of a gas with a low excitation level leads to ionisation of the main gas at a much lower electron energy than the excitation energy of the main gas. For example, molecular gases can absorb the kinetic energy of the incident particles through molecular vibrational and rotational levels leading to Penning ionisation. Typically a large number of elastic collisions will spread the molecular states over a large range of vibrational and rotational levels.

3.5.2 Ionisation by Electrons

Let us consider a collision with a gas atom or molecule by an electron whose kinetic energy is above that required for ionisation. In a classical rigid sphere model, the impact of a fast moving electron may produce a singly charged particle and another electron. This is however, a simplistic picture. The general shape of the ionisation

efficiency curve is one with an initial maximum, whose peak falls away with increasing electron energy. If we look at the ionisation cross-sections of some molecules we find that they vary with energy as shown in figure 3.6. This figure indicates that the smallest atoms and ions generally have the smallest cross-sections, while the larger the atom becomes, the higher the cross-section. This is mainly due to the larger size of the electron cloud surrounding the atom or molecule.

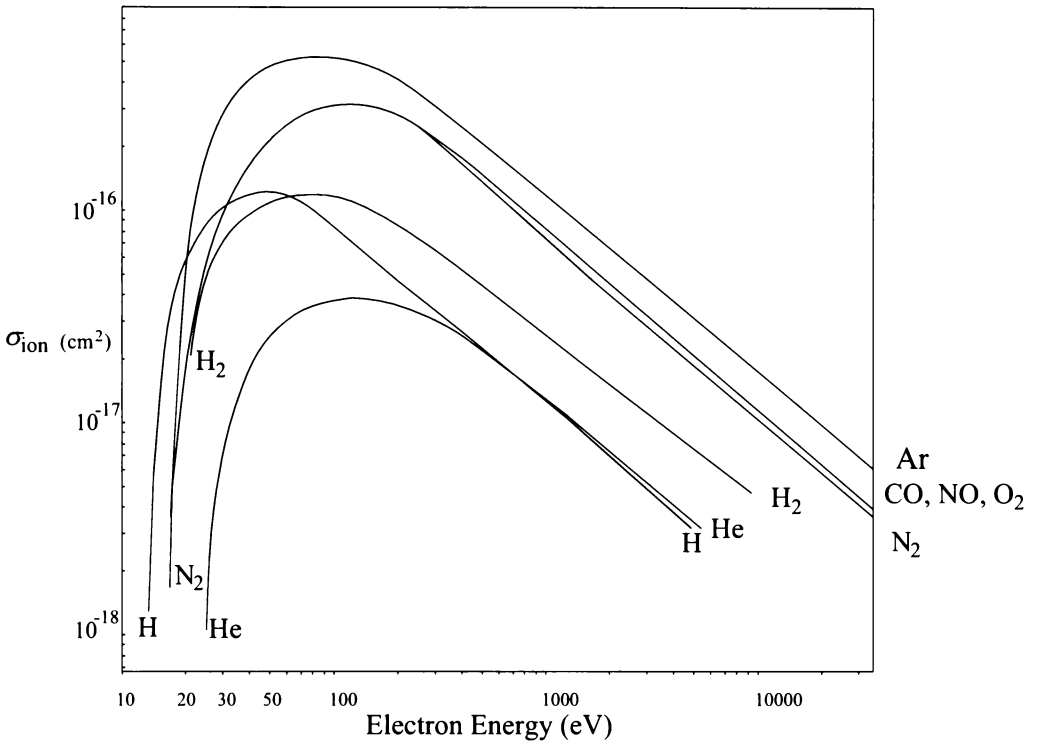

Figure 3.6 : Ionisation cross-sections for a variety of molecules and atoms from Nasser (1971).

The shape of these curves can be explained if we step away from the rigid sphere model and consider the interaction between the electromagnetic fields of the particles. We see that no ionisation occurs unless the electron has sufficient energy to ionise the particle. If the energy of the electron is below the ionisation energy only elastic collisions can take place. Once the electron reaches ionisation energy, the ionisation cross-section quickly rises until a point is reached where the interaction of the electromagnetic fields between the electron and a particular atom or molecule are maximised. The cross-section reaches its peak at this point. As the electrons have more and more energy, the interaction time becomes smaller and smaller and the amount of energy and momentum transferred decreases. The electron is now "too fast" for the fields to interact for a sufficient amount of time, and hence the ionisation efficiency and the cross-section drops.

Detailed cross-sections of N_2 and CO have been obtained from the National Institute of Standards and Technology online database available at the following URL

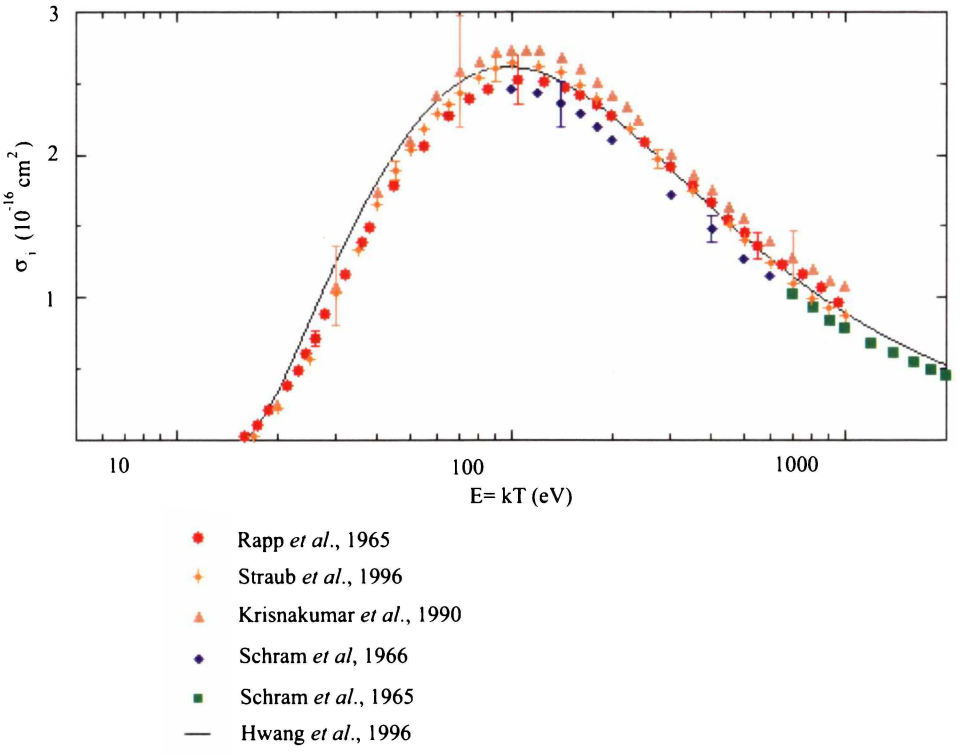

Figure 3.7 : Ionisation cross-section of molecular nitrogen.

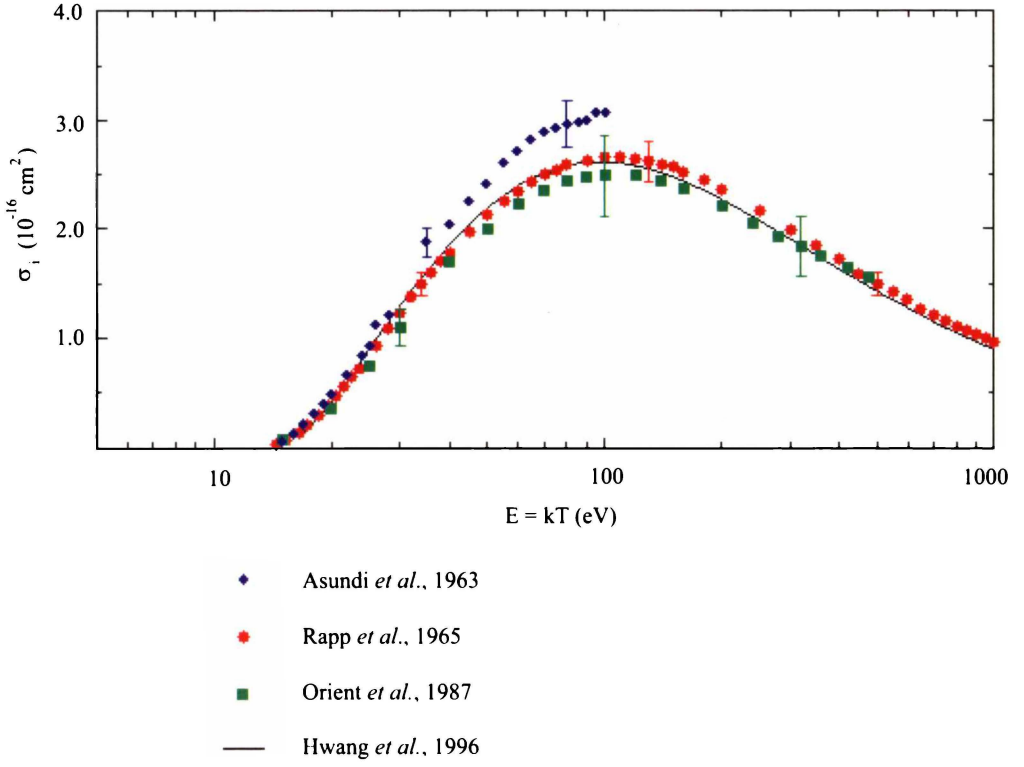

Figure 3.8 : Ionisation cross-section of carbon monoxide.

"http://physics.nist.gov". The graphs are of experimental data plotted with theoretical calculations using a Binary-Encounter-Bethe model and are shown in figures 3.7 and 3.8.

From figures 3.6 to 3.8 it can be seen that the collision cross-section for ionisation of nitrogen and carbon monoxide is almost identical over the electron energy range used in this thesis. They confirm the earlier data in figure 3.6 that the cross-section peak is at approximately 100 eV where both molecules have a cross-section of 2.6×10^{-16} cm^{-2}. It is therefore expected that carbon monoxide will exhibit a similar response to nitrogen under the same discharge conditions, a feature confirmed in later chapters.

3.5.3 Elastic Collisions by Electron Impact

Atomic and molecular elastic cross-sections for electrons are generally measured by two methods,

1) Electron beam attenuation in a gas of known pressure, usually by mono-energetic electrons.

2) Electron swarm experiments, which measure the momentum transfer cross-sections.

The first method is direct and is the oldest, whereas the second is indirect but accurate and also allows for measurement at very low electron energies. The second method is a measurement of an experimental parameter from which the elastic cross-section can be derived using equation 3.31. This results from the asymmetric scattering of an electron swarm in the direction of motion of the electrons. For elastic spheres impinging on stationary targets the scattering is symmetric. For electrons however, there is a net forward motion after collision. The angular dependence of this scattering is used to account for the asymmetry and to produce a mean free path equal to that of the symmetric scattering case. The experimental measurements match well with the theory of scattering predicted by quantum mechanics. The measured parameter is the momentum transfer cross-section, σ_m, which is related to the elastic cross-section by

$$\sigma_m = \sigma_{el}\left(1 - \cos\phi\right) \tag{3.31}$$

where ϕ is the angle between the paths before and after collision in the direction of motion of the electrons.

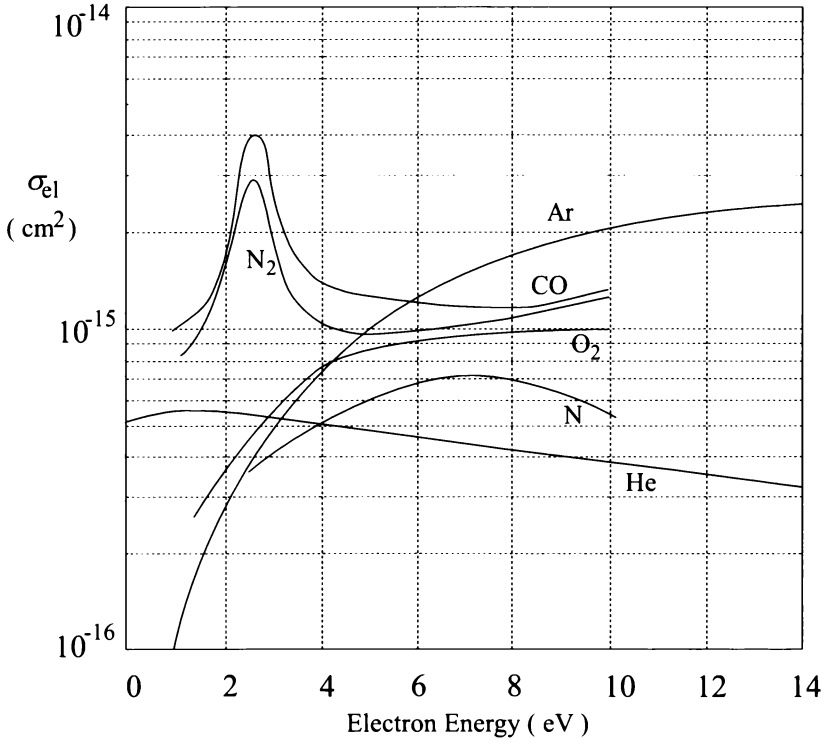

Figure 3.9 : Elastic cross-sections for electron impact from Nasser (1971) and Brown (1966).

Electron impact elastic cross-sections have been measured by numerous authors and are shown graphically in figure 3.9 for N_2, CO, N, Ar and He.

The elastic cross-section for CO is larger in magnitude than for N_2 but the curve follows the same shape. This indicates that the filled electronic orbitals of these molecules are similar in position and energy since they scatter low energy electrons almost identically. The difference in magnitude can be attributed to the larger size of the CO molecule (see section 3.7). If we look at the O_2 elastic cross-section from the same figure, we can see that at low energy, the characteristic peak found for CO and N_2 is absent. The main difference between these molecules is that O_2 has a double bond while CO and N_2 have triple bonds. This indicates the different scattering behaviour is most likely caused by the increased electron density generated by the triple bond.

3.5.4 Excitation Cross-Section

Excitation cross-sections are measured experimentally at pressures lower than 5×10^{-4} Pa where radiation trapping from resonances as well as excitation transfer are negligible. These factors are largely responsible for the differing values of excitation cross-sections measured by various researchers. Collisions of the second kind can be important for the excitation or ionisation of atoms by bound electrons in collisions

between atoms or molecules. This can be either by autoionisation or by collisions of two excited atoms. In autoionisation more than one electron in the atom is excited which may lead to the ejection of an electron with kinetic energy equal to the difference in the particle energy and the ionisation energy.

Molecule	Electronic State	Wavelength (Å)	Bands	Mean Radiative Life-time (seconds)
N_2	$A\ ^3\Sigma_u^+$	2009.79		$< 10^{-2}$
	$a\ ^1\Pi g$	1450.19		$\sim 2 \times 10^{-2}$
N_2^+	$B\ ^2\Sigma_u^+$	3911.44	(0, 0)	$6.58 \pm 0.35 \times 10^{-8}$
CO^+	$A\ ^2\Pi i$	4900.16	(1, 0)	$2.78 \pm 0.2 \times 10^{-6}$
			(1, 1)	$2.78 \pm 0.2 \times 10^{-6}$
			(2, 0)	$2.61 \pm 0.2 \times 10^{-6}$
			(2, 1)	$2.61 \pm 0.2 \times 10^{-6}$
			(3, 0)	$2.36 \pm 0.15 \times 10^{-6}$
			(4, 0)	$2.22 \pm 0.13 \times 10^{-6}$
			(5, 0)	$2.11 \pm 0.13 \times 10^{-6}$

Table 3.2 : Mean radiative lifetimes of excited and ionised molecules taken from von Engel (1965) and Bates (1962).

The collision of two excited states is effective for producing ionisation when the excitation energy is about half the ionisation energy and when the excited states are stable i.e., the excited states have a long lifetime. For example, the appearance of He_2^+ occurs via excited atoms by the reactions

$$1)\ He + e \rightarrow He^* + e \tag{3.32}$$

$$2)\ He^* + He \rightarrow He_2^+ + e \tag{3.33}$$

where the minimum combined impact energy required for equation 3.33 is 23.2 eV. The lifetimes of excited states of gases relevant to our work are reproduced in table 3.2.

In general, collisions between electrons and molecules will raise the bound electrons to higher states of rotation and/or vibration. If the electron energy is sufficient, excitation can occur and lead to the emission of light, the dissociation of the molecule, or transfer of the energy to other particles.

For nitrogen, figure 3.10 shows the excitation cross-section for electron collisions leading to the C state of N_2 reproduced from von Engel (1965). This excitation cross-section shows a maximum almost immediately after the threshold, and then tails off with higher electron energies. The C state decays into the B state by the

emission of light, which is known as the second positive band. Dissociation by electron collision occurs only at electron energies above 24 eV where the expected products are $N^+ + N$ from the Franck-Condon principle.

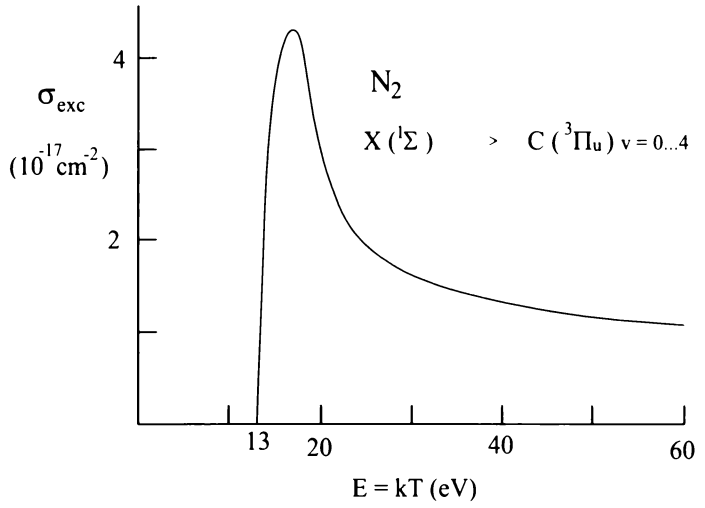

Figure 3.10 : Excitation cross-section for the C state of molecular nitrogen.

3.5.5 Other Forms of Ionisation

Most other methods of producing ionisation in a plasma are of little interest to us since the cross-sections are far below those of collisional excitation and ionisation. Typically these cross-sections are around, or below 10^{-18} cm^{-2} in magnitude. Molecular gas experiments have shown that at least 400 eV is required in order for self ionisation by the gas to be initiated. This is largely due to the energy loss mechanism for the scattering of particles in their own gas. This is an efficient loss mechanism where on average one third of the energetic particle's energy is lost in an elastic collision. There is therefore a very low probability of a molecule attaining the necessary energy for a successful ionisation collision with an identical molecule. Even for atoms, approximately 60 eV is required for self ionisation in argon (Nasser, 1971).

The important exception is charge transfer collisions, which have a large cross-section. However they do require moderate ion energies for the process to be initiated. By charge transfer we mean

$$A^+ + B \rightarrow A + B^+ \tag{3.34}$$

where A and B are usually of the same nuclear species, i.e. Ar^+ and Ar.

Charge transfer collisions do not add to the density of the plasma since the ionisation charge is simply transferred to a different atom or molecule. It does allow the formation of fast neutrals which are generated by the transfer of charge from fast

ions during the collision process. Charge transfer processes may possibly affect the plasmas created for the experiments described in this thesis. This effect however, will alter the mobilities of the ions. Figure 3.11, taken from von Engel (1965), shows the charge transfer cross-sections for several species including N, N_2 and Ar.

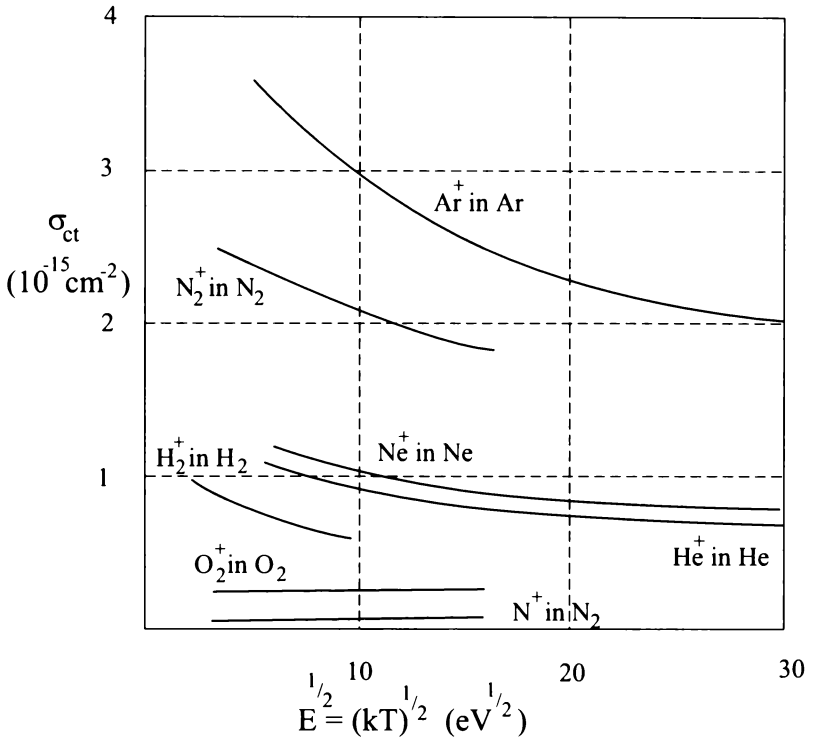

Figure 3.11 : Charge transfer cross-sections for ionised species in their parent gas.

One important fact is that the charge transfer cross-sections for ions in their own gas are, with a few exceptions, orders of magnitude larger than the same ions in any other gas. This has been explained using wave mechanics by von Engel (1965) and Bates (1962). The charge transfer process is more probable the nearer the collision is to energy resonance, or the smaller the amount of energy transferred in a collision of this nature. This energy transfer is minimised for ions moving in their own gas. From figure 3.11 it is apparent that the charge transfer cross-sections are larger (in general) for atoms rather than molecules. This is because for homonuclear and heteronuclear molecules, the energy transfer is minimised when the radii of the colliding molecules are the same. This requirement seems quite stringent in that when higher vibrational levels of the same state do not correspond, the measured charge transfer reactions are not as large as expected, even without considering the differing excited and ionised states. Again, for a detailed quantum mechanical discussion, see Bates (1962).

3.6 Diffusion

There are many different mechanisms available for the escape of electrons and ions to the boundary walls. Diffusion is one such major loss mechanism for plasmas and DC discharges in general. Figure 3.12 depicts the relevant diffusion mechanisms against an arbitrary scale.

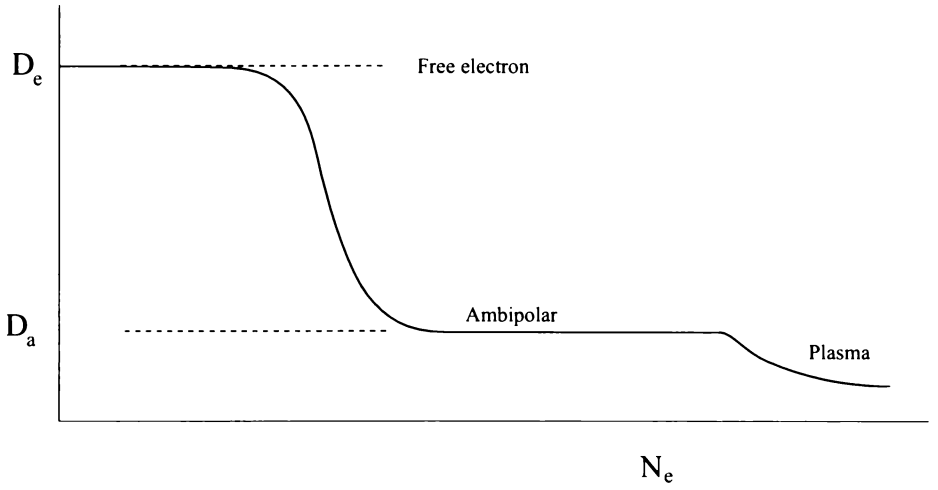

Figure 3.12 : A schematic description of diffusion vs. electron density showing three regimes where D_e and D_a are the electron and ambipolar diffusion rates respectively.

Figure 3.12 is used to illustrate that different types of diffusion dominate as the electron density regions in the DC discharge change. In particular, the mid point of the transition between free electron and ambipolar diffusion occurs when the characteristic free electron diffusion length equals the Debye length. Generally ambipolar diffusion becomes the dominant diffusion method when the density of the electrons is above $n_e = 10^8$ cm^{-3}. Experiments have been performed by Meek and Craggs (1978) where this transition region shows up clearly. We will look at electron diffusion briefly to see why it is distinguished from ambipolar diffusion and plasma diffusion.

3.6.1 Electron and Ion Mobility and Diffusion

When a swarm of electrons or ions in a gas is subject to an electric field, $\boldsymbol{E}$, the swarm moves as a whole so that its centre of mass moves with a velocity, $\boldsymbol{w}$, parallel to the electric field direction. This velocity, $\boldsymbol{w}$, is called the drift velocity of the charged particles. At sufficiently low values of $\boldsymbol{E}$, the drift velocity for ions is proportional to $\boldsymbol{E}$ and inversely proportional to the gas density. This leads to the definition of mobility, μ, of the ions where

$$\boldsymbol{w} = \mu \boldsymbol{E} \tag{3.35}$$

The mobility is more commonly denoted in terms of the standard temperature and pressure where the reduced mobility, μ_0, is used, so that equation 3.35 becomes

$$\mu_0 = 3.7215\times10^{-20}\,\mu\left(\frac{\boldsymbol{E}}{n}\right)^{-1} \tag{3.36}$$

where n is the gas density and μ_0 has units of $cm^2\ V^{-1}\ s^{-1}$.

If we consider a time invariant density concentration gradient it can be shown that in three dimensions

$$\boldsymbol{J}_j = -D_j\,\nabla n_j \tag{3.37}$$

where $\boldsymbol{J}$ is the number of particles crossing the gradient (the particle current), D is the diffusion coefficient, n is the particle density while the subscript j is the particle species. D is the constant of proportionality between the rate of flow and the concentration gradient. Furthermore, in cases with a time-varying concentration gradient it can also be shown that

$$\frac{\partial n_j}{\partial t} + \nabla\cdot\boldsymbol{J}_j = 0 \tag{3.38}$$

This is called the continuity equation (Nasser, 1971).

If we now reconsider the swarm of electrons under the conditions when drift and diffusion occur together when an electric force of $e\boldsymbol{E}$ is directed parallel to the z axis, following Meek and Craggs (1978), we can write a continuity equation based on the non-destruction of charged particles as

$$\frac{\partial n_j}{\partial t} - D_j\nabla^2 n_j + \boldsymbol{w}_j\frac{\partial n_j}{\partial z} = 0 \tag{3.39}$$

For electrons with a Maxwellian distribution it can be shown that

$$\frac{D_e}{\mu_e} = \frac{2}{3e}\left(\tfrac{1}{2}m\bar{v}_e^{\,2}\right) = \frac{kT_e}{e} \tag{3.40}$$

For any other distribution function equation 3.39 becomes

$$\frac{D_e}{\mu_e} = \frac{F}{e}\cdot\tfrac{1}{2}mv_e^{\,2} \tag{3.41}$$

where F is a dimensionless factor given by Meek and Craggs (1978).

When the ions are in thermal equilibrium with the gas molecules, the drift and diffusion coefficients are related through the same equations 3.40 and 3.41 but the mobility is modified. The calculation for mobility of ions with low values of E/n

assumes that the dominant interaction between the ions and molecules is that of polarisation. For ions moving in their own parent gas, the mobility is

$$\mu = 0.64 \frac{e\lambda_i}{mw_i} \tag{3.42}$$

where λ_i, is the mean free path of the ions in its parent gas. For ions in a foreign gas the mobility is

$$\mu = 0.815 \frac{e\lambda_i}{mw_i} \left(\frac{m+M}{m} \right)^{1/2} \tag{3.43}$$

where m and M are the mass of the ion and neutral foreign gas molecule respectively.

3.6.2 Ambipolar Diffusion

In a plasma, Coulomb interactions will modify the mobility and diffusion rates. Ambipolar diffusion describes the situation when the ion and electron diffusion rates are equal. This occurs for two reasons. Since the electrons have higher velocities than the ions due to mass differences, electrons tend to diffuse towards the walls much faster than ions. This creates an electric field in the boundary region of the plasma which tends to retard the electrons and accelerate the ions. A steady state condition is typically reached where electrons and ions diffuse at the same velocity since they are constrained by Coulomb forces of the charge separation, or equality of the boundary electric field produced by the initial excess of electrons lost. A direct measure of the depth of this charge separation is the Debye length which, in essence, is how far a particle of one charge is screened by particles of the opposite charge.

The flux of particles of either sign is (Meek and Craggs (1978), Nasser (1971), and von Engel (1965))

$$n_{\pm} \bar{v}_{\pm} = -D_{\pm} \frac{dn_{\pm}}{dx} + n_{\pm} \mu_{\pm} \boldsymbol{E} \tag{3.44}$$

where $\bar{v}_{\pm}$ is the mean velocity, μ the appropriate ionic mobility, $\boldsymbol{E}$ is the electric field where $\boldsymbol{E} = E\,\underline{\hat{x}}$, and $\underline{\hat{x}}$ is normal to the boundary surface. We can set the ion and electron densities to be equal and hence eliminate $\boldsymbol{E}$ from the equation.

$$\bar{v} = \frac{D_+ \mu_- + D_- \mu_+}{\mu_+ + \mu_-} \frac{1}{n} \frac{dn}{dx} \tag{3.45}$$

Since $nv = dn/dt$

$$\frac{dn}{dt} = -D_a \frac{dn}{dx} \tag{3.46}$$

where

$$D_a = \frac{D_+\mu_- + D_-\mu_+}{\mu_+ + \mu_-} \tag{3.47}$$

is the ambipolar diffusion coefficient.
Since

$$\frac{\mu_+}{D_+} = \frac{e}{kT_+} \quad \text{and} \quad \frac{\mu_-}{D_-} = \frac{e}{kT_-} \tag{3.48}$$

when $T_e >> T_+$, as is common in many plasmas

$$\frac{D_-}{\mu_-} \gg \frac{D_+}{\mu_+} \tag{3.49}$$

and we obtain

$$D_a = D_+ \frac{T_e}{T_+} = D_- \frac{\mu_+}{\mu_-} \tag{3.50}$$

Hence the values of the ambipolar diffusion coefficient may be obtained from the mobilities and diffusion coefficients of the particular gas present. It is also interesting to note that the ambipolar diffusion coefficient is greater than the ion diffusion coefficient, but much less than the electron coefficient, $D_i < D_a \ll D_e$. Thus ambipolar diffusion greatly reduces the electron loss rate from a plasma.

This is essentially the same argument used to derive the Bohm condition discussed in chapter four where the sheath formation at a boundary wall or a probe retards the electrons so that only those with velocities in the high energy tail of the Boltzmann distribution can reach the boundary and be collected. This condition also requires the ions to enter the sheath with an energy equal to half the electron temperature.

It must be emphasised that this charge separation occurs over the Debye length at the boundary, e.g. the walls of the chamber. The Debye length for the plasma conditions in this thesis were typically a millimetre in length. Figure 3.13 illustrates this point graphically.

In figure 3.13, from right to left, n_0 is the bulk plasma density at infinity, n is the density in the sheath region while the subscripts i and e refer to the ion and electron densities inside the Debye length. The voltage curve at the boundary wall is also shown.

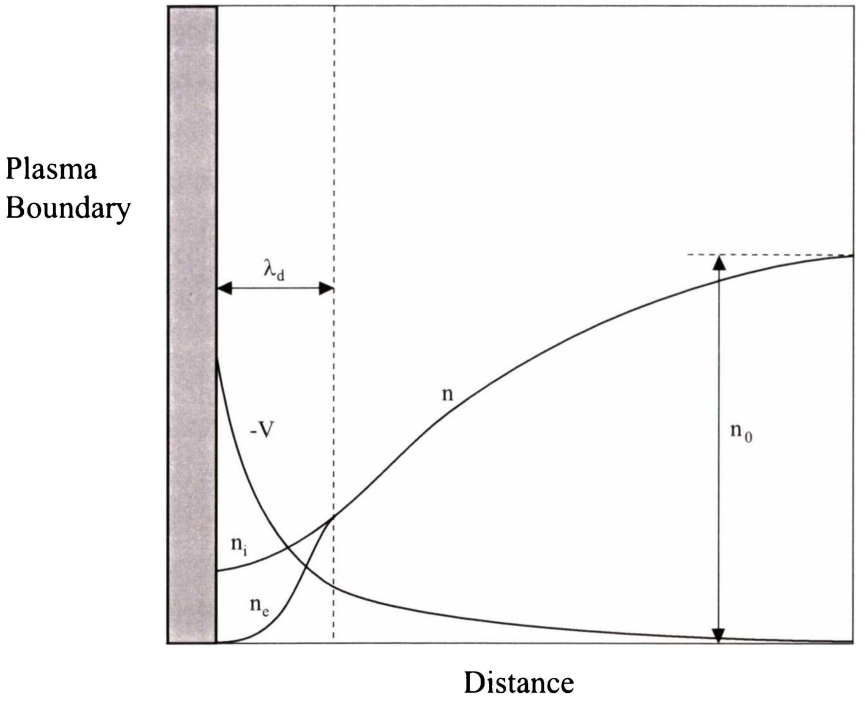

Figure 3.13 : Charge separation at the sheath boundary inside the Debye length showing the effects of ambipolar diffusion.

3.7 Molecular Data and Mean Free Path Calculations

3.7.1 Radii and Mean Free Paths

The determination of mean free paths is not easy to achieve accurately. Simply put, molecules are not spherical but are elliptical in shape and so have at least two equivalent radii. Another complication is that we do not know the energy distribution of the electrons accelerated from the filaments as they traverse the plasma chamber. Since the collision cross-sections change with electron energy a full theoretical treatment would be required to determine this which would be difficult and beyond the scope of this thesis.

Considering molecules (diatomics) in general, the asymmetrical nature of their effective surface means that any cross-sections are an average value since they are a dumbbell shape. There are virtually always enough molecules in a plasma at the experimental operating pressures for this technique to be accurate. From the physical picture, if we imagine the molecule to be rotating with 3 degrees of freedom we can see that the maximum and minimum cross-sections of a diatomic molecule occurs when it is broadside and when it is end on respectively. If we now concentrate on the radii of molecules such as nitrogen and carbon monoxide we immediately find other

problems. For example, the determination of the molecular radii using different techniques gives different measurements. Measurements such as N-N bond lengths, atomic radii of the nitrogen atom, covalent radii, packing radii, enthalpy changes, molecular refraction, viscosity measurements, and van der Waals radii all provide inconsistent values. Even a quick search of internet websites such as webelements.com, immediately show significant variations in the radii of nitrogen. These data are summarised in table 3.3.

	N-N,C-O Length (radius)	Atomic (radius)	Covalent Bond (radius)	Crystal Packing (diameter)	Molecular Length (radius)	Refraction (diameter)	Viscosity (diameter)	van der Waals (diameter)
N_2	1.10	0.65	0.75	4.00	1.09	2.4	3.16	3.14 (N_2) 1.55 (N)
CO	-	-	-	4.3	1.22	-	3.8	3.16 (CO)
Cr	2.5	1.4	1.27	1.25	-	-	-	-

Table 3.3: Different values for the radii and diameter (in angstroms) of the main plasma molecules and atoms.

The usual practice is to take the radius of molecules to be 70% of the van der Waals radius. This provides values of 1.1 Å for both nitrogen and carbon monoxide which are the values we will use to determine the particle cross-sections and hence the mean free paths.

3.7.2 Comparison between N_2 and CO

To further compare the similarities between CO and N_2, their bonding structure and their photoelectron spectra will now be examined.

3.7.2.1 Bonding Structure

Molecular orbital theory is the process where the construction of the orbitals of the molecule are built up using approximations to the wave equation solutions for each atom. The electrons are then fed into the energy levels to build up the electronic structure of the molecule. The molecular orbital diagram of nitrogen compared to carbon monoxide is shown in figure 3.14 where they can be seen to be identical in structure. Molecules that exhibit this similarity are termed isoelectronic.

Comparison of the molecular diagrams of nitrogen and carbon monoxide show that although the levels found are the same, the energy of the levels are slightly different. This is expected and the differences that do arise are caused by the energy

differences in the s and p orbitals of carbon and oxygen from which the hybridised orbitals are created. In nitrogen these levels are identical since N_2 contains two identical, indistinguishable atoms. In comparison we find that the $2\pi_u$ level of CO has the same stability as for N_2, but the electrons in $2\sigma_g$ orbital are less tightly bound, indicating a greater contribution from the carbon $2p_z$ orbital. Conversely, those in the $1\sigma_u$ level are more tightly bound (greater oxygen contribution) than in the respective orbital of N_2.

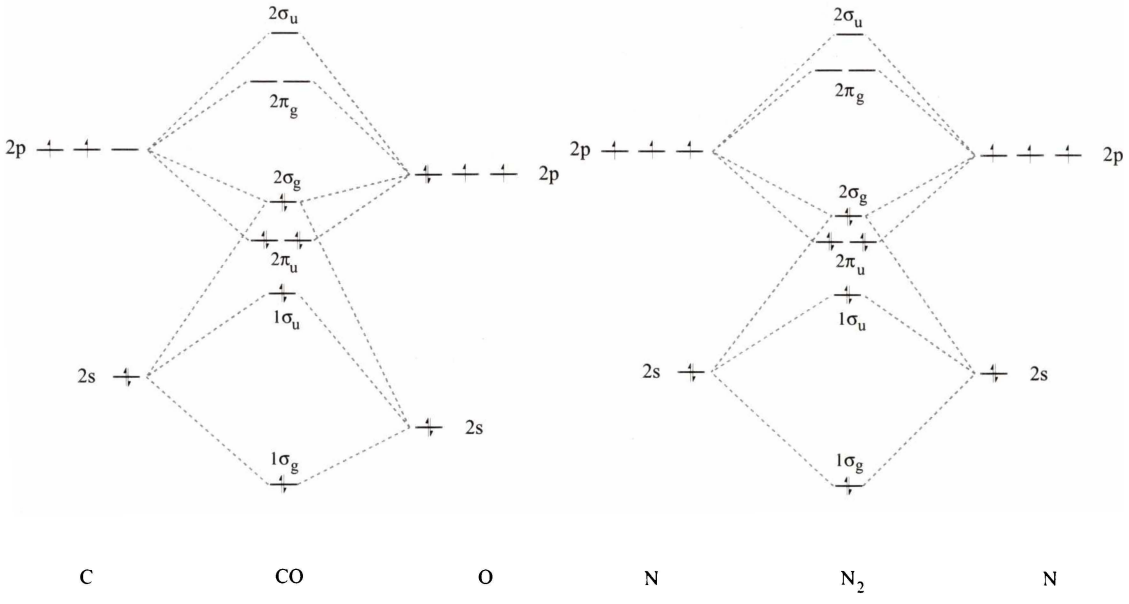

Figure 3.14 : The molecular orbital diagrams of nitrogen and carbon monoxide showing the energy levels created from the combined atoms.

3.7.2.2 Molecular Photoelectron Spectroscopy

This is the study of electronic states in the gaseous phase and involves radiating the vapour in question with a helium emission spectrum from a DC discharge. The strongest line is He 584 Å (21.22 eV) which accounts for 98% of the emission from the spectrum. This light ionises the vapour and produces a beam of electrons from which the kinetic energy spectrum can be obtained. The resulting plot produces peaks with positions corresponding to transitions between electronic levels. Band structures can also be resolved when these transitions occur to different vibrational states. Identification of the peaks produced leads to values for the energy levels of the electronic states as well as the vibrational spacing. The number of vibrational levels also identifies the nature of the electron removed from the electronic state. The spectra for nitrogen and carbon monoxide shown in figures 3.15 and 3.16 has been reproduced from Turner *et al.* (1970). Both spectra show nearly identical

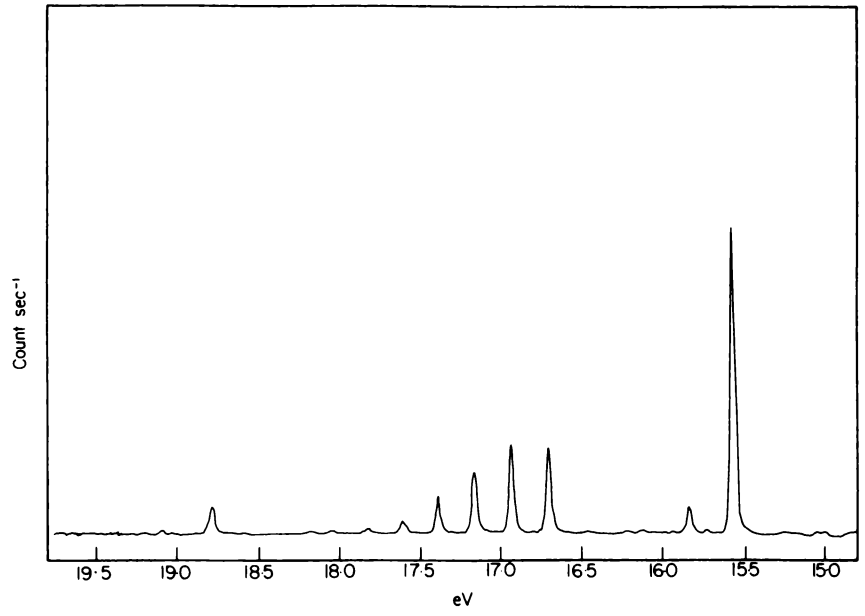

Figure 3.15 : The photoelectron spectrum for the nitrogen molecule.

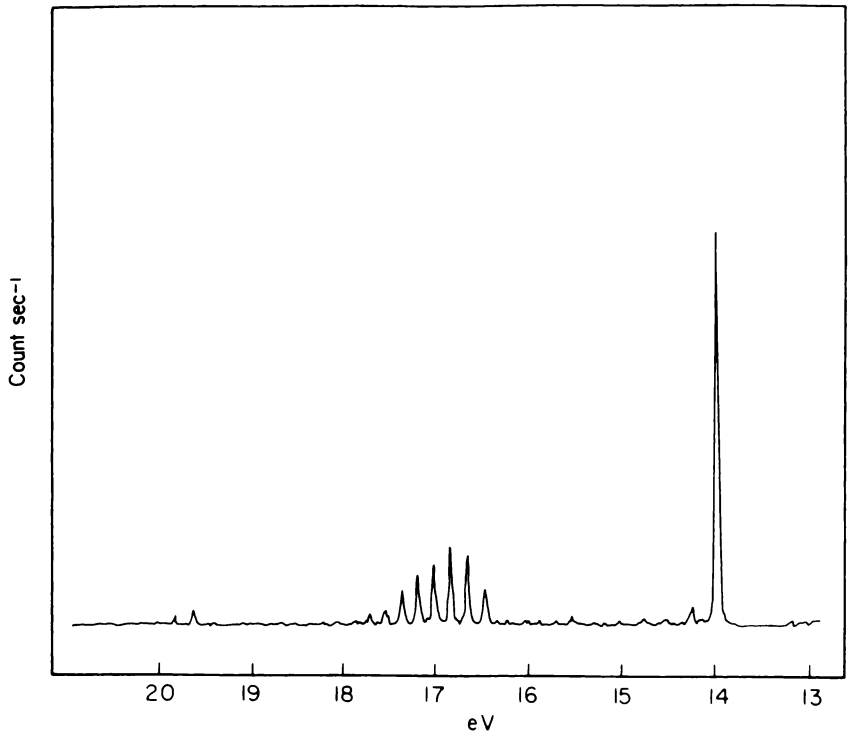

Figure 3.16 : The photoelectron spectrum for carbon monoxide.

features and they compare well to the energy levels found using molecular orbital theory. The differences are due to the deviation away from symmetry for CO as opposed to the symmetrical N_2 molecule causing the hybridised orbitals to change in energy or bonding strength.

(1) Nitrogen,

Three bands are obtained for nitrogen corresponding to the removal of an electron from the $2\sigma_g$, $2\pi_u$, and the $1\sigma_u$ orbitals producing the ionised states $X^2\Sigma_g^+$, $A^2\Pi_u$ and $B^2\Sigma_u^+$. The ionisation energies, from the first peak, are measured as 15.57, 16.69, and 18.75 eV respectively. The first band $2\sigma_g$, indicates the electron removed is essentially non-bonding although there is a small vibrational spacing decrease. The second band results from the removal of a strongly bonding electron in the $2\pi_u$ orbital. This band shows at least seven vibrational components as well as a decreased vibrational spacing. The third band is from a nominally antibonding orbital indicated by the increase in vibrational spacing.

(2) Carbon monoxide

The spectrum for carbon monoxide is essentially the same as for nitrogen. In comparison, the $2\sigma_g$ orbital appears even less bonding than in nitrogen while the $1\sigma_u$ orbital appears slightly bonding. The $2\pi_u$ orbital is still strongly bonding showing the same vibrational structure as N_2. The ionisation potentials for carbon monoxide are 14.01, 16.53 and 19.68 eV respectively.

From this method the following data are obtained and reproduced in table 3.4.

Molecule	Electronic State	Separation (10^{-8} cm)	Ionisation Potential	Vibrational Spacing (cm^{-1})
N_2	$X^1\Sigma_g^+$	1.094	–	2360
N_2^+	$X^2\Sigma_g^+$	1.16	15.57	2207
N_2^+	$A^2\Pi_u$		16.69	1810
N_2^+	$B^2\Sigma_u^+$	1.075	18.75	2420
N_2^+	$C\ ^2\Sigma^+$	1.21		2050
CO	$X^1\Sigma_g^+$	1.125	–	2170
CO^+	$X^2\Sigma_g^+$	1.1150	14.01	2214
CO^+	$A^2\Pi_u$	1.2436	16.53	1562
CO^+	$B^2\Sigma_u^+$	1.1686	19.68	1734

Table 3.4 : Ionisation potentials, ionic states, equilibrium separation and vibrational constants for nitrogen and carbon monoxide.

3.8 Conclusion

It can be seen in this chapter that the fundamental parameters controlling a plasma discharge are complex and sometimes the data is not well known. Even if the cross-sections were fully known, calculation parameters such as ionisation rates will still be uncertain. This is because such rates are dependent on the velocity distribution of the electrons emitted from the filaments. This distribution is unknown and only simulation or modelling of the discharge could provide qualitative answers. As we will see later in the experimental Langmuir probe measurements, the electron distribution in the main plasma body does not conform to any standard equilibrium distribution.

The diffusion of the particles to the plasma boundary is controlled by the imposition of quasi-neutrality determined by the discharge on itself. Simply put, the diffusion of the electrons is limited by the Debye length. The Debye length controls the separation of the charges, or the shielding of one charge from those of opposite charge, to maintain quasi-neutrality. Thus, electrons cannot stream out of the plasma at will since the positive charge built up by their removal restricts the initial motion. Even though these values can be calculated from mobility measurements, a simple experimental validation of these rates can be made. The density change across the radius of the discharge tube can be obtained by Langmuir probe measurements and hence an experimental plot of figure 3.13 can be obtained. If this profile is flat, the diffusion of electrons is severely retarded. If there is a significant gradient, the electron diffusion rates will be closer and closer to their value in free space which implies that the ratio of the drift current to the random current can be qualitatively determined.

From the comparison of molecular nitrogen with carbon monoxide, no significant differences should be found in the behaviour of plasma discharge containing either or both gases. The data presented for various cross-sections, along with the fact that they are isoelectronic molecules, indicate that these molecules are more alike than a comparative homonuclear molecule such as oxygen. Experimentally it will be seen in the spectroscopic results that the spectra of these molecules is almost indistinguishable, since in this discharge configuration, the primary ionisation of the neutral species is to the $B^2\Sigma_u^+$ level for which the electron lost is from the $2\pi_u$ energy level. For nitrogen and carbon monoxide, these levels are almost identical in energy.

3.9 References

Asundi, R. K., J. D. Craggs and M. V. Kurepa, 1963, Proc. Phys. Soc. London, **82**, pp 967.

Bates, D.R, 1962, Ed., *Atomic and Molecular Processes*, (Academic, New York).

Brown, S. C., 1966, *Basic Data of Plasma Physics*, (M.I.T. Press, London)

Hwang, W., Y.-K. Kim and M.E. Rudd, 1996, J. Chem. Phys., **104**, pp 2956.

Krishnakumar, E., and S. K. Srivastava, 1990, J. Phys. B, **23**, pp 1893.

Massey, Sir H., 1979, *Atomic and Molecular Collisions*, (Taylor and Francis, London)

Meek, J. M., and J. D. Craggs, 1978, Eds., *Electrical Breakdown of Gases*, (Wiley-Interscience, New York).

Nasser, E., 1971, *Fundamentals of Gaseous Ionisation and Plasma Electronics* (Wiley-Interscience, New York).

Orient, O. J., and S. K. Srivastava, 1987, J. Phys. B, **20**, pp 3923.

Rapp, D., and P. Englander-Golden, 1965, J. Chem. Phys., **43**, pp 1464.

Schram, B. L., F. J. de Heer, M. J. van der Wiel and J. Kistenmaker, 1965, Physica, **31**, pp 94.

Schram, B. L., H. R. Moustafa, J. Schutten and F. J. de Heer, 1966, Physica, **32**, 734.

Straub, H. C., P. Renault, B. G. Lindsay, K. A. Smith and R. F. Stebbings, 1996, Phys. Rev. A, **54**, pp 2146.

Turner, D. W., C. Baker, A. D. Baker, and C. R. Brindle, 1970, *Molecular Photoelectron Spectroscopy*, (Wiley Interscience, London).

Weast, R. C, and M. J. Astle, 1979, Eds., *CRC Handbook of Physics and Chemistry*, (CRC, Boca Raton, Florida).

Von Engel, A., 1965, *Ionized Gases*, (Clarendon, Oxford, England).

Chapter 4 Review of Langmuir Probes

4.1 Introduction

The aim of this chapter is to summarise the theories necessary to analyse experimental data obtained from Langmuir probes. A variety of methods is available to analyse the data, from the work Langmuir (1961) to the elaborate calculations of Chen (1965A) and Laframboise (1966). Whether the plasma is collisional or collision-free affects the theories used and the values of the characteristic parameters such as the Debye length and mean free paths. The application of probe analysis is somewhat difficult since initially one does not know which theory to apply without knowing what state the plasma is in. Conversely one does not know the state of the plasma until a theory is applied. The best approach is to use the simplest theories to roughly determine the parameters and then to progressively apply more complex analysis to determine the plasma parameters with greater accuracy and precision. We will follow the development of the theory from a historical viewpoint explaining why modifications were necessary to the original work of Langmuir and his colleagues. From the monochromator analysis discussed in chapter five, the ion temperature is only slightly elevated above room temperature and hence we will concentrate the theoretical analysis on the orbital motion approach and the zero temperature limit solutions for cylindrical probes as calculated by Chen (1965A).

The analyses of Langmuir probe data becomes more accurate and precise with increasing numbers of data points collected. This allows a more precise determination of the plasma potential from the derivatives of the characteristic. In the experiments detailed in this thesis, an automated multiranging electronic acquisition system using LabVIEW and a data acquisition card were used to apply voltage to the probe(s) and to read back the current generated from the application of this voltage. This allowed accurate recording of Langmuir probe current-voltage characteristics, and hence accurate analysis of plasma properties (unlike many cases in the literature).

4.2 Basic Langmuir Probe Theory

4.2.1 Single Probes

The first theory describing the current-voltage (I-V) characteristics of electrical probes in a plasma was completed by Irving Langmuir (1961). The general parameters of this theory are:

(a) the plasma is infinite, homogeneous, and quasineutral in the absence of the probe,
(b) the hotter component of the plasma (for our work, the electrons) is collected, so that the distribution at the sheath edge boundary is approximately Maxwellian with $T_e >> T_+$,
(c) the mean free paths of the electrons and ions are much greater than the probe or sheath dimensions or any other characteristic length,
(d) each particle hitting the probe is collected, i.e. not reflected, and does not cause emission of secondary particles on collision with the probe,
(e) the sheath boundary is well defined, and
(f) the sheath thickness is small compared to probe dimensions.

Given these conditions, the probe current is independent of the exact shape of the potential surrounding the probe. Initially we will look at a simple system that was originally derived for planar probes. However, these results are equally valid for any probe geometry. From figure 4.1 we see that the applied potential difference between the probe surface and the chamber wall, U, comprises two voltages: (i) V_{sp}, the potential drop between the chamber wall and the sheath edge, and (ii) V_p the potential drop between the sheath boundary and the probe surface.

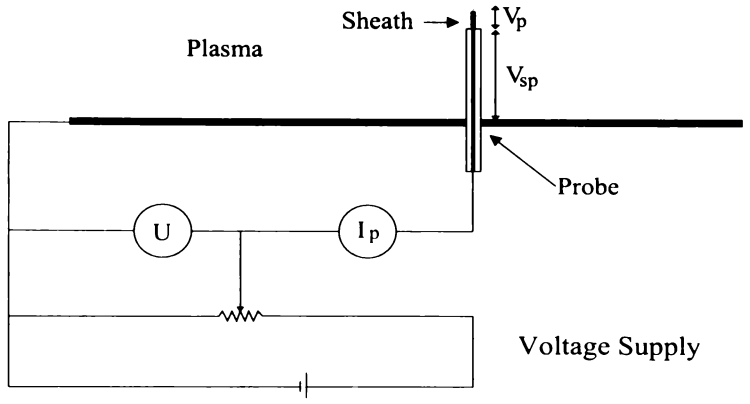

Figure 4.1 : General probe circuit and definition of parameters.

Thus we have

$$U = V_{sp} + V_{p.} \tag{4.1}$$

If the probe is isolated then there can be no current flow. Therefore the number of electrons and ions arriving at the probe surface per unit of time must be equal (assuming the ions are singly charged). Since electrons are much lighter than ions and are generally the hotter species, the probe must develop a negative potential with respect to the plasma to repel excess incident electrons and attract additional ions to retain the zero current flow. Even when the electron temperature is the same as the ions, this condition holds since the mean electron velocity exceeds that of the ions by $(m_i/m_e)^{1/2}$ where m is the particle mass. From classical Maxwellian theory the mean particle velocity of species j is

$$v_j = \left(\frac{8kT_j}{\pi m_j} \right)^{1/2} \tag{4.2}$$

where k is Boltzmann's constant.

In order to gain an overall view of the physical situation for a non-isolated probe, it is useful to look at a qualitative I-V curve such as that shown in figure 4.2. In these plots, negative (electron) current is plotted against the probe voltage. At the point V_{sp}, the probe is at the same potential as the plasma, i.e. $V_p = 0$, $U = V_{sp}$. There is no electric field at this point between the probe and plasma and so an excess of electrons flow to the probe. To the right of this point (region D), if we increase the probe voltage, electrons are accelerated to the probe while the ions are repelled. Thus

there is an increase of negative charge on the probe that normally forms a thin sheath. In this region the current can therefore be attributed to the effect of the electron distribution in the plasma.

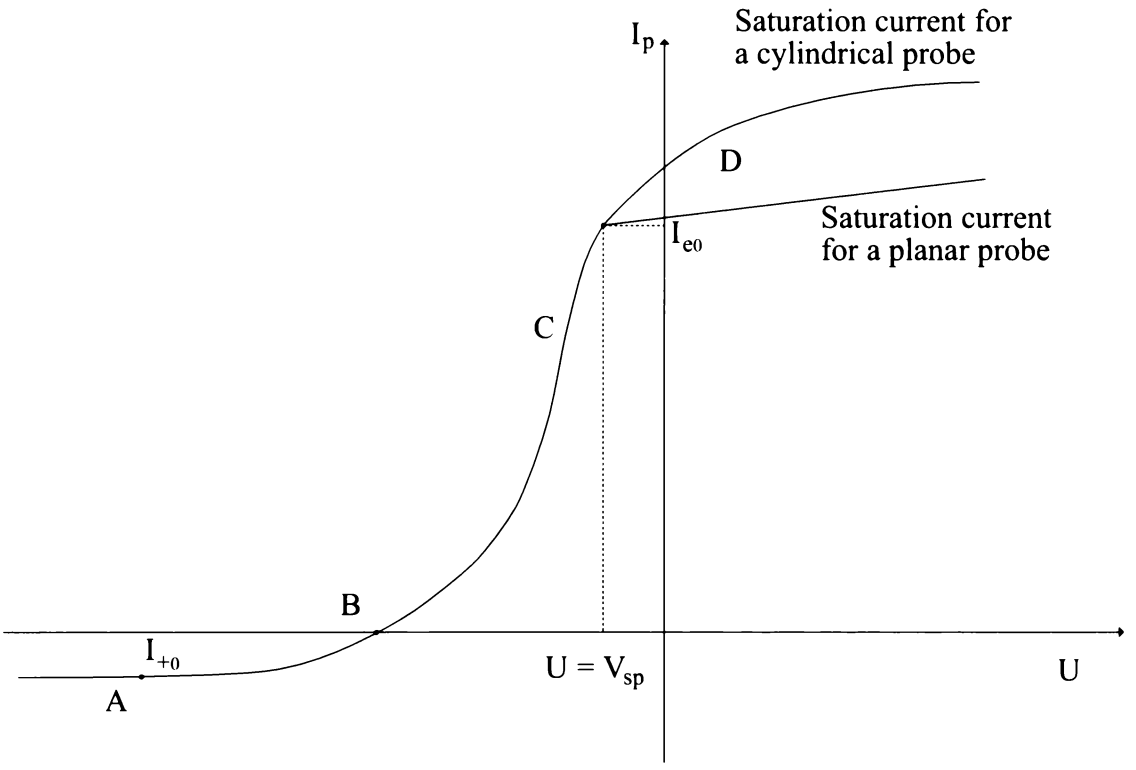

Figure 4.2 : Idealized current-voltage characteristics for a single Langmuir probe.

The slow increase in current with increasing voltage above $U = V_{sp}$ is largely caused by an increase in the sheath width. This is called the saturation regime. If we now lower the probe voltage below V_{sp} (region C) we start repelling electrons and attracting ions. As we lower the voltage, increasingly higher energy electrons are unable to overcome the probe potential barrier and if the electron distribution is Maxwellian, once the ion contribution had been removed, the shape of the curve will be exponential. This is called the transition regime, and extends to the point B where the probe current is zero. At this point the probe is biased sufficiently to repel all electrons apart from the flux necessary to balance the ion current i.e. $I_+ = I_-$. If we reduce the probe potential even further (region A) eventually all electrons are repelled and an ion sheath is produced with the ion saturation current being collected by the probe.

We can now examine Langmuir's theory and the equations derived to determine plasma parameters such as the electron temperature, T_e, and the plasma

density, n_0. We will first consider the positive ion collection region (AB) of the probe characteristic. A detailed analysis will be considered fully in the section dealing with double probes (section 4.2.2). The first attempt to develop a theory of positive ion collection was by Mott-Smith and Langmuir (1926) based on the assumption that the plasma surrounding a negative probe could be split into two principal regions: the positive space charge region (ion sheath) into which no electrons can penetrate; and the undisturbed plasma where electron and ion concentrations are equal. However, Tonks and Langmuir (1929A and 1929B) found that the ratio between ion and electron currents was much larger than the theory based on these assumptions predicted. This discrepancy, as noted by Bernstein and Rabinowitz (1959), is caused by the ions entering the sheath with an energy higher than their thermal energy and results from the breakdown of assumption e) stated at the start of this section.

Between the ion sheath and the undisturbed plasma there is a transition region where neutrality is modified due to the removal of ions from the sheath. Most of the potential drop occurs in the ion sheath with a small potential drop across the quasineutral transition region. However, when the ion temperature is much lower than the electron temperature, the weak field that penetrates into the plasma is large enough to distort the random thermal motion of the ions. This gives the ions a velocity directed towards the probe with their energy determined by the potential drop across the transition region. The formation of a space charge sheath does not occur until the probe is made more negative so that most of the electrons are repelled, i.e. $-eV_s = kT_e/2$, (assuming the electrons have a Maxwellian distribution). Thus the transition region is penetrated by a potential where the ions gain an energy of $kT_e/2$. This "presheath" potential is almost independent of the probe potential. This sheath criterion also applies to the collection of electrons. For a comprehensive discussion and derivation the reader is referred to the original work of Bohm (1949) and the comprehensive review of Riemann (1991). The consequences of this sheath criterion for the normal case where $T_i << T_e$ are as follows. In part D of the I-V characteristic in figure 4.2, the electrons are accelerated towards the probe so that they must enter the sheath with a drift velocity greater than $(kT_e / m_e)^{1/2}$. Since this is small compared to the random thermal velocity of the electrons, the distortion of the electron energy at the sheath edge is minimal and can be approximated by the undisturbed plasma value. However, in part A of the curve, the sheath criterion implies that the ions must have a

directional velocity greater than $(kT_e / m_i)^{1/2}$ which is much greater than their random thermal velocity. Hence the velocity at the sheath edge is unknown and must be calculated (refer to section 4.22 on double probes). This is essentially the reason probes are insensitive to ion temperature. It also implies that the ions are captured within a radius larger than the sheath radius. This is illustrated in figure 4.3 where the subscripts *s* and *p* refer to the sheath and probe respectively.

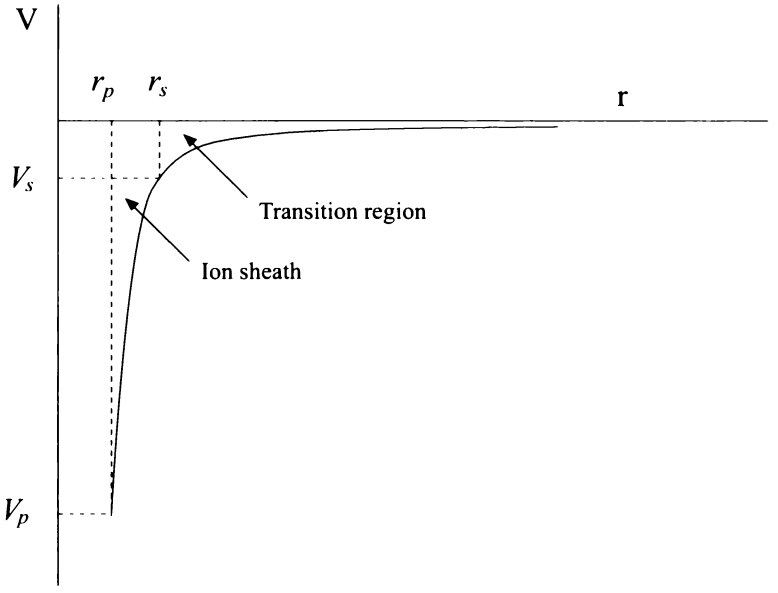

Figure 4.3 : Potential distribution showing the presheath region for a negative probe where *s* and *p* represent the sheath and the probe respectively so that V_s is the sheath voltage.

An approximation of the ion current to the probe can be made using simple physical analyses. Since the ions enter the sheath region with an energy equivalent to half the average electron energy, the velocity the ions achieve can be expressed at the sheath boundary as

$$v_s = \left(\frac{2eV_s}{m_+} \right)^{1/2} \tag{4.3}$$

where m_+ is the ion mass. The electron concentration at the boundary can be expressed as

$$n_e = n_0 \, e^{\left(eV_s / kT_e \right)} \tag{4.4}$$

where n_0 is the undisturbed plasma density, e is the exponential function (exp) and e is the electron charge. An approximate value for the ion current can now be given as

$$I_+ = eA_s \left(\frac{2eV_s}{m_+} \right)^{1/2} n_0 \, e^{\left(eV_s / kT_e \right)} \tag{4.5}$$

where A_s is the sheath area. Substituting for eV_s we obtain

$$I_+ = x \, n_0 \, e \left(\frac{kT_e}{m_+} \right)^{1/2} A_s \tag{4.6}$$

where x is a coefficient the order of 0.6. The value of x depends on the energy of the ions entering the sheath which is weakly temperature dependent, for $-eV_s = kT_e/2$, $x = 0.6$. It should be noted that the ion current is dependent on the electron temperature.

We will now consider the portion of the I-V characteristic where electron flow dominates (B-D on figure 4.2). If we traverse along this curve to the right from point B, increasing numbers of electrons overcome the potential barrier between the probe and the plasma. Near B only the high energy electrons of the distribution reach the probe. As the potential difference falls, an increasing portion of the electron distribution can make the crossing until electrons of any energy in the distribution can access the probe and saturation is reached. The density distribution of the electrons in this region is described by Boltzmann's law:

$$n_e = n_0 \, e^{\left(\frac{eV_p}{kT_e} \right)} \tag{4.7}$$

The mean random electron current at the sheath edge is

$$I_{e0} = -\frac{1}{4} n_0 e v_e A_p \tag{4.8}$$

where v_e and A_p are the mean electron velocity and the probe area respectively. Substituting for velocity and density and taking into account the ion current, we find that the total electron current I_e and the total probe I_p current are

$$\begin{aligned} I_e &= -\frac{1}{4} n_0 e \, v_e A_p \, e^{\left(\frac{eV_p}{kT_e} \right)} \\ I_p &= I_{+0} + I_{e0} \, e^{\left(\frac{eV_p}{kT_e} \right)} \end{aligned} \tag{4.9}$$

Experimentally this is a useful description since a logarithmic plot of the I-V characteristic will result in a straight line of slope e/kT_e. Deviations from this equation

are found experimentally since the distribution will generally not be truly Maxwellian. However, these equations give an simple and easy rough estimate of the plasma density and temperature.

4.2.2 Double Probes

Double probe are similar in nature to single probes and the same Langmuir theory holds. The main difference is that the current to a double probe is limited by Kirchoffs law and hence they are designed for use in low current plasmas where a single probe would draw to much current and distort the plasma equilibrium. It should be noted that single probes are in fact an extremely unbalanced double probe arrangement where the second "probe" is the area of the chamber walls, usually taken to be a probe of infinite size.

A system of two or more connected Langmuir probes was first proposed by Johnson and Malter (1950). The basis of this procedure was to be able to use Langmuir probes in afterglow plasma systems, or those where no external reference points exist, i.e. RF plasmas. Since conception, the use of double probes has migrated to all types of plasmas as the theory and analysis of ion current collection has been satisfactorily determined. Furthermore it is prudent to simultaneously operate single and double probes in a plasma in order to cross-reference the results. This provides a double check on the plasma parameters in question. Double probes are also (by their configuration) limited by the fact that the ion current is the maximum current drawn to either electrode. This minimises the perturbing effects of the probes on the plasma system.

In a typical arrangement, two probes are biased with respect to each other, while they remain insulated from ground. The entire system "floats" with fluctuations in the plasma potential and thus is capable of following variations in this potential. The geometry of the system is shown in figure 4.4.

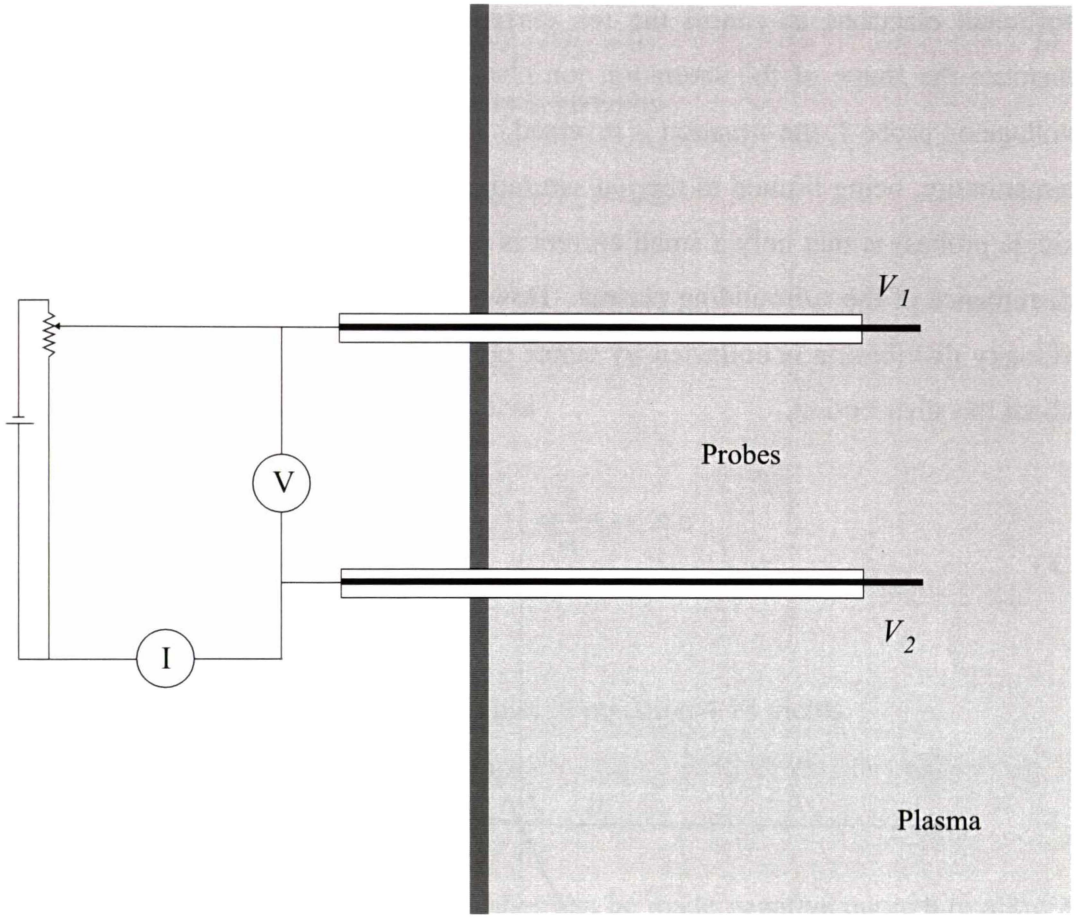

Figure 4.4 : A generalized representation of a double probe system.

The general double probe system comprises two Langmuir probes, normally with electrodes of identical shape and size, which are connected to a voltage source of reversible polarity. The current to each probe is governed by the same equations as for single probes. A voltage can be applied between the probes and we shall assume that V_1 is positive relative to V_2 and thus

$$V = V_1 - V_2 > 0 \tag{4.10}$$

A current flow between probe 2 and probe 1 is positive by definition. The double probe characteristic (DPC) is shown in figure 4.5 for the symmetrical case. At $V = 0$ both probes are at the floating potential which is negative with respect to the plasma and there is no net current flow. If V is made slightly positive, V_1 will become less negative and V_2 more negative, thus more electrons will flow to probe 1 and fewer to probe 2. This results in a positive current flow from probe 2 to probe 1. For a large positive voltage, probe 2 will become highly negative drawing the ion saturation current. Probe 1 may still be negative but close enough to the sheath voltage to collect

sufficient electrons to cancel the ion current drawn by probe 2. Hence probe 1 matches the shape of the saturation ion characteristic of probe 2. With a negative voltage on probe 1, the situation is reversed. Thus the current drawn to each probe has a maximum, being limited to the ion saturation current. The advantage (compared to single probes) is that only a small current is drawn to the probes resulting in minimal disturbance of the surrounding plasma. However, only a small portion of the electron velocity distribution is collected by either probe hence no information can be gained about this distribution.

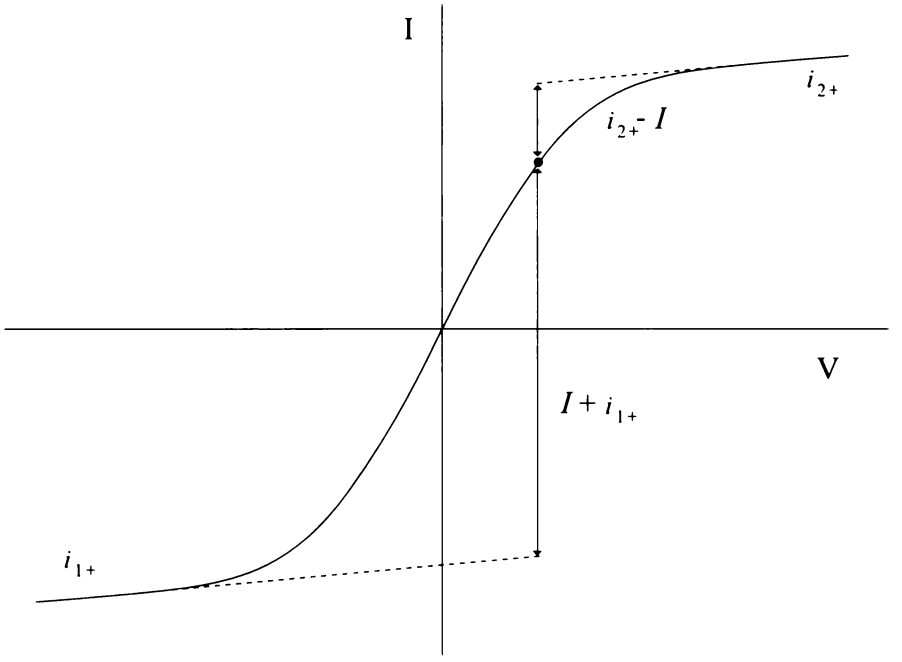

Figure 4.5 : A symmetrical double probe characteristic representation.

The current to each probe is determined by the same equations as for single probes (equations 4.9). For electron retardation at a probe potential of V_p with respect to the plasma, the electron current is

$$I_e = \frac{1}{4} n_0 e \, v_e A_p \mathrm{e}^{\left(\frac{eV_p}{kT_e}\right)} \tag{4.11}$$

This value is different for each probe depending on the localised parameters and the nature of each probe, since V_p is different for each probe. The two probes are a coupled system bound by Kirchoff's law. If we define i_{1+}, i_{2+}, I_{1e} and I_{2e} to be the ion and electron currents to each probe respectively, then for the floating system we require

$$i_{1+} + i_{2+} - I_{1e} - I_{2e} = 0 \tag{4.12}$$

The current I flowing in the external loop is given by

$$i_{2+} - I_{2e} - (i_{1+} - I_{1e}) = 2I \tag{4.13}$$

Combining these equations gives us

$$I = I_{1e} - i_{1+} = i_{2+} - I_{2e} \tag{4.14}$$

Using equations 4.11 and 4.14 we find that

$$\begin{aligned} I + i_{1+} &= \frac{1}{4} n_0 e v_e A_1 \mathrm{e}^{\left(\frac{eV_1}{kT_e}\right)} = \frac{1}{4} n_0 e v_e A_1 \mathrm{e}^{\left(\frac{e(V+V_2)}{kT_e}\right)} \\ &= I_{2e} \frac{A_1}{A_2} \mathrm{e}^{\left(\frac{eV}{kT_e}\right)} \end{aligned} \tag{4.15}$$

Repeating this approach for the second part of equation 4.14 yields

$$\frac{I + i_{1+}}{i_{2+} - I} = \frac{A_1}{A_2} \mathrm{e}^{\left(\frac{eV}{kT_e}\right)} \tag{4.16}$$

A premise for this theory is that the probes can be made negative enough to allow the accurate extrapolation necessary to determine the saturation current values in equation 4.16. This extrapolation is shown in figure 4.5. Taking a semi-log plot of equation 4.16 allows the electron temperature to be obtained from the slope of the graph. A simpler method also exists to obtain the electron temperature but requires that the ion current be independent of the potential. Using this assumption we find that

$$\frac{\mathrm{d}I}{\mathrm{d}V} = \frac{\mathrm{d}I_{1e}}{\mathrm{d}V} = -\frac{\mathrm{d}I_{2e}}{\mathrm{d}V} \quad ; \quad 1 = \frac{\mathrm{d}V_1}{\mathrm{d}V} - \frac{\mathrm{d}V_2}{\mathrm{d}V} \tag{4.17}$$

Using equations 4.17,and 4.11 we have

$$A_1 \mathrm{e}^{\left(\frac{eV_1}{kT_e}\right)} \frac{\mathrm{d}V_1}{\mathrm{d}V} + A_2 \mathrm{e}^{\left(\frac{eV_2}{kT_e}\right)} \left(\frac{\mathrm{d}V_1}{\mathrm{d}V} - 1\right) = 0 \tag{4.18}$$

At $V = 0$, $V_1 = V_2$ and so

$$\left.\frac{\mathrm{d}V_1}{\mathrm{d}V}\right|_0 = \frac{A_2}{A_1 + A_2} \tag{4.19}$$

Thus

$$\left.\frac{\mathrm{d}I}{\mathrm{d}V}\right|_0 = \left(\frac{A_1 A_2}{A_1 + A_2}\right)\frac{1}{4} n_0 e v_e A_p \frac{e}{kT_e} \mathrm{e}^{\left(\frac{eV_p}{kT_e}\right)} \tag{4.20}$$

If we approximate the ion and electron random Maxwellian currents as

$$j_+ = j_e \mathrm{e}^{\left(\frac{eV_p}{kT_e}\right)} \tag{4.21}$$

we have

$$\left.\frac{\mathrm{d}I}{\mathrm{d}V}\right|_0 = \left(\frac{A_1 A_2}{A_1 + A_2}\right) j_+ \frac{e}{kT_e} \mathrm{e}^{\left(\frac{eV_p}{kT_e}\right)} \tag{4.22}$$

Finally using $i_{1+} = A_1 j_+$ and $i_{2+} = A_2 j_+$ we have

$$\left.\frac{\mathrm{d}I}{\mathrm{d}V}\right|_0 = \frac{e}{kT_e}\frac{i_{1+} i_{2+}}{i_{1+} + i_{2+}} \tag{4.23}$$

from which the electron temperature can be measured. Once this is known, the density can be calculated from either the ion saturation current equations or from the following theories.

4.2.3 The Second Derivative

Langmuir was also the first to suggest that by measuring $\mathrm{d}^2 I_e / \mathrm{d}V_p^2$ as a function of V_p the distribution function could be determined. Druyvesteyn (1930) analysed the case of cylindrical and spherical probes and suggested that this relationship should apply to any non-concave probe. Several derivations have been completed to show the relationship between the second derivative and the collected current. They are all based on equations describing the collection of electrons and can be found in the books of Swift and Schwar (1970), Schott (1968) as well as in the papers of Allen (1992), and Kagan and Perel (1964). This last derivation by Kagan and Perel (1964) is the one presented by Swift and Schwar and proves that the relationship between the distribution functions and the second derivative is valid for any concave surface. These results will not be derived but are stated in equations 4.24.

$$\frac{\partial^2 I}{\partial V^2} = \frac{1}{4} A_p e^2 \left(\frac{2e}{m_e V}\right)^{1/2} f_E(\varepsilon) \quad = \frac{1}{4} A_p e^3 \left(\frac{2}{m_e}\right)^{1/2} f_P(\varepsilon) \tag{4.24}$$

$f_E(\varepsilon)$ and $f_P(\varepsilon)$ represent the electron energy distribution function (EEDF) and the electron energy probability (velocity) function (EEPF) respectively, and $\varepsilon = eV$. In the calculation of the second derivative, a number of papers use the tables presented by Savitzky and Golay (1964).

These tables are calculated by using Stirling's central difference method on the generalised form of Newton's forward difference formula. Having used these tables, we have found the following: two of the tables which could be used for the purposes of Langmuir probe analysis have errors. These are column 5 in table VI, and column 9 in table IV. These should read 2, -1, -2, -1, 2 and 86, -142, -193, -129, 0, 129, 193, 142, -86 respectively. There is a compromise in using these tables: the advantage of using them is that the second derivative can be calculated directly without having to calculate the first derivative. The disadvantage is that the minimum number of data points used to calculate the second derivative is five. This means that the second derivative is averaged over these five points. For sharp transitional data around the knee region, this can lead to a smoothing or averaging effect where the knee becomes less well defined than it would be using a simple two-point differentiation method. This averaging has the effect of smoothing the second differential and can lead to lower peak values and hence a flatter distribution curve. This effect causes an underestimation of the plasma density when the EEDF is integrated. From experience, the larger the number of data points the better is the fit to the "true" value using the simple Newton method since the effect of averaging becomes less noticeable. With higher and higher terms added, e.g. using a 25-point differential term, the second derivative curve becomes meaningless since it is now far removed from the true second derivative by the averaging process. Using the method of Savitzky and Golay (1964) will not necessarily produce incorrect results, but one must be aware of the pitfalls and limitations of such methods.

4.3 Orbital and Radial Motion Theories

If we now look at cylindrical and spherical probes in more detail we have the additional requirement that the potential distribution is symmetrical with respect to the probe. Particles can now move in orbits about the probe under the influence of a centralised force. Poisson's equation is now more complicated and the density is also

a function of the potential. A solution of Poisson's equation must be found numerically but in some situations the probe current can be determined without knowing the radial distribution of the potential, $V(r)$.

4.3.1 Orbital Motion Limited

Orbital motion limited (OML) behaviour of the charged species is one of important early theories for the current collected by spherical and cylindrical probes and is based on the following premise for the probe current: the current is that collected by the probe when none of undisturbed particles in the plasma capable of reaching the probe are excluded from doing so from energy considerations, i.e. there is no potential barrier for particle collection by the probe and no reflected particles. The theory is discussed in the books of Chung *et al.* (1975), Swift and Schwar (1970), Chen (1965B), Schott (1968), Allen *et al.* (1957), Allen (1992), and Bohm (1949) as well as the original treatment of the problem by Mott-Smith and Langmuir (1926).

We will follow the approach of Swift and Schwar (1970) for the generalised cylindrical form of this theory. Using the conservation laws for energy and angular momentum we have:

$$E = \frac{1}{2} m_e \left(u^2 + v^2 + w^2\right) - eV(r) \tag{4.25}$$

$$J = m_e v\, r \tag{4.26}$$

where E is the particle energy, $V(r)$ is the potential distribution and J is the angular momentum. If $f(u_s, v_s, w_s)du_s dv_s dw_s$ is the number of electrons per unit volume at the sheath edge having velocity components in the range u_s to $u_s + du_s$, v_s to $v_s + dv_s$, and w_s to $w_s + dw_s$ and if r_s is the sheath radius, the flux of electrons (i.e. the particle current) in this velocity range crossing the sheath edge is

$$dJ_e = 2\pi\, r_s L\, u_s f(u_s, v_s, w_s)\, du_s dv_s dw_s \tag{4.27}$$

where it is assumed that the cylinder length L is sufficiently large compared to the probe radius for the velocity component parallel to the axis of the cylinder to make no contribution to the electron flux. The coordinate system is shown in figure 4.6.

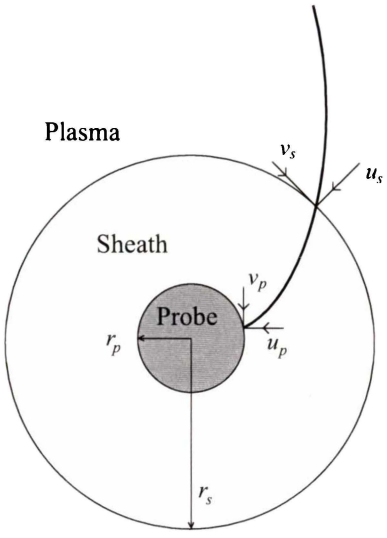

Figure 4.6 : The graphical representation of the probe and the sheath showing the coordinate system used. Taken from Swift and Schwar (1970).

Since the velocity components at the sheath edge are u_s, v_s, and w_s and the components at the probe's surface are u_p, v_p, and w_p, then from the energy conservation equations we have

$$\frac{1}{2}m_e\left(u_s^2+v_s^2+w_s^2\right)=\frac{1}{2}m_e\left(u_p^2+v_p^2+w_p^2\right)-eV_p \tag{4.28}$$

$$m_e v_s r_s = m_e v_p r_p \tag{4.29}$$

where V_p is the probe voltage. Solving for the radial and tangential components only (since w_s make no contribution) at the probe's surface, from equation 4.28 and 4.29 we find

$$v_p = v_s\left(\frac{r_s}{r_p}\right) \tag{4.30}$$

$$u_p^2 = u_s^2 - v_s^2\left[\left(\frac{r_s}{r_p}\right)^2 - 1\right] + \frac{2eV_p}{m_e} \tag{4.31}$$

An electron is collected when its radial velocity component at the probe's surface is greater than zero. Using this limit and rearranging equation 4.31 we find the tangential velocity v_s must be in the range

$$0 \le v_s^2 \le \left[\frac{r_p^2}{r_s^2 - r_p^2}\right]\left[u_s^2 + \frac{2eV_p}{m_e}\right] \tag{4.32}$$

For electron collection, zero is the smallest value u_s can take for positive V_p. For negative V_p, the limit is $(-2eV_p/m_e)^{1/2}$. Thus upper and lower limits of u_s are $+\infty$ and 0 while the limits of w_s are $\pm\infty$. Using this, the integral of equation 4.27 becomes

$$J_e = 2\pi r_s L \int_0^{\infty} \int_{-v_s}^{v_s} \int_{-\infty}^{\infty} u_s f(u_s, v_s, w_s) du_s dv_s dw_s \tag{4.33}$$

For a Maxwellian velocity distribution of electrons at the sheath edge

$$f(u_s, v_s, w_s) du_s dv_s dw_s = N_0 \left(\frac{m_e}{2\pi k T_e} \right)^{3/2} e^{\left[-\frac{m_e}{2kT_e}\left(u_s^2 + v_s^2 + w_s^2\right) \right]} du_s dv_s dw_s \tag{4.34}$$

Substituting for $f(u_s, v_s, w_s)$ and integrating we obtain

$$J_e = 2\pi r_p L N_0 \left(\frac{kT_e}{2\pi m_e} \right)^{1/2} \left\{ \frac{r_s}{r_p} \left[1 - erfc\left(\frac{r_p^2 \eta}{r_s^2 - r_p^2} \right)^{1/2} \right] + e^{\eta} erfc\left(\frac{r_s^2 \eta}{r_s^2 - r_p^2} \right)^{1/2} \right\} \tag{4.35}$$

where $\eta = \dfrac{eV_p}{kT_e}$ and

$$erfc(x) \equiv \frac{2}{\sqrt{\pi}} \int_x^{\infty} e^{-y^2} dy \tag{4.36}$$

Equation 4.35 is complicated and not really useful for experimental work because too many variables are unknown. We have to know the sheath radius, r_s and its dependency on V_p. If we examine the limits of equation 4.35 for the sheath radius r_s tending to infinity, i.e. the thick sheath limit, equation 4.35 can be simplified to

$$J_e = 2\pi r_p L N_0 \left(\frac{kT_e}{2\pi m_e} \right)^{1/2} \left(\frac{2}{\sqrt{\pi}} \eta^{1/2} + e^{\eta} erfc\left(\eta^{1/2} \right) \right) \tag{4.37}$$

With further simplification and taking into account the comparison of the curves of figure 4.7, equation 4.37 can be approximated by

$$J_e = 2\pi r_p L N_0 \left(\frac{kT_e}{2\pi m_e} \right)^{1/2} \frac{2}{\sqrt{\pi}} (1 + \eta)^{1/2} \tag{4.38}$$

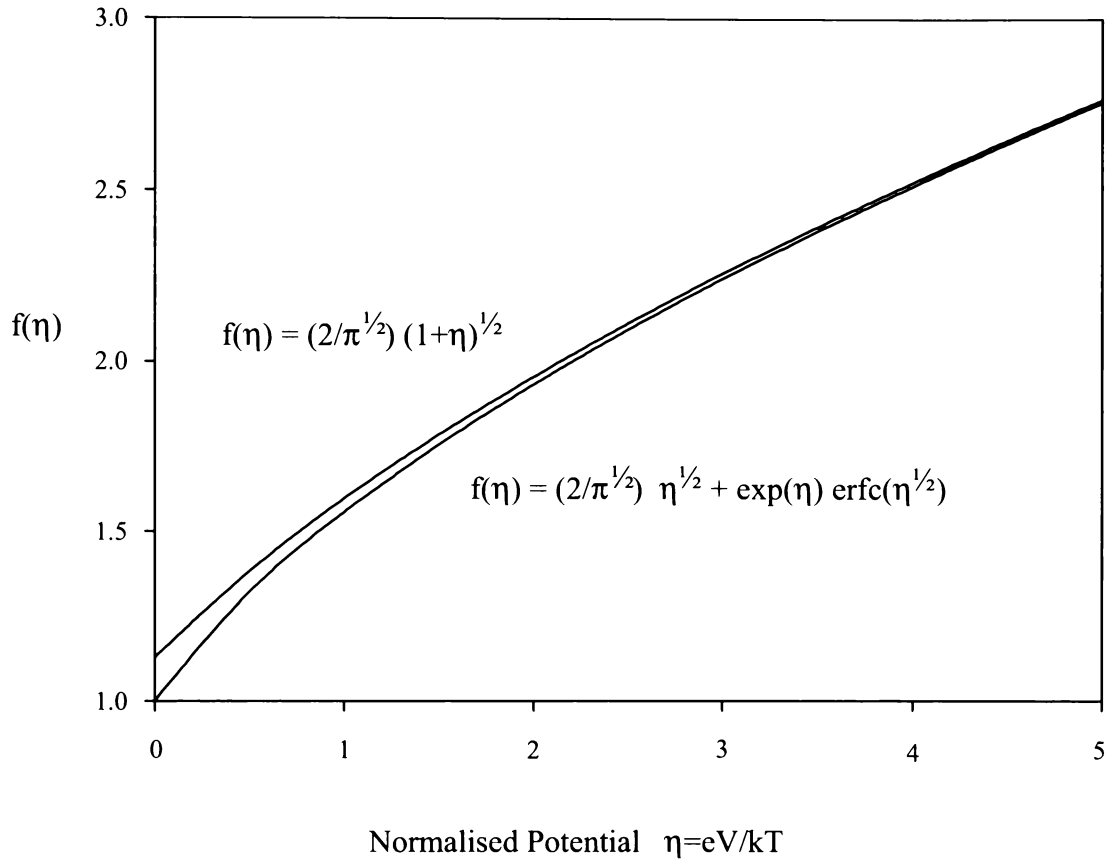

Figure 4.7 : A plot of equations 4.37 and 4.38 showing the basis of the simplifying assumptions.

Equation 4.38 is now in a form useful for experimental comparison with the experimental data. If we rearrange equation 4.38 into the physical parameters measured we find that:

$$I_i = A_p N_0 e \left(\frac{kT_i}{2\pi m_i} \right)^{\frac{1}{2}} \frac{2}{\sqrt{\pi}} \left(1 - \frac{eV_0}{kT_i} \right)^{\frac{1}{2}} \tag{4.39}$$

where A_p is the probe area, N_0 is the plasma density and V_0 is the voltage applied to the probe referenced to the plasma potential. If OML is followed, the gradient of I^2 vs. V_0 will produce a linear fit determining the density, while the intercept at $I = 0$ passes through the space potential if $T_i \rightarrow 0$. Equation 4.39 is also valid for electron collection and the equation is modified simply by replacing the ion terms with the respective electron values. In this case the intercept occurs at a value of T_e (eV) away from the space potential. In practice the plotted experimental I^2 vs. V_0 curves are often linear, but as noted by Tonks and Langmuir (1929) the intercept at $I = 0$ is often not at the space potential raising questions about the application of equation 4.39. The underlying problem in the validity of this equation is that there is no way to determine

if the condition $r_s/r_p \rightarrow \infty$ is satisfied when the electrons and ions move with orbital motion since the sheath thickness cannot be determined (Swift and Schwar (1970)).

Equation 4.39 for the thick sheath limit of the probe region is important because it provides an upper limit on the current collected by a Langmuir probe, since potential barriers can only reduce the number of particles reaching the probes.

4.3.2 Radial Motion

In the Langmuir theory it is assumed that the velocity distribution function of the particles is known at the sheath edge. However, when the colder species is collected, the ions must obtain a drift velocity upon entering the sheath. This causes problems if the sheath edge is taken close to the probe since the ion distribution is unknown. If the sheath edge is taken to be far enough away to include the presheath area, where the electric fields impart the drift velocity, then an absorption radius does not exist. Unfortunately this means that the ion current is not independent of the potential shape and Poisson's equation must be solved for the potential.

A full examination of all the theories for the positive ion characteristics will not be given as it is beyond the scope of the analyses needed for the experimental data. However, a detailed treatment will be given for the zero ion temperature case since this is the relevant applicable theory. The approach of using this theory has been somewhat retrospective in use. The simple analysis previously outlined was used to analyse the data to obtain characteristic lengths such as the Debye length. This enabled the writer to determine the relevant theories for ion collection.

There is also some debate with the overlapping theories derived by Laframboise (1966) and by other authors such as Allen *et al.* (1957), Bernstein and Rabinowitz (1959) and Chen (1965A, 1965B). The main differences are whether orbital motion or radial motion is present, and whether the ions initially have an isotropic or Maxwellian distribution. The full differences are many-fold and are complex in argument and physical nature. However, the point is that no single theory can be used to calculate the ion current to a Langmuir probe. The theory used in this work is that of Chen (1965A, 1965B) as there has been some debate over the work of Laframboise (1966) and its validity in experimental practice. The theory derived by Laframboise (1966) is the best in content and nature, providing a more realistic, physical starting point from the initial assumptions. Unfortunately, the results of the

theory don't match experimental results as well as the theory first proposed by Bernstein and Rabinowitz (1959). This theoretical problem also hinges on the geometry of the probes, as cylindrical and spherical probes have different theoretical limits as $T_i/T_e \rightarrow 0$. Cylindrical probes have been used in this work and will use the simplest of these theories (which is complex enough) to analyse the ion current data. This is the zero temperature limit ($T_i/T_e \rightarrow 0$) which is the theory proposed by Allen *et al.* (1957). The justification for this theory is that the ion saturation current is almost independent of kT_i. In calculations originally done by Bohm (1949), coefficients of 0.57 and 0.54 were obtained instead of 0.6 in equation 4.6 for ion energies of 0.001 and 0.5 times kT_e respectively.

All the later ion current theories are extensions of the OML theory. The OML theory simply considers particles as collected when they hit the probe, although some may hit at a grazing angle. The extension of this theory is based on an absorption radius that may exist outside the probe radius where all particles crossing this boundary are collected by the probe. The initial consideration of this premise was attempted by Bernstein and Rabinowitz (1959) and extended by Chen (1965A) for an isotropic distribution of ions. Laframboise (1966) again extended the theory to include a Maxwellian distribution of the attracted species. The limit of zero temperature for this theory reduces the equations to the standard OML theory.

The following equations will only be stated as their derivation provides no new information on the analyses of the experimental data. The reader is referred to quoted literature for a comprehensive derivation. It should also be noted that the following equations are in cgs units and appropriate conversion of fundamental units is necessary to compare the experimental data with the theory as has been done in equation 4.43.

Following the approach of Chen (1965A) for a cylindrical probe, and for $\beta = 0$, where $\beta = T_+/T_e$, we have the following equation

$$\frac{\mathrm{d}}{\mathrm{d}\xi}\left(\xi\frac{\mathrm{d}\eta}{\mathrm{d}\xi}\right) - J\eta^{-1/2} + \xi \mathrm{e}^{-\eta} = 0 \tag{4.40}$$

or with $\zeta = \xi J^{-1}$

$$\frac{1}{J^2}\frac{\mathrm{d}}{\mathrm{d}\zeta}\left(\zeta\frac{\mathrm{d}\eta}{\mathrm{d}\zeta}\right) - \eta^{-1/2} + \zeta \mathrm{e}^{-\eta} = 0 \tag{4.41}$$

The definitions of the variables in cgs units are:

$$\xi = \frac{r}{h} \; ; h = \left(\frac{kT_e}{4\pi n_0 e^2} \right)^{1/2} ; \eta = -\frac{eV}{kT_e} ; J = I_+ \frac{e}{kT_e} \left(\frac{m_i}{2\pi n_0 Z} \right)^{1/2} \tag{4.42}$$

With SI units, from Chen and Arnush (2001), the variables become

$$\xi = \frac{r}{h} \; ; \quad h = \left(\frac{\varepsilon_0 kT_e}{n_0 e^2} \right)^{1/2} ; \quad \eta = -\frac{eV}{kT_e} ; \quad J = \frac{1}{2\pi\sqrt{2}} \frac{I_i}{n_0} \frac{1}{hc_s} ; \quad c_s = \left(\frac{kT_e}{m_i} \right)^{1/2} \tag{4.43}$$

where Z is the ion charge number and I_i is the particle current per unit length. All the variables are normalised, so for example, ξ is the radial distance divided by the Debye length (h). These equations are valid if the distribution of angular momenta L at ∞ is a delta function around $L = 0$, i.e. the ion distribution is uniform in energy. In practice, the collisionless equations are valid up to a mean free path λ, with the validity condition being

$$\frac{-E_+}{eV_p} << \frac{r_p}{\lambda^2} \tag{4.44}$$

Equations 4.40 and 4.41 are both useful to solve for different circumstances. Equation 4.41 calculates the curves on a universal scale and a fixed value of ξ and so is useful to determine how far into the plasma the iteration needs to start in order to obtain an accurate solution. Equation 4.40 is preferentially used to calculate the cross-plotting data to obtain curves of η vs. $J\xi$ for constant ξ even though it means that the starting point becomes a quasi-variable.

In order to numerically solve these equations it is necessary to start the integration in the plasma region and iterate up to the probe surface since the potential at the probe surface is unknown. This requires an initial starting condition where the plasma solution is valid ($\eta \rightarrow 0$). The integration method chosen to solve the family of curves (η vs. ξ or ξ/J, for a constant J) was a Runge - Kutta formulation, taken from Garcia (1994) and Press (1992), where ξ is taken to be equivalent to ξ_p. Two versions of this method, a fourth order (rk4) and an adaptive stepping algorithm (rka) were used to solve equations 4.40 and 4.41.

In the adaptive method, one inputs a minimum error setting along with the starting conditions and the algorithm decreases the step size until this error is met. The next point is again subject to the same process and hence the entire method allows

the sensitivity of the solution to the step size to be evaluated. However, this process means that the step size is variable, and hence the solution cannot be stopped at a particular value of ξ (or ξ/J) so that crossplots of the solutions ($J\xi$ vs. η for constant ξ) cannot be easily calculated. This is also an advantage since the adaptive method can be used to determine the step sizes necessary for accurate determination of the solutions to equations 4.40 and 4.41, which could then be used in the rk4 algorithm to allow integration of the solution to a specific value of ξ. If this integration, for each value of J, is stopped at the same ξ value, the crossplots can be generated automatically. Figures 4.8 a and b show the solutions to equation 4.41 using the rk4 algorithm on linear and log - log axes respectively. Similarly, figures 4.9 a and b show the same solutions using the rka algorithm.

Having determined the necessary minimum starting points we can generate cross plot curves of η vs. $J\xi$ for constant ξ. These curves, as noted by Chen (1965A), when placed on a log - log axis reveal the proportionality of the ion current dependence on the normalized voltage. We have extended the original calculations to higher and lower limits in order to observe the limiting behaviour of the ion saturation current. Figure 4.10 is the original figure 10 from Chen (1965A). Figure 4.11 shows a recalculation of this plot over a much larger parameter space where it can be seen that *all* curves have a slope of approximately two in the limit of small η. Furthermore it is shown in figure 4.12 that the some of the solutions presented by Chen (1965A) appear to be inaccurate. In a later paper (Chen (2001)) he presumes that a draftsman has fitted curves to similar data plots generated by Laframboise (1966) so one would expect this is what occurred in his 1965A paper. The source of the discrepancy may be from this manual curve fitting technique or from inaccurate numerical solutions. Irrespective of this, the approximate solutions to these original curves, as discussed in the next section, will contain these errors and hence will carried through into the temperatures and densities obtained from application of these approximations to the experimental data.

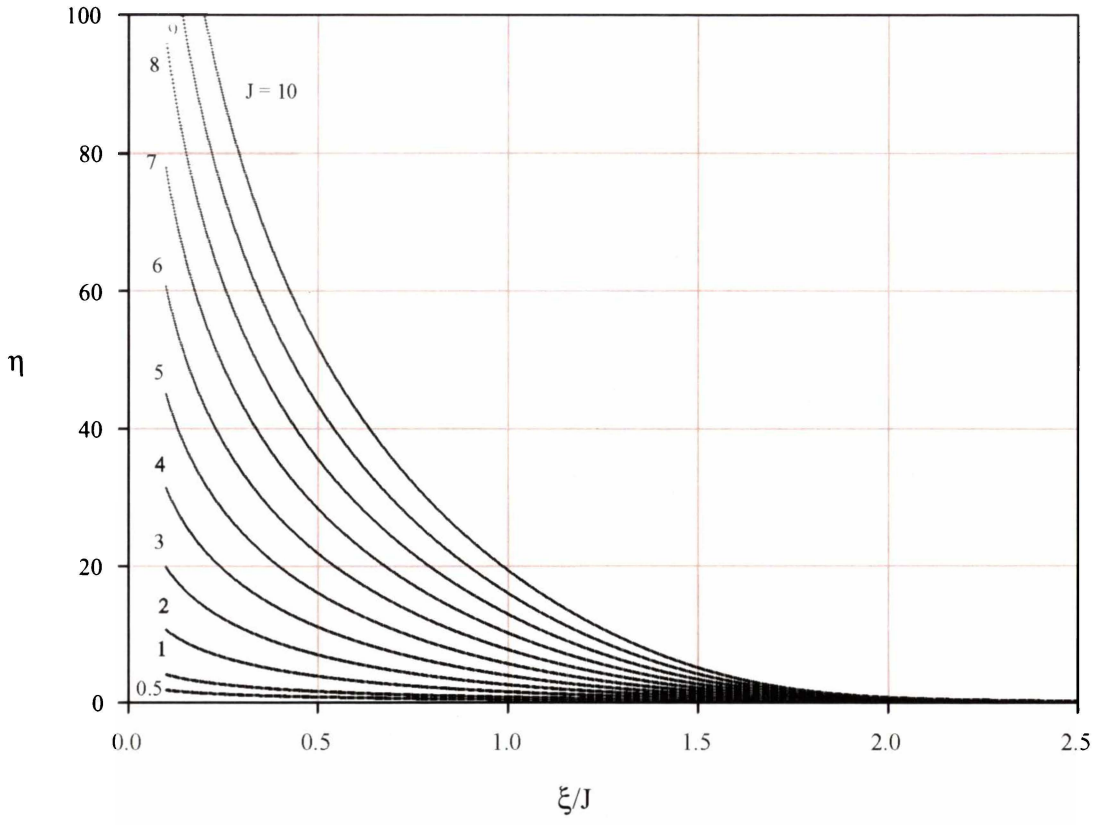

Figure 4.8 a : Solutions of equation 4.41 on a linear scale using a fix step Runge-Kutta algorithm.

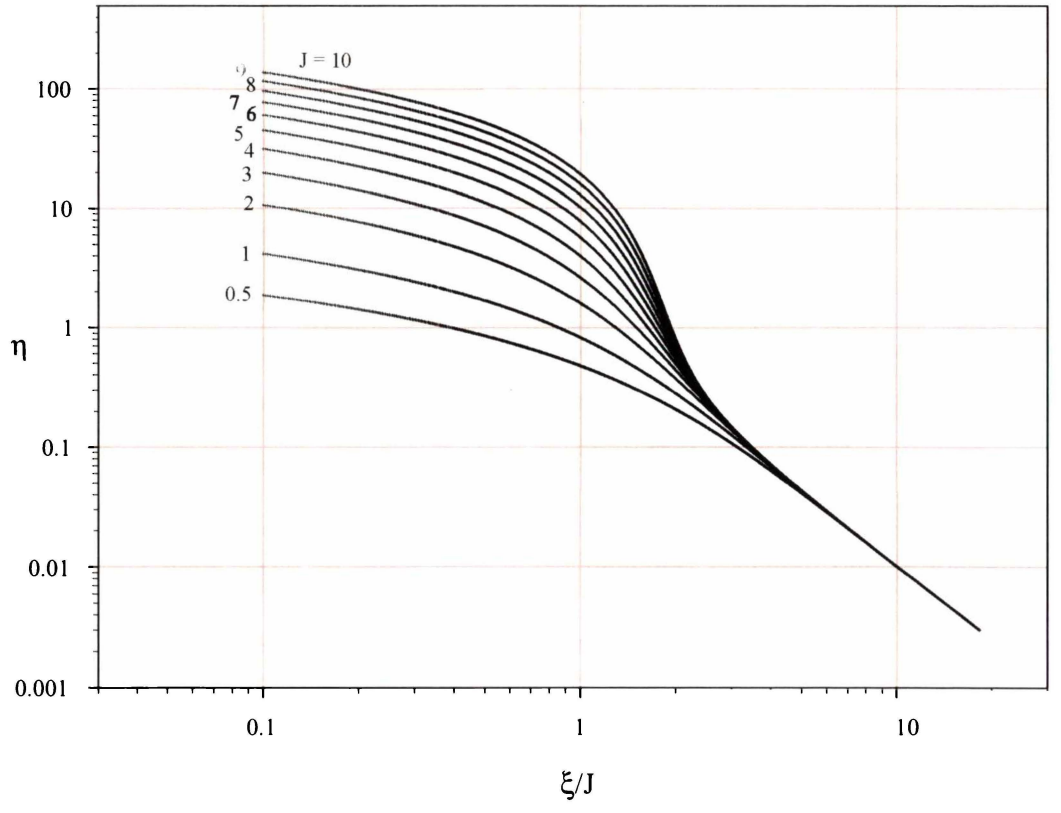

Figure 4.8 b : Solutions of equation 4.41 on a expanded logarithmic scale showing the plasma solution using a fix step Runge-Kutta algorithm.

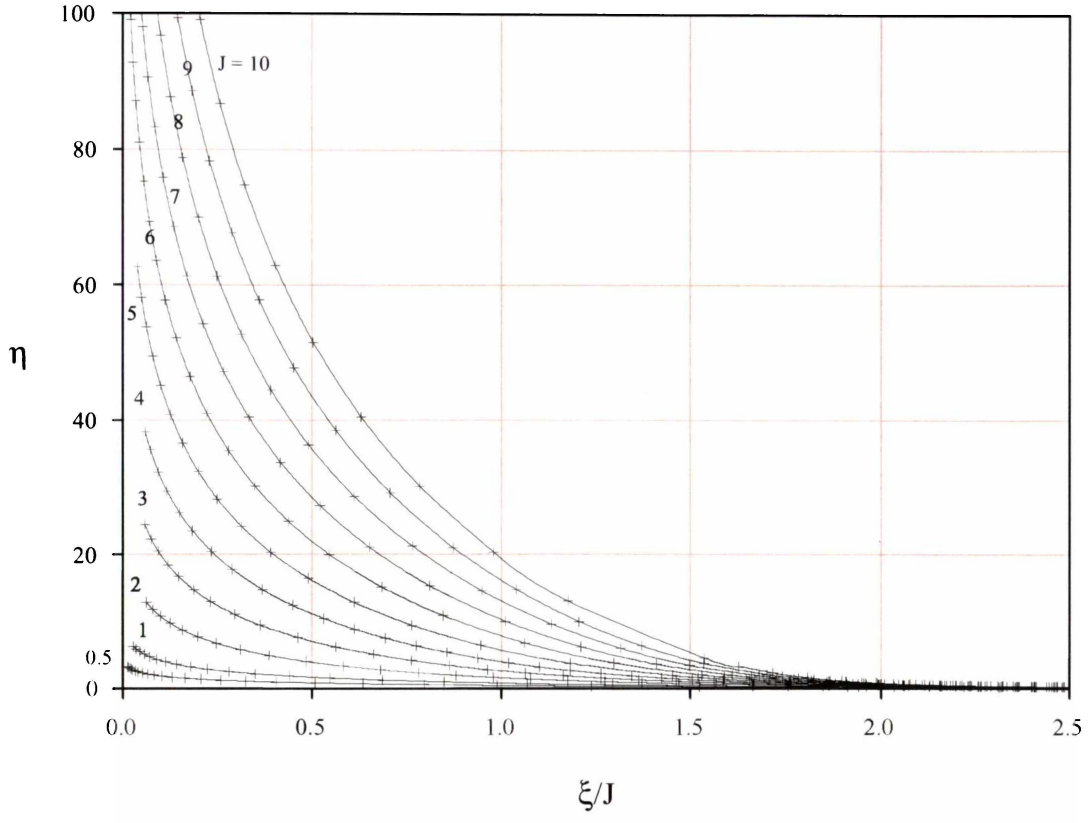

Figure 4.9 a : Solutions of equation 4.41 on a linear scale using an adaptive stepping Runge-Kutta algorithm.

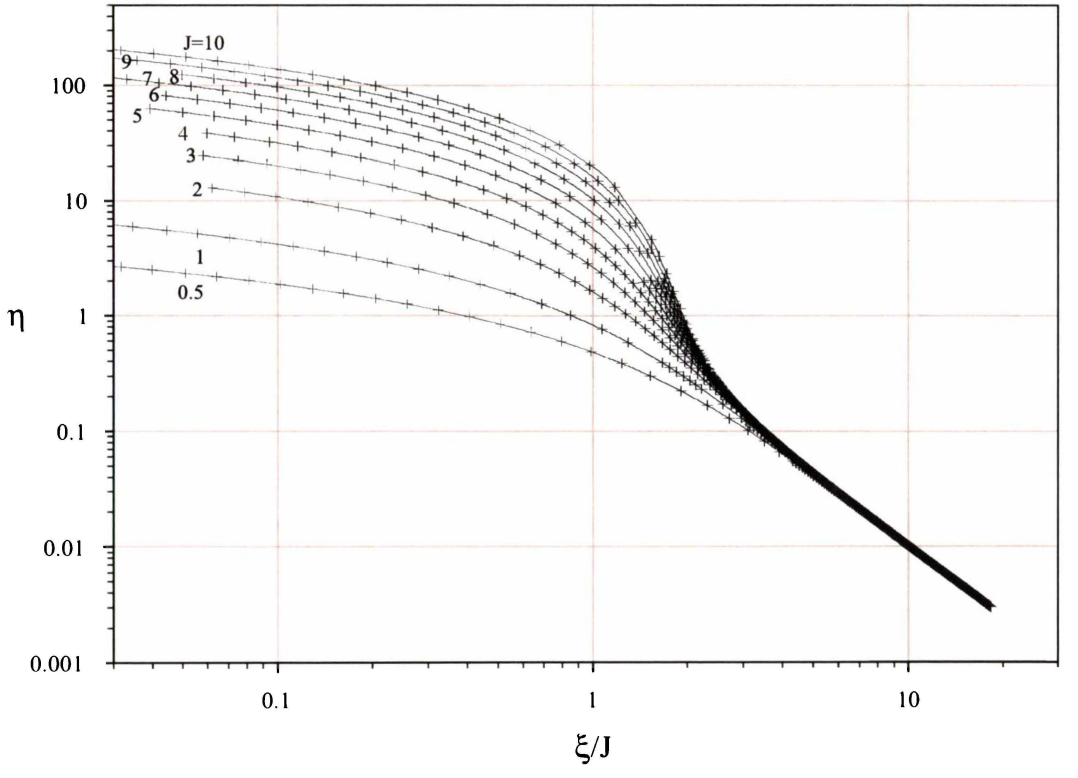

Figure 4.9 b : Solutions of equation 4.41 on a expanded logarithmic scale showing the plasma solution using an adaptive stepping Runge-Kutta algorithm.

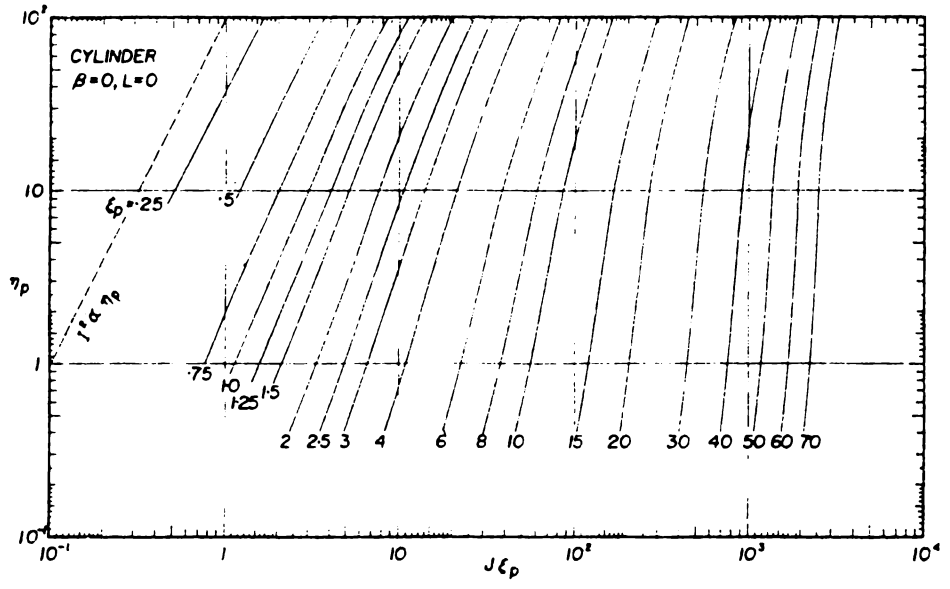

Figure 4.10 : The original figure 10 from Chen (1965A) showing the dependence of η on $J\xi$.

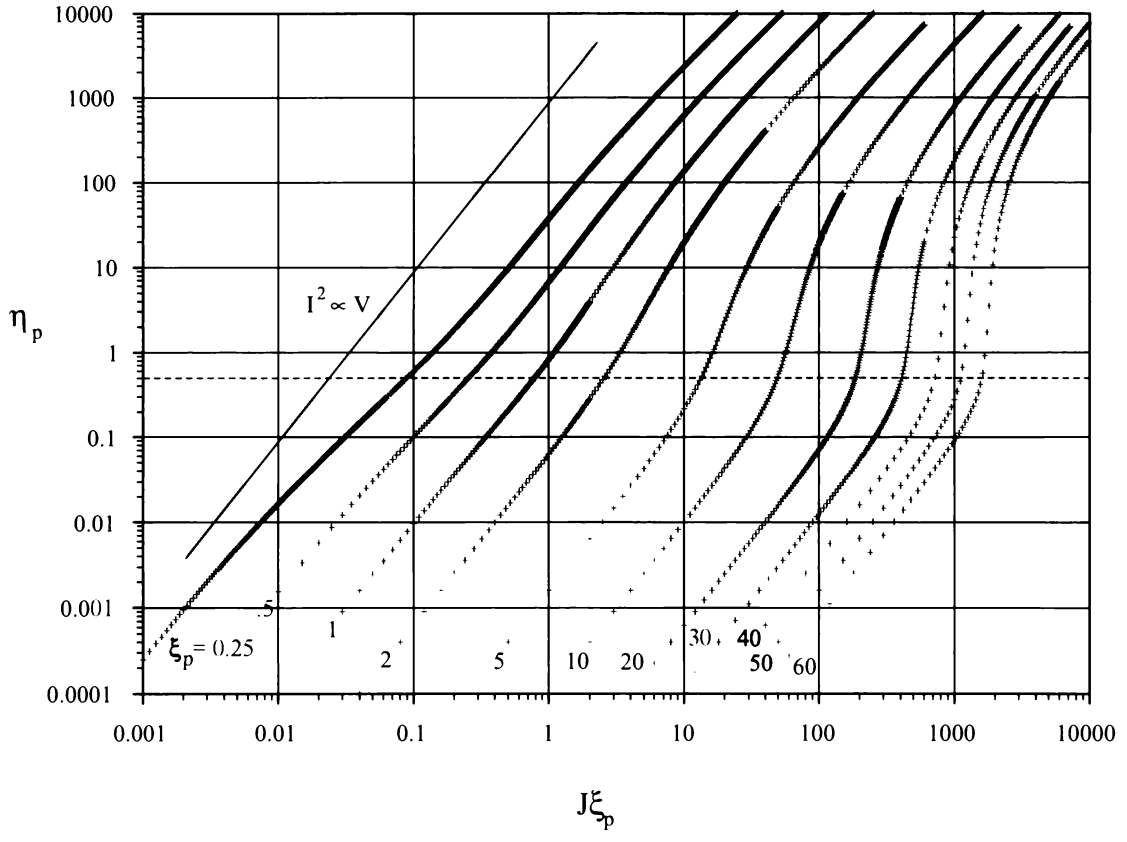

Figure 4.11 : An extended calculation of figure 4.12 covering a higher and lower range allowing the full nature of the solution to be seen.

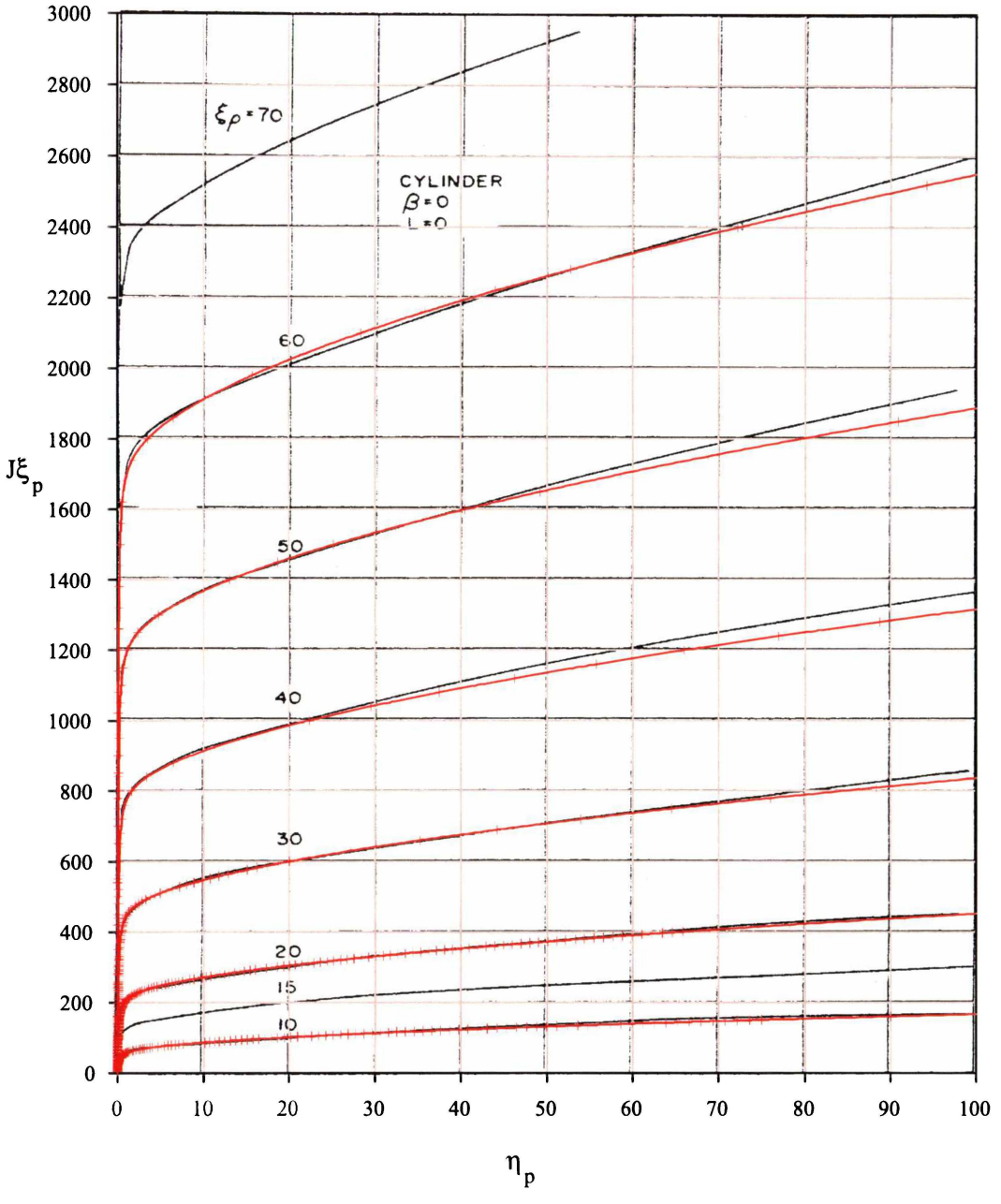

Figure 4.12 : An overlay plot showing the numerical solutions obtained in this thesis against those calculated by Chen (1965A) allowing the discrepancies to be observed. The solutions computed in this thesis are red.

4.4 Analysis of the Radial Motion Numerical Solutions

The question still remains whether the OML or radial motion theory is followed and as such we need a method to determine what theory is valid for any experimental data obtained. It was noted by Chen (1965A, 1965B) who extended the calculations of Bernstein and Rabinowitz (1959) to cylindrical probes, that for intermediary values of η, both theories appear to have a dependence of $I^2 \propto V$. Since for OML the slope of the ion and electron saturation currents is fixed at two, we need a method to determine the slopes of the ion saturation currents for the radial motion solutions to see what differences occur compared to OML. Thus we need to recalculate and re-examine the numerical solutions presented in the preceding section.

A method to determine which theory is followed, including those not examined here, has been neatly summarised by Chen (2001). In this paper approximate fits are made to numerical solutions from which, by iteration, a self consistent temperature and density can be obtained. Theoretical curves generated by these approximate solutions are plotted against the experimental data for comparison. This method is the one used by authors in general but it does not show in what regions the theory matches the experimental data since the temperature and density obtained from the analysis may be incorrect. A second solution to compare experimental and theoretical probe data which avoids this problem is to plot the experimental data, converted to the normalised parameters using equation 4.43, against the theoretical solutions. This method will show over what current and voltage ranges the experimental data matches the theoretical solutions.

To determine the difference between the radial and orbital motion theories, we need to determine the gradients of the radial solutions. To observe the theoretical variation of the slope of the ion current against the normalized voltage we need to be able to differentiate the logarithm of the η vs. $J\xi$ curves and graph them against $\eta\,(V)$. These plots are presented in figures 4.13 a and b for different ranges of ξ. Figure 4.14 shows the same data for the ξ = 0.25 to 10 range over a normalized potential range expected to cover most experimental Langmuir probe applied potentials.

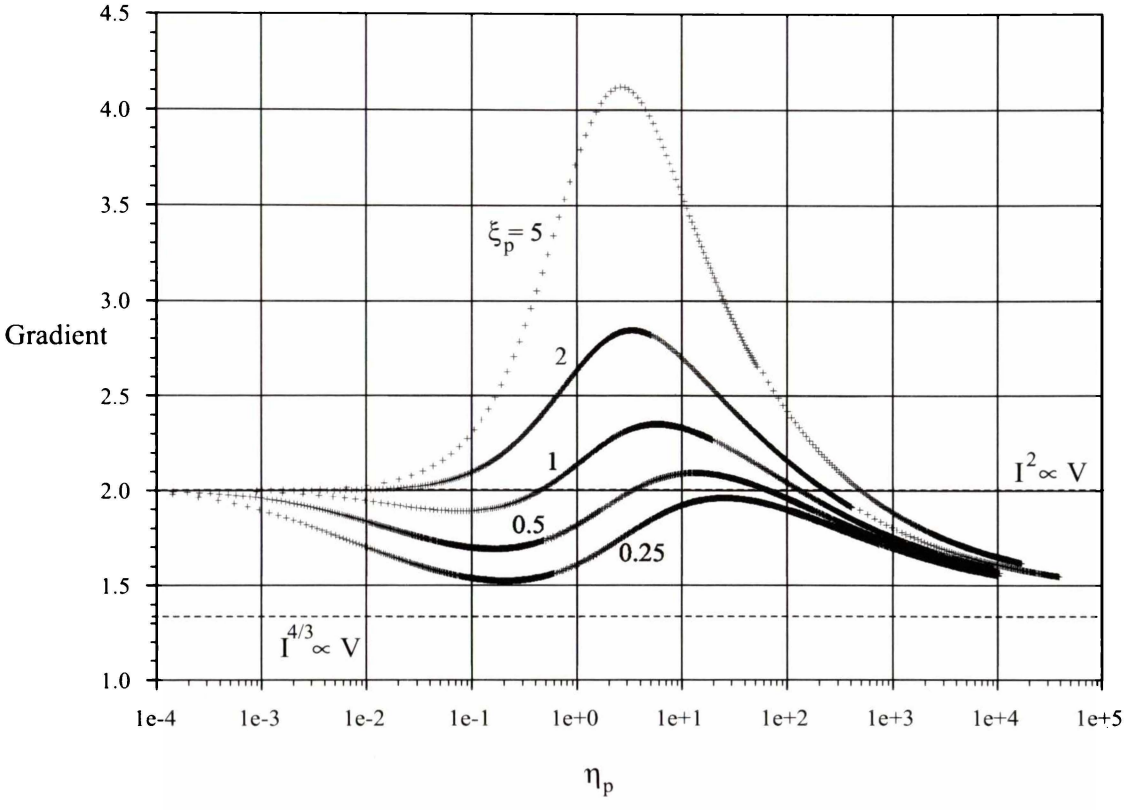

Figure 4.13 a : Gradients of the theoretical ion saturation curves plotted against the applied voltage for small ξ.

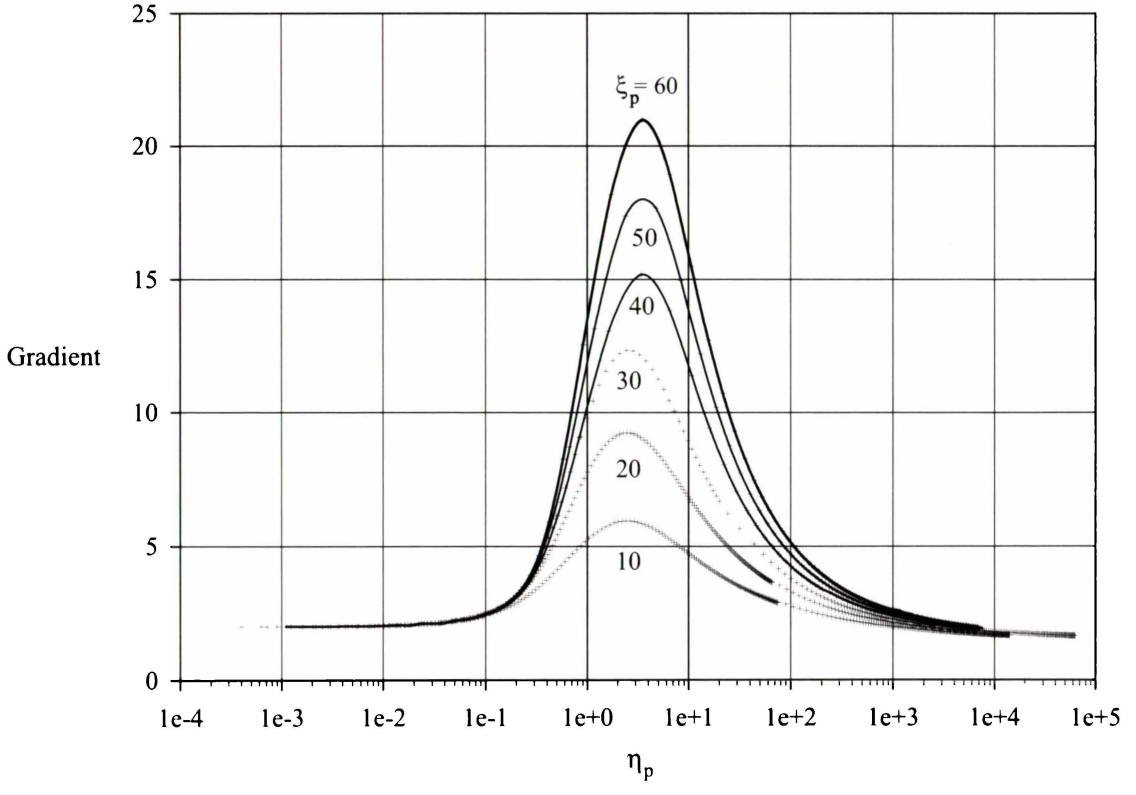

Figure 4.13 b : Gradients of the theoretical ion saturation curves plotted against the applied voltage for large ξ.

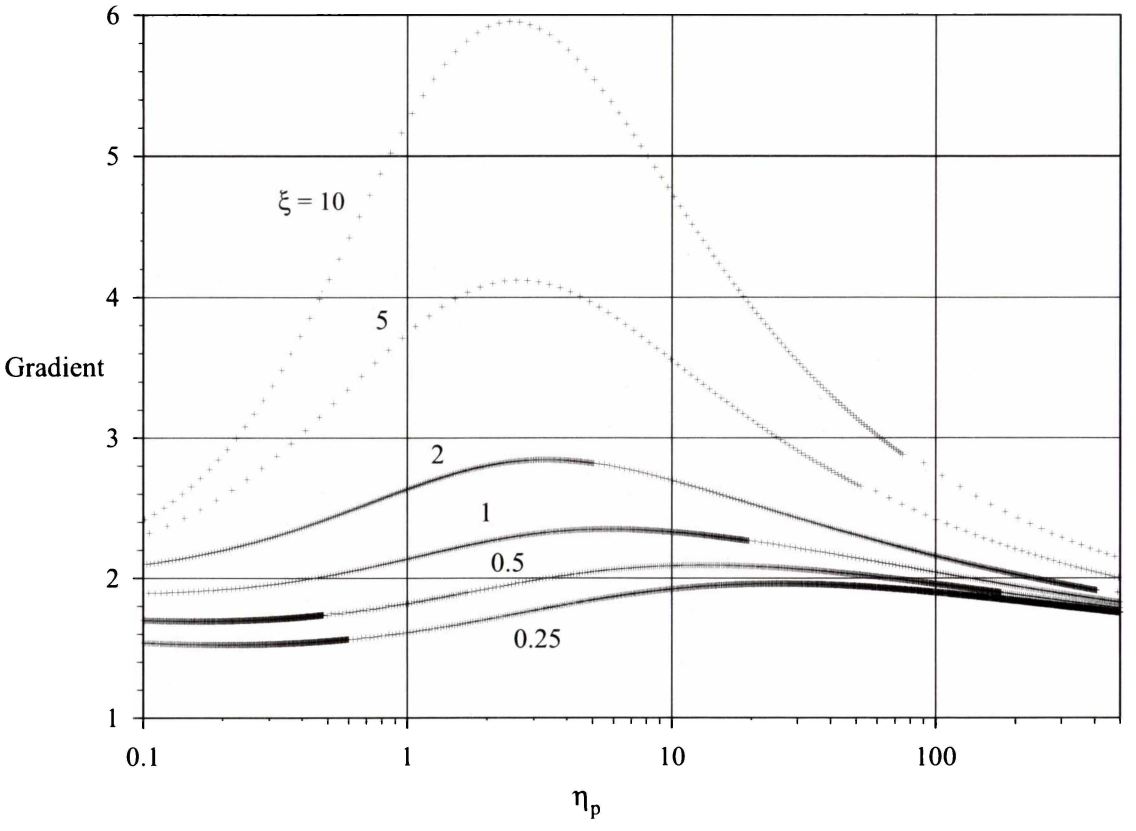

Figure 4.14 : Gradients of the theoretical ion saturation curves plotted against the applied voltage over the normal applied experimental voltage range for low ξ.

4.4.1 Discussion of the Numerical Solutions.

From figures 4.11 and 4.13 a and b it can be seen that the solutions to equation 4.40 follow two limiting forms in the extreme cases; when $\eta \rightarrow 0$ and when $\eta \rightarrow \infty$ where the solutions tend to the form $I^2 \propto V$ and $I^{4/3} \propto V$ respectively.

4.4.1.1 The Applied Voltage Tends to Zero

In the limit when the voltage applied to the probe is almost zero and is decreasing (with respect to the space potential), the solutions for *all* values of ξ solved tend to the OML dependence of the current on the voltage.

However, for $\xi \leq 1$ it can be seen in figure 4.13 a that the dependence of the ion current temporarily falls below the expected $I^2 \propto V$ and a minima occurs. This indicates that some ions that enter the sheath are not collected. Since these solutions are for the zero temperature limit where only radial motion is present, according to

Bernstein and Rabinowitz (1959), no particles can be trapped in a potential well around the probe. The solutions do indicate that some orbiting must occur even though the ions have no initial angular momentum. This appears to be the effect shown by Laframboise (1966) for cylinders, that the angular momentum can be finite if $V(r)$ varies slower than $1/r^2$.

Such low values of ξ are at the boundary between the OML and radial motion theories and hence the minima can also be adequately described using OML theory. This indicates that the decrease in the gradients below the limit of two occurs when the impact parameter becomes larger than the probe radius. The ions can now orbit the probe and escape. It should be noted that the potential values the orbiting occurs at will also contain an electron component since the high energy tail of the electron distribution can penetrate the sheath at these voltage ranges. What effect these electrons will have when incorporated into the numerical solutions for the ions is not clear.

Following OML theory, when $r_s > r_p$ the limiting form of the ion collection is given by equation 4.39. For $r_s \cong r_p$ the ion current tends to equation 4.45 where the collection area is simply the probe area.

$$I_i = A_p n_0 e \left(\frac{kT_i}{2\pi m_i} \right)^{1/2} \tag{4.45}$$

When $r_s > r_p$ ($\xi \rightarrow 0$) the collecting surface is the impact parameter, $r_p(1\text{-}eV_p/kT_i)^{1/2}$, but when $r_s \approx r_p$ ($\xi \rightarrow 1$) the collecting surface can be approximated by the probe radius. The transition between these two regimes in the numerical results (figure 4.13 a) occurs for $\xi \cong 1$ as expected from equations 4.39 and 4.45. As the voltage to the probe rises, so does the impact parameter and thus the ion current collected increases until the effects of space charge limitation become noticeable.

When $\xi < 1$ the impact parameter determines an effective collection radius. Whether the ions entering this radius are destined to hit the probe or not depends on whether the ions have a velocity above or below a critical limit given by Schott (1968). Restating the impact parameter in terms of velocity we have

$$r_s^2 = r_p^2 \left(1 - \frac{2eV_p}{mv_c^2} \right) \tag{4.46}$$

which defines the critical velocity as

$$v_c = \left(\frac{\frac{-2eV_p}{m_i}}{\frac{r_s^2}{r_p^2} - 1} \right)^{1/2} \tag{4.47}$$

Ions with velocities lower than the critical velocity are captured and the impact parameter defines the capture radius and the current is sheath limited. Conversely, those with velocities larger than the impact parameter have the possibility to enter the sheath radius but miss the probe and hence the current is orbit limited.

For $\xi < 1$ the particles attracted to the probe can orbit inside the sheath region and still miss the probe. This effect appears when the field in the sheath is weak and the attraction is small corresponding to the minimums in the curves in figure 4.13 a where $\eta \cong 0.2$. As the applied voltage to the probe is reduced, the impact parameter decreases to the probe radius and the $I^2 \propto V$ dependence is recovered. As the probe voltage is raised above this minimum value, the number of particles that can orbit the probe and escape also reduces since the energy the ions gain in the potential field raises the critical velocity until it is much greater than the random thermal motion of the ions. Thus a point will be reached where no ions have a sufficiently fast motion to escape the sheath.

4.4.1.2 The Applied Voltage Tends to Infinity

For all values of ξ when $\eta \geq 1000$, the gradient of the constant ξ curves tend to the limit of 4/3 in accordance with the Child-Langmuir law of space charge emission. However, even if T_e = 5 eV we can immediately see from figures 4.13 a and b that a potential of -200 V must be applied to the probe for the gradient of any ξ value to fall significantly below 2. For lower electron temperatures this applied voltage becomes even more negative. At these values, the effects of collisions inside the sheath and secondary electron emission from the probe itself will become significant. In these instances, even if the ion currents drawn to the probe rigorously follow this theory, the currents collected at highly negative potentials are not expected to match the theoretical predictions due to these effects.

Regardless of the ξ value, at some particular voltage, as $r_s \rightarrow r_p$ the Bohm criterion must be fulfilled and the ion current is given by

$$I_+ = e n_0 A_s \left(\frac{2e|V_s|}{m_+} \right)^{1/2} e^{\left(\frac{eV_s}{kT_e} \right)} \tag{4.48}$$

If one substitutes the Bohm equality of $e|V_s| \equiv kT_e/2$, the normal Bohm current results.

$$I_+ = \alpha n_0 e \left(\frac{kT_e}{m_+} \right)^{1/2} A_s \tag{4.49}$$

where $\alpha \approx 0.5$.

Equation 4.49 is often used to estimate the ion density and is normally calculated from the current obtained at the most negative potential applied to the probe. It also predicts that the ion saturation current is independent of the applied voltage, which from figures 4.13 a and b never happens (it requires the gradient to be zero). Furthermore, the prediction of equation 4.49 will become increasingly inaccurate as ξ rises since it is likely that the most negative potential applied to the probe will fall in a region where the gradient is high (see figure 4.14).

4.4.1.3 Validity of the Solutions

1 *Lower limit on* η

As $\eta \rightarrow 0$ or $J\xi \rightarrow 0$ ($I_i \rightarrow 0$) there are two limits on the validity of the solutions (ξ = constant). The first is from the accuracy of the numerical calculations in these two limits as the initial starting point (plasma solution) must be varied. For example, if we wish to calculate the value of η for $\xi = 1$ when $J = 0.01$ we find that ξ/J is 100, well beyond the limits of the starting conditions shown in figure 4.9 b. However, we can adjust the starting position of the plasma solution, and for this example with a 10,000 point iteration step, an accurate solution can be obtained for the $\xi/J = 1800$ starting point. Naturally, higher values of ξ/J can be used as starting points if the step size is increased. However, no further benefit is gained in the accuracy of the solution since at $\xi/J = 1800$ the value of η obtained is accurate to at least 5 significant figures. This accuracy has been tested by starting the numerical integration at the maximum possible plasma solution and slowly lowering to see what value of ξ/J produces a variation in the fifth significant figure. For the above example a starting point of $\xi/J = 350$ is required to cause such a deviation. Furthermore, the values of the

first derivative of equations 4.40 and 4.41 are also plotted with the solution to observe instabilities in the solution. None have been observed in the above example.

The limitation at small η values is governed by experimental measurements since the ion current cannot be solely collected. The measured current comprises an electron and an ion component for which the separation of these two contributing factors will determine the lower limit of η. The deviation from the theoretical curves will be determined by the electron temperature and what type of velocity distribution the electrons have. A Maxwellian distribution will naturally have a higher limit on the value of η than will a Druyvesteyn or a beam-type velocity distribution where the high energy tail is depleted.

2 *Upper limit on* η

As the potential applied to the probe is raised, the condition of validity given by equation 4.44 will not hold past a particular potential value. Clearly this limit is dependent not only on the collision cross-sections of a particular gas, but also on the pressure the measurements are performed at. Thus specific values of η cannot be given but it is expected that the higher limit of η given in figure 4.14 is an over estimation of practical experimental values. Secondary electron emission and charge-transfer collisions should become increasingly significant when the ions reaching the probe can acquire an energy over 200 eV.

4.4.2 Orbital or Radial Motion?

From the preceding section it was determined that the radial motion solutions produce a varying gradient depending on the ratio of the probe radius to the Debye length. This ratio determines the density and temperature in the plasma and hence controls the rate at which ions are collected by the probe as the applied voltage is varied. OML on the other hand predicts that *all* curves will have a gradient of two, independent of the plasma density and temperature in the ion collection region.

To experimentally check whether, at any value of ξ, the ion current is following the OML or radial motion theories (or neither), the slopes of the experimental curves need to be found. Since I-V curves are routinely differentiated numerically to obtain distribution functions and the space charge voltage, it requires

little extra effort to achieve. For single probes, the potential applied to the probe needs to be renormalized to the space potential. From the knowledge of the electron temperature, the experimental data can be converted into the dimensionless variables given in equations 4.42 or 4.43 and the differentiation can be performed. If the normal processes such as collisions and ionization play no part inside the sheath radius, the experimental data should either have a gradient of 2, indicating OML behaviour or follow the gradients of the theoretical plots shown in figure 4.14. The results of this analysis will determine which (if either) of these theories is followed and hence the appropriate equation or method to use for the density calculation.

4.5 Summary

It can be seen in this chapter that although the I - V characteristic of a Langmuir probe is simple in practise to acquire, the interpretation of the data is complex. Many pitfalls exist for those not well acquainted with the subtleties contained in the various theories. The most common failure appears to be the assumption that OML conditions control the electron and ion current collection and it appears that this theory is preferentially used because of its easy application to the data. However, this is not necessarily the case and further checks such as the intercept position of the gradient are commonly overlooked.

Contrary to the standard practise of generating artificial theoretical curves from approximations to the numerical solutions using the temperature and density from these approximations, it has been shown that an equivalent, and perhaps better solution is to present the data in a format consistent with the theoretical solutions in order to see the applicable range where the theory holds. We have determined a new method for the analysis of the I - V characteristics to achieve this goal and have shown that orbital motion occurs even with a fully radial theory when the ions have zero initial energy. Summarising, the following results have been obtained:

1) A quick iterative method has been developed to solve the zero ion temperature case of ion saturation currents to cylindrical probes. The code or data will be made freely available.

2) A method has been outlined where experimental data from a double or single Langmuir probe can be compared to theoretical predictions for the orbital motion and

the zero temperature limit radial motion theory. This method allows determination of which theory is valid from the experimental data and requires little extra effort compared to the normal Langmuir probe data analysis. The density can thus be obtained from the relevant theory and can be compared to other methods of determination allowing effects of collisions in the sheath and probe emission phenomena to be obtained.

3) An examination of the transition region where the OML and the radial motion theories overlap was discussed. Minima are shown to occur in the numerical solutions for $\xi \leq 1$ when the ions have no initial angular momentum. It is postulated that these minima are equivalent to the onset of OML sheath limited collection of the ions.

4) The onset of the Child - Langmuir law was shown to occur at much larger voltages than previously thought, and is independent of the probe to Debye length ratios. Well before this potential is reached collisional effects within the sheath and secondary emission from the probe(s) will be apparent.

4.6 References

Allen, J. E., 1992, Physica Scripta, **45**, p 497.

Allen, J. E., R. L. F. Boyd, P. Renyolds, 1957, Proc. Phys. Soc. (London), **70**, p 297.

Bernstein, I. B., and I. Rabinowitz, 1959, Phys. Fluids, **2**, p 112.

Bohm, D., 1949, *The Characteristics of Electrical Discharges in Magnetic Fields* (McGraw-Hill, New York).

Chen, F. F., 1965A, J. Nuc. Ener.C., **7**, p 47.

Chen, F. F., 1965B, *Plasma Diagnostic Techniques*, edited by R. H. Huddlestone and S. L. Leonard (Academic Press, London).

Chen, F., F., 2001, Phys. Plasmas, **8**, 6, p3029.

Chen, F. F., and D. Arnush, 2001, Phys. of Plasmas, **8**, 11 p 5051.

Chung, P. M., L. Talbot, and K. J. Touryan, 1975, *Electrical Probes in Stationary and Flowing Plasmas* (Springer-Verlag, New York).

Druyvesteyn, M. J., 1930, Z. Phys, **64**, p 781.

Garcia, A. L., 1994, *Numerical Methods for Physics*, (Prentice Hall, New Jersey).

Johnson, E. O., and L. Malter, 1950, Phys. Rev., **80**, 1, p 58.

Kagan, Y. M., and V. I. Perel, 1964, Soviet Phys. Usp., **6**, p 767.

Laframboise, J. G., 1966, *Fourth symposium on Rarefied Gas Dynamics*, edited by J. H. De Leeuw (Academic Press, New York), **Vol II**, p 22.

Langmuir, I., 1961, *Collected works of Irving Langmuir* (Permagon Press, New York) **Vol 4**.

Mott-Smith, H., and I. Langmuir, 1926, Phys. Rev., **28**, p 727.

Press, W. H., 1992, *Numerical Recipies in C: The art of scientific computing*, (Cambridge University Press).

Riemann, K-U., 1991, J. Phys D: Appl. Phys, **24**, p 493.

Savitsky, A., and M. J. E. Golay, 1964, Anal. Chem. **36**, 8, p 1627.

Schott, L., 1968, *Plasma Diagnostics* edited by W.Lochte-Holtgreven (North Holland Publishing Company, Amsterdam).

Swift, J. D., and M. J. R., Schwar, 1970, *Electrical Probes for Plasma Diagnostics* (Iliffe, London).

Tonks, L., and I. Langmuir, 1929A, Phys. Rev., **34**, p 876.

Tonks, L., and I. Langmuir, 1929B, Phys. Rev., **33**, p 195.

Chapter 5 Experimental Equipment

5.1 Introduction

All equipment used for plasma generation in this work was designed and built at the University of Waikato. This includes the circuits and the rest of the hardware associated with the Langmuir probes and all the power supplies used for plasma generation. Items such as the mass flow controllers, and pressure gauges were bought for these experiments.

This chapter will cover the design and operation of the vacuum chamber, power supplies, automated Langmuir probes, and the monochromator operation. Calibration the Langmuir probe system and the subsequent data analysis will be summarised in chapter seven, while the monochromator calibration and results will be covered in chapter six.

5.2 The Vacuum Chamber

The main equipment constructed was a cylindrical vacuum chamber, 200 mm wide and 200 mm long. This chamber was designed to fit a 170 l/sec Pfeiffer turbo molecular pump and was constructed with eight side arms set at a 45 degree angle to each other, perpendicular to the pumping direction. The side arms have a radius of 19 mm and are 35 mm in length. These side arms were designed to house pressure gauges, sample holders, windows for spectroscopic work, and probes. Since all the fittings and mountings were made and designed "in house", considerable freedom in the arrangement of the equipment was available. A diagram of the chamber is given in figure 5.1. The chamber was tested for leaks in the welds using a Varian mass spectrometer leak detection system tuned to the helium mass. Testing and repair was repeated until no leaks could be found. Attachment of the chamber to the pumping system was accomplished by bolting the turbo pump to the chamber and bolting the chamber in the centre of a fibreboard table constructed for this apparatus. A schematic representation of the equipment assembly is presented in figure 5.2 while a photograph of the entire experimental vacuum system is shown in figure 5.3.

The chamber was fitted with a pumping speed regulator placed between the chamber and the turbopump for flow rate control. The control was operated by an

external valve which, when turned, rotates one plate horizontally about its axis covering a secondary plate. The two plates had appropriate discs cut out and removed so that the holes lined up when the valve was open and similarly the holes were mismatched when the valve was closed. A diagram of the apparatus is shown in figure 5.4.

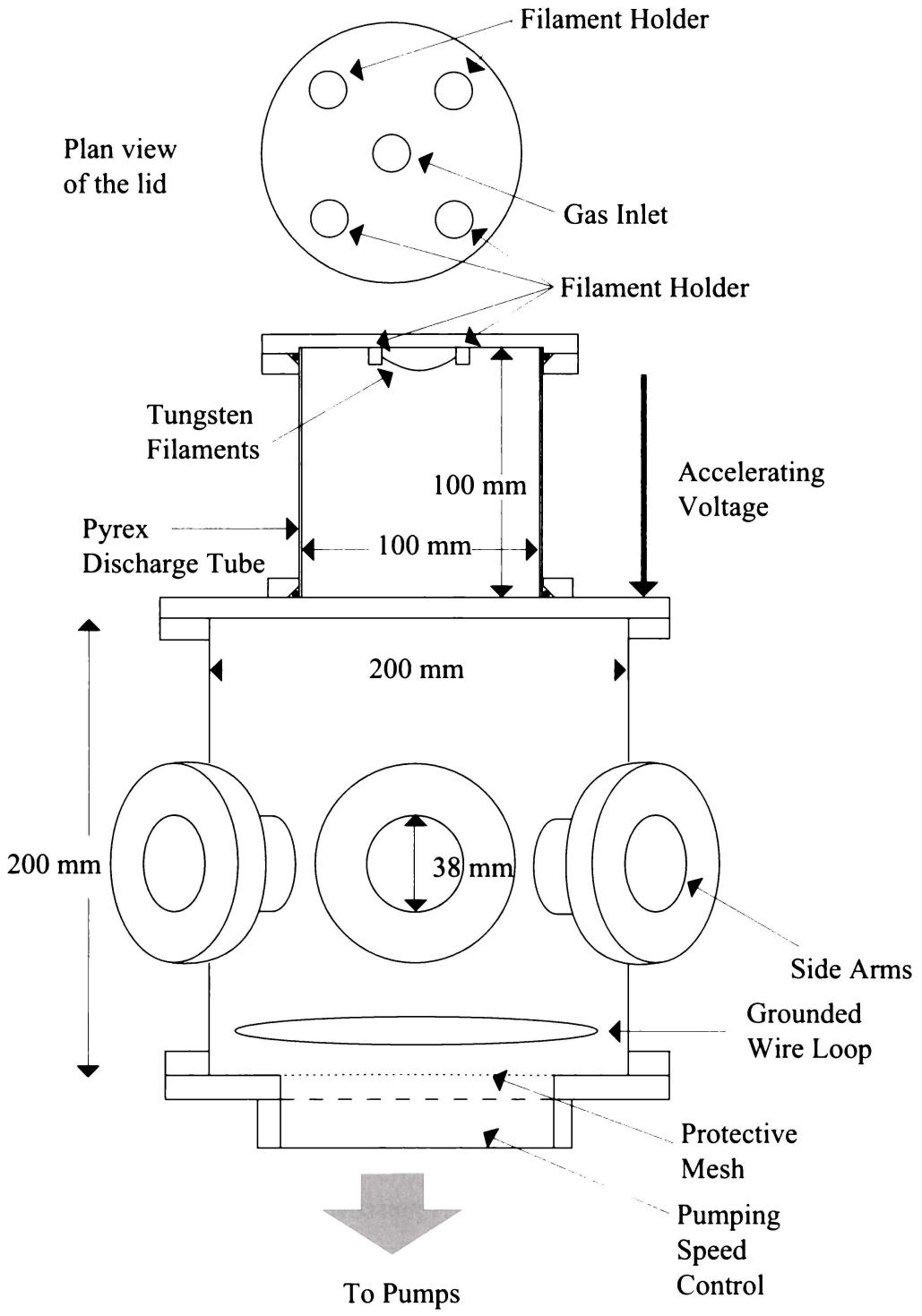

Figure 5.1: Diagram of the experimental DC discharge chamber.

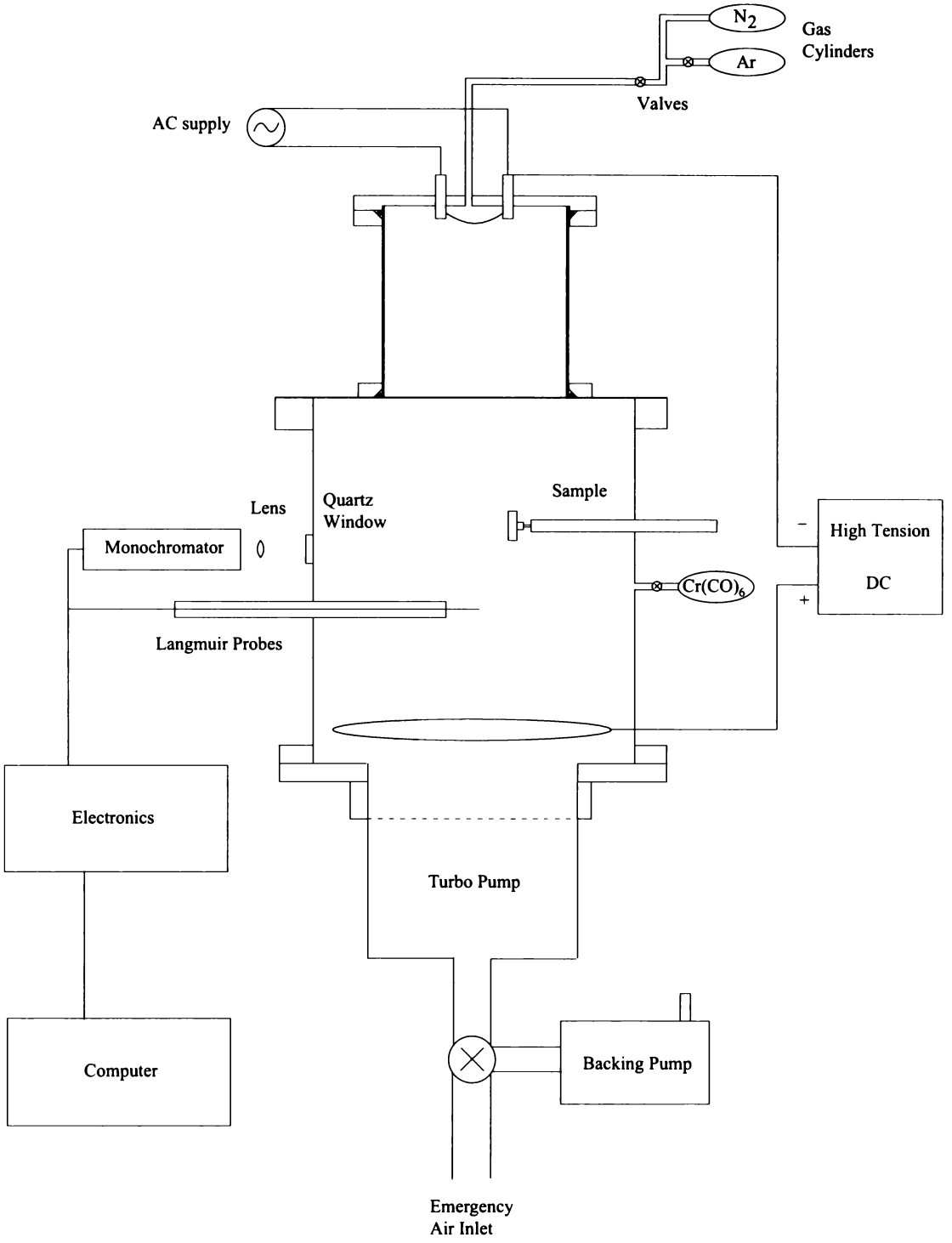

Figure 5.2 : The schematic layout of the plasma system showing the main features and gas inlets.

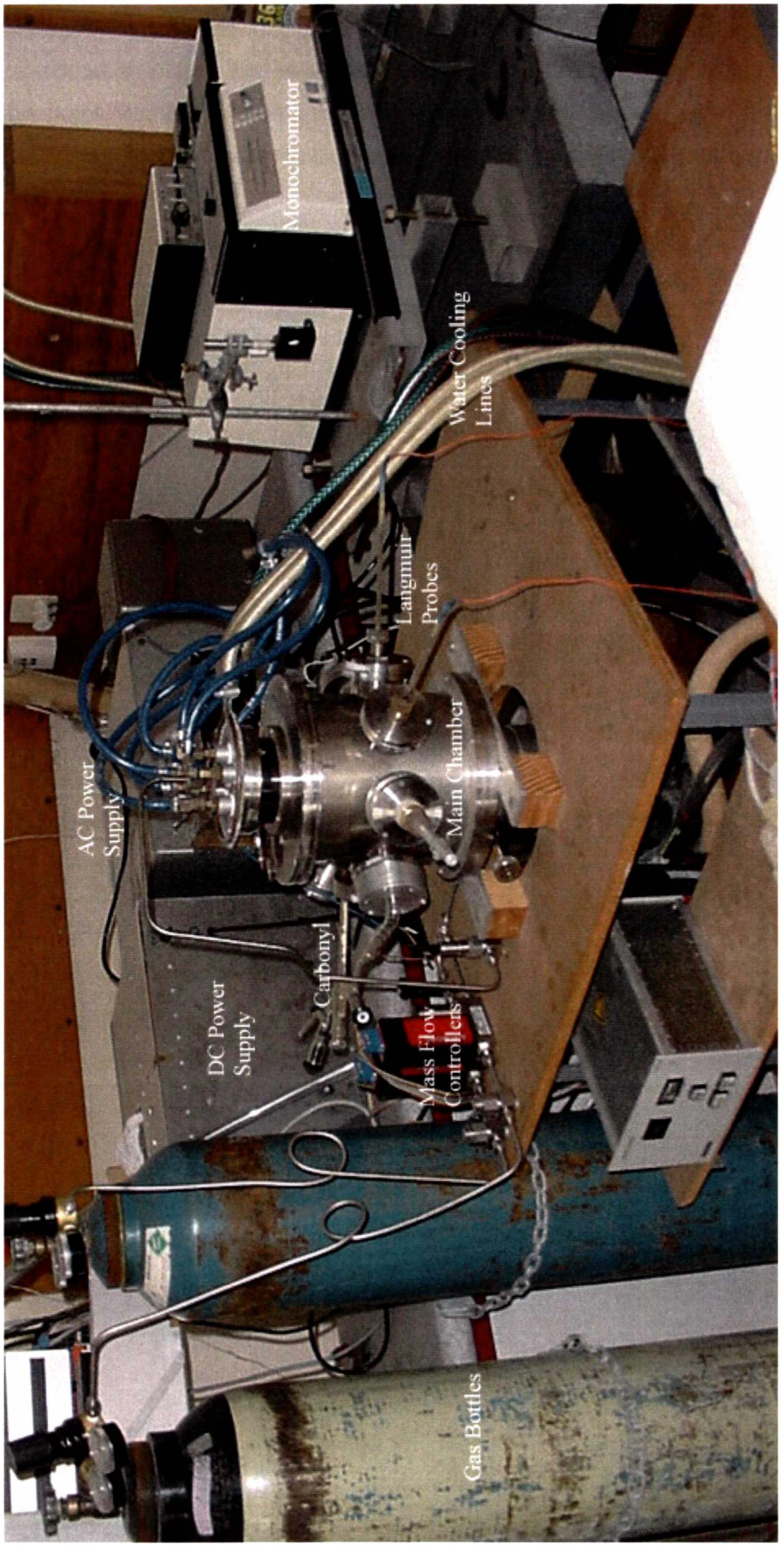

Figure 5.3 : A photograph of the experimental vacuum chamber used for coating experiments.

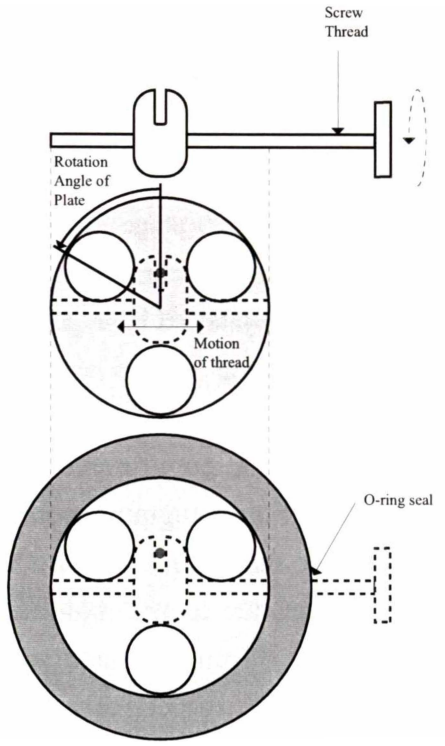

Figure 5.4 : Diagrammatic layout of the pumping speed controller.

Two heated tungsten filaments with a wire diameter of 0.7 mm were used to provide a constant source of electrons to maintain the discharge. The filaments were held at an estimated temperature of 2700 °C. The stainless steel filament holders were electrically insulated from the chamber lid by glass insulators. These insulators possess a high melting point, yet were not brittle. Initially Teflon and boron nitride were used as insulators, but were found to be unsuitable. The holders were water cooled to dissipate the heat generated by the high running temperature to avoid the Viton O-rings melting.

The discharge was operated by accelerating electrons from the filaments through the Pyrex discharge tube into the main body of the chamber by a voltage of up to 400 V DC. The electrons were generated by thermionic emission from the filaments and created the plasma by collisions with the gas particles in the chamber and the Pyrex tube. The filament holders, used as the cathodes, had a negative voltage while the wire loop located approximately 280 mm away as shown in figure 5.1 was used as the anode to complete the current loop of the power supplies.

The pressure variation with turns to close the controller was investigated and it was found that the chamber pressure increase was minimal until more than 8 turns out of a possible 12 had been completed. Nearly closing this valve allowed longer containment lifetimes of the particles inside the vacuum chamber, and hence a longer equilibrium time for the particles. It also acted as a sensitive pressure control mechanism for the gas mixture in the plasma.

5.2.1 Pumping System

The main pumping unit was a Pfeiffer turbo-molecular pump, model TPU 170, while the backing pump was a Javac two stage rotary vane pump, model JDX 220. The ultimate pressure of this pumping combination, quoted by the manufacturer, is 1×10^{-9} mbar (1×10^{-7} Pa). For our system a base pressure of less than 1×10^{-4} mbar could be achieved in one hour. If the system was left running continuously, the background pressure was approximately 2×10^{-6} mbar irrespective of the mountings on the side arms. This gave us a comfortable margin of error to minimise contamination since the operation of the Langmuir probe and coating experiments was at pressures around 10^{-2} mbar. The theoretical pressure limit was never reached in the experimental vacuum configuration due to the multitude of O-ring seals needed to attach the experimental equipment. From the manufacturer's tests, the volume flow rates for N_2 and He are 170 and 130 ls^{-1} respectively. No data are given for CO or Ar but they are expected to be similar to the nitrogen rate. The pumping flow rate is constant up to 10^{-3} mbar with the flow rate falling below 10 ls^{-1} at pressures higher than 0.1 mbar. Experiments were operated in conditions between these two pressures (10^{-2} mbar) where it was estimated that the flow rate was 80 ls^{-1}. The control valve was closed 6 - 10 turns during experiments to further slow the pumping rate and to reduce the throughput of gas allowing molecules and ions a longer time in the chamber. As a standard procedure for experimental work, the vacuum system was always operated with a splinter shield in place below the main chamber covering the exit to the pump, (shown in figure 5.1) to protect the pump against accidents.

5.2.2 Pressure Measurement

Preliminary pressure measurements early on in the research were achieved with an Edwards Pirani gauge, a Penning gauge and an ionisation gauge. The first two gauges were calibrated against the Leybold-Heraeus model IM210 ionisation gauge (10^{-2} mbar to 10^{-10} mbar) for accuracy. The pressure range of the first two gauges did not overlap well and the calibration achieved was nonlinear and could not be matched to the scale provided by the manufacturer probably because these gauges and associated control units were over 40 years old. This problem was remedied by the purchase of Leybold Inficon Capacitance Diaphragm gauge (model CR 090, 10^{-4} to 1 torr) which had a pressure range complimentary to the ionisation gauge. This gauge has the advantage that the voltage reading is a linear function of pressure, independent of gas type, and has a quoted accuracy of 0.2%. The new capacitance gauge agreed

with the pressure measurement of the ionisation range across the overlapping pressure ranges of both instruments. Both these gauges were attached to the vacuum chamber by mounting them on the side arms of the main chamber with flanges. Cylindrical spacers were placed between the chamber arms and the gauges to prevent contamination by the plasma and abnormal readings in the case of the ionisation gauge. The ionisation gauge was always turned off before a plasma was generated to avoid burning out the filaments since the electrons from the plasma were collected by the gauge, saturating the detector.

5.2.3 The Gas Control System

5.2.3.1 The Carbonyl Sample Holder

The containment of the carbonyl was external from the vacuum system. A glass vessel shown in figure 5.5 was designed and custom made to hold the carbonyl. Entry to the plasma discharge was through one of the side ports on the main vacuum chamber. The B14 socket was joined to its female counterpart, a B14 cone adaptor that was connected to the sidearm with a modified plate to allow this attachment.

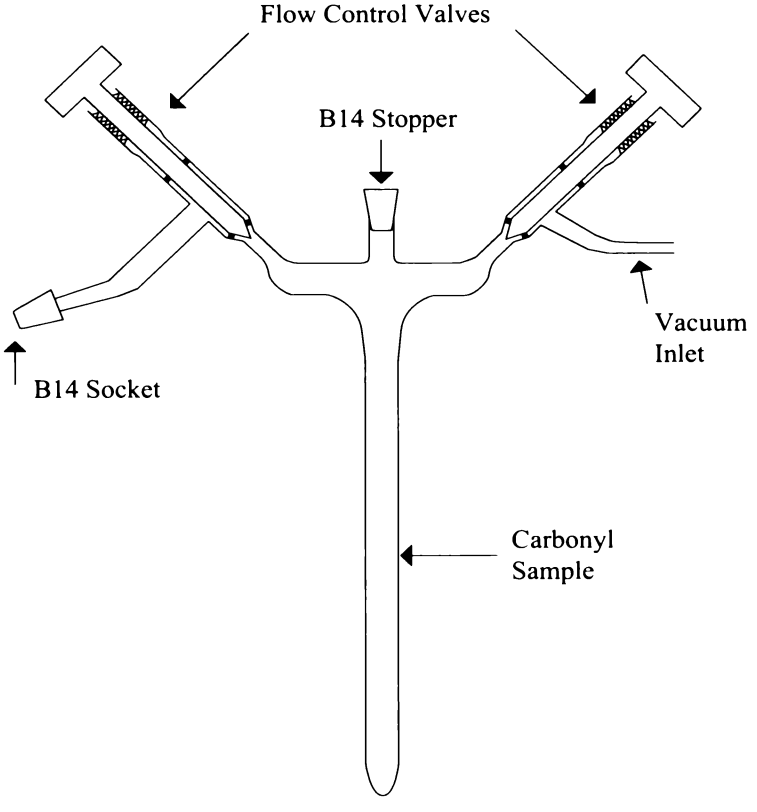

Figure 5.5 : Schematic diagram of the carbonyl sample holder.

The tube has a 5 mm diameter with the minimum bore between the sample and the vacuum also being 5 mm diameter where the B-14 cone is attached to the rest of the sample holder. Satisfactory pressure increases from a base vacuum were obtained through the B-14 connectors when the carbonyl was present. Aligning the holder horizontally to expose as much surface area of the solid carbonyl as possible allowed pressures to be reached where experiments could be performed, and provided a crude control mechanism for the partial pressure of the sublimed chromium carbonyl.

5.2.3.2 The Mass Flow Controller

To accurately control the gas pressure (carrier and carbonyl partial pressures) mass flow controllers were installed on the main chamber. These were two Aalborg AFC 2600 flow controllers and a matching mass flow command module, PROC2. Two flow units, one for argon and one for nitrogen, were obtained along with a dual control module capable of mixing both gas types. These units were calibrated by the manufacturer and were capable of providing flow rates in the range of 0-100 sccm (standard cubic centimetres per minute). Fittings provided to and from the controllers were standard ¼" Swagelok fittings. The entire gas line, from the gas bottles to the vacuum chamber was a ¼" external diameter stainless steel tubing with an approximate internal bore of 4 mm. The tubing was joined so that both tubes from each controller could be mixed before entering the vacuum chamber. The mixing of the gases occurred midway through the tubing well before they exhausted into the main chamber. The carrier gases entered the vacuum system directly between the filaments on the top flange above the Pyrex tube. The full tubing configuration can be seen in figure 5.3 while the entry orifice to the vacuum is shown in figure 5.1.

These controllers had an accuracy of ±1% with a repeatability factor of ±0.2% (both over full scale deflection). The flow rates themselves were not as important as the pressure control they provided, but the flow rates did allow calculations of the lifetimes of the particles in the vacuum system before they were swept out of the chamber.

5.3 Langmuir Probes and Control Electronic

In this section we will first review previous control and acquisition systems and then present the system used to acquire data from the experiments in this thesis. The automated process of acquiring Langmuir data switched from chart recorders and oscilloscopes to personal computers when the latter became common-place and thus we will start our review from this point since the older methods are now obsolete.

5.3.1 Previous Data Acquisition Systems

Early attempts to digitally acquire Langmuir probe data from plasmas were an expensive and time consuming process until personal computers became widely available. Ironically one of the first of these systems was highly advanced, superseding later acquisition hardware even up to the present day. Hopkins *et al.* (1987) described a complex, remarkably comprehensive and advanced automatic Langmuir probe acquisition and analysis system. This was a great achievement for the level of complexity compared to the level of software and hardware personal computers had at this time. The probe was controlled by a ±30 V sweep over 1000 points. This sweep could be offset from zero to -150 V. The data acquisition system chose from multiple resistors for the best current resolution and calculated the plasma parameters such as density and electron temperature automatically at the end of acquisition.

Later acquisition systems used methods such as simple boxcar averaging to an oscilloscope as employed by Shindo *et al.* (1988) or the more elaborate systems of Sudit and Woods (1993). The majority of these methods used a current sensing resistor in series with the Langmuir probe. This is the simplest method of recording the voltage across, and current drawn to, the probe. Although simple to implement, there are certain problems with this approach. The first is whether to float the sensing resistor and ground the power supply as done by Fujita and Yamazaki (1988), Fang *et al.* (1990), Spatenka *et al.* (1992), and Neumann *et al.* (1995) or conversely, to float the power supply and ground one side of the sensing resistor as seen in the methods of Hopkins *et al.* (1987), Friedmann *et al.* (1993), Kimura and Ohe (1993), Hansen *et al.* (1994), and Duffey *et al.* (1996). Both methods have drawbacks noted by Duffey *et al.* (1996). Detection of the differential voltage signal is difficult since neither side of the sensing resistor is grounded in the first case. In the second case, floating the power supply adds complications to the circuit design as well as obscuring the relationship between the voltage from the supply and the probe potential. Another difficulty, for both configurations, is the need to correct the voltage applied to the probe for the potential developed across the current sensing resistor. This correction is necessary to ensure the actual voltage applied to the probe is recorded, but the data is now not evenly spaced. The data spacing must be linear for the calculation of the electron energy distribution function (EEDF) if the second derivative is calculated directly from the procedure of Savitsky and Golay (1964). This calculation procedure is based on a numerical differentiation method which requires the data points in the independent variable to be evenly spaced, i.e. the probe voltage. Sudit and Woods (1993) have devised a method to solve this difficulty by manipulating the corrected data. The generalised circuit configurations are shown in figure 5.6.

For all the complexities of these systems they still need to be corrected for the voltage drop over the current sensing resistor and they could only acquire the full probe characteristic using a single sensing resistor at a time.

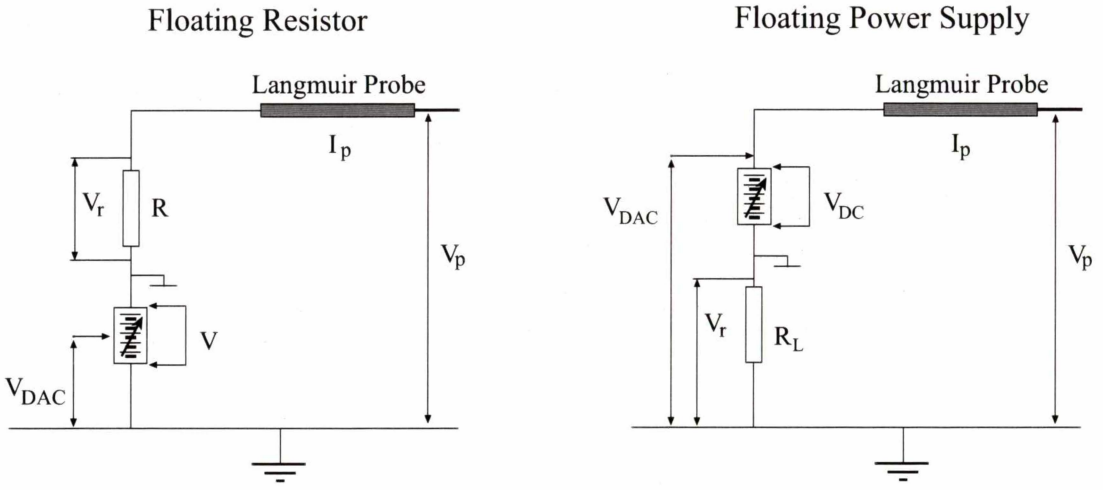

Figure 5.6 : General schematic diagrams for Langmuir probe circuits found in the literature.

5.3.2 Probe Construction

Small single cylindrical electrical probes were used in the experiments to measure plasma parameters. These were the main diagnostic tools for determining the electron temperature and the electron/ion density in the plasma. With this data, comparisons could be made with the (less accurate) values obtained from spectroscopic analysis. The probes, in general, consisted of 0.2 mm diameter tungsten wire protruding from a hollow tube of alumina of external diameter 2.6 mm enclosed in a glass tube with a 6 mm external diameter. The shielding of the probe was staggered with 10 mm of wire protruding from the alumina and 8.4 mm of the alumina protruding from the glass to minimise the effects of these solids on the collection of particles at the probe. The layers were sealed with a low vapour pressure adhesive which had no noticeable effect on the base pressure of the vacuum system. This meant that the adhesive did not allow air from outside the vacuum chamber to pass through it, i.e. it was an impermeable barrier, and that no plasticizers or other organic compounds from which the adhesive was made were being released into the vacuum. This type of probe was chosen to suit the conditions of the plasma. Additional probes of varying diameter, from 0.06 to 0.4 mm, were constructed and tested. The 0.2 mm tungsten wire provided the most suitable current range for the control electronics to record. The probes were expected to fulfil the condition $L >> r_p > \lambda_d$ where L is the smallest dimension of the plasma chamber and λ_d is the Debye length. A cylindrical probe geometry was chosen for ease of construction and for more favourable responses to

plasma conditions than spherical probes. Probes of this geometry have been reported in research on plasmas of a similar form to that used here, for example that of Sudit and Woods (1993). The probe construction is shown in figure 5.7.

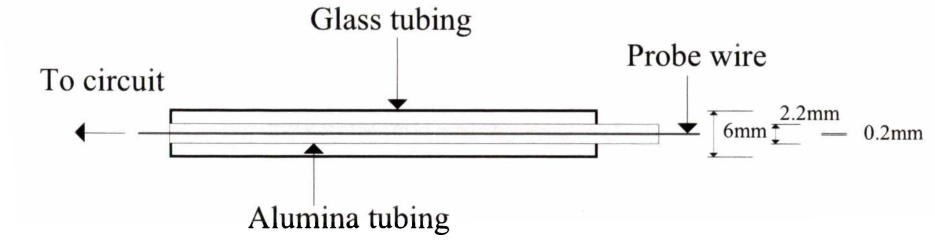

Figure 5.7 : Illustration of the Langmuir probe construction.

5.3.3 Langmuir Probe Control System

5.3.3.1 Hardware and Electronics

A completely automated control system was built for the recording of data from the Langmuir probes. Sophisticated electronics had to be designed, constructed, and tested before experimental data could be obtained. The specifications for the design were based on simulation voltage-current data obtained by inserting the expected temperature and density ranges into the various probe theories discussed in chapter four. From this study, it was determined that the voltage applied to the probe would need to be ±70 V while the current range required measurement from nanoamperes to milliamperes in order to measure, with full resolution, the ion and electron saturation currents drawn to the single and double probes.

The system was based on a personal computer utilising a National Instruments data acquisition board (DAQ) model MIO-16H9, LabVIEW software and associated electronics. Current detection was achieved through the use of a transimpedance amplifier. The specifications of the system are as follows:

(1) Linear sweep voltage adjustable between +70 and -70 V.
(2) Current detection from 10 nA to 100 mA using automatic gain switching.
(3) Simultaneous pointwise acquisition of both signals.
(4) Data acquisition rate of 100 Hz with gain switching.
(5) Data acquisition rate of 8000 Hz for a fixed gain.
(6) 12 bit resolution for input and output.
(7) Fully floating control system allowing the use of double probes.

The system was designed for the implementation of double probes as well as single probes. This required modifications to the general probe circuits cited in the literature to enable the system to be fully floating. The modification is shown in figure 5.8 in comparison to the two configurations found in the literature.

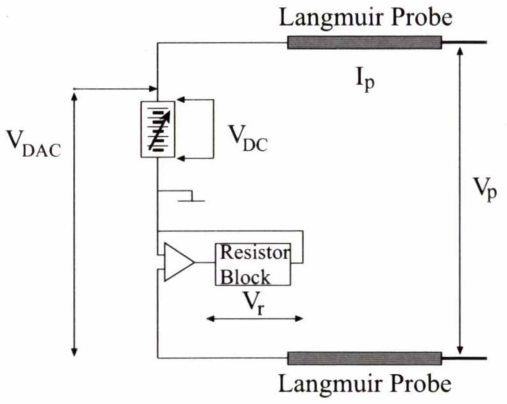

Figure 5.8 : A simplified schematic diagram of the main Langmuir probe circuit designs.

Figure 5.9 illustrates the main components of our circuit. The use of a transimpedance amplifier allows the Langmuir probe current to be measured without affecting the voltage applied to the probe and eliminates the need for the conventional current sensing resistor. This design isolates the current sensing resistors from the probe voltage as the feedback loop ensures both the inputs to the operational amplifier are at the same potential. The current sensing resistors are therefore effectively removed from the probe system allowing us to simply float the power supply to obtain an entirely floating system referenced to a virtual ground. This design avoids the problems and corrections necessary to the raw data found by authors such as Sudit and Woods (1993).

The full circuit design is based on two circuit boards. The first board splits the 50 pin cable from the DAQ board into its separate components i.e. analogue input and output, digital input and output (DIO). Specific lines are then connected to the probe driver circuit shown in figure 5.9. Each Langmuir probe circuit requires one input and output line and four DIO lines for control of the transimpedance gain resistors. Two such circuits can be simultaneously run. The probe circuit can also be used for general current detection from other instruments such as photomultipliers attached to a monochromator. A photograph of the circuit boards is shown in figure 5.10.

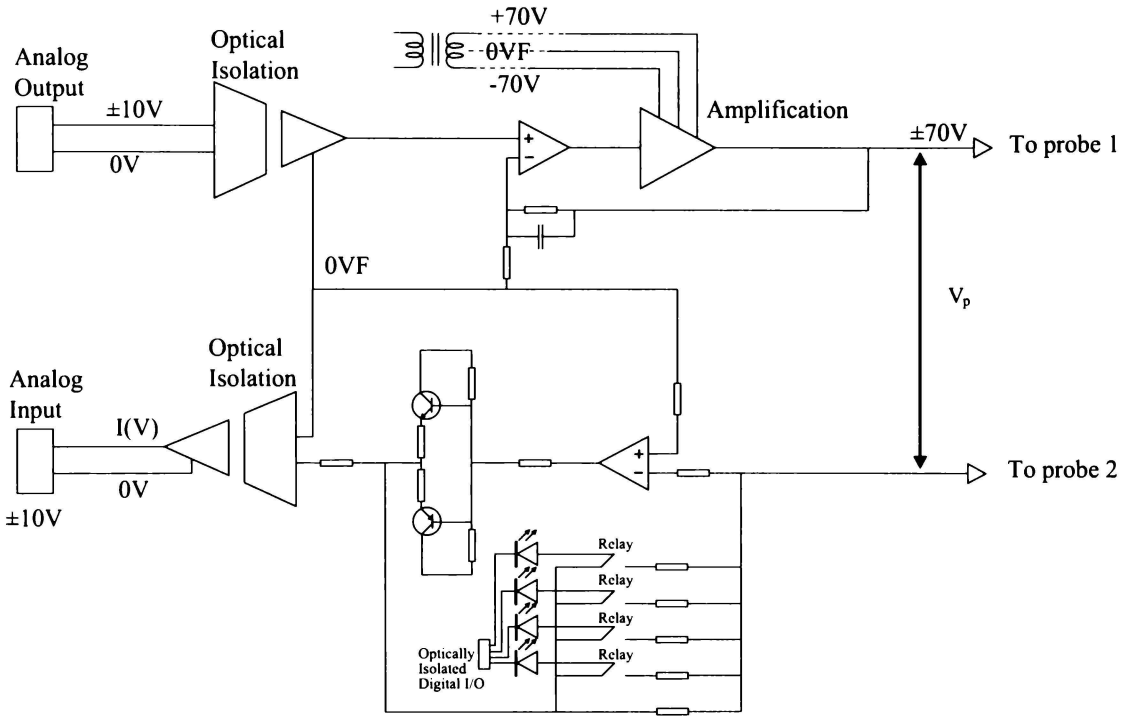

Figure 5.9 : A simplified circuit diagram of the Langmuir probe data acquisition circuit.

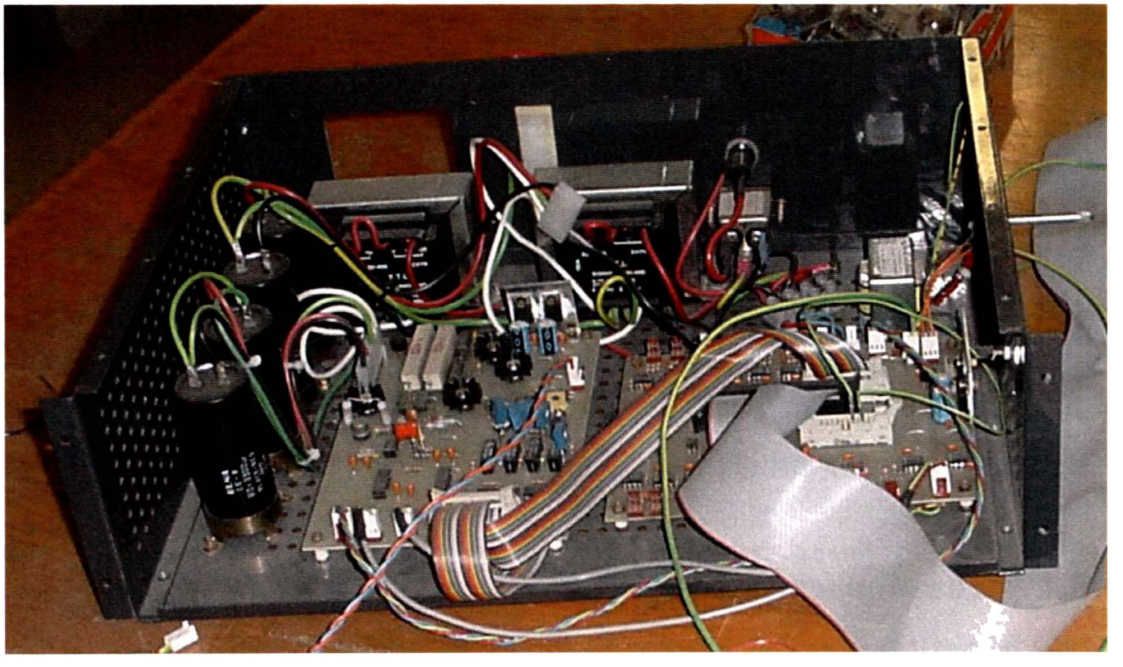

Figure 5.10 : The actual circuit built for the data acquisition for Langmuir probes.

5.3.3.2 Software and Measurement

The programs written to control the acquisition can be operated in several modes:

(1) single point operation where a voltage is written to the probe and the current is recorded,

(2) slew mode, using a repetitive ramp voltage starting either high or low to acquire any number of probe traces; or

(3) using a triangle wave as the voltage source for the measurement of hysteresis.

Normal operation of the system is in mode two. The ±10 V from the DAQ card is converted to a ±70 V output to the Langmuir probe. The current from the probe is recorded for each voltage step at a rate of up to 100 samples per second. During acquisition, the voltage across the gain resistor is checked after each point is recorded to ensure that the voltage is within operational range. If the voltage is out of range, the system automatically switches to a more appropriate gain resistor. This feature is especially useful when single probes are used, as it permits the same accuracy in recording the ion and electron currents, since the saturation values of each are orders of magnitude different. Gain switching causes the acquisition to slow significantly for two reasons. Firstly, the data must be analysed in real time to allow the system to check the voltage levels and determine whether to switch gains in response to extreme values from the sensing resistor. This requires additional processing by the control system to ensure the data are within saturation limits. Secondly, the time delay to switch the mechanical relays using the DIO lines is much greater than the input/output channel switching times of the DAQ board. Including system overheads (e.g. system software), the maximum sample rate is 100 samples per second. However, without the gain switching portion of the program, the system can record several scans, each consisting of up to 4096 (12 bits) samples, per second. Using LabVIEW as the programming language gives extensive flexibility in control of the circuitry and easily allows automatic post processing of the acquired data such as differentiation. A summary of the Langmuir probe system has been published by Pilling *et al.* (2003) in Review of Scientific Instruments.

5.4 The Monochromator

The monochromator used for the measurements of spectral profiles was a GCA/McPherson Model EU/E-700 Scanning Monochromator equipped with an automatic filter selection module and a photomultiplier unit. The output from the

photomultiplier could be measured directly with the same automated acquisition system used for the Langmuir probes. A new series of programs were written which effectively turned the probe acquisition system into an automated current sensing machine capable of providing the resolution described in the previous section. Not only did this allow automated data acquisition from the monochromator, but also the correction of the raw recorded data against previously determined optical properties of the monochromator and its surroundings. In other words, the raw data could be corrected for the detection efficiency of the photomultiplier across all wavelengths.

Line intensities from the monochromator were recorded in these experiments as it was the only way that specific individual excited and ionised species could be identified. Full calibration of the equipment was not possible since a true black-body was not available. Calibration was achieved against a "grey" rather than a black-body to determine the detection efficiency of the unit as a whole against wavelength. The calibration source was a tungsten ribbon lamp heated to a constant temperature. However it was not, and can never be, in thermal equilibrium with its surroundings (the ribbon is encased in a vacuum tube) and hence the ribbon is "grey" rather than a black-body.

5.4.1 General Features

Monochromators can be used to provide a large amount of raw data on profiles, intensities and half-widths of spectral lines from which the desired plasma parameters such as density, temperature and ionisation percentage can be calculated. Two particularly important reasons for using spectroscopic investigation are that there is no disturbance of the plasma since it is not an intrusive process, and the information content in a calibrated spectrum is very large. A precision of 1% can be obtained for intensity measurements using monochromators with aperture ratios of *f*/10 and carefully regulated photomultiplier power supplies (provided errors in line intensity calibration and drifts in the plasma are compensated). Drifts in the discharge behaviour were limited by the continual monitoring of the plasma parameters such as the discharge current and gas pressure, and by ensuring the discharge current was constant. Even with these checks, some drift in the plasma parameters still occurred. Since we had a stationary plasma, automatic recording was invaluable for obtaining line profiles and intensities.

The photomultiplier tube chosen to record the data was a EMI model 9785B (trialkali) selected for its wide wavelength response curve. From spectral tables, the emission of light was expected to cover a range from 2000-7000 Å. The sensitivity of the photomultiplier as a function of wavelength is shown in figure 5.11.

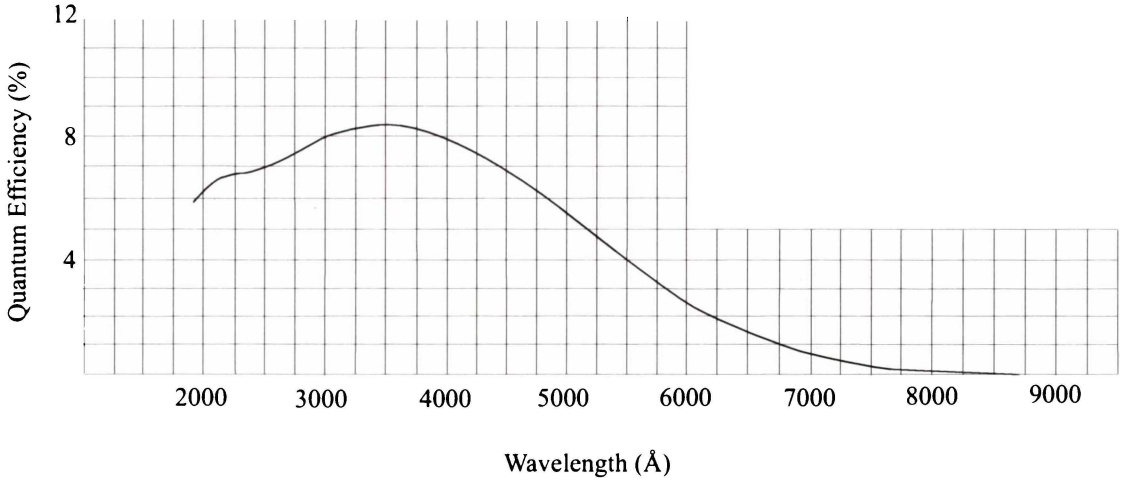

Figure 5.11 : Spectral response of the EMI 9785B photomultiplier.

The GCA/McPherson monochromator was designed for high resolution wavelength control for a broad range of applications. The design includes a common optical axis with an aperture ratio of *f*/6.8 at 2000 Å and a focal length of 350 mm. The resolution provided by the optics is better than one angstrom with line widths to below half an angstrom. However, resolution limits quoted by Griem (1964) are 0.2 Å for *f*/10 falling to 2 Å for monochromators with *f*/5. Stray light is limited to $\leq 0.1\%$ over the 2,000 - 10,000 Å measurement range with a quoted accuracy of ±1 Å throughout this range. The grating is 48 mm x 48 mm with 1180 lines mm^{-1} and a blaze wavelength of 2500 Å. Advantages of this grating include high resolving power, high luminous power near the blaze angle, constant resolving power and dispersion across the spectrum. Disadvantages include low transmittance outside the blaze range with diffraction orders needing to be separated. The concave mirrors in the optical system are parabolic with a 5 cm diameter and a 35 cm focal length. There is also a 25 x 35 mm folding plane mirror. A coating of magnesium fluoride protects the surface of the parabolic mirrors which have been corrected for wavelength and image reproducibility. The entrance slit width has a mechanical range of 5-2000 microns with a 3 mm slit height defined by the aperture size.

The lay-out of the optical system has the entrance and exit slit positions fixed while the grating is rotated to select a particular wavelength range i.e., a phase grating system is used. The output from the exit slit is detected by a side looking photomultiplier unit. The scan rate on the wavelength control unit could be varied from 0.05-20 $Å s^{-1}$ in the increasing wavelength direction.

5.4.2 Dispersion

The resolution of the GCA/McPherson monochromator is limited by the wavelength dispersion if other factors, such as the various forms of stray light are ignored. The wavelength dispersion is expressed as the change in wavelength ($d\lambda$) with change in viewing angle ($d\theta$) of the grating. The grating equation can be written as

$$\frac{d\lambda}{dx} = \frac{2d\cos\theta\cos\phi}{rn} \tag{5.1}$$

where x is the distance along the focal plane, r is the distance between the grating and the slit, θ is the angle of grating rotation and ϕ is the exit-beam angle (17.5°), and n is the diffraction order. The grating has 1180 lines mm^{-1} so the distance between each line is 8475 Å. For $\theta = 0$, $dx/d\lambda = 23.1$ Åmm^{-1} so that for a 10 micron slit there is a theoretical bandwidth of 0.23 Å. This corresponds to about 10% of the experimental bandwidths of the lines measured in our work and provided ample resolution.

The aperture height and width were 2.5 mm and 4 mm respectively, implying a slit height of 2.5 mm. The resolution of the monochromator depends on both slit height and width. The spectral resolution is essentially linearly dependent on the slit width while the slit height governs the curvature of the line. The spectral line curvature is significant only at slit heights greater than 3 mm and slit widths less than 20 microns. Both variables are limiting factors of the resolution.

5.4.3 Experimental Set-up

Light from the plasma was directed to the monochromator by using a quality lens to focus the plasma on to the slit entrance. The lens was initially positioned by focusing the emission from a 6 V bulb placed in the centre of the plasma chamber, into the monochromator slit entrance. Using this method it was possible to determine when the image was focused at the slit entrance and hence permit positioning of the lens at the correct distance between the plasma and the monochromator. Alignment of the monochromator relative to the plasma in all three dimensions was achieved with a helium-neon laser. The laser was adjusted in position so that its beam was perpendicular to the exit slit where the light travels to the photomultiplier tube. The monochromator was adjusted to the wavelength of the laser and the beam, if correctly positioned, exited at the entry slit. The beam was then tracked through a darkened room so that its position passed directly through the centre of the lens, and two optical windows placed opposite each other on the chamber sidearms.

This alignment allowed the light emitted from plasma along this path to be processed by the monochromator and the spectral signal recorded from the

photomultiplier tube output. The lens used to focus light into the monochromator had a focal length of 110 mm and a diameter of 25 mm. Since the mirrors in the monochromator had a 50 mm radius and a focal length of 350 mm, this allowed a maximum angle of 4.1° into the entry slit. For prudent measurements using 40 mm of the mirrors and 20 mm of the lens we find that the acceptance angle is 3.5°. Using these values, the lens position was calculated to be 163 mm from the entrance slit and 340 mm from the centre of the plasma. This means that the total angle subtended for light collection in the plasma is 2.4°. These distances fitted the experimental lay-out well since the lens could be positioned on the backboard supporting the monochromator where it could be solidly fixed in place. These dimensions are shown in figure 5.12 for clarity.

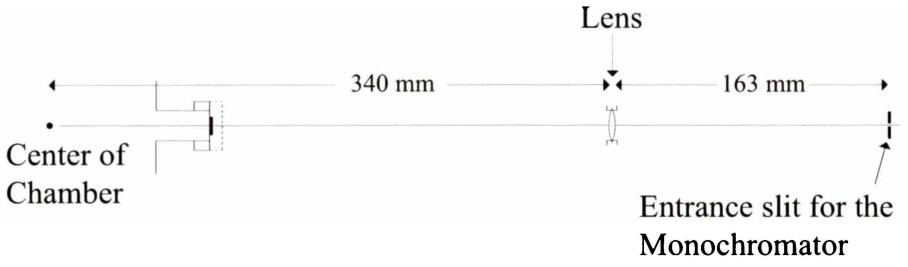

Figure 5.12 : Schematic layout of the light entry to the monochromator.

5.5 Power Supplies

Initially the plasma produced had an insufficient density of metal ions to successfully coat substrates introduced into the plasma. Several modifications to the power supplies were needed to boost the plasma density sufficiently to produce satisfactory coatings. The power supplies were modified in several stages until a satisfactory combination was achieved. First, the transformer that provides power to the filament was doubled in capacity to provide more current to a dual filament system, in order to provide a greater number of free electrons to the plasma. Secondly, the DC power supply providing the electric field for accelerating the electrons was also replaced with a larger model sufficient to provide the current required to adequately accelerate the increased number of free electrons to the required velocity for ionising collisions. Changes in the DC power supply configuration were necessary to increase the energy density to sustain a denser plasma. A further configuration change was needed in this power supply to achieve the right combination of voltage and current for suitable plasma creation. Modification of the discharge configuration was also needed. Instead of accelerating the electrons from the filaments to the chamber wall, the chamber had to been left floating. An electrically isolated circular wire loop was inserted into the vacuum system at the bottom of the chamber. The loop was then used

as the common ground point for the plasma electrons instead of the chamber walls. This modification has increased the plasma density and temperature to a level that produces a sufficient number of ions for the coating process. Coating of the substrates could now be carried out in a controllable manner by applying a voltage to the substrate appropriate to the plasma density, temperature, and composition.

With reference to figure 5.2 the operating procedure to strike and maintain a discharge is as follows. Once the vacuum system is in a suitable state to initiate a discharge, the filament current is raised until the filaments glow strongly at optical wavelengths. The DC bias across the chamber is then raised until a plasma is struck. If at 450 V the discharge fails to ignite, the voltage is lowered, the AC filament current is raised further and then the DC bias is then raised again. Once the discharge is initiated, the filament current and the DC bias can be lowered and adjusted in conjunction with each other to the required voltage and current levels.

5.6 References

Duffey, B., A. Cheetham, and J. Rayner, 1996, J. of Elec. Electronic Eng. Aust., **16,** 12, p 91.

Fang, D., R. R. Williams, and R. K. Marcus, 1990, J. Anal. At. Spectrom., **5**, p 569.

Friedmann, J. B., C. Ritter, S. Bisgaard, and J. L. Shoet, 1993, J. Vac. Sci. Technol. A, **11**, 4, p 1145.

Fujita, F., and H. Yamazaki, 1988, Jap. J. of App. Physics, **27**, 8, p 1477.

Griem, H. R., 1962, *Plasma Spectroscopy* (McGraw-Hill, New York).

Hansen, K., T. Klinger, and A. Piel, 1994, Rev. Sci. Inst., **65**, 8, p 2615.

Hopkins, M. B., W. G. Graham and T. J. Griffin, 1987, Rev. Sci. Inst., **58,** 3, p 475.

Kimura, T., and K. Ohe, 1993, Rev. Sci. Inst., **64**, 11, p 3274.

Neumann, G., M. Kammeyer, and B. Schneemann, 1995, Meas. Sci. Technol., **6**, p 391.

Shindo, H., M. Konishi, and T. Tamaru, 1988, Rev. Sci. Instrum., **59**, 9, p 2002.

Spatenka, P., R. Studeny, and H. Suhr, 1992, Meas. Sci. Technol., **3**, p 704.

Pilling, L. S., E. L. Bydder, and D. A. Carnegie, 2003, Rev. Sci. Inst, **73**, 7, p 3341.

Savitsky, A., and M. J. E. Golay, 1964, Anal. Chem. **36**, 8, p 1627.

Sudit, I. D., and R. C. Woods, 1993, Rev. Sci. Inst., **64**, 9, p 2440.

Chapter 6 Spectroscopic Theory and Analysis

6.1 Introduction

Spectroscopic observations can provide valuable insights into the nature of plasmas even in the absence of a theoretical analysis. The emission lines show what excited and ionised species are present although the quantities of these species will generally be unknown. Experimentally, it was necessary to study the emission spectra from the gases investigated to confirm the assumptions of the Langmuir probe theories.

For spectroscopic data in low temperature plasmas, such as those described in this thesis, none of the theories from total thermodynamic equilibrium to the corona model apply or are of any practical experimental use. The corona model can be applied to the plasma generated in this research, but the theory describing the model is limited to hydrogen-like ions and atoms. For example, theoretical calculations of constants involving oscillator strengths for argon are wrong by two orders of magnitude compared to experimentally determined values. It is expected that the theoretically determined constants for a multi-species plasma containing diatomic molecules would be in error by a similar order to those found for argon.

However, spectral lines emitted from the discharge do give insights into the processes and the states of the molecules and ions in the plasma. A theory has been developed by Czernichowski (1987) based on theoretical vibrational band intensities to analyse the temperature of the excited species for a 2000 K to 7000 K temperature range. Sahli *et al.*(1993) extended this range from 300 K to 1000 K. These theories are based on the intensity of vibrational lines, in the particular excited state of diatomic molecules relative to the band head intensity. Theoretical comparisons are available for the nitrogen molecule which allows us to determine the ion temperature. The concept of "temperature" for the ions is however, somewhat tenuous as it applies only to a particular species in a particular electronic or molecular state.

This chapter introduces elementary molecular spectroscopic theory after which transition theory and specific energy levels of nitrogen and carbon monoxide molecules will be presented. Relevant theories will then be discussed for the analysis of the light emission from the plasma and the approaches of various authors to

overcome the above problems will be examined. A comparison of the experimental spectroscopic data will then be presented along with the conclusions of this analysis.

6.2 Diatomic Molecules

The classification of the electronic states for molecules is very similar to the atomic classification, however, the states are not "pure" electronic states. The energy of a molecule can be approximated by the following equation

$$E = E_e + E_v + E_r \tag{6.1}$$

Thus the total energy, E is the sum of the contributions from the electronic (E_e), vibrational (E_v) and the rotational (E_r) states.

(a) *Rotation Spectra*

These are from transitions that take place between rotational levels of a molecule in a particular vibrational and electronic level.

(b) *Rotation-Vibration Spectra*

Transitions take place from the rotational levels of a given vibrational level to the rotational levels of another vibrational level.

(c) *Electronic Spectra*

These are from transitions which involve a change in the electronic states and encompass all states as transitions are from a rotational level and vibrational level of one electronic state to the rotational and vibrational levels of another electronic state.

We are specifically interested in the various transitions of nitrogen and carbon monoxide molecules. The different transitions can be used to determine the electron temperatures, molecular temperatures (rotational, vibrational) and gas temperatures. In order to calculate these values we will need to consider all of the above transitions.

6.2.1 Molecular Rotation

The simplest model for molecular rotation is the dumbbell model in which the system is considered as two point masses m_1 and m_2 connected through their centre of mass by a massless rod of length r. The molecule rotates about its centre of mass. This two body problem can be reduced to an equivalent one body problem of reduced mass μ. The rotational energy for both cases is given by

$$E_r = \tfrac{1}{2} I\omega^2, \text{ where } I = \mu r^2 = m_1 r_1^2 + m_2 r_2^2 \tag{6.2}$$

where I is the moment of inertia, ω is the angular velocity and r_1, r_2 are the distances of m_1 and m_2 from the centre of mass. Since the angular momentum L of the molecule is quantised according to the equation

$$L^2 = l(l+1)\hbar^2 \tag{6.3}$$

where l is an integer, the energy of a given level is

$$E = \frac{l(l+1)\hbar^2}{2I} = Bhcl(l+1) \tag{6.4}$$

where we set $\hbar^2 / 2I = Bhc$. Since the selection rule for a transition is $\Delta l = \pm 1$, this implies that the rotational lines are separated by a wavenumber, $\Delta\tilde{\nu}$, where

$$\Delta\tilde{\nu} = 2B \text{ cm}^{-1} \tag{6.5}$$

Values of B have been obtained for nitrogen and carbon monoxide and are presented in table 6.1 from Alonso and Finn (1968).

Molecule	$\hbar^2/2I$	B (cm^{-1})
N_2	2.28×10^{-4}	2.010
CO	2.38×10^{-4}	1.931

Table 6.1 : Rotational constants for diatomic molecules of interest.

As discussed in section 6.2.3, the value of r varies according to the minimum in the potential energy curve of the specific electronic state of the molecule causing a corresponding change in B. The potential curves vary from state to state according to the electron distribution. Further details of radii changes are given in Herzberg (1950).

6.2.2 Molecular Vibration

To a first approximation, the nuclei vibrate about their equilibrium separation in simple harmonic motion. The potential for this is

$$V(x) = \tfrac{1}{2} kx^2 \tag{6.6}$$

with the energy of vibration being given by

$$E_v = (v + \tfrac{1}{2})\hbar\omega_0 \tag{6.7}$$

where $v = 0, 1, 2, \ldots$. The energy levels are quantised with the selection rule $\Delta v = \pm 1$ for electric dipole radiation. The radiation is of a frequency $\omega_0 / 2\pi$ which is emitted in

the infra-red spectrum. However, only molecules with a permanent electric dipole moment can suffer transitions. Those without, such as N_2, do not show purely vibrational transitions.

The true potential is anharmonic and can be approximated by adding higher order terms to equation 6.6. Another approximation to these potential curves is the Morse potential, see Herzberg (1950), which, for a given electron configuration, is

$$V_p(r) = D\left[1-e^{-\beta(r-r_0)}\right]^2 \tag{6.8}$$

where D is the dissociation energy of the molecule, r_0 the equilibrium interatomic separation, and β a constant specific for each molecule. The electronic potential energy representation of a diatomic molecule is shown in figure 6.1.

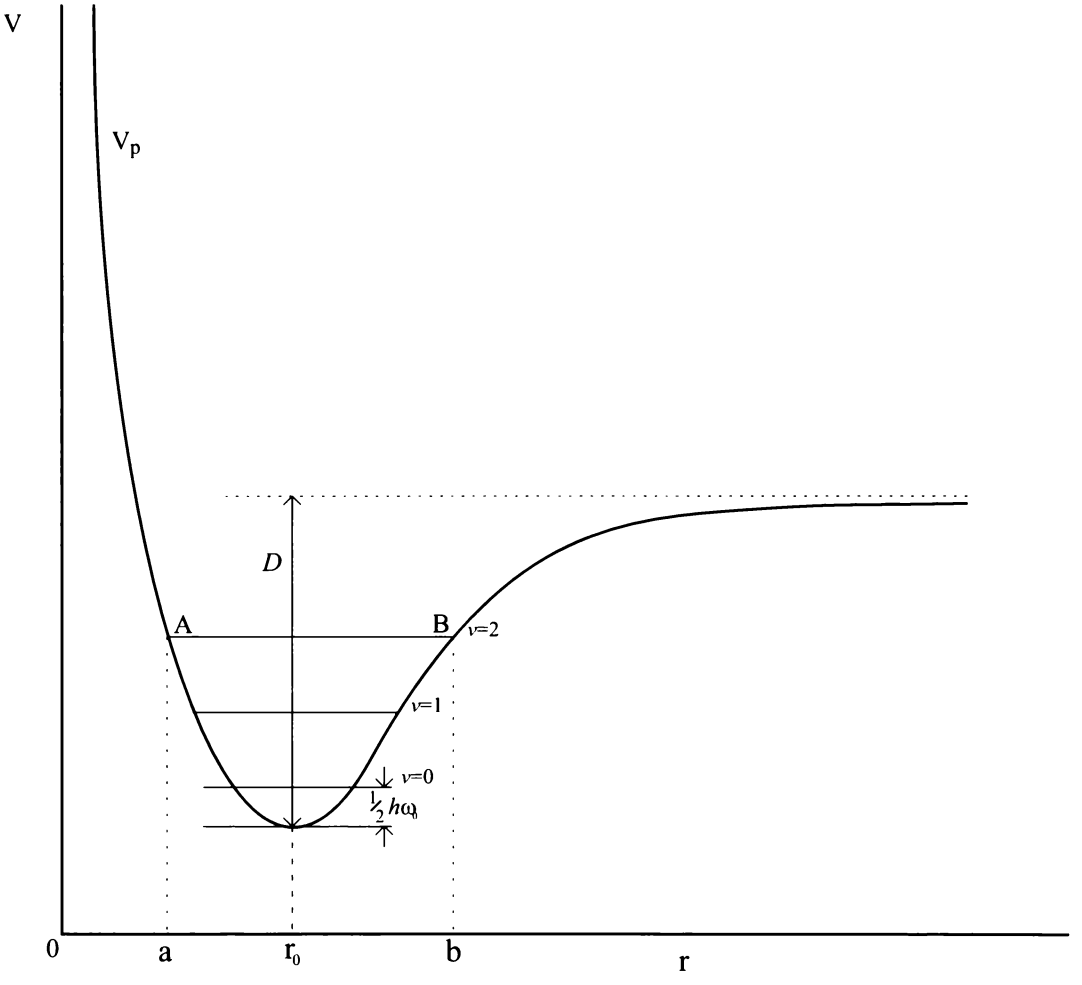

Figure 6.1 : Vibrational potential energy in a diatomic molecule.

We can also have coupling of both vibrational and rotational transitions for which the total energy of the molecule is given by

$$E_v = (v+\tfrac{1}{2})\hbar\omega_0 + \frac{l(l+1)\hbar^2}{2I} \tag{6.9}$$

In general $\hbar^2/2I$ is much smaller (~10^{-4} eV) than $\hbar\omega_0$ (~10^{-1} eV) so there are many rotational levels for each vibrational level. This means that for each vibrational transition there may be many possible rotational transitions that can occur, giving rise to the P and Q branches of the bands found experimentally. So instead of finding single lines there are band systems with each line corresponding to a transition between the rotational levels within the vibration transition.

6.2.3 Electronic Transitions

Molecules can have many electronic configurations with most of these being excited states. For excited states in general, the equilibrium distance between nuclei is different from the ground state and can affect the possible transitions between electronic levels.

Each electronic state accommodates many vibrational and rotational levels which may change along with an electronic transition. The total energy of the molecule can be written from equation 6.1 as

$$E = E_e + (v+\tfrac{1}{2})\hbar\omega_0 + \frac{\hbar^2}{2I}l(l+1)\,. \tag{6.10}$$

The change in the energy for a transition between electronic levels is

$$\Delta E = \Delta E_e + \Delta E_v + \Delta E_r \tag{6.11}$$

which can be rewritten as

$$\begin{aligned}\Delta E = &\left[E_e''-E_e'\right] + \left[(v''+\tfrac{1}{2})\hbar\omega_0'' - (v'+\tfrac{1}{2})\hbar\omega_0'\right] \\ &+ \left[\frac{\hbar^2}{2I''}l''(l''+1) - \frac{\hbar^2}{2I'}l'(l'+1)\right]\end{aligned} \tag{6.12}$$

where the double prime denotes states of higher electronic energy. The radiation frequency that is emitted or absorbed is

$$\nu = \nu_e + \nu_v + \nu_r \tag{6.13}$$

Since ν_e is the largest contribution, the transitions occur as bands, where each band represents the electronic term plus the changes in the various vibrational and rotational levels. The possible values for the total frequencies emitted can be found from the selection rules. The principal transitions between energy levels are dipole transitions with the general selection rules

$$\Delta l = 0, \pm 1 \quad \text{with the restriction} \quad l'' = 0 \not\leftrightarrow l' = 0 \tag{6.14}$$

for the rotational level. The transition $\Delta l = 0$ is allowed due to the change in configuration during the transition. However the restriction in condition 6.14 is necessary to conserve angular momentum. The spin selection rule is

$$\Delta S = 0 \tag{6.15}$$

as the spin must be the same in both electronic levels. However, this rule is not rigorously followed.

The vibrational selection rule is more complicated as changes in the internuclear distance between nuclei must be taken into account. Electronic transitions occur on a time scale of 10^{-16} s while nuclear transitions occur in the time scale 10^{-13} s so that during an electronic transition the nuclear separation is unchanged. After transition, the molecule adjusts itself in its new electronic state. From classical theory, the most probable vibrational transitions occur when the relative nuclear velocity is zero. Such a zero occurs when the nuclei reach their turning point at the end of their oscillation so the most probable transitions occur when, at the time of transition, the nuclei are at one end of their oscillation and are at the same internuclear distance for both the initial and final states. For absorption or emission this is known as the Franck-Condon principle.

In general, the state from which the transition is occurring, i.e. the initial state, is in the lowest vibrational level and a transition can occur to any vibrational level in the final state, depending on separation and overlap of the states which is not restricted by the usual selection rule

$$\Delta v = \pm 1 \tag{6.16}$$

These selection rules may vary depending on the nature of the transition, but can be generalised for transitions of similar states. A generalisation was carried out for various approximations on the coupling of the quantum numbers by Hund. The cases he considered now bear his name.

6.2.3.1 The Franck-Condon Principle

For a potential energy diagram which contains the appropriate electronic states, transitions are expected to occur vertically from each turning point in the initial state (usually the ground state) to the overlapping regions of the excited states. The area inside these turning points is called the Franck-Condon region and for absorption rises vertically from the zero vibrational level of the ground state of the molecule. For emission, the electronic state will initially be in the zero vibrational state, while the

final state will be the various vibrational levels in the lower electronic state. The vertical overlap is used since the molecule changes electronic states 1000 times faster than the change in internuclear separation corresponding to the new electronic state, shown in figure 6.2.

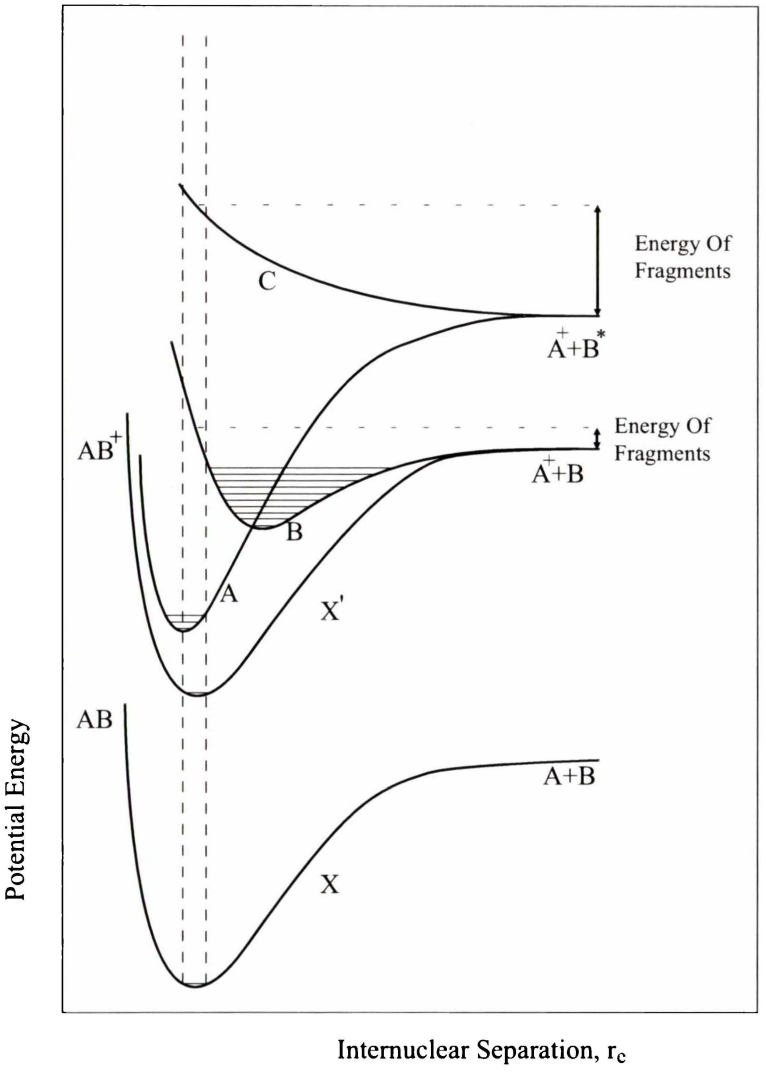

Figure 6.2 : Potential energy curves for a diatomic molecule, AB, in the ground state and its ion, AB^+ in the ground state and three excited states, A, B, C.

For the Franck-Condon principle in emission, if the upper state is stable for a time greater than the time needed for the lowest vibrational state to be reached, we can say that the transition occurs from the zero vibrational level of the upper state to whatever vibrational states are available in the final electronic state following the same vertical transitions.

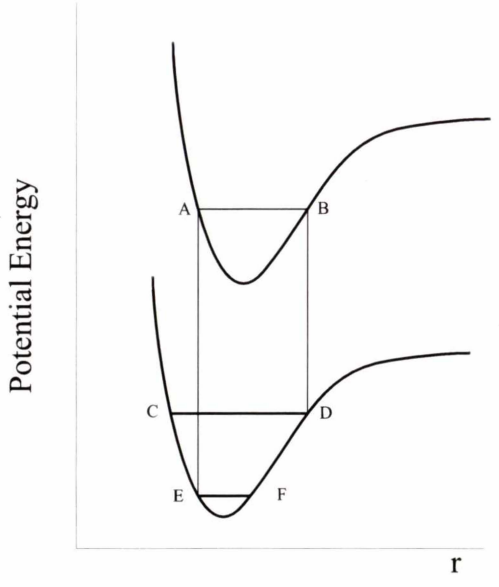

Figure 6.3 : Franck-Condon diagram for transmission.

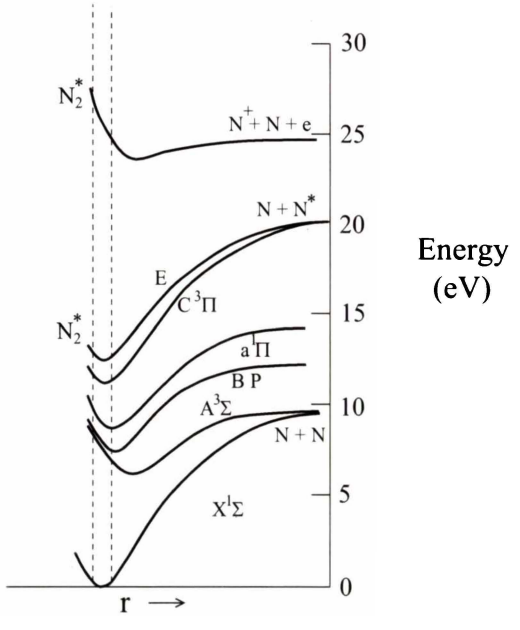

Figure 6.4 : Electronic states of N_2 vs. radial separation of the two atoms showing transitions from the ground state.

Referring to figure 6.3, during the vibration in the upper state, the molecule stays preferentially at the turning points A and B while passing through the intermediate values rapidly, as previously mentioned. The consequence is that jumps between electronic levels occur at these points. So for a jump from position A, the final state is in position E, which forms the left hand side of the new vibrational motion between E and F. For a jump from position B, the final state is in position D

which forms the right hand side of the new vibrational motion between C and D. Thus there are two values of energy which can immediately be obtained by such transitions corresponding to two intensity maxima in the spectra as both turning points have the same transition probability. Once in the final state, the system is expected to slide down the potential curve to the zero vibration level depending on the average particle energy, assuming no further transitions (or electron collisions) take place.

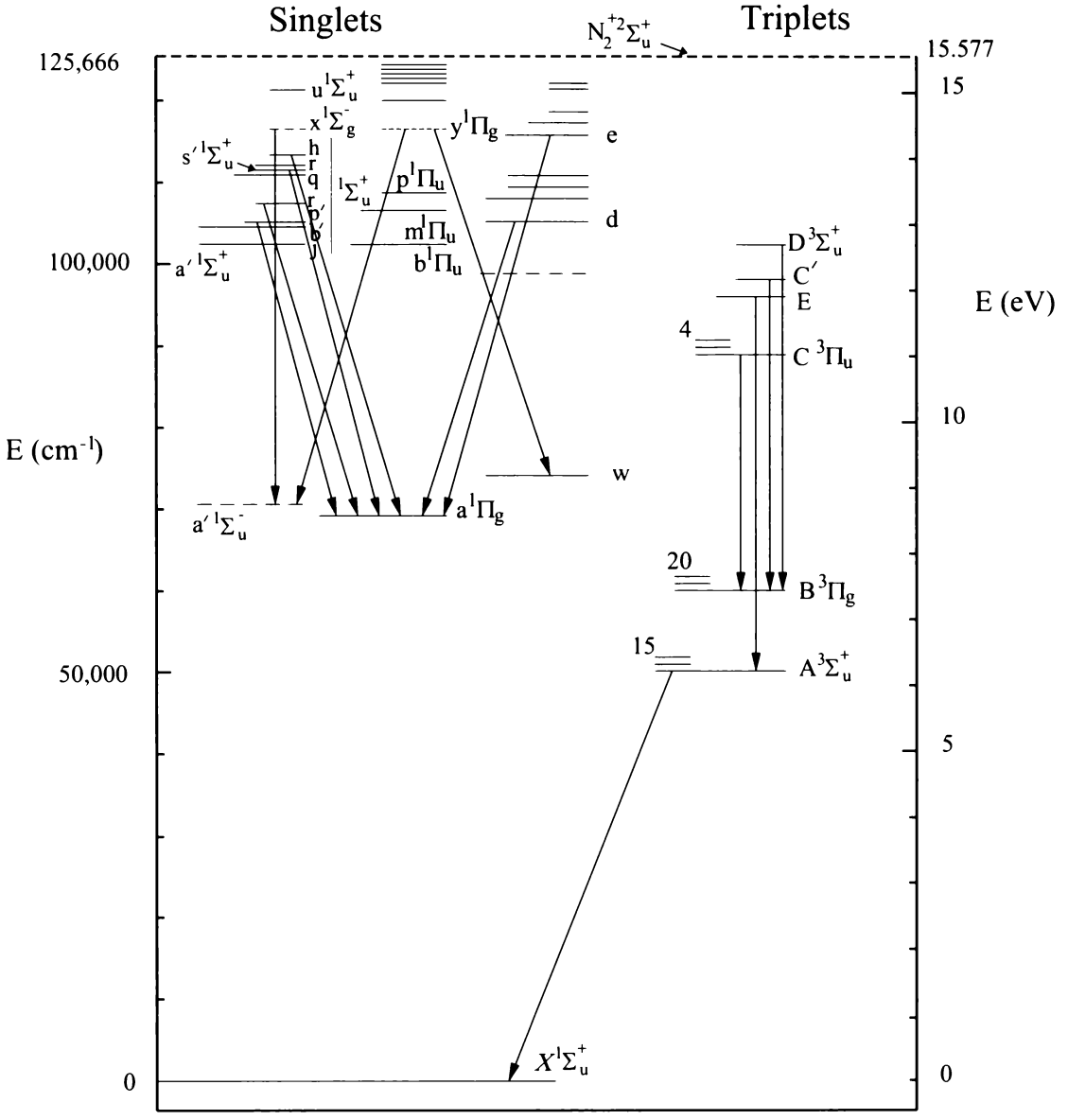

Figure 6.5 : Electronic structure of diatomic nitrogen.

In reality the transition overlap is more complex than the Franck-Condon diagrams suggest since the transition probability can be non-zero over a large vibrational range in the final state. In wave mechanics, the probability distribution of the vibrational levels is given by the eigenfunctions of the Schrödinger equation for the harmonic oscillator. These eigenfunctions are found to be the orthogonal Hermite

polynomials from which the probability distributions can be obtained. The probability of a transition occurring to vibrational levels in an excited electronic state is proportional to the overlap of the probabilities at a particular radius. For emission, the overlap is the same, so the most intense transitions to lower electronic levels occurs to vibrational levels with the maximum overlap. In general there will be two such progressions, one from each turning point producing varying intensity transitions (and wavelengths) to lower and lower vibrational levels in the final state. Figure 6.4 shows the electronic states of N_2 vs. radial distance for which the overlaps for transition from the ground state are shown, from von Engel (1965).

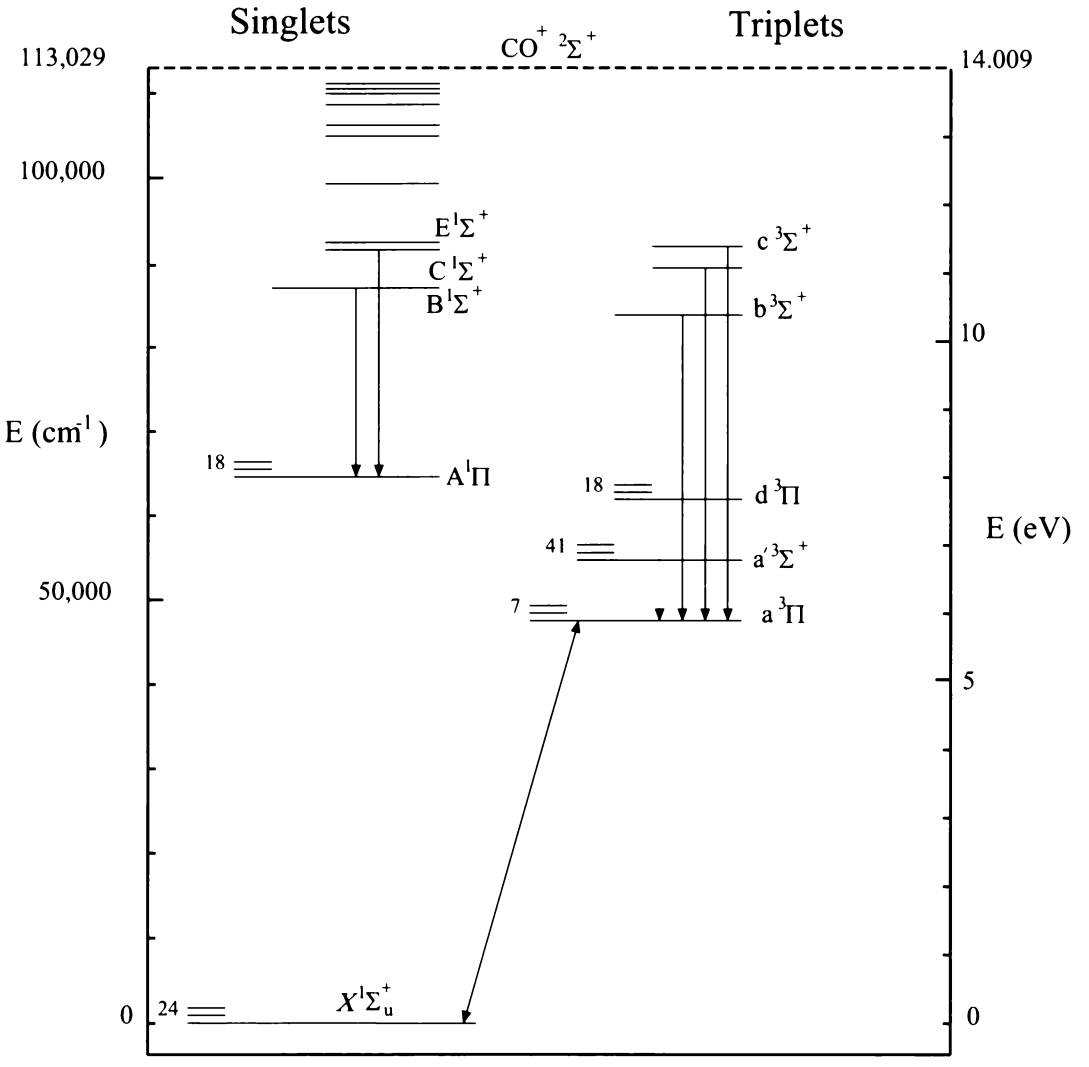

Figure 6.6 : Electronic structure of carbon monoxide.

Figures 6.5 and 6.6, taken from Herzberg (1950), show transitions detectable in the 2,000 - 5,000 Å wavelength range. Short lines give the number of vibrational states while the longer lines show the electronic levels. The transition of common DC

discharge band structures and atomic transitions of N_2, CO, and Cr are presented in Appendix A and should be examined in conjunction with these electronic structures.

6.3 Spectroscopic Plasma Models

The light emission from a low temperature, laboratory steady state plasma occurs from the bound electrons in molecules (ionised or neutral) in their excited states (electronic, vibrational and rotational) falling to a lower state or to the ground state. The excitation of the bound electrons is controlled by collisional impact with free electrons in the plasma. Thus if the electron distribution in the plasma is Maxwellian or close to it, the light emission from the plasma will be directly related to the distribution function and the temperature and density of the electrons can be calculated. However, if the distribution of the electrons across their energy range is unknown, or not Maxwellian, the theoretical analysis becomes increasingly complex and less reliable.

As the neutral pressure is reduced in a plasma, collisional equilibrium becomes less likely since the mean free paths increase and the distribution function changes shape. It has been noted by Hopkins (1995) that once the gas pressure falls below 0.13 mbar (10^{-2} torr) in argon, the distribution changes from Maxwellian to a Druyvesten type function.

Quite often, the desirable parameters of a plasma used for etching or coating are not equilibrium conditions. If true equilibrium was achieved in a plasma, equivalent thin film coatings could be achieved by other means (for example, electrolytic chrome plating methods) which would render the films generated in a plasma of little use except in cases where the other methods cannot be used. Thus plasmas of interest tend to be non-equilibrium in nature and thus directly oppose the tenets that spectroscopic analysis is based on.

There are several models which describe the light emitted from a plasma and each has restrictions necessary for theory to be applied. We will present them in a format from the most to the least restrictive, providing highlights and the applicability of the model. The first model which we will briefly describe is that for a plasma in thermodynamic equilibrium. This model is of little use to an experimentalist since the equilibrium includes the radiation emitted and reabsorbed by the plasma. This implies that no radiation from the plasma can be measured since none of it escapes in this model. Hence we will start our discussion with local thermodynamic equilibrium

6.3.1 Local Thermodynamic Equilibrium

A common plasma state is one that is close to thermodynamic equilibrium (TE), called local thermodynamic equilibrium (LTE). In this state all distributions apart from the radiation energy follow the Boltzmann distribution law. The model assumes that the populations of the species present in a plasma are determined by particle collision processes and the distributions of such respond instantaneously to any change in the plasma parameters. Each creation or destruction process is balanced by its reverse reaction and these pair processes proceed at equal rates (except of course radiation energy which can escape). The reactions generally considered to be of importance are;

a) Emission and absorption of spectral lines

$$M_k \rightleftharpoons M_i + h\nu_{ik} \tag{6.17}$$

b) Photo-recombination and photo-ionisation

$$M_{z,i} + e \rightleftharpoons M_{z-1,k} + h\nu \tag{6.18}$$

c) Super-elastic collisions with electrons, ($E_{kin} > E'_{kin}$)

$$M_i + e(E_{kin}) \rightleftharpoons M_k + e(E'_{kin}) \tag{6.19}$$

d) Excitation and deexcitation by heavy particles, ($E_{kin} > E'_{kin}$)

$$M_i + M'(E_{kin}) \rightleftharpoons M_k + M'(E_{kin}) \tag{6.20}$$

e) Ionisation by electrons and three-body recombination

$$M_{z-1,k} + e(E_{kin}) \rightleftharpoons M_{z,i} + e(E'_{kin}) + e \tag{6.21}$$

where z is the ionised state of the atom or molecule, M, while the subscripts i and k are different electronic states. The distribution functions, at any point in time or space, are determined by the local plasma parameter values. In this state all the distribution functions apart from the radiation energy are described by the Boltzmann distribution. The population distribution is determined by the statistical mechanics law of equipartition and does not require collision cross-sections for its calculation.

If the free electrons are distributed among the energy levels available to them their velocities will have a Maxwellian distribution. Hence the number of electrons of mass m and speeds between v and $v + \mathrm{d}v$ is

$$\mathrm{d}n_v = 4\pi N_e \left(\frac{m}{2\pi kT_e}\right)^{3/2} \mathrm{e}^{\left(-\frac{mv^2}{2kT_e}\right)} v^2 \mathrm{d}v \tag{6.22}$$

where N_e is the total density of the free electrons and T_e is the electron temperature.

From Griem (1964) for the bound levels, the population densities are governed by the Boltzmann and Saha equations:

$$\frac{N_p}{N_q} = \frac{w_p}{w_q} \mathrm{e}^{\left(\frac{\chi_{p,q}}{kT_e}\right)} \tag{6.23}$$

$$\frac{N_{z+1,g}}{N_{z,g}} = \frac{2w_{z+1,g}}{w_{z,g}} \left(\frac{2\pi mkT_e}{h^2}\right)^{3/2} \mathrm{e}^{\left(\frac{\chi_{z,g}}{kT_e}\right)} \tag{6.24}$$

where N_p, N_q, $N_{z+1,g}$, and $N_{z,g}$ are the population densities of the various levels denoted by the quantum numbers p, q, and g (the latter being the ground state) and ionic charge $z + 1$, and z. The term w is used to denote the statistical weight or partition function of the level indicated by the subscripts, $\chi_{p,q}$ is the energy difference between level p and q, while $\chi_{z,g}$ is the ionization energy of the atom of charge z in its ground level g. The intensity of a spectral line arising from the transition between two bound levels p and q is

$$I_{p,q} = \frac{1}{4\pi} \int N_p A_{p,q}\, h\nu_{p,q}\, \mathrm{d}s \tag{6.25}$$

where $A_{p,q}$ is the atomic transition probability, and $h\nu_{p,q}$ is the photon energy. The integration is taken over the depth of the plasma viewed by the detector with the intensity $I_{p,q}$ measured in power per unit area per unit of solid angle.

If the plasma is at a sufficiently low density, the probability of a radiative transition becomes comparable to the probability of a collisional transition, deviations from LTE are apparent and the theory no longer holds. This is because in an optically thin plasma the emission process is not balanced by its inverse and the distribution functions deviate away from a Boltzmann distribution. Another way to look at it is that $T_e \neq T_i \neq T_n$. For the plasma to be in LTE the following condition derived by Griem (1964) must apply (it is a necessary but not a sufficient condition of LTE)

$$n_e \geq 9\times10^{17} \left(\frac{E}{E_H}\right)^3 \left(\frac{kT_e}{E_H}\right)^{1/2} \ \mathrm{cm}^{-3} \tag{6.26}$$

where T_e is the electron temperature in eV, E_H is the ionisation energy of hydrogen while E is the highest energy transition gap in eV.

This condition is only achievable in low temperature plasmas with pressures close to atmospheric pressure, due to the collisional nature of the plasma needed. It has been shown experimentally by Hopkins (1995) that at pressures below 0.13 mbar in argon the collision rate is reduced to such an extent that a collision dominated

plasma cannot be obtained. The densities required for LTE were not achieved with the plasma generated in this thesis.

6.3.2 Partial Local Thermodynamic Equilibrium

As the name implies, partial local thermodynamic equilibrium (PLTE) is a state where LTE does not fully hold for all energy levels. In practice the radiative transitions to low energy levels are more frequent than to higher levels and thus these levels are depopulated faster than the higher terms. For complete LTE this requires many collisions during the short lifetimes of these states. PLTE calculations are appropriate as it can determine, up to what energy level, the plasma is in thermodynamic equilibrium, generally by reference to the experimental electron density. Equation 6.27, again from Griem (1964) provides the required density for the possible energy levels for which PLTE is valid.

$$N_e \geq 7\times10^{18}\frac{z^7}{n^{17/2}}\left(\frac{kT}{z^2E_H}\right)^{1/2} \quad \text{cm}^{-3} \tag{6.27}$$

where z = 1 for neutrals, z = 2 for single ionised particles, z = 3 for doubly ionised particles, and so on, where n is the quantum number level required to be within 10% of LTE. The densities required for this model to apply are above those obtained in this work and like LTE apply to atmospheric pressure plasmas in general. This model differs from LTE in that only the upper energy levels of the excited species are considered to be in a Boltzmann distribution. The functions of the lower states are unknown or assumed to be in corona equilibrium.

6.3.3 The Corona Model

When the electron densities are too low for LTE to exist, the corona model is used to describe the plasma. This model was originally constructed to describe the solar corona which is diffuse and has a low density of ionised particles. For the low densities that this model applies, practically all the processes are not fully balanced. At the densities to which this model applies in all likelihood an atom or molecule will emit spontaneously and an ionised atom or molecule will recombine by photorecombination. This model relies critically on cross-sectional data. The model is quite simplistic and works as follows: Excitation or ionisation occurs with the impact of an electron on the ground state of an atom or molecule as shown in equation 6.28.

$$M_z + e \rightarrow M_{z+1} + e + e \tag{6.28}$$

The reverse process is radiative recombination shown in equation 6.29.

$$e + M_{z+1} \rightarrow M_z + h\nu \tag{6.29}$$

where M is the excited state or level of the radiating particle. Following McWhirter (1965) and Griem (1964) we can write down an equation expressing the ionization-recombination balance as

$$N_e N_{z,g} S = N_e N_{z+1,g} \alpha \tag{6.30}$$

or

$$\frac{N_{z+1,g}}{N_{z,g}} = \frac{S}{\alpha} \tag{6.31}$$

where N_e is the electron density, $N_{z,g}$ and $N_{z+1,g}$ are the number densities of particles in the ground state and excited states respectively, while S is the collisional ionisation coefficient and α is the radiative recombination coefficient. From McWhirter (1965), and after a few approximations, this ratio is calculated as

$$\frac{S}{\alpha} = 1.18 \times 10^{-4} \frac{z^2 \chi_{z,g}^{3/4}}{\zeta T_e^{3/4}} \mathrm{e}^{\left(\frac{\chi_{z,g}}{kT_e}\right)} \tag{6.32}$$

where z is the atomic number, $\chi_{z,g}$ is the ionisation energy of the atom, and ζ is the number of outer shell electrons.

The population densities of the excited levels are determined by the balance between the rate of collisional excitation from the ground state level balanced by the rate of spontaneous decays shown in equations 6.30 and 6.31. Thus:

$$N_e N_{z,g} X_{p,q} = N_{z,g} \sum_{q<p} A_{p,q} \tag{6.33}$$

with

$$X_{p,q} = 8.50 \times 10^{-4} \frac{\bar{g} f_{p,q}}{\chi_{p,q} T_e^{1/2}} \mathrm{e}^{-\left(\frac{e\chi_{p,q}}{kT_e}\right)} \tag{6.34}$$

where $\bar{g}$ is the effective mean gaunt factor, $f_{p,q}$ is the absorption oscillator strength, $\chi_{p,q}$ is the excitation energy of the state, while the sum denotes the number of possible lower states the excited level can decay to.

The intensity of a line is given by McWhirter (1965) for an optically thin plasma as

$$I_{p,q} = \frac{1}{4\pi} \int N_e N_{z,g} X_{g,p} \frac{A_{p,q}}{\sum_{q<p} A_{p,q}} h\nu \, \mathrm{d}s \tag{6.35}$$

This model, however, is of limited practical use since the application of this theory is restricted to atoms and their ions. The application to molecules remains dubious since equations 6.32 and 6.34 were originally derived for hydrogen or hydrogen-like ions and have been adapted for a general use. Furthermore, equation 6.32 has a quoted accuracy of ±300% from McWhirter (1965) while equation 6.34 is expected to be ±100%. These errors, along with those expected in the oscillator strengths and the experimental measurements imply that the lack of accuracy of this theory makes it of little practical use. Some errors can be removed for the argon plasma experiments since there are experimental values incorporating the constants in equations 6.32 and 6.34. However, no experimental data have been found for nitrogen or carbon monoxide. Adding to the inaccuracies, application of this theory to the previously mentioned molecules from a theory based on hydrogen-like ions would not be successful since the theory takes no account of interatomic forces within the molecules, while the constants such as the oscillator strengths are less accurately known, making the total error approximately an order of magnitude. Furthermore, cross-sectional collision data of a single molecule such as nitrogen is hard to obtain and the values given by various sources vary markedly from each other.

To apply this model to a mixed combination plasma of nitrogen ions and molecules, carbon monoxide ions and molecules and chromium atoms and ions is difficult and the results need to be interpreted with great caution. For further discussion the reader is referred to the books by Griem (1964), McWhirter (1965), and Lochte-Holtgreven (1968).

6.3.4 Spectroscopic Temperature Measurements

Many steady state laboratory plasmas that emit enough light for observation are in some state of equilibrium, generally with the velocity distribution function somewhere near Maxwellian. Hence there may be local ion and electron temperatures that are measurable by spectroscopic methods. Such temperatures can be obtained by relative line intensity measurements, however density measurements require either absolute line intensities or Stark profiles. The first method requires high accuracy measurements with accurate calibration of the monochromator while the second is only applicable for densities far higher than obtained in this thesis study (LTE densities $\sim 10^{18}$ cm^{-3}). Hence, with reference to chapter three, we will concentrate on temperature measurements, giving the appropriate theory, and leave the accuracy for comparison with other diagnostic methods later in chapter seven.

There are two principal ways to determine the temperature from emission radiation from a plasma.

1) The absolute intensity integrated over the line profile combined with knowledge of the plasma composition and associated properties of the components.
2) The relative intensity of two separate, but thermodynamically linked lines from the same molecule or atom where each has a distinct energy of excitation.

The former is virtually unattainable in a laboratory plasma since complete or local thermodynamic equilibrium is seldom achieved. The latter is possible, if certain parameters such as the oscillator strengths are known.

6.3.4.1 Relative Intensities of Lines from the same Element and Ionisation Stage

This is the most commonly used method of determining temperature in a plasma by spectroscopic means. The equation used is from Griem (1964),

$$kT = \frac{E' - E}{\ln\left(\frac{I\,\lambda^3 g' f'}{I'\lambda'^3 g\ f}\right)} \tag{6.36}$$

where I, λ, g, and f are the total intensity (integrated), wavelength, statistical weight, and absorption oscillator strength, respectively of one line and E its excitation energy.

Statistical weights can be calculated from the number of orientations the total angular momentum can assume using equation 6.37

$$g_n = 2J_n + 1 \tag{6.37}$$

However, oscillator strengths are harder to obtain and almost all have significant uncertainties except for one electron systems. Data are difficult to obtain for molecules such as nitrogen and carbon monoxide making this theory hard to use in practice.

Unfortunately, if the LTE criterion is violated, no generalised formula can be used to replace equation 6.36. The next simplest situation is where the population of the lines is determined by a balance between electron collision excitations from one level and radiative transfer back to the same level. Equation 6.38 provides this measurement and is only valid if the LTE criterion in equation 6.26 is under fulfilled by at least an order of magnitude.

$$kT = \frac{E' - E}{\ln\left(\frac{I\,E^3\lambda^3 g' f'}{I'E'^3\lambda'^3 g\ f}\right)} \tag{6.38}$$

Equation 6.38 introduces greater uncertainties in the calculation because ignoring all other rate processes is never fully valid. Errors in the cross-sectional data are also included.

6.3.4.2 Relative Line Intensities of Subsequent Ionisation Stages of the same Element

The relative line intensity measurements from the same ionisation stage normally do not provide accurate temperature measurements as there is little separation between the upper levels of the two lines. Thus the ratio is insensitive to temperature changes since the energy difference between them is small. If different ionisation stages are used, then the energy difference between the lines is increased by the ionisation energy thus increasing the sensitivity. For LTE this ratio is

$$\frac{I'}{I} = \frac{f'g'\lambda^3}{fg\lambda'^3} \frac{1}{\left(4\pi^{3/2}a_0^3 N_e\right)} \left(\frac{kT}{E_H}\right)^{3/2} \mathrm{e}^{-\left(\frac{E'+E_\infty-E-\Delta E_\infty}{kT}\right)} \tag{6.39}$$

The primed quantities refer to the higher ionisation stage, E_H is the ionisation energy of hydrogen, a_0 is the Bohr radius, and ΔE_∞ is the reduction in ionisation energy, E_∞, of the lower ionisation stage. ΔE_∞ is given by equation 6.40.

$$\Delta E_\infty^{z-1} = \frac{ze^2}{4\pi\varepsilon_0\lambda_d} \tag{6.40}$$

Equation 6.39 is of practical use for LTE plasmas with densities above 10^{18} cm^{-3}. A more practical and less restrictive formula can be used if the upper energy levels follow the corona equations. This now allows the use of a relation down to densities of the order of 10^{15} cm^{-3}. Using equations 6.32, 6.33, 6.34, and 6.35 we can derive a simple equation of the form

$$\frac{I}{I'} = CT_e^{-3/4} \mathrm{e}^{\left(\frac{E_i^0 - E_{g.u}^0 + E_{g.u}^+}{kT_e}\right)} \tag{6.41}$$

where C is a constant involving the gaunt factors, energy levels, etc, and takes the form

$$C = 1.18\times10^{-4} \frac{z^2 E_i^{7/4}}{\zeta} \frac{h\nu_0}{h\nu_+} \left(\frac{\dfrac{\bar{g}_0 f_0}{E_{g.u}^0} \dfrac{A_{p.q}^0}{\sum\limits_{q<p} A_{p.q}^0}}{\dfrac{\bar{g}_+ f_+}{E_{g.u}^+} \dfrac{A_{p.q}^+}{\sum\limits_{q<p} A_{p.q}^1}} \right) \tag{6.42}$$

The variables in this equation are all defined previously. Values calculated theoretically by Desai *et al.* (1994) for this constant are about two orders of magnitude different from values determined experimentally using Langmuir probe data as a normalization base. These calculations are presented in table 6.2 for combinations of spectral intensities of argon. From the comparison of values presented in table 6.2, we can see the theoretical corona equations for the determination and calculation of the constant, C, is different from the experimental values by two orders of magnitude on average. Since argon is close in its electronic distribution of electrons to those this theory was intended for, it is expected that values for C will have to be determined experimentally for nitrogen and carbon monoxide. However, it is almost pointless to do so since the constants need to be determined from use of the Langmuir probe data. Since they are normalised by electron temperatures from another method, it is impossible to gain a true comparison between the two techniques.

Ar I (Å)	Ar II (Å)	C (theoretical)	C (experimental)
4272.17	3720.42	1.7×10^{-2}	1.80
4272.17	3737.89	1.0×10^{-3}	2.43
4272.17	4131.73	4.8×10^{-3}	0.72
3606.53	3720.42	4.0×10^{-2}	2.25
3606.53	3737.89	2.4×10^{-3}	3.04
3606.53	4131.73	1.2×10^{-2}	0.38

Table 6.2 : Values of C given in equation 6.42 compared to experimentally determined values.

In general there is no ionisation equilibrium linking molecular components or electronic levels such as N_2 and N_2^+. Thus the relative line intensity method is expected to be more valid when line intensities are compared within the same ionisation level. As previously noted, this method is also inaccurate since the energy gap between the transition levels is small.

6.3.5 Methods used by other Authors.

Along with the treatment of Desai *et al.* (1994) a variety of authors have tried many different approaches. Czernichowski (1987) noted that for nitrogen and its first molecular ion there is generally no equilibria linking the molecular states. If this is the case, then only the rotational and vibrational transitions remain valid to determine the temperature of the species. Following this with a theoretical analysis on the change in the band structure of the $B^2\Sigma_u^+ - X^2\Sigma_g^+$ transition in N_2^+ as the temperature of the ion

was changed a method was formulated to determine the experimental temperature from the observed spectra, valid from 2000 K to 7000 K.

Felts and Lopata (1988) used helium and nitrogen mixtures and the two neutral helium lines (He^1 ^1D - $^1P°$) at 492.2 nm and 667.8 nm to calculate the temperatures using equation 6.39. At 100 W input power the spectroscopic and probe temperatures agree within reason (up to 25% N_2) but deviate significantly at 200 W.

Cox *et al.* (1987) compare the Ar and Ar^+ transitions at 470.2 nm and 480.6 nm to calculate the average energy of the electron energy distribution function (EEDF) to compare to Langmuir probe data. The spectroscopic analysis was qualitative and not absolute and they could only determine the changes in the EEDF rather than elucidating the entire distribution from spectroscopic measurements. Later in the same year, the same group Hope *et al.* (1987) used a similar technique, again in an rf argon plasma. Only changes in T_e could be determined from spectroscopy since they normalised the intensity ratios to Langmuir probe temperatures to determine the unknown constant in equation 6.41 where it was found that C = 0.62. The method appears to be identical to that used later by Desai *et al.* (1994).

Fancey and Matthews (1991) used the same equation in a DC argon plasma and the values of C determined by Hope *et al.* (1987) as well as their own estimated ones. The values for C were 1647, 33.9 and 0.62 which covers a considerable range in magnitude. Again the temperature values from the spectroscopic data were relative, having been normalised to the Langmuir probe data. Shatas *et al.* (1992) also used the same calibration method for argon, but in a microwave generated plasma. They found the constant C was best fitted with a value of 2 and temperatures from the Langmuir probes and the line intensity ratios was close. However, the Langmuir probe data presented is poor, with a voltage resolution of 2 volts. The temperature curve fits are highly non-linear (ln I vs. V) and the magnetic field effects on the collection of particles by the probe seems to be ignored. The good match between optical and probe temperatures appears to be good fortuitous rather than experimentally sound.

At higher pressures of 0.27 - 5.33 mbar (0.2 - 4 Torr) Angstadt *et al.* (1993) were able to get good agreement between spectroscopic and Langmuir probe temperature measurements. A DC plasma of argon or neon was generated in a six-way cross with a 7 cm tube diameter. The cathode and anode separation was around 2 cm while the voltage and range was 300 V - 3500 V allowing currents of 0 to 4.5 mA which resembles a high voltage discharge tube rather than the DC plasma used in this thesis. The temperatures obtained were low, ranging from 0.4 eV to 0.7 eV. The densities calculated from the Langmuir probe shows discrepancies up to two orders of magnitude between the electrons ($1 - 3 \times 10^9$ cm^{-3} for argon and neon) and the ion density of argon (1.2×10^{11} cm^{-3}) and neon (8×10^{10} cm^{-3}) for which no explanation is

given. However at these pressures, LTE and hence a Boltzmann distribution was assumed and temperatures were obtained using equation 6.39 for a variety of transition lines. The results agree with the findings of Hopkins (1995) in a rf plasma, that the electron distribution is Maxwellian at these pressures in a DC plasma as well and hence the excited states are in equilibrium with each other.

Again at higher pressures of 0.3 to 1 mbar Sahli *et al.* (1993) used a method very similar to that of Czernichowski (1987) to measure the rotational temperature of nitrogen used as an impurity in an oxygen discharge. The discharge was created via an electron beam (500 - 4000 eV) directed into a rf plasma generated in a narrow quartz tube. The method is applicable from 300 K to 1200 K and is complementary to the work of Czernichowski (1987). Also included in the paper of Sahli *et al.* (1993) are direct theoretical calculations showing the change in structure of the band system of the $B^2\Sigma_u^+ - X^2\Sigma_g^+$. Figures from this paper are reproduced in section 6.3.5.1 where the analysis is more detailed.

Behringer and Fantz (1994) combined spectroscopic measurements of He, Ar, and the molecular bands of N_2 to derive the EEDF for pure nitrogen and various mixtures of the aforementioned gases over the 12 to 24 eV range. Below 12 eV vibrational measurements of nitrogen were used for the calculations. The models were based on integration of the ionisation rate equations based on an ambipolar diffusion in a DC plasma combined with a corona model. These models were applicable since the discharge was contained in a cylindrical glass discharge tube 1 metre in length and 1 cm wide where the loss of electrons and ions to the walls dominates. The pressure range was 1 to 10 mbar (100 to 1000 Pa) where it was found that a Druyvesten distribution was present in the high energy tail (12 to 24 eV) and is a somewhat higher pressure than the transition found by Hopkins (1995). Once again, the fitting constant for the spectroscopic model had to be adjusted for the data to fit the temperatures and densities obtained by an analysis of Ohm's law.

At a lower pressure of 0.133 mbar (0.1 Torr) modelling several emission bands of N_2 and N_2^+ using an Abel inversion was achieved by Chelouah *et al.* (1994A) in a modified DC discharge. The emission coefficients necessary for the calculations were taken from Lochte-Holtogreven (1968). The theoretical band intensities rely on reconstructing experimental emissions from the experimental data and thus provide rotational and vibrational temperatures if the absolute intensities are known. However, this method does not easily lend itself to experimental data since an iterative fit to the numerical solution of the integrals used in the Abel inversion must be performed to obtain the temperatures. In a separate paper, Chelouah *et al.* (1994B) expanded the method used by Czernichowski (1987) for the first negative system to the second positive system of nitrogen. The modelling of the band structure provides rotational

and vibrational temperatures assuming a Boltzmann distribution. Similarly to the previous 1994 paper, the method is only briefly outlined and reference is made to other resources where the values of the rotational constants, wavelengths of the rotational structures are taken. To use this method, one would have to reconstruct the entire computational model and apply it to the experimental data since no simple method of usage is presented.

Popa (1996) used a DC discharge comprising of two hollow cylinders in a narrow quartz tube to measure the vibrational distributions with nitrogen gas. The pressures ranged from 1.3 to 4 mbar (130 to 400 Pa) where it was found that the populations of the vibrational levels in the first positive, second positive and first negative band systems followed a Boltzmann distribution. The variation of vibrational temperature with increasing current was measured for each band system and confirms the results from previous papers (see above) that a simple spectroscopic model can be applied at these pressures.

To remove some uncertainties and to compare directly the rotational temperatures with a known gas temperature value Goyette *et al.* (1998) placed a positive column discharge of nitrogen into an oven of fixed temperature. Once again the pressures were above those used in this thesis at 0.66 to 5.3 mbar (0.5 to 1 Torr) where the rotational levels were populated according to the Boltzmann distribution. The rotational temperatures matched the oven temperatures to approximately 500 °C where deviations occurred and the rotational temperatures were consistently lower than the oven temperatures. The authors indicate that equilibrium amongst the vibrational levels is not achieved even though they calculate the rotational temperatures by applying a Boltzmann distribution which assumes exactly this equilibrium.

As previously mentioned at the start of section 6.3 and confirmed experimentally by the review of the above papers, at pressures below approximately 0.5 mbar the distribution function governing the population rotational levels deviates from the Boltzmann distribution. Even when this occurs Goyette *et al.* (1998) showed that the rotational temperature still provides a useful estimate of the gas temperature below 500 °C. However at pressures of two orders of magnitude lower then theirs and far higher electron temperatures, it is unknown whether this relation is true. The simplest method to apply is that of Czernichowski (1987) since in the experimental spectroscopic measurements in this thesis a compromise had to be made in the resolving power. The slit width had to be increased in order the collect a larger number of photons so that the spectroscopic intensities were easily measurable above the detection limits of the monochromator. This mean that the resolution of the band structure was poor and hence does not easily lend itself to the models calculated by the above authors.

6.3.5.1 Rotational Temperature Measurements

If relaxation of the rotational levels in a particular band is fast enough to allow a Boltzmann distribution to exist, the rotational temperature can be measured. The work of Czernichowski (1987) in simulating the band structure for the $B^2\Sigma_u^+ - X^2\Sigma_g^+$ transition in N_2^+ and fitting the results in a simplified format for experimental use provides a method for finding the rotational temperature in ionised nitrogen molecules. Essentially the rotational temperature measured by this method was calibrated against thermocouple data and gives the gas temperature of the plasma and is valid from 2000 to 7000 K. The fitting formula is

$$T = c_1 - 10c_2 + 100c_3 A_i \left(3W_j\right)^{c_4} \tag{6.43}$$

where c_1 to c_4 are fitting constants dependent on both states, A_i is the ratio of the local maxima to the full band width height, and W_j is the full head width of the band at $j/10$ of the head peak, (j = 5, 6, 7, or 8). The observed spectra are split into 3 classes, depending on the resolution of the experimental data recorded. These classes are listed below according to wavenumber and. W_8 value.

Class C, $\Delta\sigma$=1.25 to 2.00 cm^{-1}	or	$1.65 < W_8 < 2.70$
Class D, $\Delta\sigma$=2.00 to 3.00 cm^{-1}	or	$2.70 < W_8 < 4.00$
Class E, $\Delta\sigma$=3.00 to 4.00 cm^{-1}	or	$4.00 < W_8 < 5.40$

W_8 and $\Delta\sigma$ are expressed in cm^{-1}. This seems a confusing method to determine the gas temperature, but it works well in practice and the values obtained are expected to be within 10% accuracy. The values of the fitting constants can be obtained from the original paper. The general form of the band structure for low resolution, is reproduced in figure 6.7.

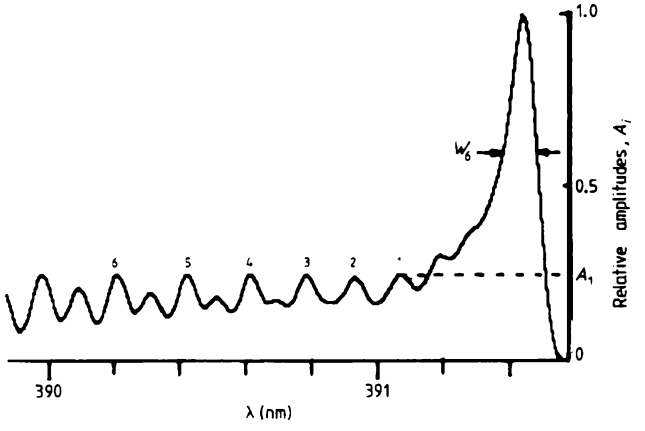

Figure 6.7 : The simulated band structure for 5,000 K when the apparatus width is 3 cm^{-1}, reproduced from Czernichowski (1987).

The method of Sahli *et al.* (1993) also involved the simulation of the $B^2\Sigma_u^+ - X^2\Sigma_g^+$ band structure, but at lower temperatures than Czernichowski (1987) and at a lower resolution where the individual rotational bands are partially resolved. Whereas Czernichowski (1987) used the relative height of the particular rotational transition (see figure 6.7), Sahli *et al.* (1993) used the slope of the band structure and calculated the relative height to the band head maximum by intersection and calculated the temperatures based on three variables, *s*, *h*, and *H*, shown in figure 6.8. The method is simpler to apply that that of Czernichowski (1987) since the instrument resolution and hence the need to choose the appropriate constants is absent.

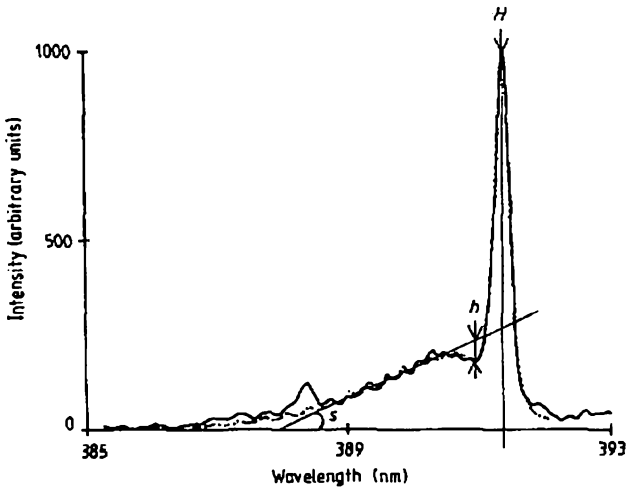

Figure 6.8 : The calculate and measured band spectrum at 800 K showing the theoretical variables employed, reproduced from Sahli *et al.* (1993).

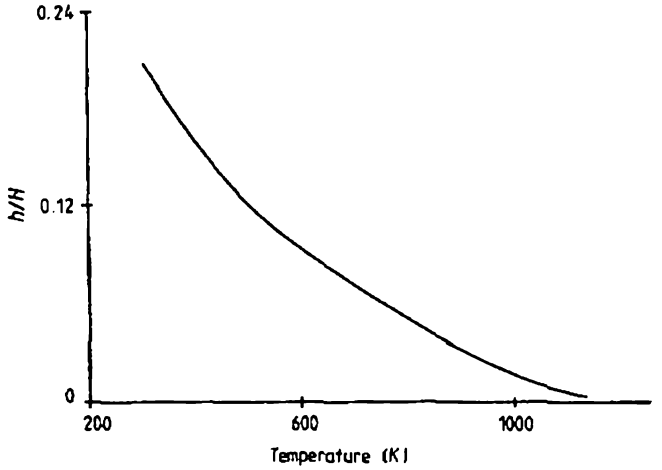

Figure 6.9 : The calibration curve generated showing temperature vs. relative band height reproduced from Sahli *et al.* (1993).

This analysis lead to a calibration curve being generated in which the temperature is a function of the ratio *h/H*. This curve is reproduced in figure 6.9.

Although both these analyses allow the calculation of the rotational temperature, the most striking feature is the general behaviour of the theoretical band structure as the rotational temperature is raised. By comparison of figures 6.7 and 6.8 it can clearly be seen that a local maximum occurs in the first few rotational bands as the temperature is lowered from 5000 K to 800 K. This is even more apparent if we observe figure 6.10 where the theoretical spectra is shown for the temperatures 300 K, 600 K, and 900 K. Observing the recorded spectra and deducing whether a local maxima occurs in this region allows the rotational temperature to be estimated at a glance. If there is a maxima present the rotational temperature is below 900 K and the analysis of Sahli *et al.* (1993) will apply. If the maxima is absent, the temperature can be calculated by the method of Czernichowski (1987).

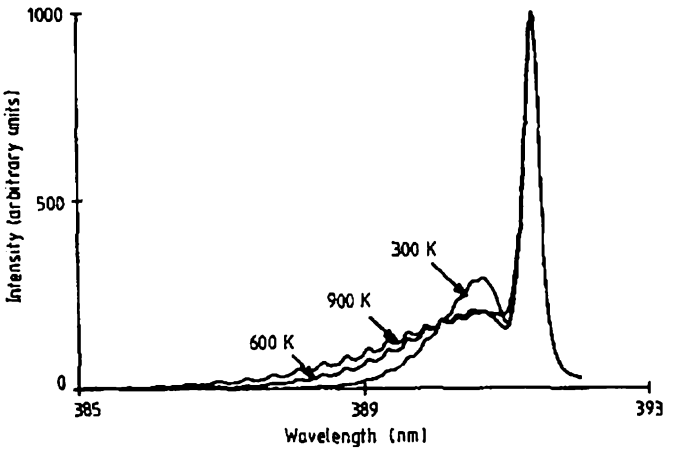

Figure 6.10 : A theoretical plot for three different temperatures (300 K, 600 K, and 900 K) taken from Sahli *et al.* (1993)

6.4 Analysis of the Monochromator Data

6.4.1 Monochromator Calibration

Calibration of the monochromator was achieved for the entire system. A tungsten ribbon lamp and an optical pyrometer were used as the blackbody and its temperature measurement control. Data were recorded using the optical emissions from the ribbon lamp with the monochromator. These could then be used to correct the sensitivity and efficiency of the light recorded from the plasma using the same optical setup. Several ranges of the monochromator settings were recorded to provide

calibration over 12 different settings to allow for most light levels expected for the plasma. These ranges are specified in table 6.3. The procedure was to orientate the monochromator/lamp assembly using a method described in detail in chapter five. The only difference was that the laser spot was aligned to hit the centre of the ribbon in the lamp at the point where the temperature was measured from. The temperature of the lamp was of some concern since a compromise existed between emission and temperature.

Slit Width (Microns)	Photomultiplier Gain Voltage (Volts)			
	600	700	800	900
100	x	x	x	x
200	x	x	x	x
300	x	x	x	x

Table 6.3 : Monochromator settings used for calibration curves from a tungsten ribbon lamp.

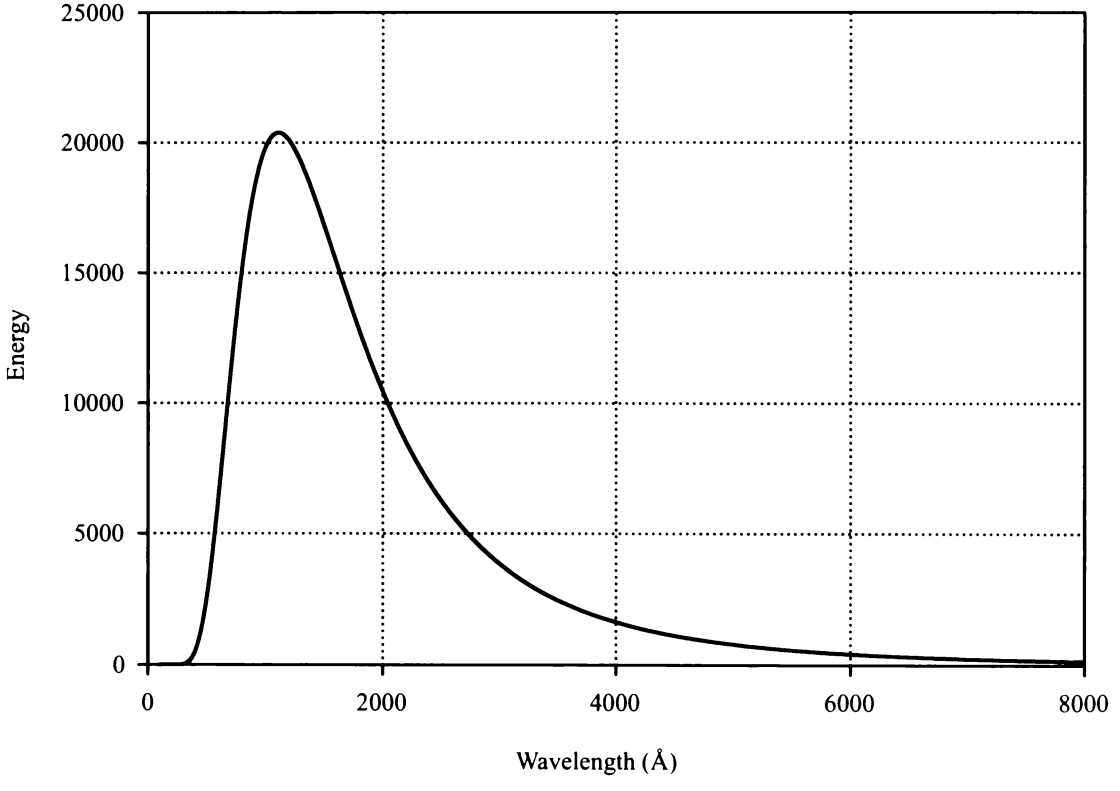

Figure 6.11 : Theoretical radiation emission from a black body at 2600 K.

Too high a temperature raises the evaporation rate of tungsten from the surface of the ribbon. This would coat the inside of the lamp tube and reduce the light penetrating the layer of tungsten now coated on the glass wall. Conversely, too low a temperature would not provide an intense enough photon emission in the wavelength range we were interested resulting in inaccurate calibration data. After analysing data pertaining to these facts (see chapter three, figure 3.3) a temperature of 2600 K was chosen for the lamp. A theoretical blackbody radiation curve at this temperature is shown in figure 6.11.

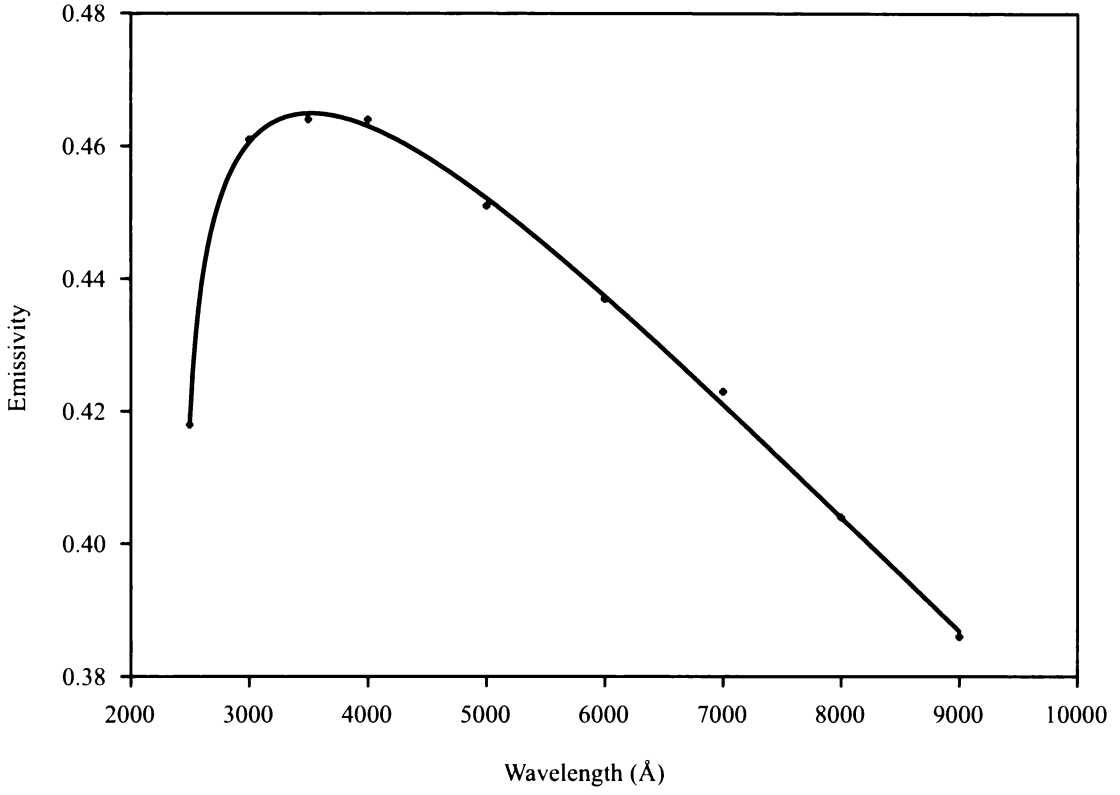

Figure 6.12 : The emissivity of tungsten plotted against wavelength.

Once the raw monochromator data were recorded for the specific ranges in table 6.3, the data needed to be corrected for the emissivity of tungsten at the emission temperature, i.e. 2600 K. Data were taken from the CRC handbook, Weast and Astle (1979). An appropriate fitting curve was used to interpolate this data. The equation for this curve could then be used in a program to correct the raw data in order to provide a series specifying corrected calibration curves of the total sensitivity of the system over a wavelength range of 2000 to 8000 Å. Figure 6.12 shows the emissivity as a function of wavelength, while equation 6.44 shows the equation used to fit this curve. This equation is a four parameter fit devised by Weibull (1951).

$$y = a\left(\frac{c-1}{c}\right)^{\frac{1-c}{c}}\left[\frac{x-x_0}{b}+\left(\frac{c-1}{c}\right)^{1/c}\right]^{c-1} e^{-\left[\frac{x-x_0}{b}+\left(\frac{c-1}{c}\right)^{1/c}\right]\left(c+\frac{c-1}{c}\right)} \quad (6.44)$$

where $a = 0.465$, $b = 19100$, $c = 1.05$, and $x_0 = 3520$.

The appropriate calibration curve was used with plasma monochromator data to correct the raw data. This is a simple process when using LabVIEW. The three sets of calibration curves are plotted in figures 6.13, 6.14 and 6.15 and show only 10% of the data points recorded. The full data set was used for correction of the experimental data. The calibration curves were recorded at a wider than normal slit width to maximise line intensities at the expense of resolution. However in initial monochromator recordings from a N_2 plasma, the resolution loss was small. Particular areas of interest were studied at a higher resolution. Over a narrow wavelength range such as broad lines or band structures the detection efficiency can be assumed to be constant. As noted previously, the generalised theory for line intensity comparison is not useful, and we shall see that even if it were so, there are few lines that can be used for ratio temperature measurements.

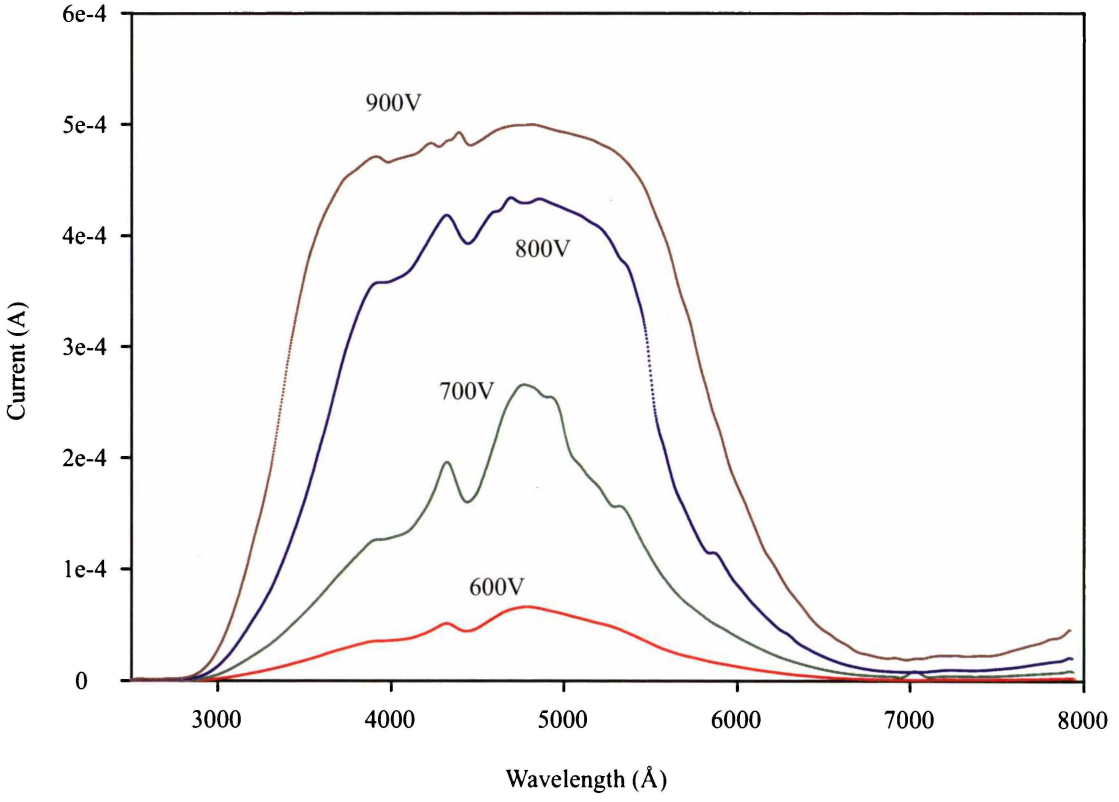

Figure 6.13 : Calibration curves for correcting raw monochromator data for a 100 micron slit width for 4 different accelerating voltages.

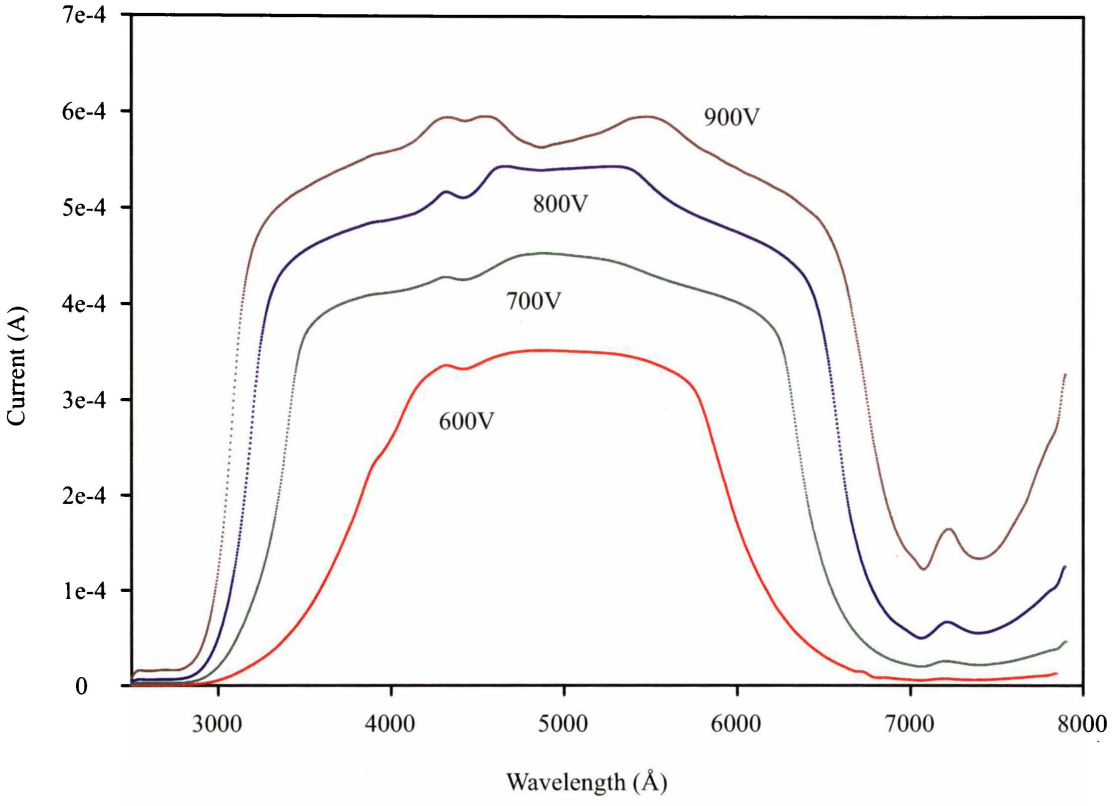

Figure 6.14 : Calibration curves for correcting raw monochromator data for a 200 micron slit width.

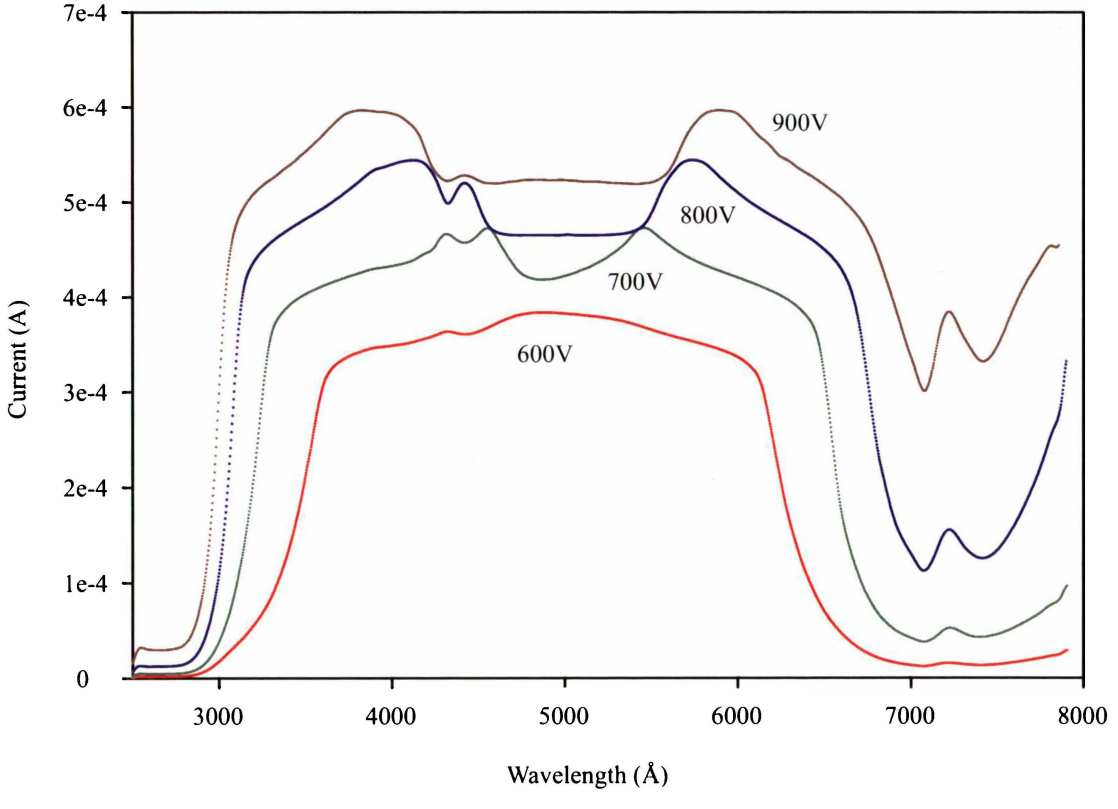

Figure 6.15 : Calibration curves for correcting raw monochromator data for a 300 micron slit width.

6.4.2 Monochromator Analysis

Experimental measurements of the monochromator data were recorded in conjunction with those from the Langmuir probes. The plasma conditions were as consistent as they could be maintained. Although there is little in the way of theory we can apply to the results to obtain spectroscopic temperatures apart from the work of Czernichowski (1987) and Sahli *et al.* (1993), we can determine what ion species were present. This allows us to roughly identify the degree of dissociation for nitrogen molecules if N^+ emission lines can be identified.

6.4.2.1 Band Structure and Identification of Species

Initially we will look at a seemingly simple nitrogen discharge, which in reality is quite complex due to the diatomic nature of the molecule. Figures 6.16 and 6.17 show the raw data and the response-corrected data respectively. Comparing these two scans we see that the minor peaks and anomalies on the raw scan are missing from the response corrected data. This is due to the scaling of the data using the curves plotted in figure 6.13. Some peaks such as that from N^+ may well be scaled out on the response corrected plot, which is why both data sets have been included here. These scans were recorded with the monochromator using a 700 V DC acceleration on the photomultiplier and a 100 micron slit width.

The spectrum is somewhat complex. Most of the peaks and bands originate from one transition, namely the second positive group. This is the transition of the C $^3\Pi_u$ state which decays to the B $^3\Pi_u$ state resulting in the emission of a photon. The variety of lines and band structures originate in the numerous rotational and vibrational levels between which transitions can occur between.

Two other features are present on these scans. These are the presence of the $B^2\Sigma_u^+$ N_2^+ transition at 3911.4 Å and the appearance of part of the first positive group at 6300 Å which is the transition between the B $^3\Pi_g$ and the $A^3\Sigma_u^+$ states. Although this transition is listed as having its 0-0 peak at 10463.5 Å the band at 6300 is the 4-1 transition. Figure 6.18 shows an expanded plot of the raw data from 3000 to 5000 Å with the major band structures identified.

Identification of possible N^+ transitions is more difficult for the following reasons. Firstly, there appears to be little dissociation of the molecule so that the concentration of N^+ will be small. Secondly, by considering the transition probability and spectroscopic wavelength tables, it is evident that most of the N and N^+ transitions occur in regions overlapping the band structures and so will be swamped out of the spectrum by the far more intense and broad N_2^+ transitions. Thirdly, the strong

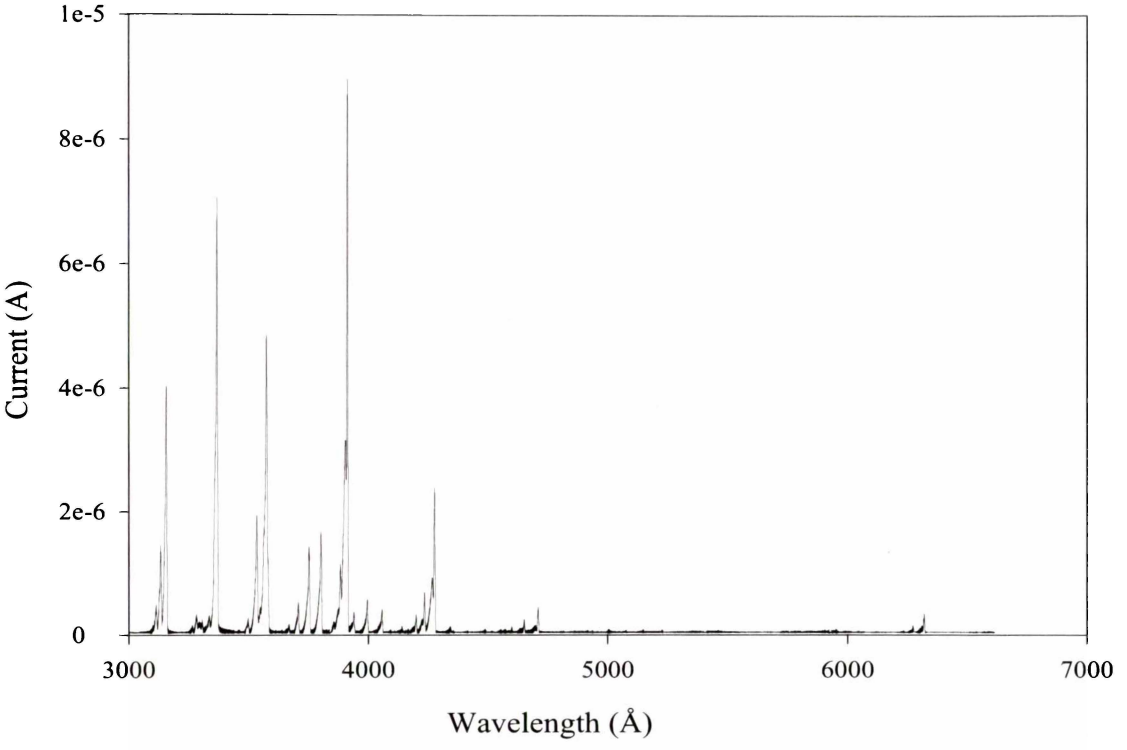

Figure 6.16 : A raw, uncorrected monochromator scan of a nitrogen discharge covering the detectable range of the photomultiplier and the instrument.

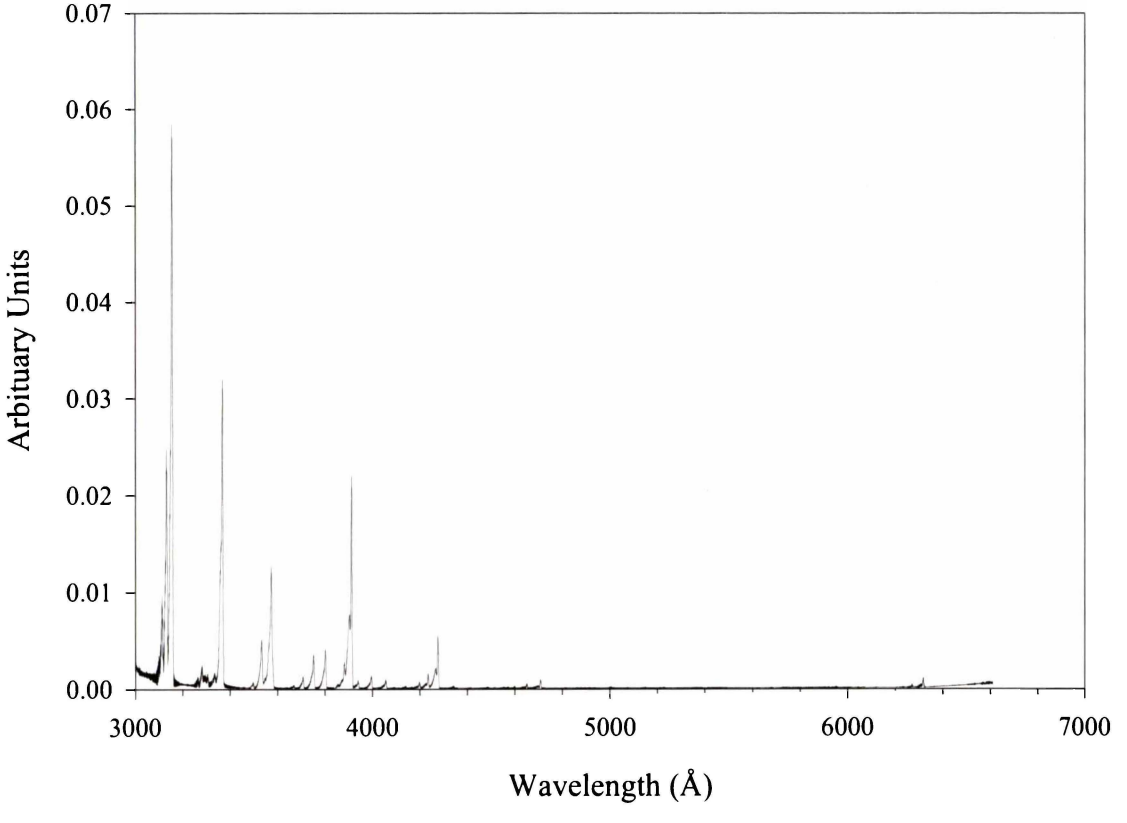

Figure 6.17 : A response corrected scan of figure 6.16 using the curves shown in figures 6.13 to 6.15.

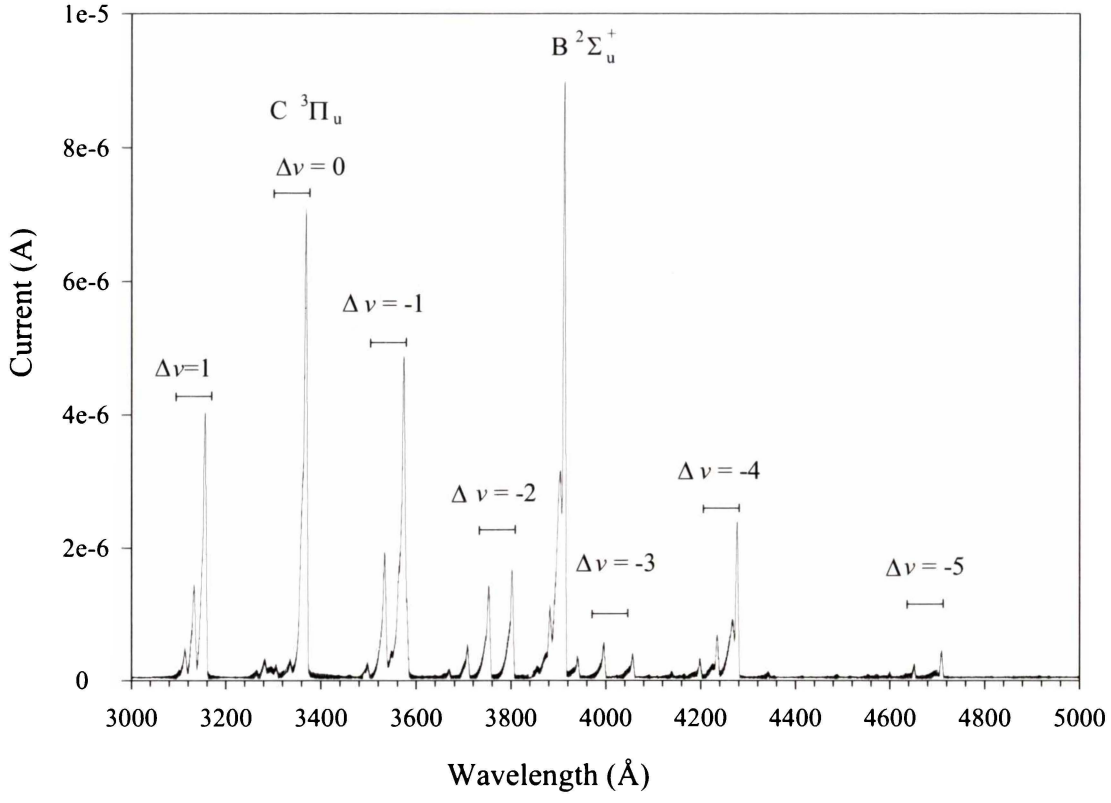

Figure 6.18 : Identified bands of the N_2 spectra. All band formations unless denoted by the transition belong to the C $^3\Pi_u$ state.

transitions, i.e. those with high transition probabilities, all occur in the ultra-violet with wavelengths ranging from 400 to 1400 Å for both N^+ and N.

In looking for emissions from these atomic atoms and ions, there are a few faintly detected "peaks" that could possibly be attributed to them. There is no certainty however, and we must therefore conclude that there is no appreciable dissociation of molecules in the plasma. This solves two problems. Firstly the probe data distributions and electron temperatures are effectively coming from one ion species, N_2^+, and as such density anomalies and dual temperature electron distributions are the result of the plasma generation method and interaction of the plasma particles. Secondly, there may also be little or negligible dissociation of carbon monoxide atoms, since the triple bond strength is almost identical to nitrogen. This last statement is very important in the context of coating experiments since impurities such as carbon and oxygen are unlikely be incorporated into the growing film if they do not exist in the plasma as atomic species.

6.4.2.2 Temperature Measurements

Before analysis of the data is presented, we considered the effect the slit width and the photomultiplier accelerating voltage had on the recorded spectrum. Figures

6.19 and 6.20 show spectra for slit widths and accelerating voltages of 100 μm, 700 V and 50 μm and 800 V respectively while the plasma discharge conditions remained constant with 200 V DC drawing an 0.5 A current. This low discharge regime was chosen to distinguish the two competing effects of resolution and light intensity.

These two spectra show clearly the effects of reducing the slit width. For the 50 μm slit, some of the peaks that are clearly visible with a 100 μm slit are barely distinguishable from the background noise level. However, to apply the results of Czernichowski (1987) a resolution provided by a slit of 50 μm or smaller was needed to approach the fitting constants he provides. The expanded portion of the $B^2\Sigma_u^+ - X^2\Sigma_g^+$ transition is shown in figures 6.21 and 6.22 for the 100 μm and 50 μm slit respectively.

For the highest resolution spectra in figure 6.22, resolution of the rotational levels occur which is absent when using a 100 μm slit. Even for this case, the value of W_8 is 6.3 cm^{-1} just outside the validity range. Furthermore it can be seen from direct observation that figures 6.21 and 6.22 have a maxima in the band region and more closely resemble the 300 K theoretical plot shown in figure 6.10 than figure 6.7 for a 5000 K temperature. Nevertheless using the analysis of Czernichowski (1987), the temperature from figure 6.22 is ~ 2400 K.

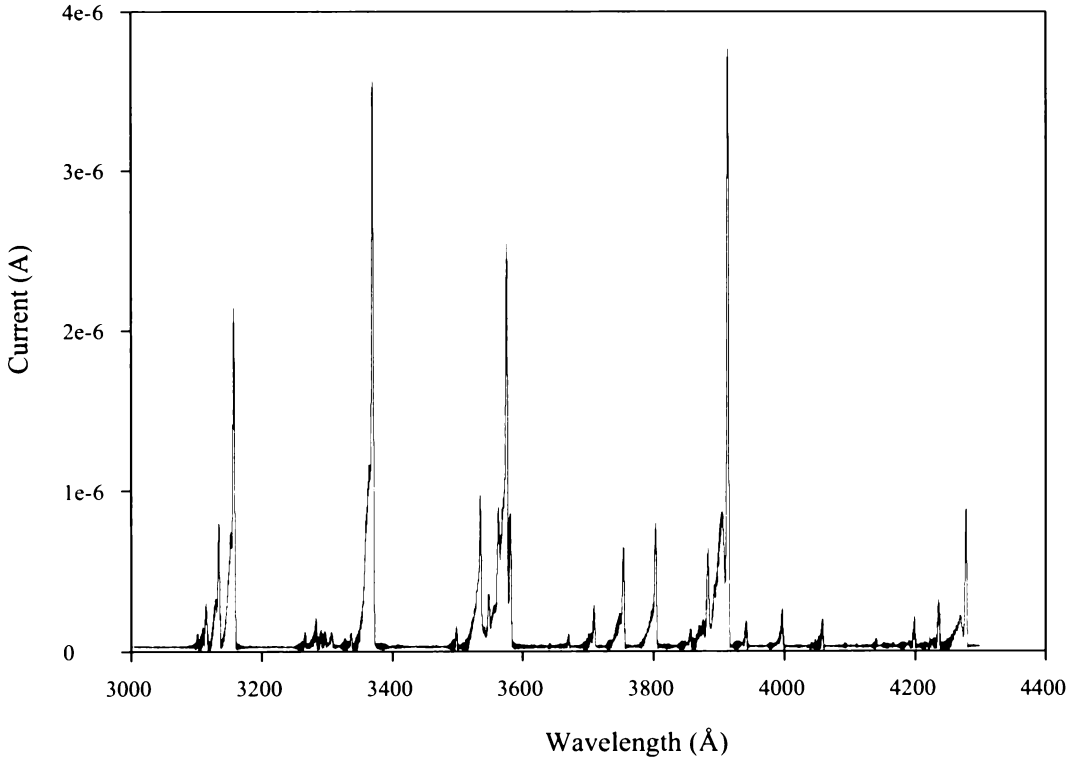

Figure 6.19 : The recorded spectrum for a 200 V, 0.5 A discharge where the slit width was 100 μm and the photomultiplier voltage gain was 700 V.

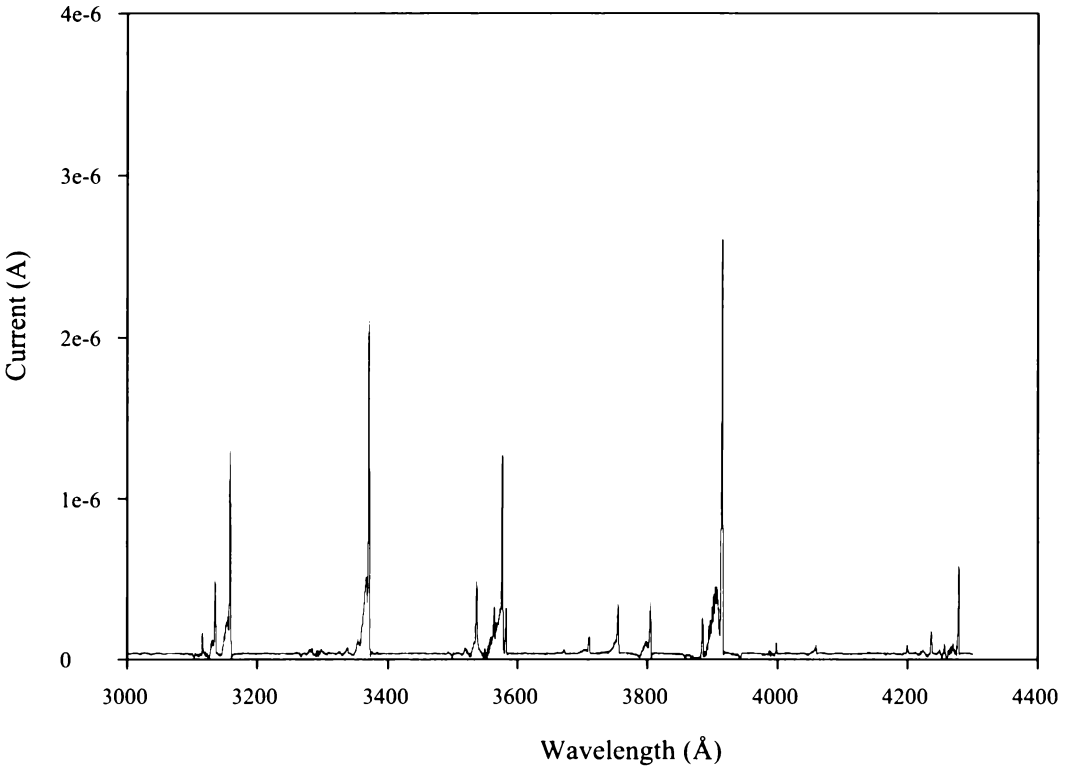

Figure 6.20 : The recorded spectrum for a 200 V, 0.5 A discharge where the slit width was 50 μm and the photomultiplier voltage gain was 800 V.

Analysing the same spectra with the method of Sahli *et al.* (1993), we find that the experimental *h/H* ratio for our data is ~ 0.34 which from the calibration plot in figure 6.9, by extrapolation, leads us to the conclusion that the temperature is below 200 K. This temperature is clearly wrong since it is at least 100 K below room temperature. Investigating this anomaly it can be seen that the calibration curve presented by Sahli *et al* (1993) appears to be incorrect. If we calculate the *h/H* ratio for the 300 K theoretical plot reproduced in figure 6.10 we obtain a ratio of 0.4 which is clearly at odds with the predicted temperature from the calibration plot. Re-examining figure 6.10, the theoretical plot generated from Sahli *et al.* (1993) for a rotational temperature of 800 K we find the ratio is 0.27 which is below our experimental value of 0.34. It is thus estimated that our experimental temperature is in the range of 400 K - 500 K. This rotational temperature is taken to be the correct value deeming the temperature obtained from the analysis of Czernichowski (1987) incorrect.

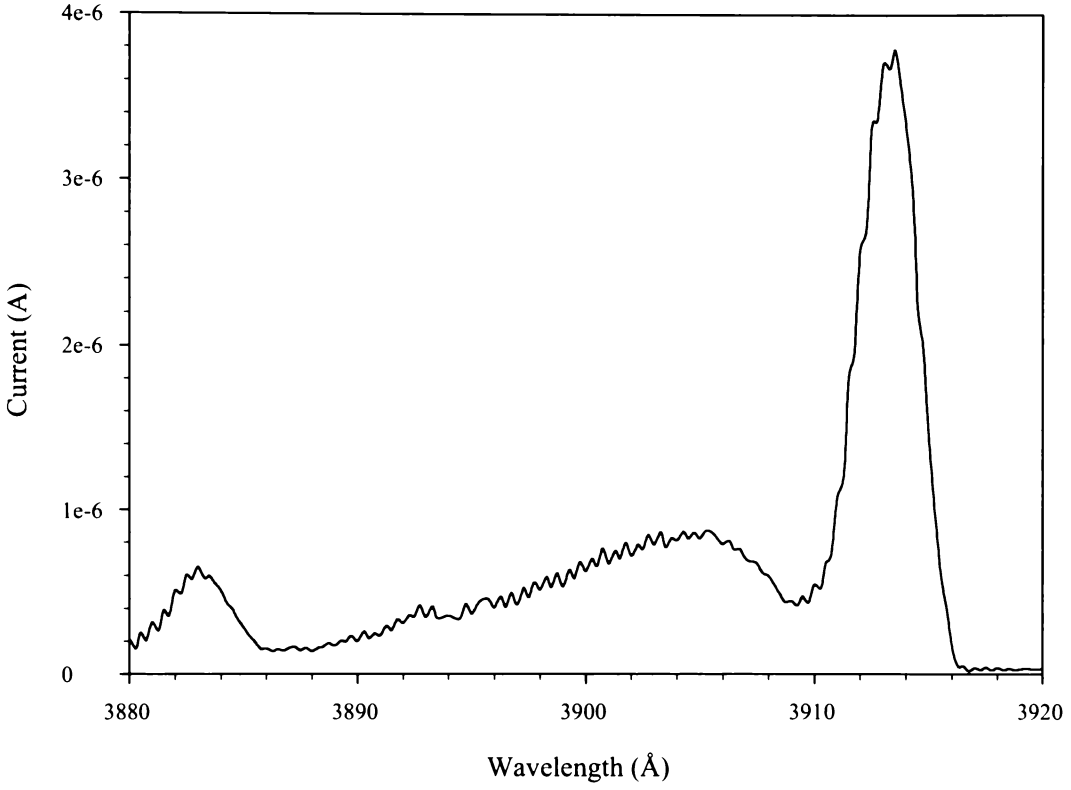

Figure 6.21 : The $B^2\Sigma_u^+ - X^2\Sigma_g^+$ transition for a 100 μm slit and a 700 V photomultiplier voltage when the plasma discharge conditions were 200 V and 0.5 A.

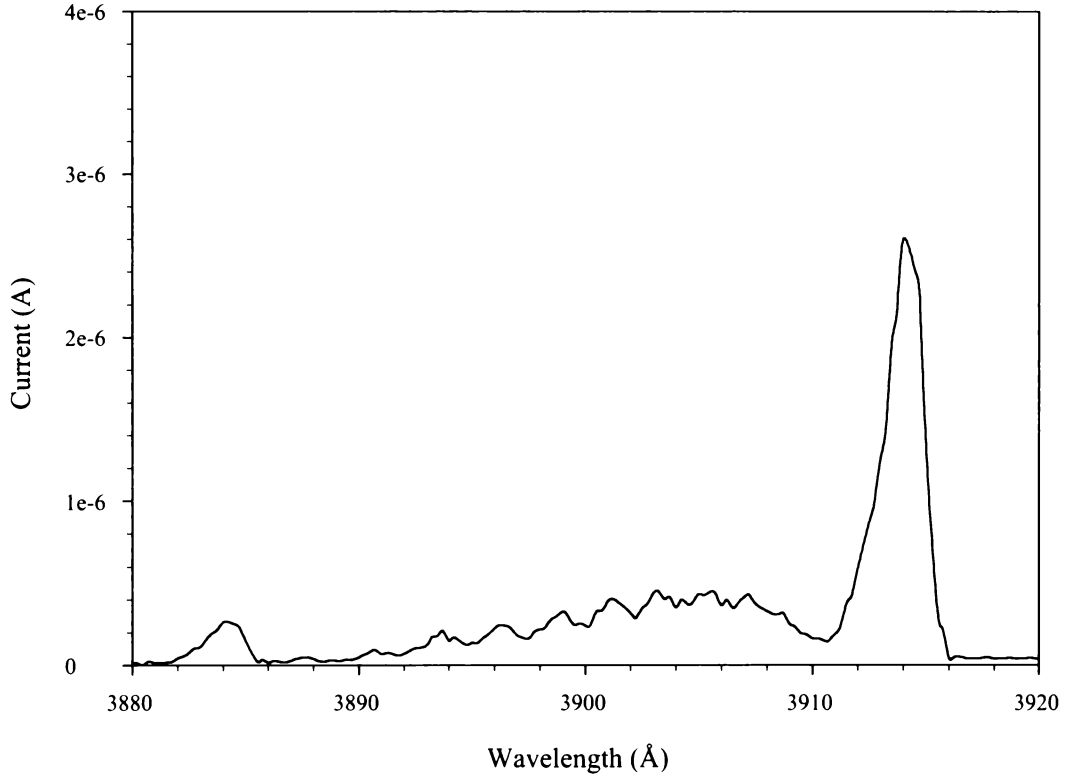

Figure 6.22 : The $B^2\Sigma_u^+ - X^2\Sigma_g^+$ transition for a 50 μm slit and a 800 V photomultiplier voltage when the plasma discharge conditions were 200 V and 0.5 A.

The full range of $B^2\Sigma_u^+ - X^2\Sigma_g^+$ transitions for the 0.5 A to 3.0 A range (using the operating conditions in section 5.5) for accelerating voltages of 200 V and 300 V respectively are shown in figures 6.23 and 6.24 respectively. From these figures we can see that although the band head intensity rises with an increasing plasma current, so do the rotational intensities.

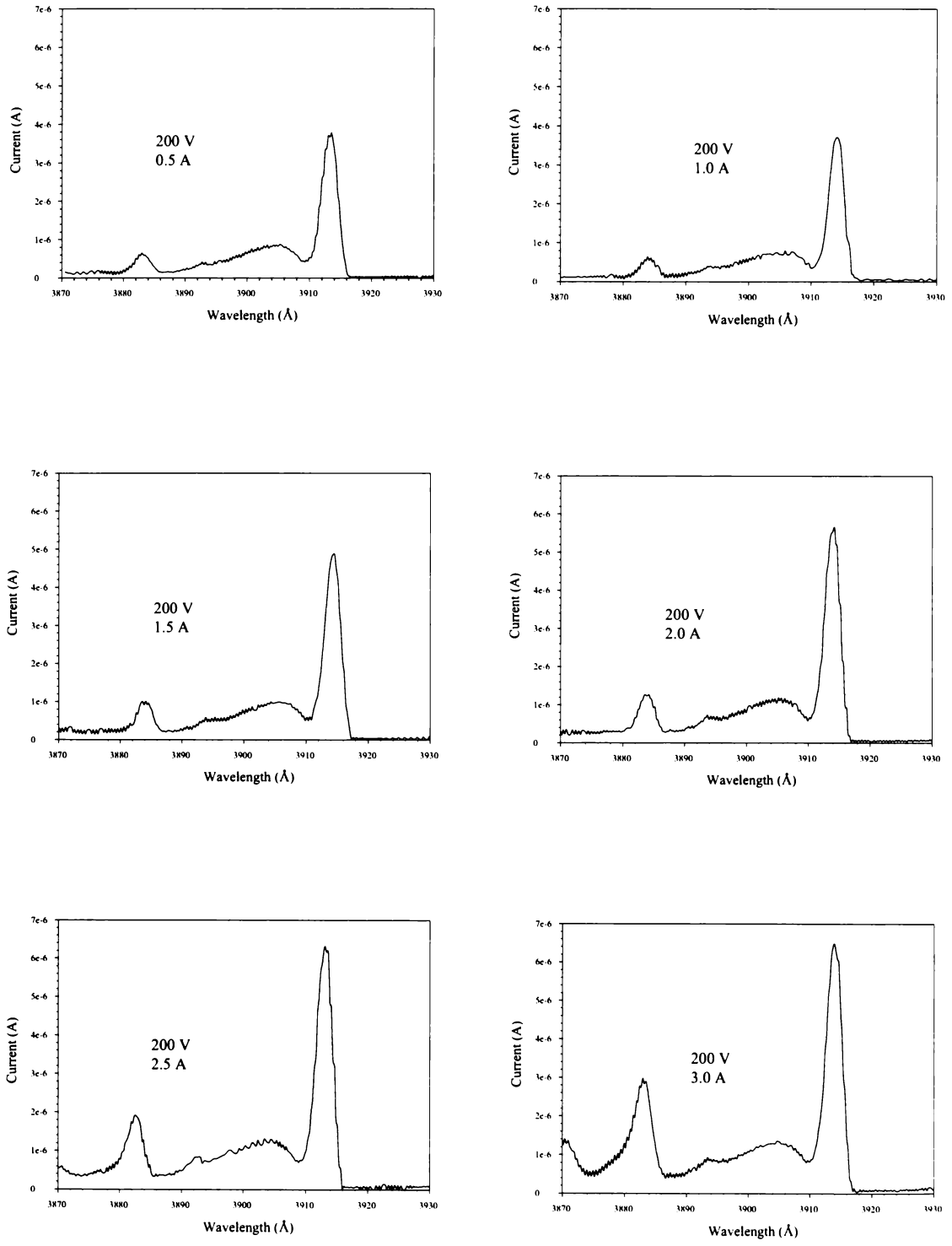

Figure 6.23 : The $B^2\Sigma_u^+ - X^2\Sigma_g^+$ transition for a 100 μm slit and a 700 V for a 200 V DC discharge.

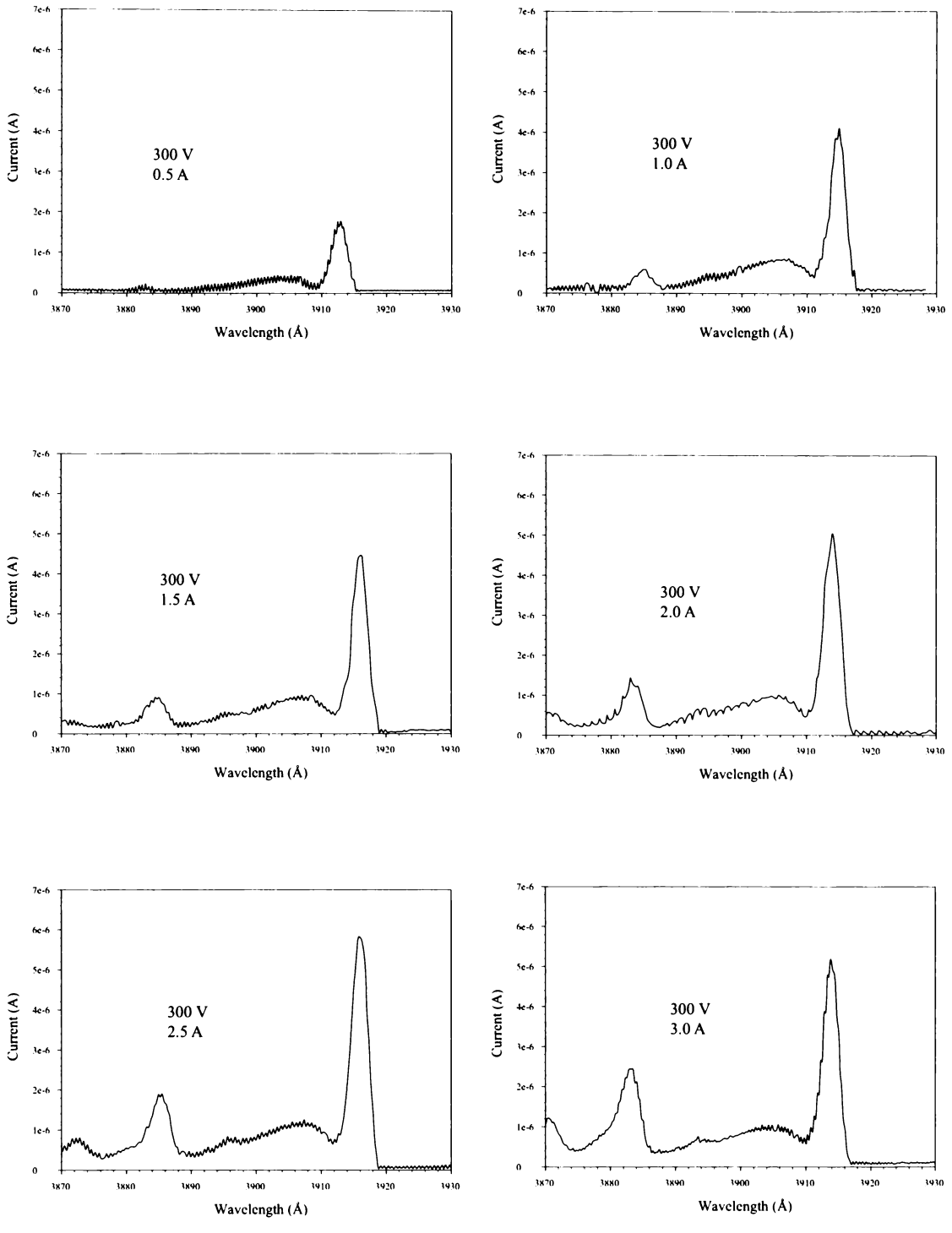

Figure 6.24 : The $B^2\Sigma_u^+ - X^2\Sigma_g^+$ transition for a 100 μm slit and a 700 V for a 300 V DC discharge.

The relative ratios of the band head to the rotational levels, from analysis of figures 6.23 and 6.24 remains relatively constant with *h/H* ratios between 0.29 and 0.34. The temperatures are thus somewhere between 400 K and 600 K. It can be observed that there is a slight dependence of the temperature on the discharge current for each discharge voltage. It can also be deduced from these figures that there appears to be no temperature dependence on the applied DC voltage across the plasma since the ratios

of the same plasma current with differing applied voltages are within the measurement error.

It is interesting to note the development of the 1-1 band head at approximately 3884 Å as the discharge current is raised. The 1^{st} order vibrational band becomes increasing populated with respect to the 0^{th} order band head as a relative intensity ratio. Whether this becomes the preferred ionisation mechanism from the 0^{th} order ground state, or it represents ionisation from the 1^{st} order ground state, (presumably from excited states that have decayed to excited neutral states and are re-excited) is unknown.

6.5 Discussion

Although the above analysis appears to have eliminated all available standard theoretical spectroscopic methods of plasma measurement from the present study, the experimental spectroscopic data obtained here did prove useful. The spectroscopic study did provide direct observation of excited states and allowed some estimates to be made of their relative concentrations, such as the absence of atomic nitrogen. These observations were a valuable tool in determining the most suitable pressure and power combinations upon which to concentrate the experimental work.

Rotational temperatures were able to be obtained that indicate the excited species have a temperature slightly above room temperature. It should be noted however, that since there is no equilibria linking the states, as previously discussed, these temperature measurements can only be assumed to be correct for this particular transition, or excited state. Having noted this, it is not expected that other species will have a temperature well above the ambient gas temperature and hence the general approximation that the plasma gas can be considered to be at room temperature appears to be valid.

6.6 References

Alonso, M., and E. F. Finn, 1968, *Fundamental University Physics* III : *Quantum and Statistical Physics*, (Addison-Wesley Publishing, New York).

Angstadt, A. D, J. Whelan, and K. R. Hess, 1993, Microchem. J., **47**, p 206.

Behringer, K., and U. Fantz, 1994, J. Phys. D: Appl. Phys., **27,** p 2128.

Chelouah, A., E. Marode, and G. Hartmann, 1994A, J. Phys. D: Appl. Phys., **27**, p 770.

Chelouah, A., E. Marode, G. Hartmann, and S. Achat, 1994B, J. Phys. D: Appl. Phys., **27**, p 940.

Cox, T. I., and V. G. I. Deshmukh, D. A. Hope, A. J. Hydes, N. St.J. Braithwaite, and N. M. P. Benjamin, 1987, J. Phys. D: Appl. Phys., **20** p 820.

Czernichowski, A., 1987, J.Appl. Phys., **20**, p 559.

Desai, T. M., S. V. Gogawale, A. B. Shukla, N. K. Joshi, U. S. Salgaonkar, and G. L. Bale, 1994, Vacuum, **36**, 3, p 223.

Fancey, K.S., and A. Matthews, 1991, Vacuum, **42**, 15, p1013.

Felts, J., and E. Lopata, 1988, J. Vac. Sci. Technol. A, **6**, 3, p 2051.

Griem, H. R., 1964, *Plasma Spectroscopy*, (McGraw-Hill, London).

Goyette, A. N., J. R. Peck, Y. Matsuda, L. W. Anderson, and J. E. Lawler, 1998, J. Phys. D: Appl. Phys., **31**. p 1556.

Hope, D. A. O., T. I. Cox, and V. G. I. Deshmukh, 1987, Vacuum, **37**, 3/4, p 275.

Herzberg, G., 1950, *Molecular Structure and Molecular Spectra* I : *Spectra of Diatomic Molecules*, (Van Nostrand Reinhold, New York).

Hopkins, M. B., 1995, J. Res. Natl. Inst. Stand. Technol., **100**, p 415.

Lochte-Holtogreven, W., 1968, *Plasma Diagnostics*, edited by W. Lochte-Holtgreven, (North Holland Publishing Company, Amsterdam).

McWhirter, R. W. P., 1965, in *Plasma Diagnostic Techniques*, edited by R. H. Huddlestone, and S. L. Leonard, (Academic Press, New York), Ch 5, p. 201.

Popa, S. D., 1996, J. Phys. D: Appl. Phys., **29**, p 411.

Sahli, K., L. Hochard, and A. M. Pointu, Meas. Sci. Technol., 1993, **4**, p 685.

Shatas, A. A., Y. Z. Hu, and E. A. Irene, 1992, J. Vac. Sci. Technol. A, **10**, 5, p 3119.

Von Engel, A., 1965, *Ionized Gases* (Clarendon, Oxford, England).

Weast, R. C., and M. J. Astle, 1979, Eds., *CRC Handbook of Chemistry and Physics,* (59^{th} edition, CRC, Boca Raton, Florida).

Weibull, W., J. Appl. Mech., 1951, **18**, p 293.

Chapter 7 Langmuir Probe Analysis

7.1 Introduction

This chapter deals with the Langmuir probe results of the experiments in nitrogen as well as deposition experiments. Before the coating experiments started, a full characterisation of nitrogen and argon plasmas was to be completed to find the best operating conditions for both. It was discovered that argon was very hard to initiate as a plasma and produced poor results in terms of density and temperature in relation to the power input. The nitrogen plasma did however, readily produce a stable discharge which was suitable for analysis. Since the carbonyl easily dissociates to produce carbon monoxide, which from chapter three is as close to nitrogen as one can expect from a molecule containing two different atoms, it was expected to behave like nitrogen but unlike argon. For this reason no preliminary pure argon plasmas have been analysed but we did find that the nitrogen/argon-carbonyl mixed plasma responded like its nitrogen counterpart for Langmuir probe analyses. Spectroscopic evidence for this will be presented in chapter eight.

Results of the initial experiments, from the calibration and analysis of the Langmuir probes will be discussed in this chapter. All experiments were conducted by recording single and double probe data as well as a monochromator scan from 3000 to 6000 Å. A full analysis of the probe data using the theories detailed in chapter four was completed to determine the plasma electron temperature and density with the best possible accuracy.

The monochromator data from the wavelength scans of spectral emissions from the plasma were beneficial even though full spectroscopic theory could not be readily applied. These data, discussed in chapter six, enabled the identification and confirmation of emission lines from various atoms and molecules and indicated which ionised species were present. This was the only method of determining if molecular dissociation had occurred and for investigating ionisation of such atoms. The absence of ions with differing masses is a basic assumption of the Langmuir probe ion collection theories.

7.2 Langmuir Probe Calibration

Since the automated Langmuir probe electronics has a gain switching system built into it, shown in figures 5.8 and 5.9, it was necessary to make sure each gain setting matched with the beginning and end points of the other gain settings. This was to avoid overlap of gain regions and to leave no gaps in the current levels measured. For each gain setting, the exact current generated in the gain resistors was obtained by reading the voltage generated across these resistors, and these data are sent back into the data acquisition system.

Initially appropriate resistors were placed into the main circuit board with approximately the correct values for recording the current ranges we wanted. The resistor positions in the circuit are shown in figure 5.9. The nominated values used were 1 MΩ, 100 kΩ, 10 kΩ, 1 kΩ, and 100 Ω. The system was designed so that the 1 MΩ resistor was always in the circuit, and then the other four resistors were switched in and out of parallel with this resistor allowing for the gain change to occur. In practice the actual resistance values mattered little since each resistor was accompanied by a second variable pot resistor which was used to adjust the measured resistance for the current at each gain setting. The resistance of each of the resistor pairs was measured using an impedance meter for accuracy and then the data acquisition system was run. Calibration of each gain level was achieved by adjusting the recorded data level so that it precisely matched the experimental current flowing through a meter in the simulated probe circuit. These external probe simulation resistors were 10 MΩ, 1 MΩ, 100 kΩ, 10 kΩ and 1 kΩ. Values an order of magnitude higher than the gain setting resistors were chosen due to the factor of 10 scaling of the output voltage from the data acquisition card (±70 V output, ±10 V input). The resistance values of these test resistors were then checked by plotting the voltage-current data on a linear graph and taking the slope of the resulting line.

Adjustment of the gain resistance values was necessary to bring the total resistance values recorded from the test resistors into agreement with their actual values. Furthermore, it was necessary to match the upper and lower limits of each gain setting with the range of the higher and lower gain settings immediately adjacent to it. This was entirely possible with this system and the values ultimately recorded matched very closely, in fact they all matched to the fourth significant figure resulting in errors of less than 0.1% for the current calibration while the gain endpoint matching was exact. The use of the transimpedance amplifier allowed both calibration adjustments to be made with little effort, and allowed the full system to be calibrated, including the effects of contact resistance. Tests on the overlap of the gain settings were achieved by applying the voltage output from the data acquisition system through a 5.65 kΩ resistor in series with a diode. Since diodes have a large and

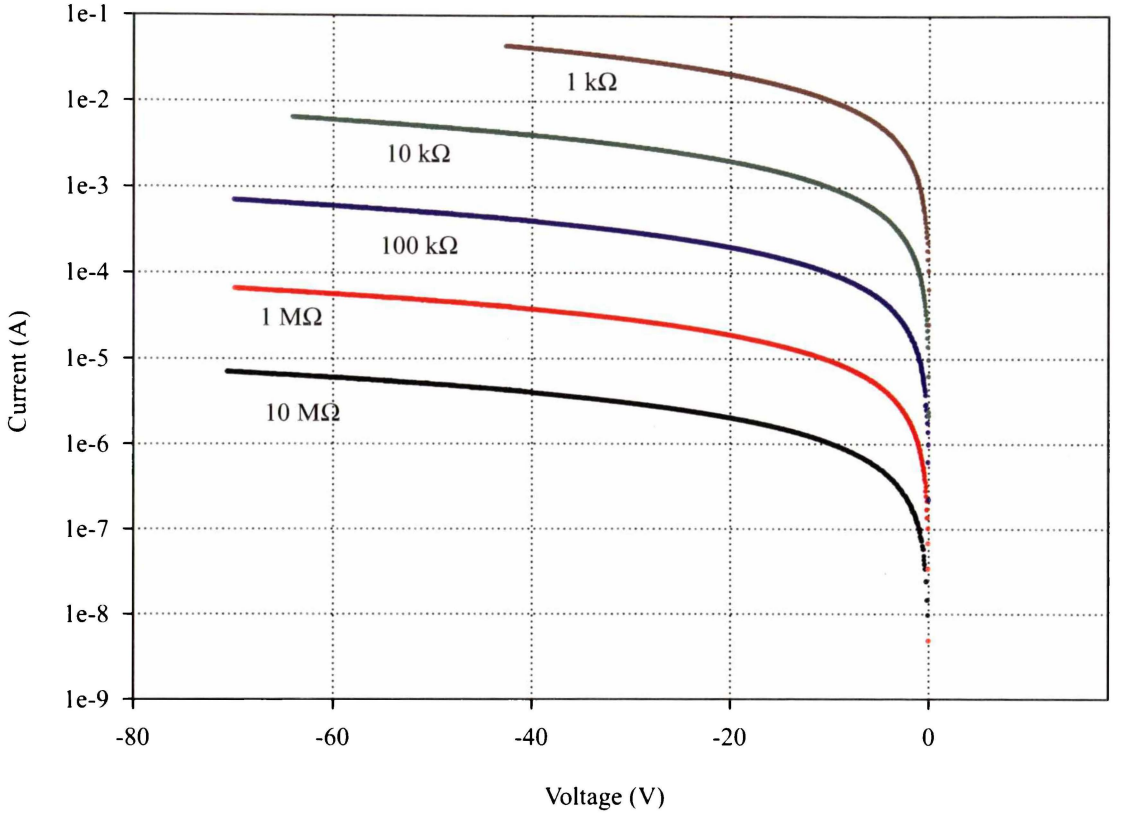

Figure 7.1 : A graph of resistance values showing the current ranges of each.

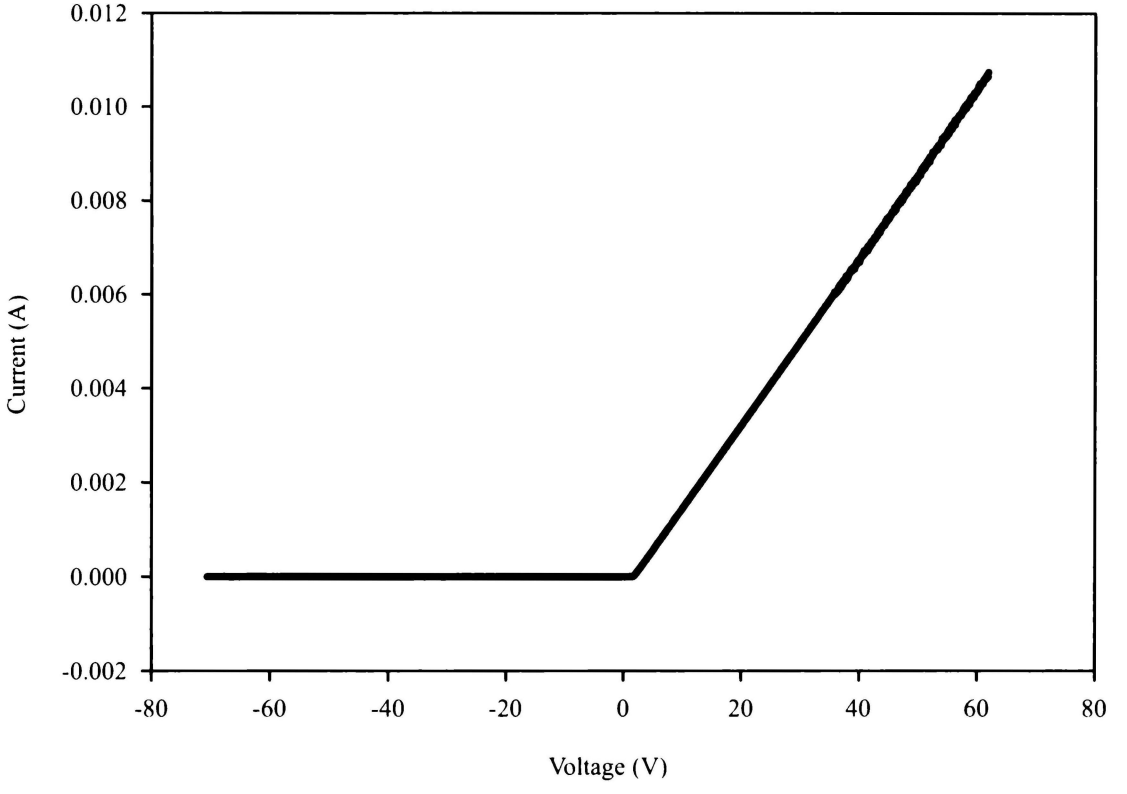

Figure 7.2 : A graph of the current through a resistor-diode combination from +60 V to -70 V.

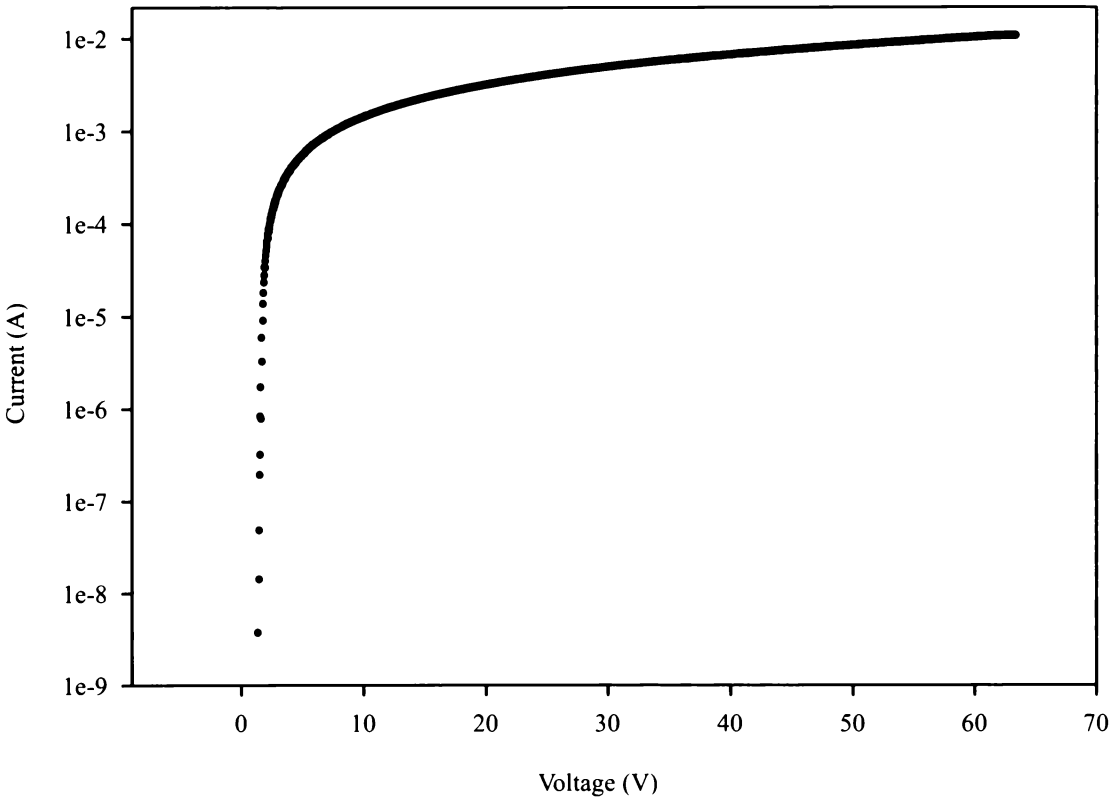

Figure 7.3 : A replot of figure 7.2 using a y-axis log scale highlighting the full current range of the gain switching system to record current and voltage simultaneously.

non-linear current range as the applied voltage is varied from the reverse to forward directions this allowed a good test of the gain system.

Graphs of the calibration data are presented in figures 7.1, 7.2 and 7.3. Figure 7.1 shows the current through all the test resistance values plotted on the same axis, while figure 7.2 shows the current flowing through a resistor-diode combination. Figure 7.3 plots the current through the diode test system on a log scale showing the current range possible using the gain switching system.

7.3 Initial Experiments

The experiments reported here were conducted after all modifications to the power supplies described in chapter five were completed. Earlier experiments before and during modifications show fewer features and are of less interest than later experiments because of the lower densities and electron temperatures recorded in the plasma. Both Langmuir probe and spectroscopic data were recorded in these experiments, to allow the general order of magnitude of the plasma parameters and the types of excited species to be determined. It will be seminal and instructive to

follow the full analysis of the recorded data, as it highlights the importance of the properties of the data acquisition systems.

For each experiment, a number of single and double probe scans were taken at varying resolutions. It was found that at least 1024 samples needed to be recorded to give a sufficient resolution around the knee region in order for numerical differentiation to provide useful analysis. Monochromator data were also recorded for each experiment over a 3000 - 6500 Å range.

These experiments were conducted in a nitrogen plasma at approximately 1×10^{-2} mbar over two discharge potentials (200 and 300 V) and six current ranges (0.5 – 3.0 A in 0.5 A steps) to categorise the plasma over power levels from 100 to 900 W. As with all experiments there is some uncertainty in the pressure. This is because the AC power input feeding the filaments generates substantial amounts of heat and causes the plasma chamber temperature to rise, even with two independent forms of water cooling, thus raising the average gas temperature in the chamber.

7.3.1 Single Probes

A typical single probe characteristic with its first and second derivative is shown in figure 7.4. The derivatives are the preferential method of determining the space potential of the plasma. The alternative, less accurate method, is extrapolation of the knee region shown in figure 4.2. Figure 7.5 shows a semilog plot of the current data in figure 7.4 allowing calculation of the electron temperature from the slope of the curve. Care must be taken when generating these graphs to ensure that the ion current is subtracted properly from the electron current. Minor variations in ion current can lead to large changes in the log plot due to the sensitivity of the high energy electron tail to the subtraction process. The ion current subtracted for this plot was the value found by extrapolation at the intersection of the knee in the I-V characteristic on the x axis. This occurred at 9.1 V. The knee was taken to be at the voltage where the second derivative crosses the x axis. This is standard practice for single probes, but it is more open to interpretation for double probe analysis. A discussion and detailed analysis of these problems is discussed later in this chapter.

Using this semilog plot method, we find from figure 7.5 that we have a two temperature electron distribution, i.e. there are two distinct electron distribution functions each with its own characteristic temperature. These values are 0.63 eV and 1.83 eV. If we substitute these temperatures back into the standard Langmuir equation (equation 4.9) and taking the electron saturation current to be 1×10^{-2} A we get values for the densities of 6.52×10^{10} cm^{-3} and 3.83×10^{10} cm^{-3} for 0.63 and 1.83 eV temperatures respectively.. From the analysis of probe theories (equations 4.6,

4.9, and 4.39). used in chapter five to estimate the voltage and current parameters used for the design automated Langmuir probe circuitry these density values are approximately the order of magnitude expected although the electron temperatures seem a little low.

Figure 7.6 shows the electron energy probability function (EEPF) (the slope of which gives the electron temperature) while figure 7.7 displays the electron energy distribution function (EEDF) in comparison to a Maxwellian distribution. The Maxwellian distribution is matched for the peak placement on the experimental plot. This figure shows marked deviation from the theory which signifies that the plasma is far away from thermodynamic equilibrium. The lack of a high energy tail implies that all electrons within this energy range lose their energy almost immediately in collisional processes with the particles present in the plasma. The integral of the area under the experimental EEDF gives an electron density of 4.30×10^{10} cm^{-3} which is a better agreement than expected since the theory is derived for a Maxwellian distribution.

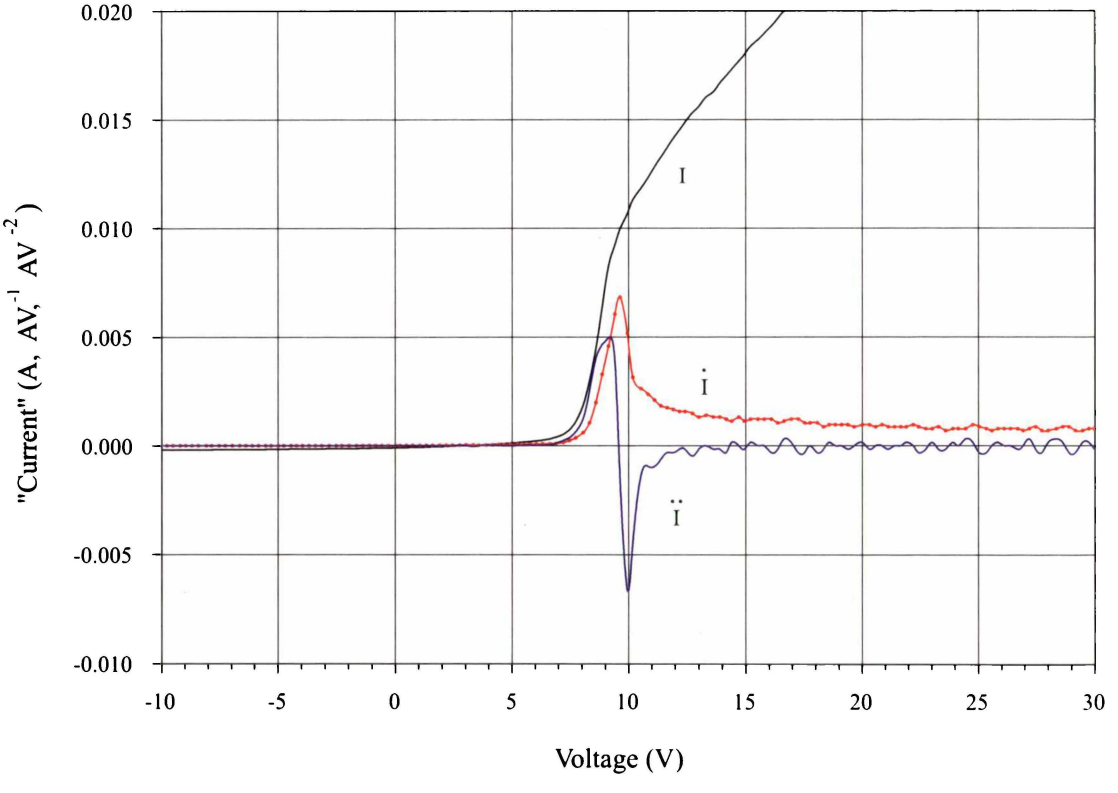

Figure 7.4 : A plot of a single Langmuir probe characteristic with its first and second differentials. The black line is the raw probe data, the red line is the first differential, while the blue line is the second differential. These data were recorded in a N_2 plasma at a pressure of 5×10^{-3} mbar.

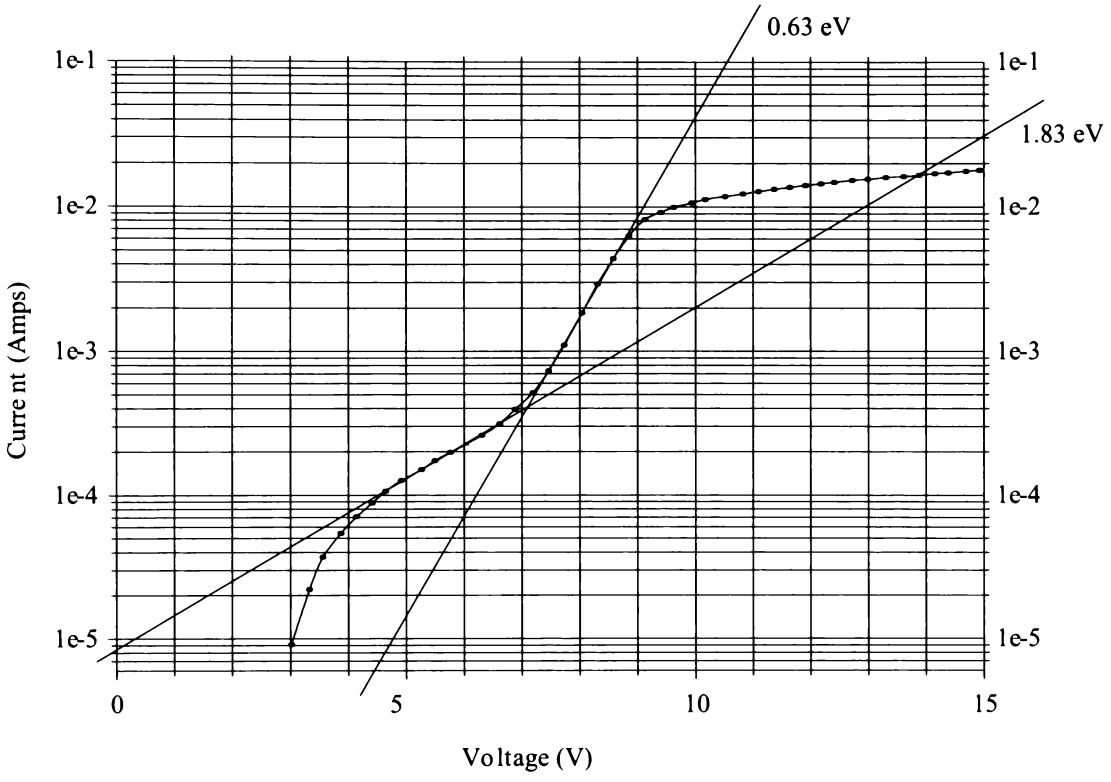

Figure 7.5 : A log plot of the I-V characteristic shown in figure 7.4 showing two groups of electrons with different temperatures.

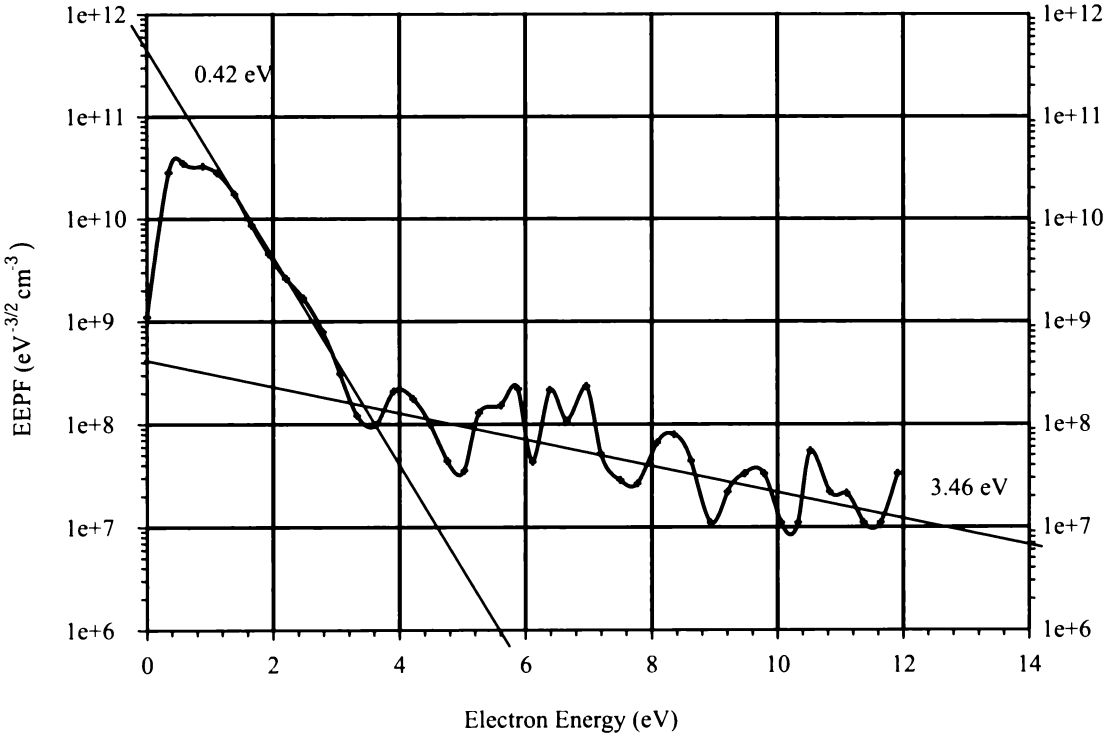

Figure 7.6 : The electron energy probability function (EEPF) showing a two temperature distribution.

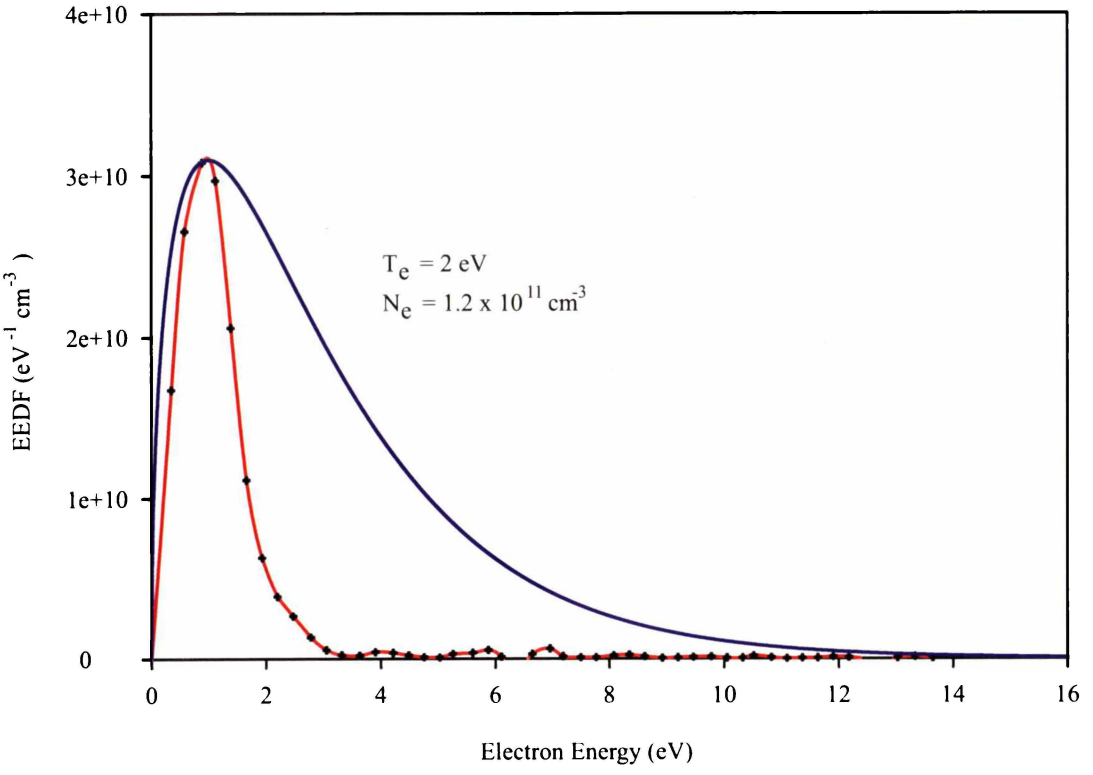

Figure 7.7 : The electron energy distribution function (EEDF) with a theoretical curve plotted to match the peak height of the experimental data.

When calculating the derivatives of the I-V characteristic one problem becomes apparent. This is the issue of how smooth and uniform the recorded I-V characteristic has to be. Some authors have used averaging techniques, smoothing polynomials, and various other numerical methods to try to manipulate such data to a more amenable form. As with the ion current subtraction, this procedure needs to be employed with great care since small changes intended to smooth the data can result in large changes to the high energy tail. However, the electron temperatures (0.42 and 3.46 eV) and the density obtained by this method seem to be in agreement with the logarithmic method. As noted in the chapter on Langmuir probes, any method requiring the calculation of the second derivative has a potential for error.

If we calculate the Debye length from these densities and temperatures we find that it is the same order of magnitude as the probe radius. This implies that we are on the boundary of the transition between space charge limited and orbital motion limited theories. In OML theory (equation 4.39) the square of the electron (or ion) saturation current plotted against the applied voltage yields a straight line The density and temperature can be obtained from the slope and the intercept of this plot. This method

is also valid for the ion saturation regime. This experimental data plot for the electron saturation current is shown in figure 7.8.

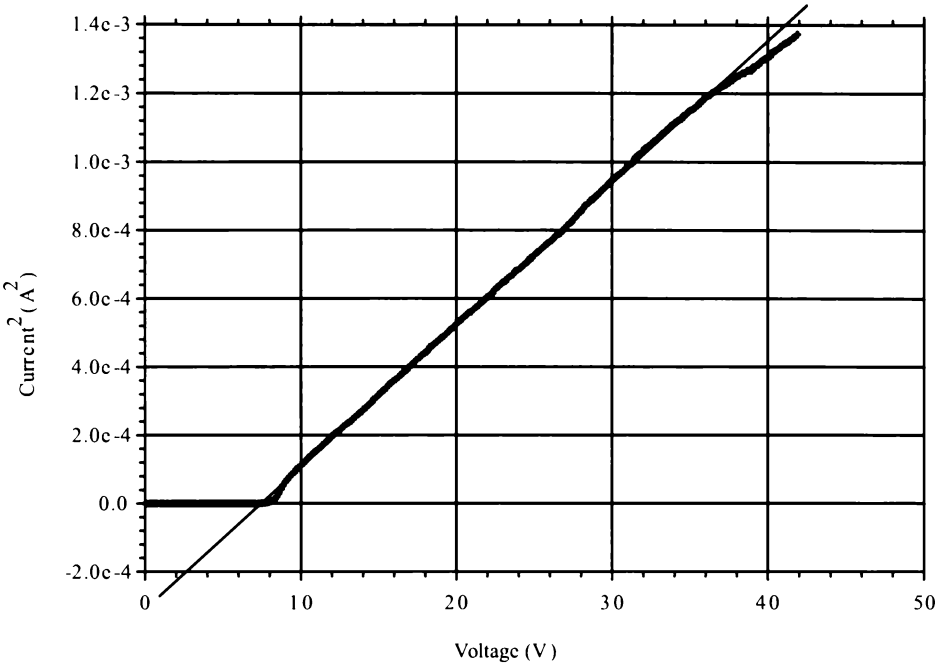

Figure 7.8 : A plot of the square of the current against voltage. In effect an I^2 - V characteristic. The data used are the same as figure 7.4.

From figure 7.8 we find a slope of 4.10×10^{-5} and an intercept of 7.5 V. This yields an electron temperature of 3 eV and an electron density of 3.52×10^{10} cm^{-3}. As noted in chapter four, the density and temperature are obtained independently of one another and thus errors are not carried through from one value to another as they are in the standard Langmuir theory, i.e. to obtain the density from the standard Langmuir theory, the electron temperature needs to be known and thus the errors in the temperature measurement add to the errors in determining the density.

Overall, the calculations from the different theories for temperature and density from these data are reasonably constant. The temperatures show some variation but the densities seem in good agreement.

7.3.2 Double Probes

Data from double probes were acquired in conjunction with the single probe experiments as a second method of determining the plasma properties from probe analysis to provide a check on the data and on the models used to analyse the data. The use of double probes also allows the more complete analysis of the radial theory from chapter four to be used. A typical data plot (300 V, 1.0 A) of the I - V characteristic from double probes is presented in figure 7.9. These data were recorded at the same time as the single probe data above and hence were acquired at the same plasma operating conditions.

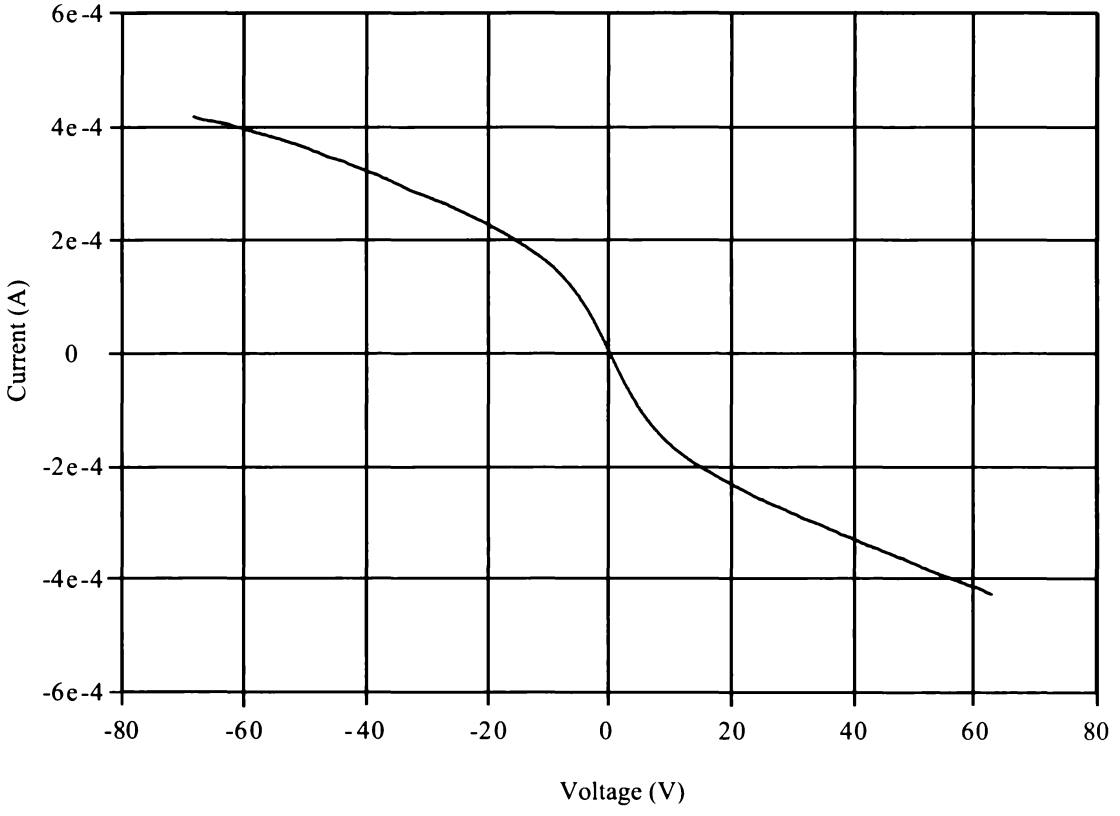

Figure 7.9: A typical double probe characteristic for the 300 V, 1.0 A plasma conditions.

Using the theory in chapter four we can determine the electron temperature (equation 4.23) and density of the plasma (OML and radial motion) in a similar manner to the single probe analysis. The slope at the origin is a point of inflection and we require the slope at this point for the calculations. This is again best determined using differentiation since the first derivative of the I-V data will give the slope. This is shown in figure 7.10. From figure 7.10 and 7.9 the temperature is calculated to be 2.8 eV which is consistent with those calculated so far.

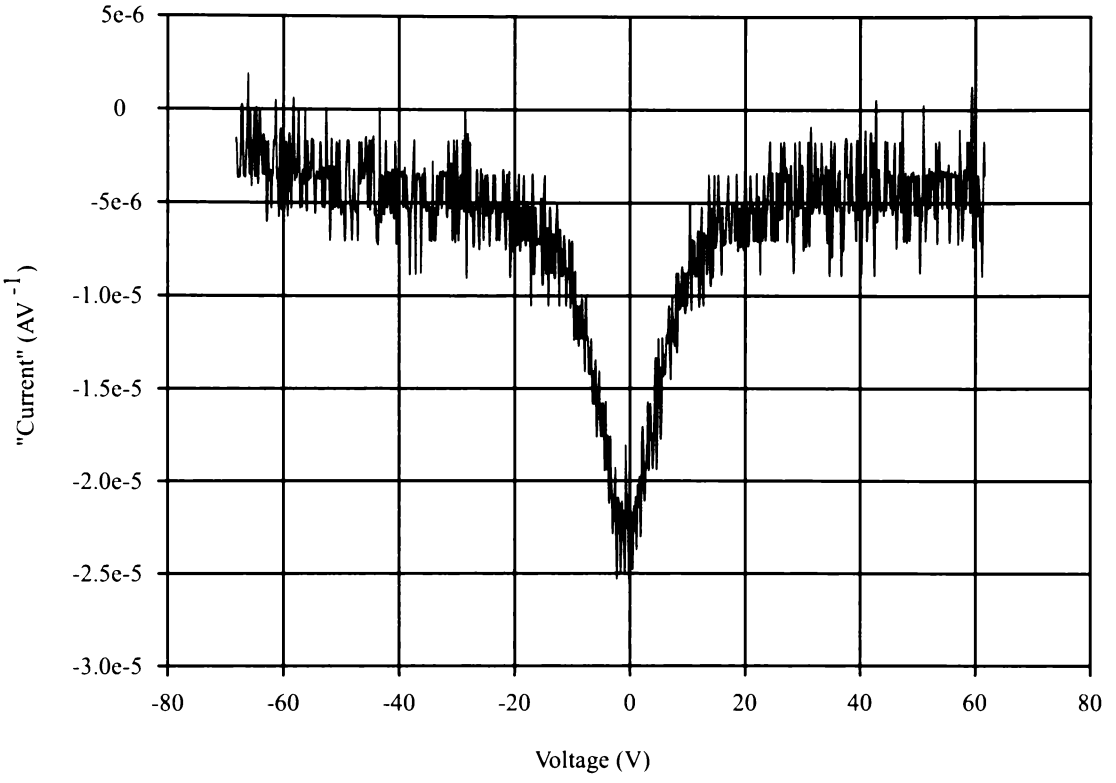

Figure 7.10 : The first derivative of the unsmoothed data curve in figure 7.9, as calculated using numerical differentiation.

The analysis of the theory of Chen (1965) re-evaluated in chapter four allows us to manipulate the experimental data and compare these to the theoretical data such as those presented in figure 4.12 to find an optimal match. This analysis requires the temperature of the plasma whose characteristic is shown in figure 7.9 to be already known by a different method, in order to determine the ion density using the positive ion region of the experimental data. These plots are shown in figure 7.11.

The plots allow us to determine which theoretical curve best fits the experimental data. This then gives us a value of ξ_p from which the density is easily calculated from equations 4.42 or 4.43, and yields a value of 1.38×10^{10} cm^{-3} which is in reasonable agreement with the density obtained from the EEDF distribution.

As with the OML theory for electrons, the same general model can be applied to ions to provide a comparison between the radial and orbital theories. The electron temperature can be obtained from these plots as in the case of the single probes giving a direct comparison between the temperatures from both saturation regions of the plot. The ion current graph equivalent to figure 7.8 is shown in figure 7.12.

The slopes of the different saturation curves give values of 2.60×10^{-9} A^{2}V^{-1} and 2.73×10^{-9} A^{2}V^{-1} reading them from left to right on figure 7.12. These slopes in turn yield ion densities of 6.35×10^{10} cm^{-3} and 6.50×10^{10} cm^{-3} respectively.

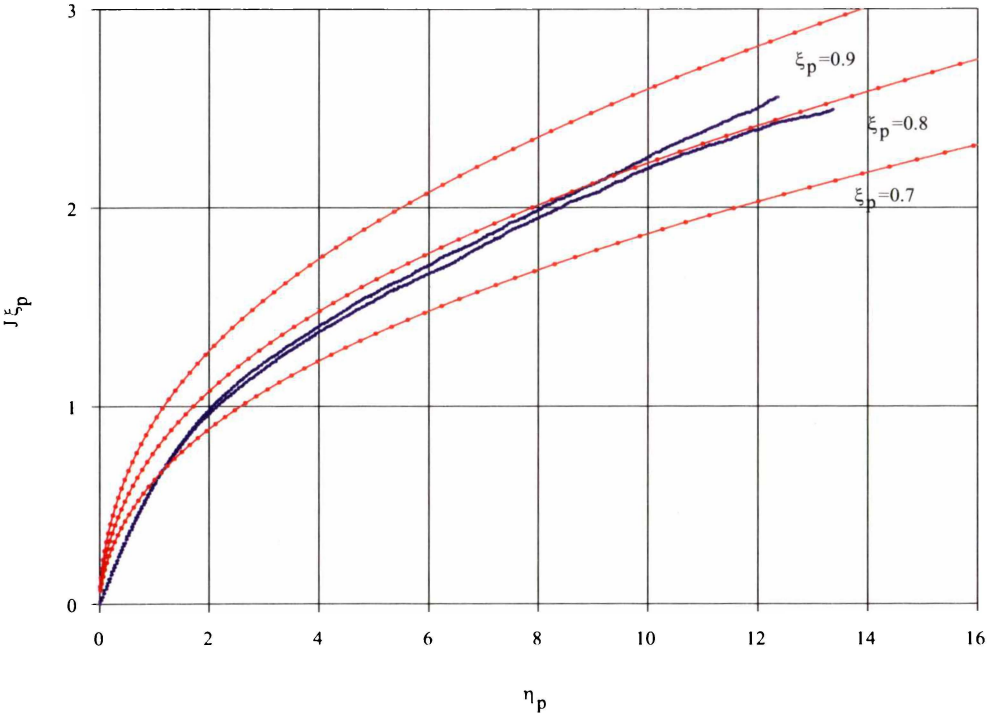

Figure 7.11 : A plot showing the experimental (blue) and theoretical data (red) using the theory of Chen applied to the ion distribution of a double probe characteristic. The best curve fit was taken to be for the ξ_p value of 0.8.

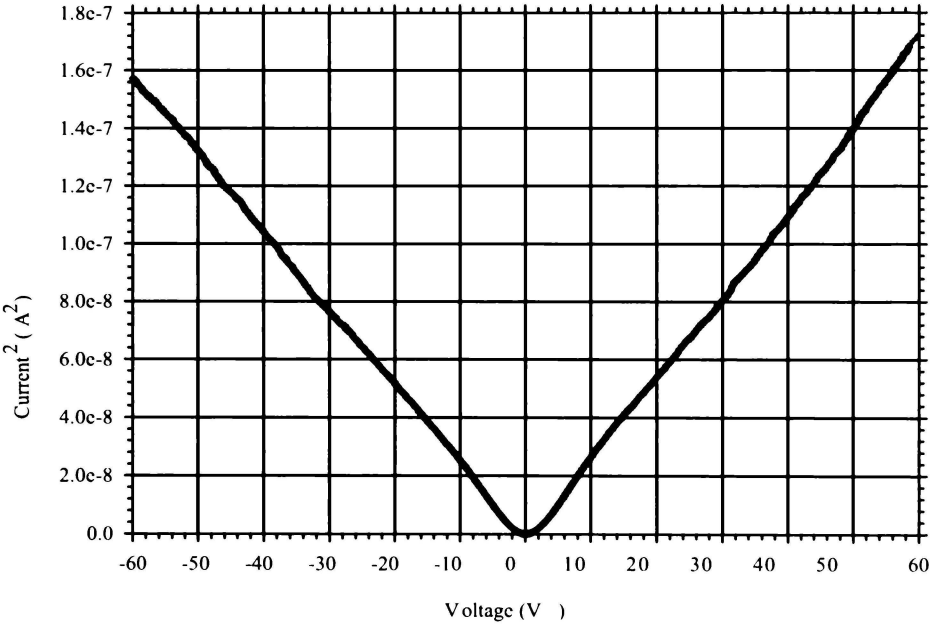

Figure 7.12 : An OML ion current graph plotting the square of the ion saturation current against the voltage. Both saturation regions for the double probe data have been included for comparison.

7.3.3 Analysis and Summary of the Langmuir Probe Data

Following the previous analyses, there are several methods involving different theories that can be used to determine the electron temperature and the density of the plasma. Each theory gives different electron temperatures and densities of the plasma, even for simultaneously recorded data. The differences that appear must be related to the different methods of calculation, and to a lesser degree the accuracy of acquiring the data. The main differences are the discrepancies between the electron temperatures from the single and double probe data and the densities from the ion and electron calculations. It is apparent from section 4.22 that the double probe data will not show up dual temperature distributions since the high energy electrons are not collected by this type of probe arrangement. There are still advantages in using double probe methods since they provide far less spatial disturbance of the plasma.

The full range of data has been obtained and analysed using the previously outlined methods. The data sets show discrepancies and highlight what theories and equations for calculation of the temperature and density of the plasma are best. It will be seen that the most accurate calculations occur for the double probes for temperature determination and the OML method used on the single probe electron saturation curves for the density. Figure 7.13 shows the temperatures calculated using the double and single probe data (for the high temperature single probe case) for the 200 V range of measurements (0.5 A to 3 A). Figure 7.14 shows the equivalent data for the 300 V range of measurements.

Each set of plasma conditions, for example 200 V acceleration potential and 1 A discharge current, had multiple single and double probe measurements recorded. This provided a two-fold check. The first was to check the plasma acquisition system for accuracy and repeatability while the second was to measure any variation in the plasma parameters at specific set values of the plasma discharge. It can be seen that the double probe temperatures are more accurate and precise. The regression curves of each slope from which the temperatures were calculated (for double and single probes) had a minimum regression coefficient of 0.995 and were often greater than 0.999. This indicates that the errors in determining the temperatures are about or below the errors inherent in the acquisition system. The estimated errors in each temperature value will be nominally assigned as 2% for now. Similarly, the error values and regression coefficients are the same, if not more accurate for the density calculations and hence all values quoted (temperature and density) can be assumed to have an error of ±2%. The density calculations are presented as a series of four figures. There are two plots for each accelerating voltage range.

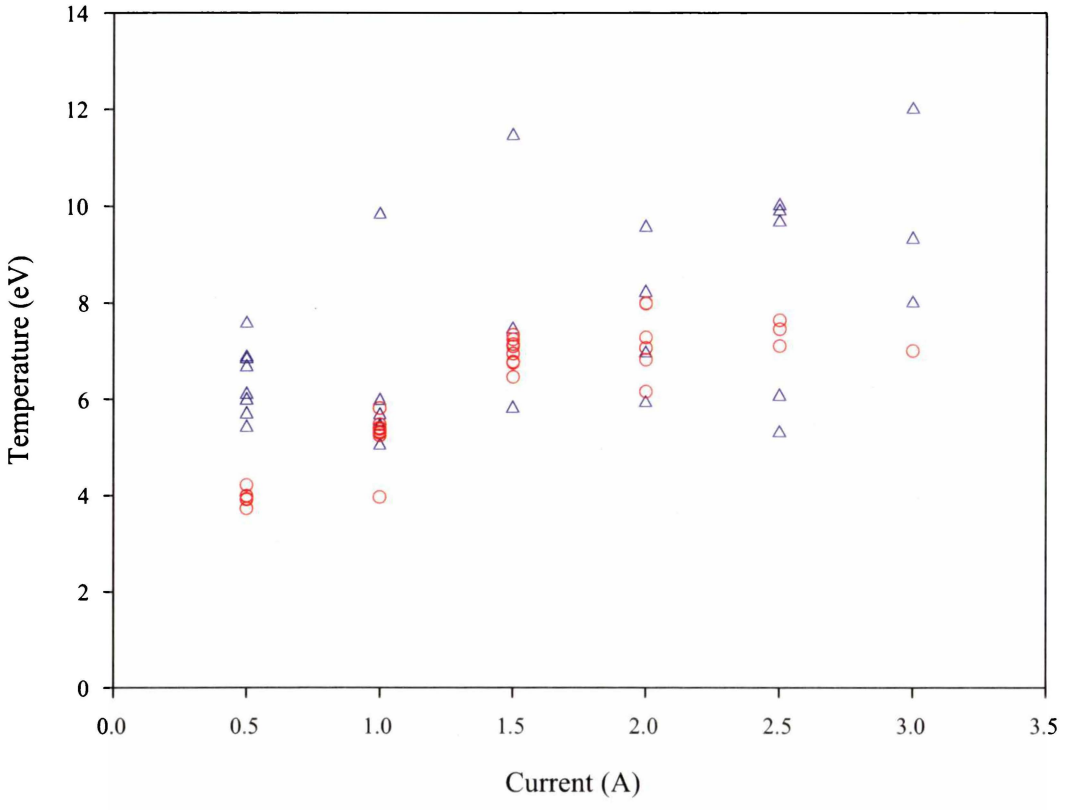

Figure 7.13 : Temperature summary for single and double Langmuir probes at 200 V acceleration potential. The triangles are the single probe (high) data while the circles are the double probe data.

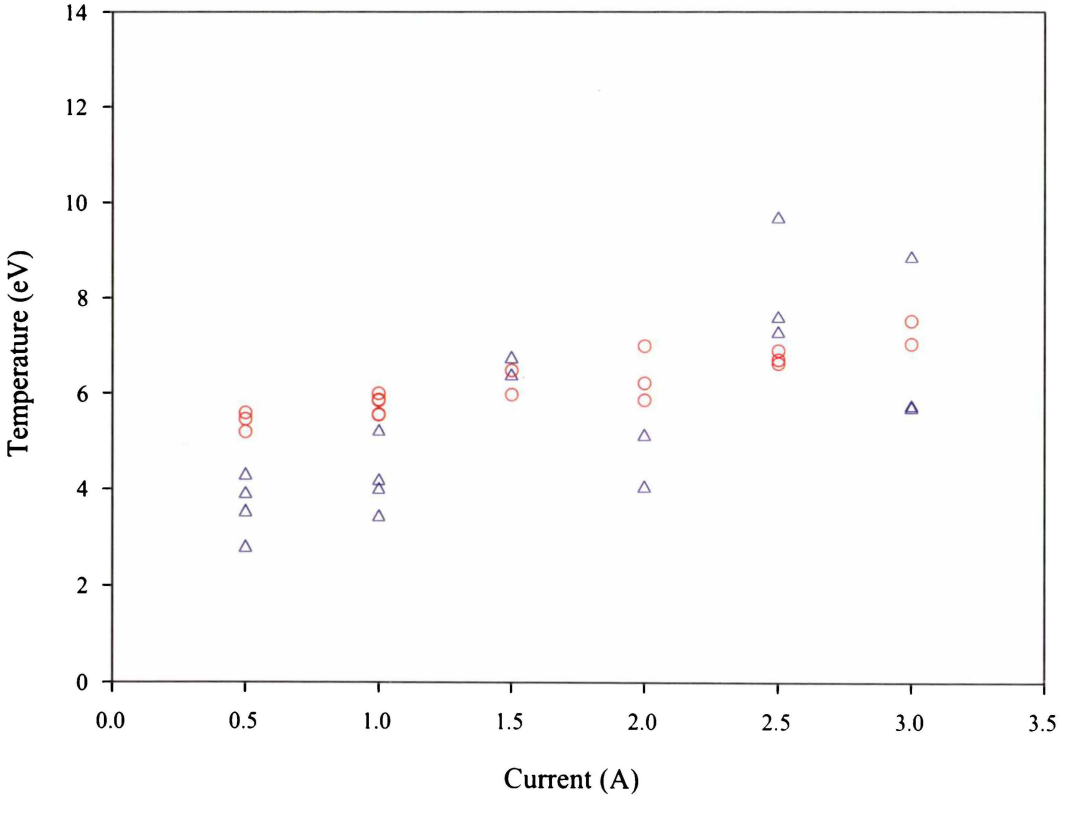

Figure 7.14 : Temperature summary for single and double Langmuir probes at 300 V acceleration potential. The triangles are the single probe (high) data while the circles are the double probe data.

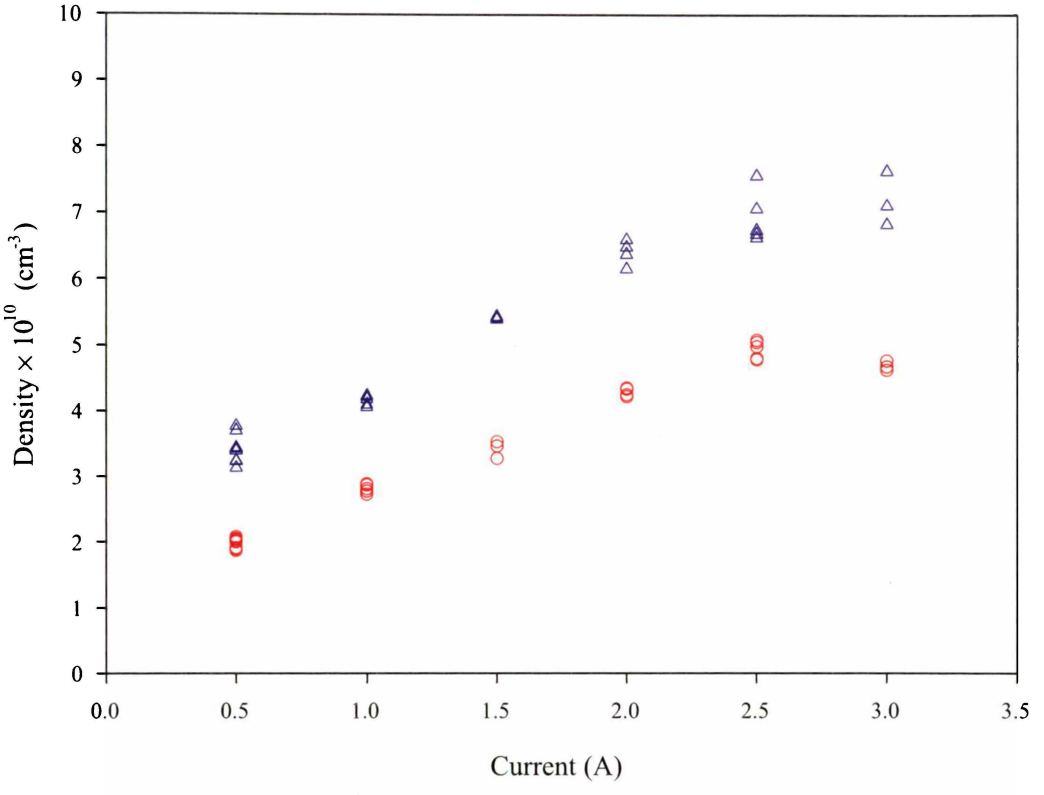

Figure 7.15 : Density calculations using the single probe ion (triangles) and electron (circles) saturation curves for a 200 V acceleration potential.

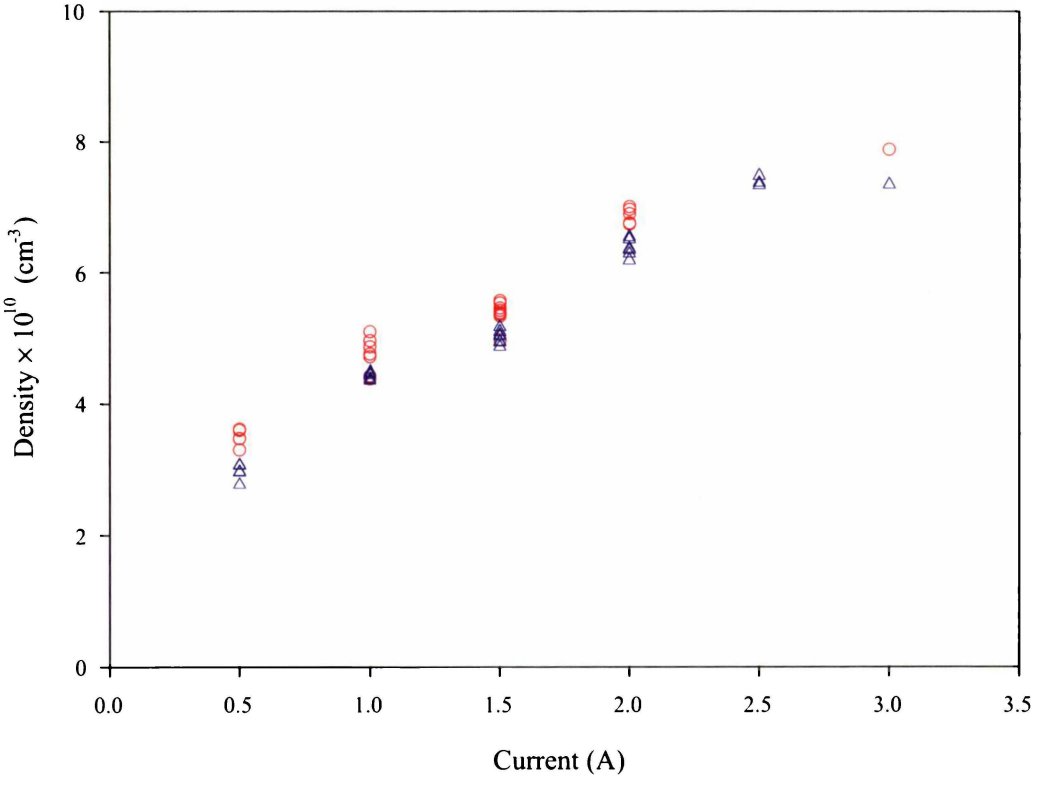

Figure 7.16 : Density calculations using the double probe data positive (triangles) and negative (circles) saturation curves for a 200 V acceleration potential.

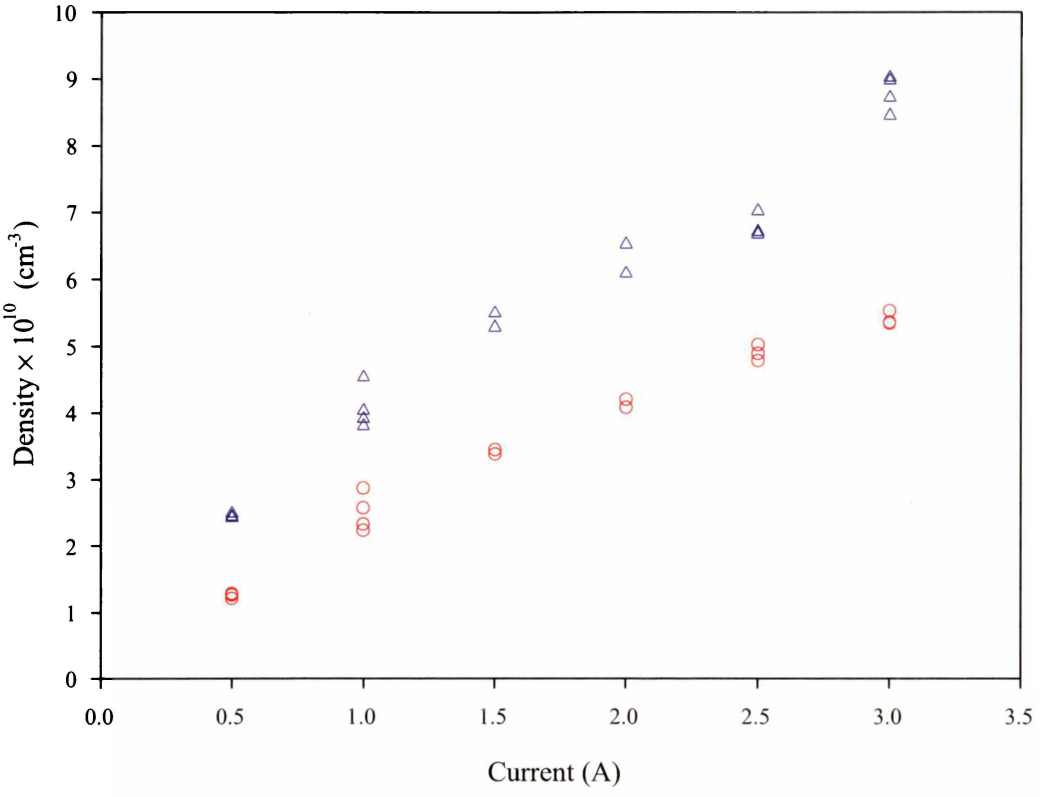

Figure 7.17 : Density calculations using the single probe ion (triangles) and electron (circles) saturation curves for a 300 V acceleration potential.

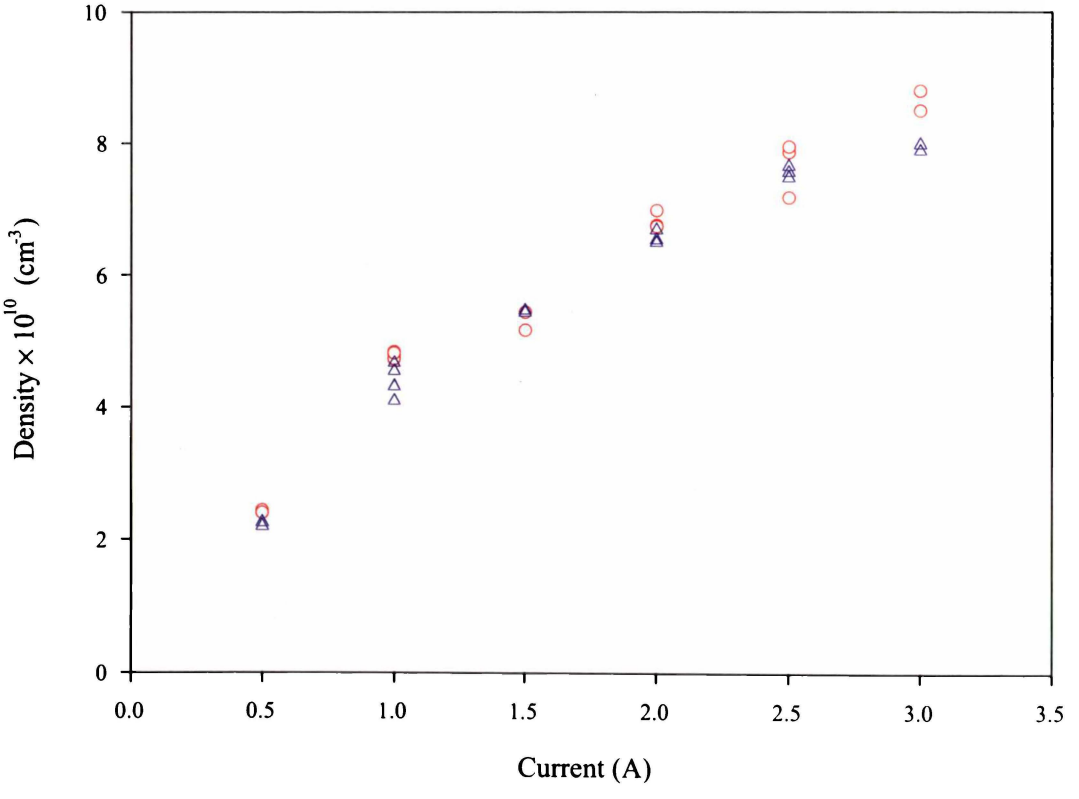

Figure 7.18 : Density calculations using the double probe data positive (triangles) and negative (circles) saturation curves for a 300 V acceleration potential.

These density plots are separated into those from the single probe ion and electron current saturation curves while the second plot for each acceleration potential are the densities calculated from the positive and negative branch of the ion saturation curves for the double probe data. Figures 7.15 and 7.16 are for 200 V acceleration potential while figures 7.17 and 7.18 are for the 300 V data. Two features highlighted by these plots are immediately obvious. Firstly the 200 V data (temperatures and pressures) are more uneven and exhibit a drop in temperature and density at the higher plasma current ranges compared to the 300 V acceleration potential data. This indicates that the plasma is more stable and consistent with a 300 V acceleration potential than it is at 200 V. This feature is applicable to the discharge configuration and can be considered to be a peculiarity of the discharge geometry and conditions of the plasma experiments as a whole. Secondly, and probably more importantly in the wider nature of Langmuir probe diagnostics is the inaccuracy of the single probe temperatures and variation between the ion and electron density values. The primary reason for this temperature variation exhibited in the above graphs is the sensitivity of these calculations to the determination and subsequent removal of the ion current portion from the total current drawn to the probes(s). It must be noted that this problem is exacerbated by the dual temperature distribution found in this plasma system. This is discussed in the next section where the problem is clarified and the extent of the sensitivity of the plasma parameters to the ion current removal is determined.

It should be noted that this problem is applicable to plasmas in general and researchers who have relied on single probe or double probes, taking one or two measurements to determine the plasma parameters are likely to have obtained values with systematic errors. At the very least the plasma parameters are likely to be outside the errors quoted (if any).

7.3.4 Determination of the Variation of the Ion Current on Temperature

To determine the nature of this problem and the sensitivity of the plasma parameters to the ion current removal, a theoretical single probe characteristic was generated. This allows us to specify the plasma parameters so we can use the analysis of sections 7.3.1 and 7.3.2 to work backwards with the data to measure the variation of the experimentally determined parameters compared to those chosen. In analysing the experimental data in the above section it was obvious that the variations and errors introduced in determining the ion current were not from the curve fit to the experimental data, but seem more likely to arise from the projection or extrapolation of that curve fit up to the space charge potential or "knee" in the I-V curve where that ion current value is obtained.

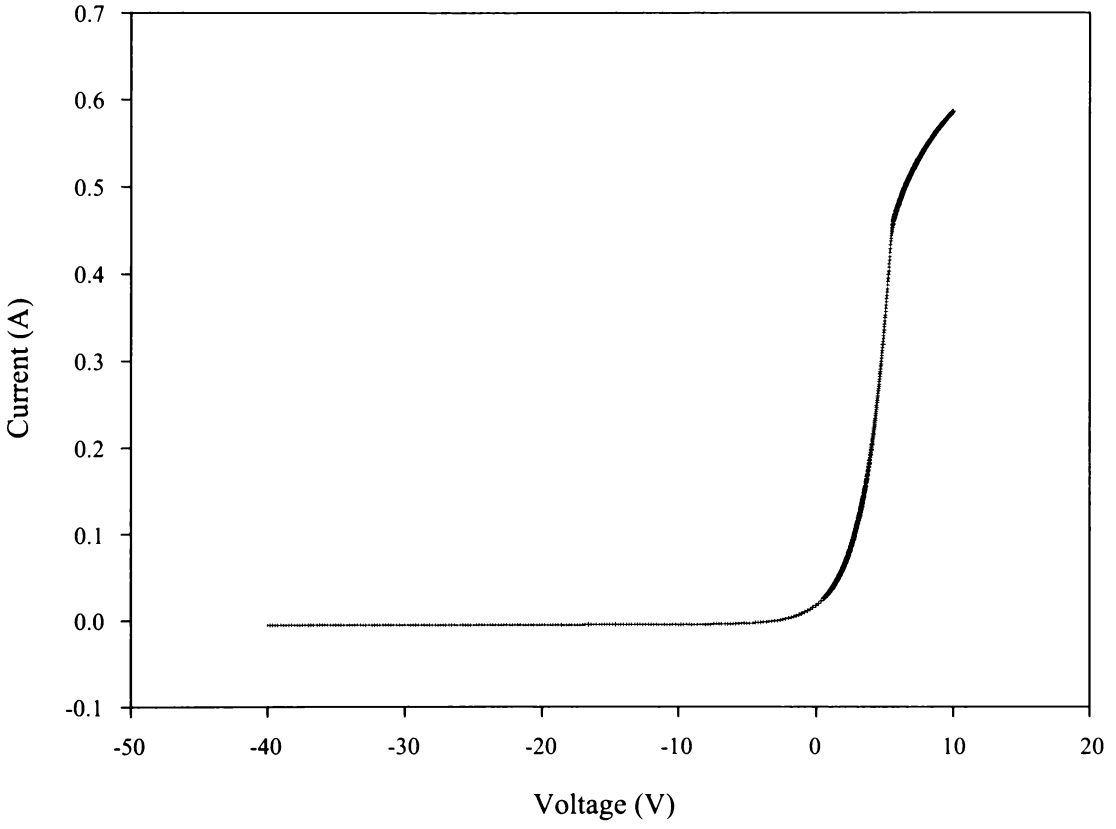

Figure 7.19 : A theoretical single Langmuir probe I-V characteristic.

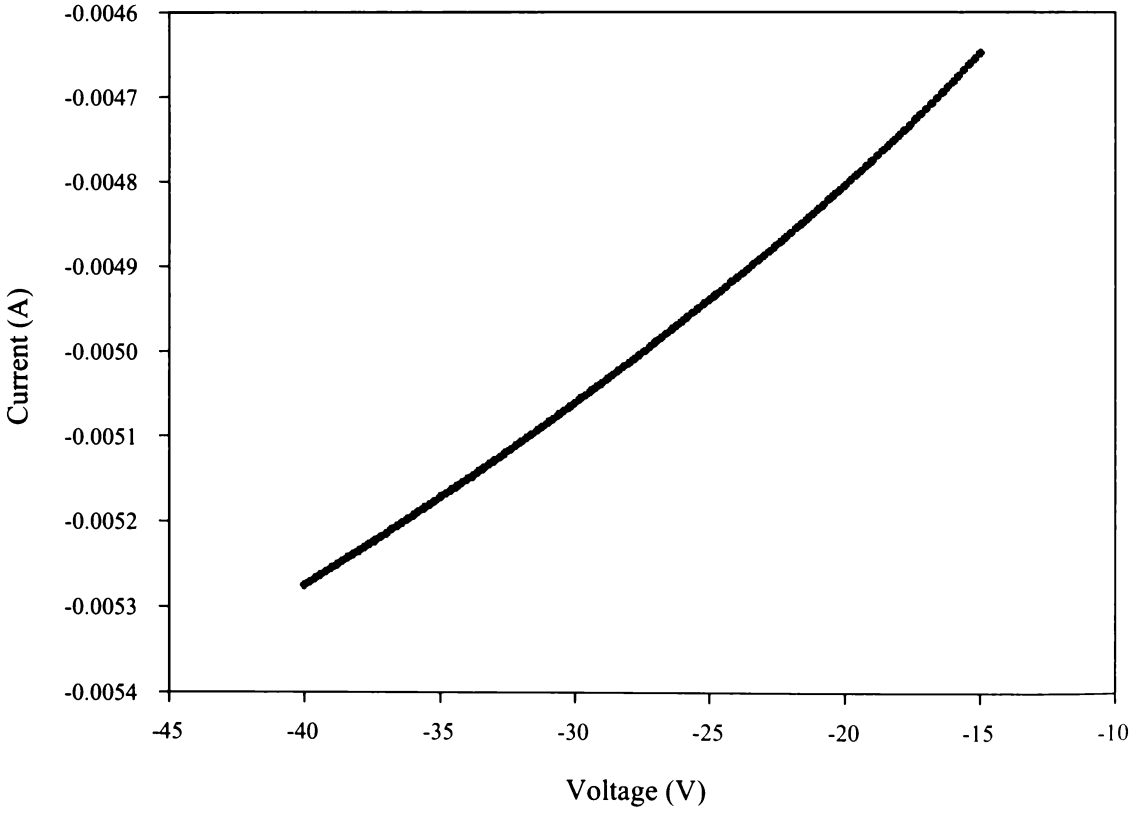

Figure 7.20 : The ion current portion of the theoretical single probe characteristic shown in figure 7.19.

Figure 7.19 shows the theoretical single probe characteristic generated for examination while figure 7.20 expands the ion current saturation region so the problem can be viewed. The full curve was generated using equations 4.9 and 4.39. If we observe the nature of figure 7.19 and figure 7.20 in light of the previous problems we find the following: Figure 7.19, similar to experimentally determined curves never reaches a constant saturation regime (by design) as shown in chapter four. Theoretically the only case where the ion saturation is constant was derived by Bohm (1949) and is given by equation 4.6, since there is no dependence of the current on applied voltage. For OML and radial motion, the current *is* dependent on the applied voltage which can be observed in equations 4.39 and 4.40. A good discussion of this linearity can be found in a later paper by Chen (2001). Experimentally the linearity of the saturation currents is more complicated. This is because the increase in the saturation current occurs by the expansion of the sheath area in previously undisturbed plasma regions where the density need not be constant and often is falling due to the diffusion of the charged particles to the walls of the vacuum chamber. This renders Bohms equation (4.6) an approximation that is not rigorously followed since it predicts that the ion current is independent of the applied potential.

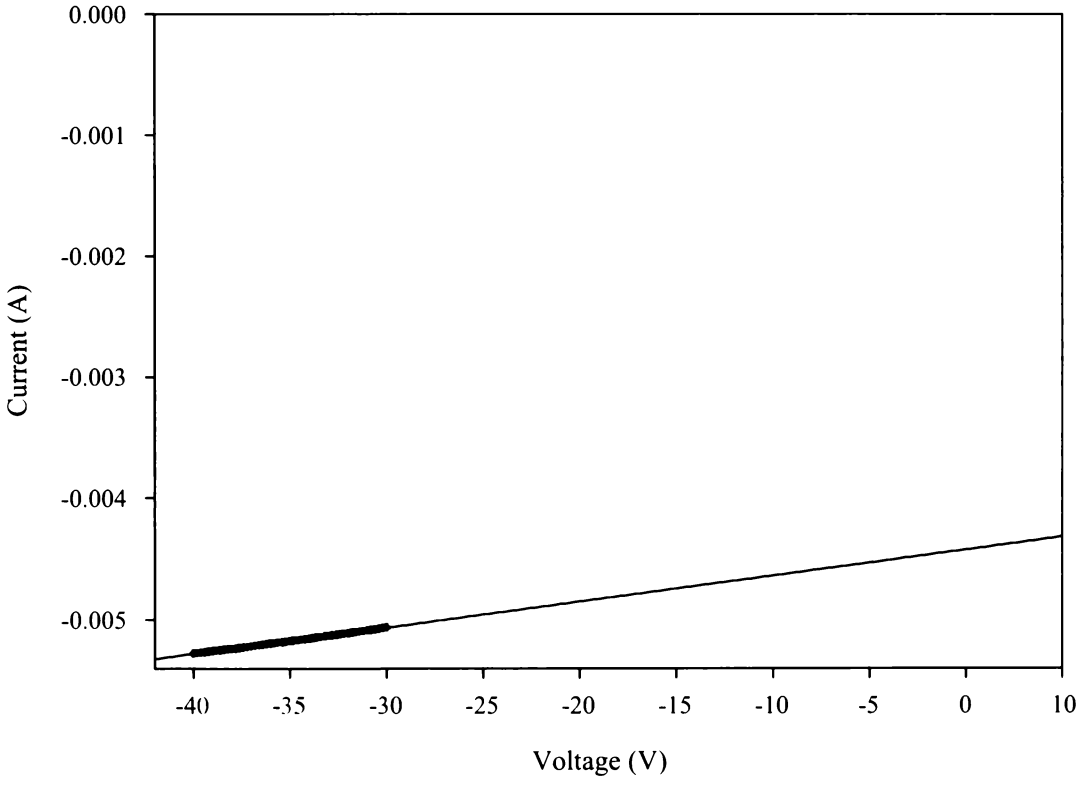

Figure 7.21 : The ion current curve fit to the theoretical single probe characteristic shown in figure 7.19.

Examining figures 7.19 and 7.20 we see that there are two limiting problems. The first is over what voltage range do we calculate the ion current? Should this be -40 V to -35 V or to -30 V or even to -25 V? The second is related to this initial choice. If we chose a 10 V range (-40 V to -30 V) the errors in extrapolating the curve fit to the space charge potential (4.45 V) will be larger that those of choosing a wider, say 20 V range where the curve fit will be poorer.

Figure 7.21 shows a curve fit to the saturation current over the -40 to -30 V range. The saturation current is 4.32×10^{-3} A. The ion current at -40 V is 5.2750×10^{-3} A so that the ion saturation current represents 82% of the total current. For comparison, figure 7.22 shows the standard semilog plot (equation 4.9) with ion currents subtracted at several ion current percentages. On the plot from right to left as indicated on the graph, the ion currents subtracted are 0%, 82%, 85% and 90% of the maximum ion current value.

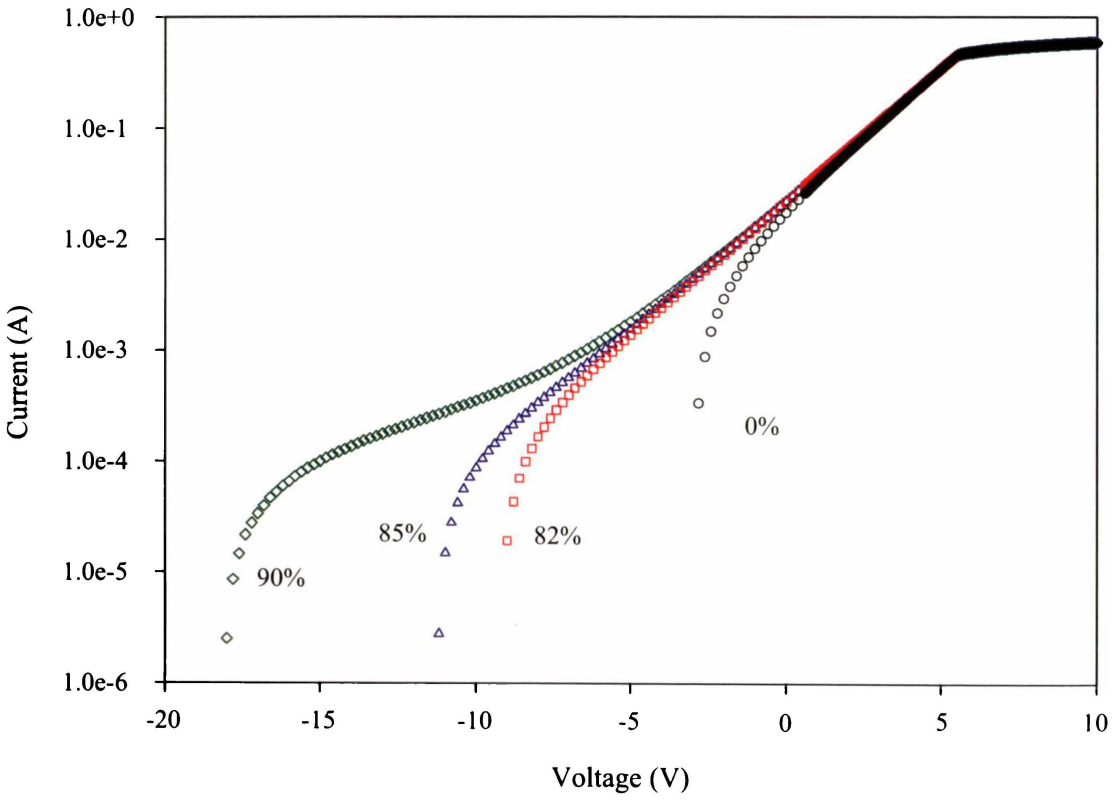

Figure 7.22 : The theoretical electron current distributions with varying percentages of the total ion saturation current removed (82% is the calculated value)

From figure 7.22 we can see the effects of changing slightly the saturation current removed from the total current. Briefly, this analysis using equation 4.9 produces a positive gradient curve whose slope is linear after which the slope asymptotically approaches infinity. Again two features are apparent. Our original curve fit to the ion

saturation current underestimated the actual ion saturation current since the 85% curve produces a extended linear portion. Secondly, the removal of 90% of the total ion current introduces a point of inflection into the curve that is identical to that exhibited by a dual electron temperature distribution. Comparing this to the original ion saturation current value, an over-estimate of the ion saturation current larger than 9.5% results in a incorrect curve appearing like a dual electron temperature distribution.

The immediate check on any single Langmuir probe I-V characteristic to determine if more than one electron distribution is present would be to calculate the semilog plot of the data *without removing the ion saturation component.* If this is done and the curve appears like the 0%, 82%, or 85% values in figure 7.22, the results indicate a single electron distribution is present. If they appear like the 90% curve in figure 7.22, the presence of dual electron temperature distributions is confirmed.

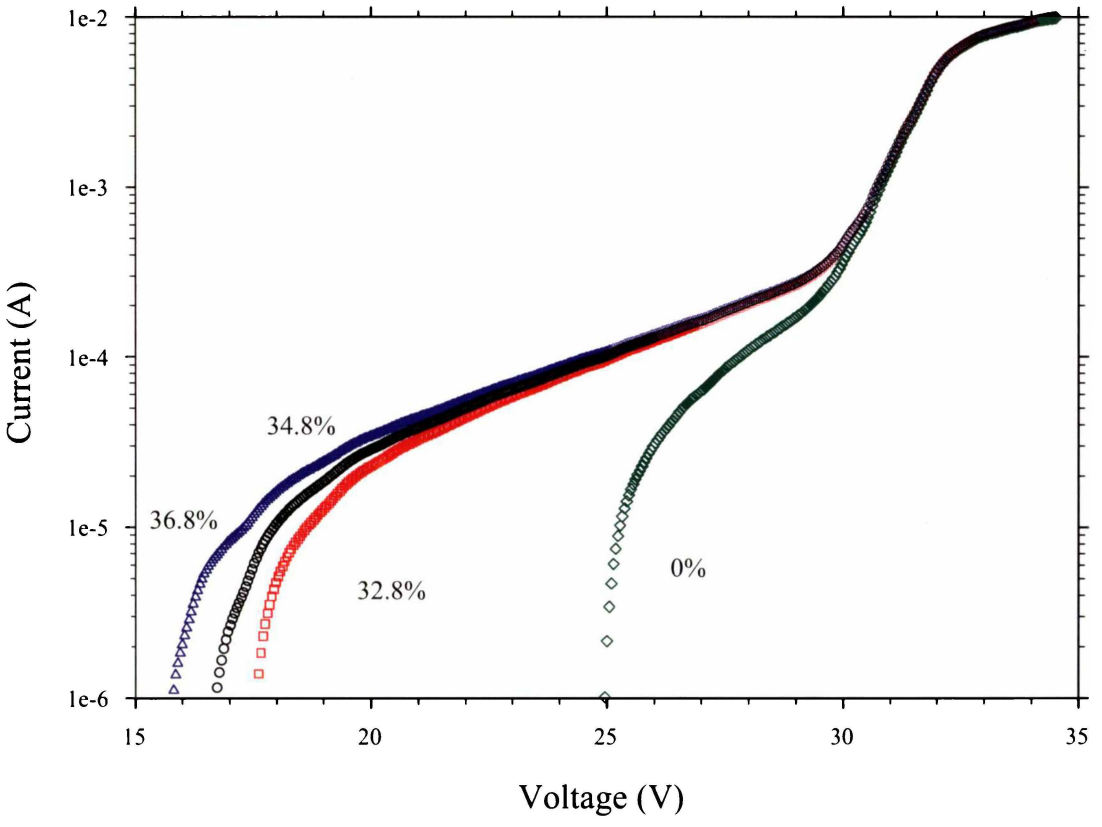

Figure 7.23 : An experimental semilog plot of a data set from the 300 V 1 A plasma conditions. The curves numbered from right to left represent 0%, 32.8%, 34.8% and 36.8% of the total maximum current where the 34.8% value is the correct calculated ion saturation curve fit.

We can now apply this theoretical treatment and error bounds to our experimental results. The experimental data set chosen for this analysis was one from

the 300 V, 1 A range. The margin of error was narrowed about the calculated ion saturation curve. The calculated ion saturation was 9.940×10^{-5} A while the total current at -47 V was 2.8580×10^{-4} A so that the ion saturation at the space charge potential was 34.8% of the total. Two different values were chosen at a ±2% range about the calculated ion saturation current. These were 1.051×10^{-4} A and 9.368×10^{-5} A. Compared to the actual saturation current these values represented a ± 5.8 % change, well inside the 9.5% previously considered. The slopes of the curve fits to the linear portion of the curve yielded temperatures of 4.44 eV and 3.99 eV compared to the "correct" value of 4.17 eV. Figure 7.23 shows these three curves as well as the 0% case.

The first feature observed from figure 7.23 is the 0% curve which clearly indicates that a two temperature distribution is present. This complicates the determination of the true ion saturation current value since the curves will never tend to an infinite slope *without* a point of inflection. Thus we cannot use the change in the curves from "linear - infinite asymptote" and "linear - inflection - infinite asymptote" as a check on the accuracy of the ion saturation value. The changes in curves exhibited in the theoretical data presented in figure 7.22 can be used to determine the correct ion saturation current.

Turning our attention to the remaining three curves in figure 7.23 we find that the curve variations and the original true value yield temperatures of 4.44 eV, 4.17 eV and 3.99 eV which approximately mirrors the percentage change from the true ion saturation value (5.8%) in error. The actual values are +6.5% and -4.3% in error about the calculated 4.17 eV temperature. If these values are projected back into the linear fit ($y = mx + c$) for the calculation of a particular ion saturation current, we find that if we leave the space charge potential the same and vary the slope of the curve fit to match the introduced variations in figure 7.23, then the errors are the same percentages: i.e. the error in the slopes for the two variations are + 6.5% and -4.3%. These are large changes for the accuracy of the measuring equipment used in this experimental work and thus confirm that this cannot be the sole source of error. By varying the calculated space charge potential we also conclude that this is also not the sole source of error since for the 36.8% curve, leaving the slope the same we require a value of 29.4 V rather than the 31.9 V obtained. The space charge value is obtained from the first and second derivative of the I-V characteristic and has an accuracy of the same magnitude as the LSB of the measuring equipment which is a maximum of 0.13 V, rather than the 2.3 V needed to obtain this error. Both these errors contribute to the variations shown. If we use them in combination they still don't account for the variation shown in the temperatures for the 300 V 1 A discharge, or any other measurement range chosen.

If we look back further to the method of calculation of the curves through equations 4.9 and 4.24 we find that the method is a cause of errors. Since we are subtracting two numbers of approximately the same value from one another to obtain a small difference, the error propagated through this subtraction becomes a far larger percentage of the final result. Since any small variation in the plasma discharge conditions will result in a change in the I-V characteristic, the subtraction process to remove the ion saturation curve includes this random error which is greatly magnified in the final curve once the ion saturation current is removed. As a final check, the same variation (2%) originally used in figure 7.23 (5.71×10^{-6} A) is applied to the whole corrected I-V characteristic so we can see the proportion of error across the entire regions where the electron temperature is calculated. As can be seen from figure 7.24 a 2% error introduces an error ranging from 10% to 2% into the region where the high temperature slope is calculated from.

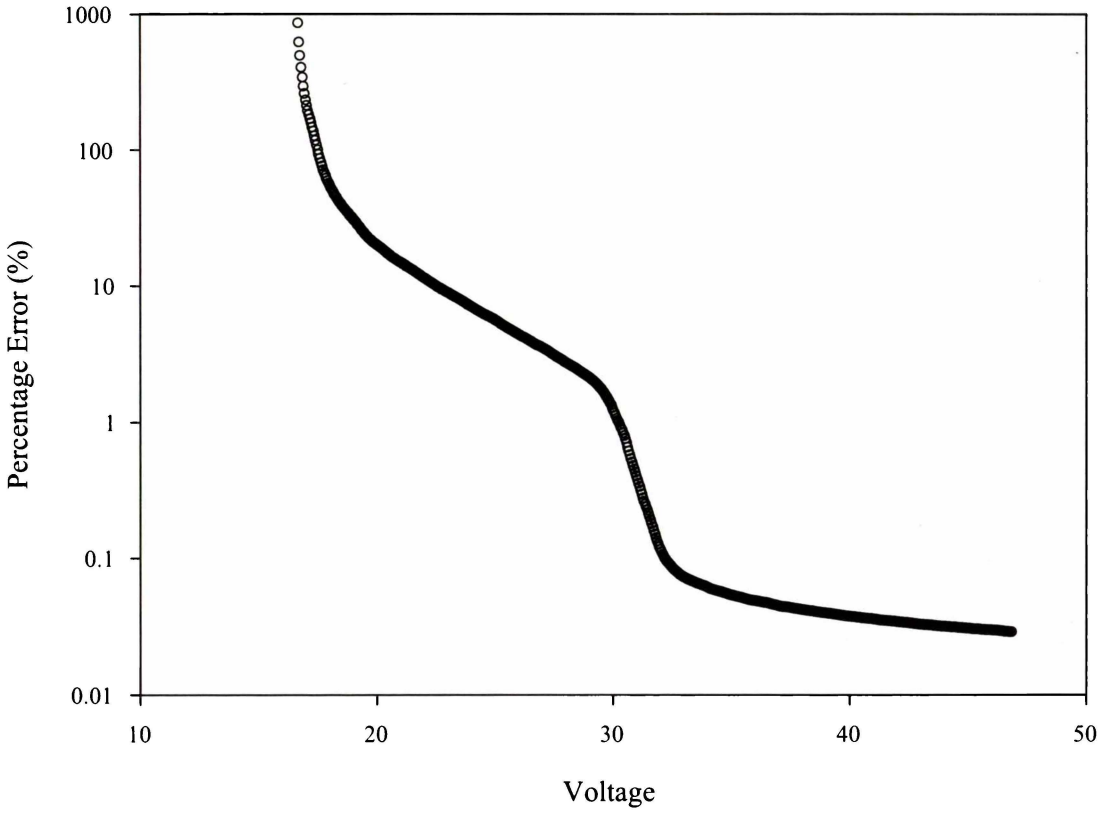

Figure 7.24 : Errors in the slope if a single probe temperature calculation using a 2% variation in the ion saturation current.

In summary, we find that even though a 2% variation in the ion saturation current produces a 2% error in the final temperature calculation, the actual variation of the electron temperatures calculated from semilog plots of the single probe electron

current are due to the errors propagated into the electron current by small variations in the plasma discharge conditions. Only minute changes in the plasma conditions (2%) are necessary to produce the variations in electron temperature shown in figures 7.13 and 7.14. We conclude that the subtractive method of removing the ion saturation current from the total current is the root cause of the problem.

Having identified the cause of error we can quickly summarise the variations (or lack of) in the remaining data, the double probe electron temperatures. For the double probe temperatures, there is no subtraction process in equation 4.23 to magnify the errors. The ion saturation currents are extrapolated to zero volts where the values of i_+ and i_- are calculated. Furthermore, the extrapolation of the saturation currents is over a smaller voltage range since the system, while operating with double probes, is now floating at the space charge potential so that "zero" volts is the space charge potential. This change in the calculation of the values means that small variations in the plasma discharge conditions are not magnified through into the calculation of the electron temperatures.

We now conclude that the double probe temperatures are the correct values of temperature since they have the least error. Since these values arise from different probe techniques we can verify the results by substituting the *double probe temperatures* into the saturation equation for the *single probes* via an rearrangement of equation 4.8 using equation 4.2. For the same data set as shown in figure 7.23 (300 V, 1 A) the typical ion saturation currents ranged from 0.97×10^{-2} A to 1.1×10^{-2} A producing densities in the range $2.81 - 2.39 \times 10^{10}$ cm^{-3}, which is in the range of the densities calculated from the electron saturation curve. Choosing the extremes of the plasma conditions, 200 V and 0.5 A, 300 V and 3 A we find that the densities calculated from the double probe temperatures match those calculated by the electron saturation current. Figure 7.25 shows a typical estimate of the electron saturation current for a 300 V, 1 A discharge.

Thus, the double probe temperatures are measuring the high energy distribution of electrons shown in the single probe data. Furthermore, the data from the double probes and single probes are self consistent. It is important to note that without *both* double and single probe analysis, the temperatures determined from either trace would be of lower accuracy due to the random errors introduced through the ion saturation currents. The double probe data in general are more accurate with lower variations that the single probe data, but if we only used double probes we would not know that there is a dual electron temperature distribution present in the plasma. Similarly, if only single probes were used, temperatures obtained would be in error, especially at high plasma current discharges.

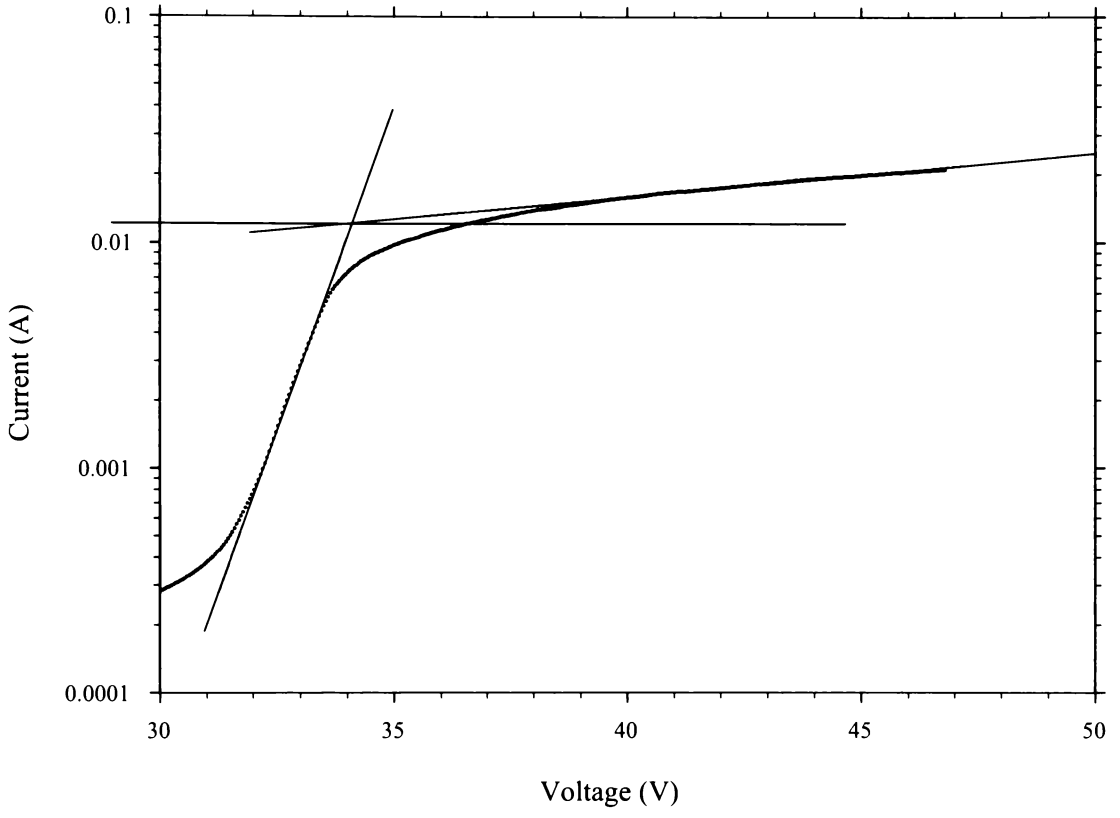

Figure 7.25 : A typical electron saturation curve fit for a 300 V 1 A discharge.

7.3.5 Variations in the Ion and Electron Current Density

From figure 7.15 through to figure 7.18 it can be seen that the electron and ion densities calculated do not match. They differ in that the electron density is consistently about 2/3 of the ion density in magnitude. The nature of the problem is different to the temperature variations since the ion saturation current is small compared to the electron saturation current so that its removal from the latter is negligible. By combining all the density calculations in a single graph, shown in figure 7.26, we can observe the problem. From this figure it can be seen that the density values for the ion currents are consistent, regardless of whether a single or double probe was used to acquire the data. This indicates that both methods are measuring the same ion current. Furthermore, the ion densities are consistently higher than the electron densities for both the radial and OML theories across all discharge voltages and current ranges while the density has little dependence on the applied DC potential but varies linearly with the discharge current.

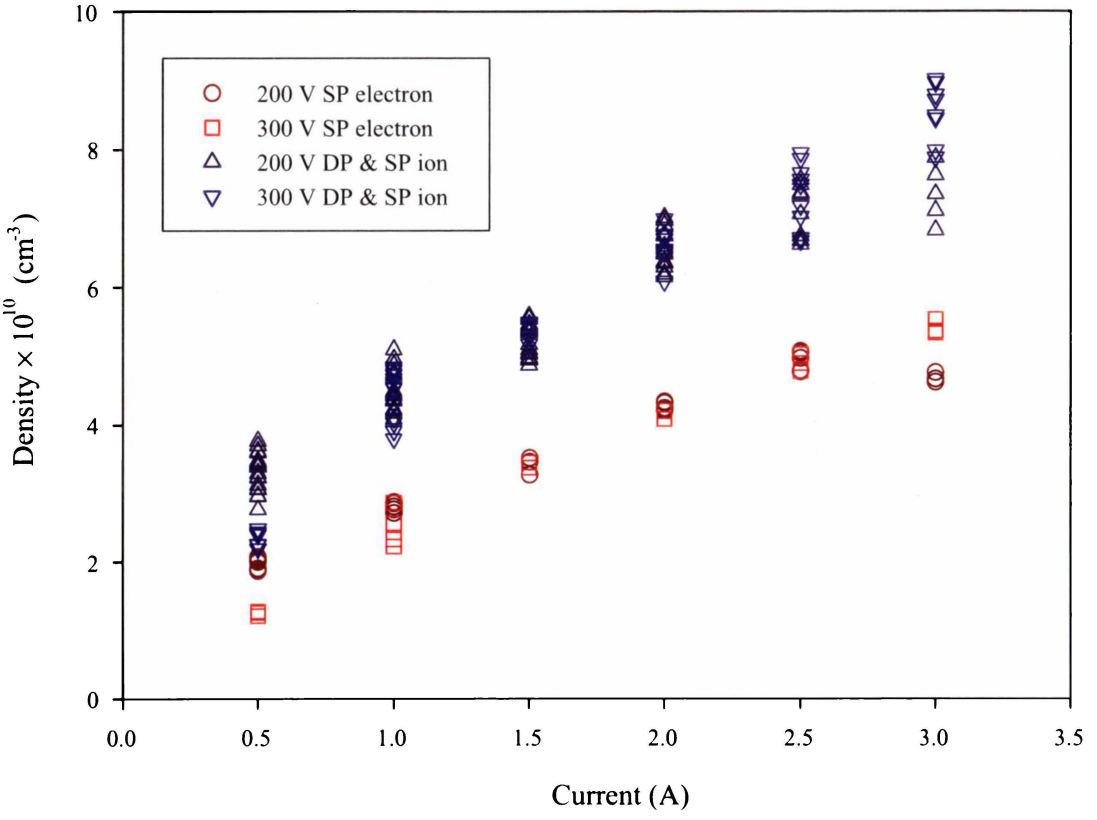

Figure 7.26 : A combined plot of the electron and ion density values incorporating figures 7.14 to 7.18.

Initially, this is somewhat perplexing since previously in this chapter it was seen that the ions obey the radial and OML theories while the electrons obeyed the OML theory. To quickly summarise, for OML the square of the saturation currents plotted against the applied voltage were linear and the intercepts passed either through the origin for double probes, or close to the space potential for single probes. With radial motion, where it was theoretically determined in chapter four that orbiting can occur, the shape of the ion current in non-dimensional units closely follows the theoretical radial motion predictions. These conditions are taken to be confirmation of OML in all publications and books encountered by the author and the difference between the ion and electron densities is normally attributed to collisions in the sheath, excessive drain of the charged species from the plasma, or differing theories giving different densities. However, in this case OML applied to ions yields a different result than OML applied to electrons.

It will now be shown that these are erroneous assumptions and that these conditions *are not sufficient to confirm OML, nor even radial motion.*

From figures 7.11 and 7.12 it appears that the ions obey both the radial and OML motion theories. From figure 4.13a, with $\xi \approx 1$ as we have in figure 7.11, this is possible since the gradient is approximately two and the standard analysis completed so far gives no indication which theory is followed. It is possible both are followed

since the radial theory indicates that orbital motion does occur. However, if we calculate the gradients of the curves and plot them against the theoretical gradients, after conversion to dimensionless coordinates, such as those in figure 4.13a, a different picture emerges. This plot is shown in figure 7.27 where we can see that although the gradient follows the general form of the experimental plots, the position is incorrect and indicates that radial motion is not followed even though it appears to be from figure 7.11.

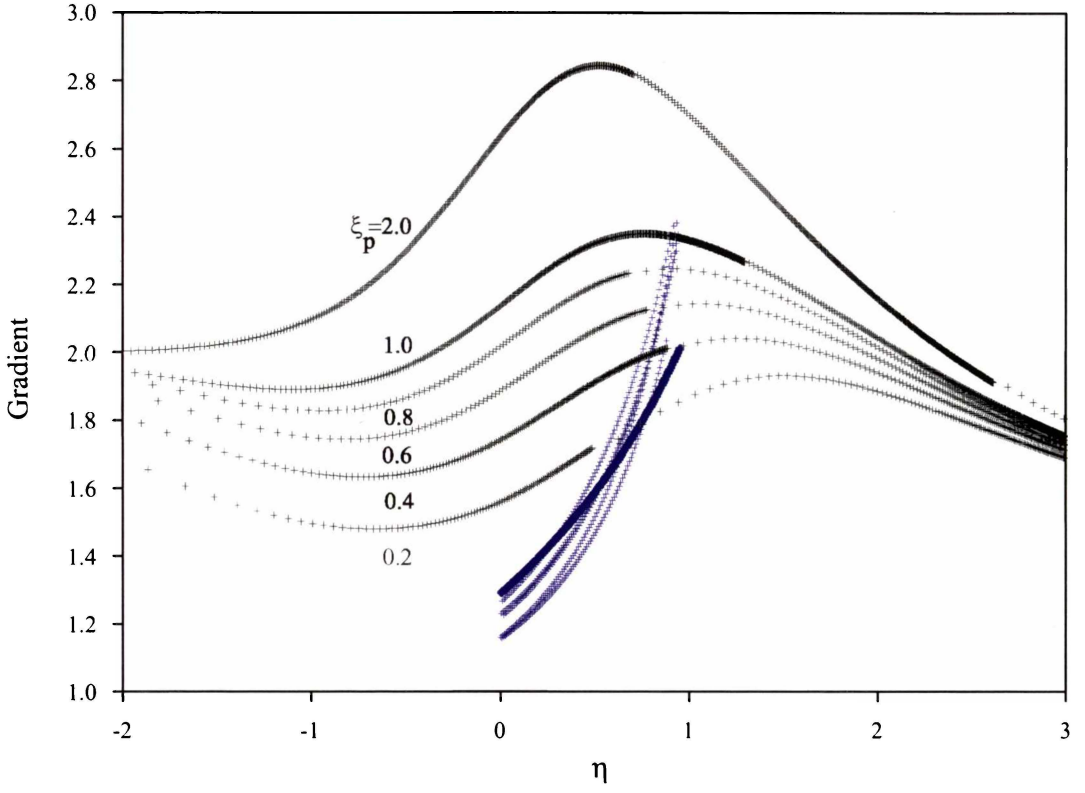

Figure 7.27 : A plot of the experimental 200 V data (0.5 A - 3.0 A) gradients (blue) of the double probe ion current plotted against the theoretical gradients (black) from the radial motion theory.

In general we can observe the slope of the saturation curves plotted against the applied potential, shown in figure 7.28. It is a trivial exercise to show that if $I^x \propto V$ ($I^x = kV$), then $x = d(\log_{10}(V)/d(\log_{10}(I))$. From this plot it can be seem that OML is not fully followed either since the gradients rises to, and passes the OML value of two for both the single and double probes. For the double probe the average of the gradient between 20 V and 60 V does tend to two and hence we should expect that the curve fit should be less accurate at these outer values and match at approximately 40 V. An indication of this can be seen in figure 7.12 where the variation is not nearly as clear as it is in figure 7.28 where the gradient is plotted. Thus, in this instance, if the OML ion density was to be correct, the gradient of the I^2 - V curve needs to be determined at -40 V (figure 7.28 shows the modulus of the applied voltage).

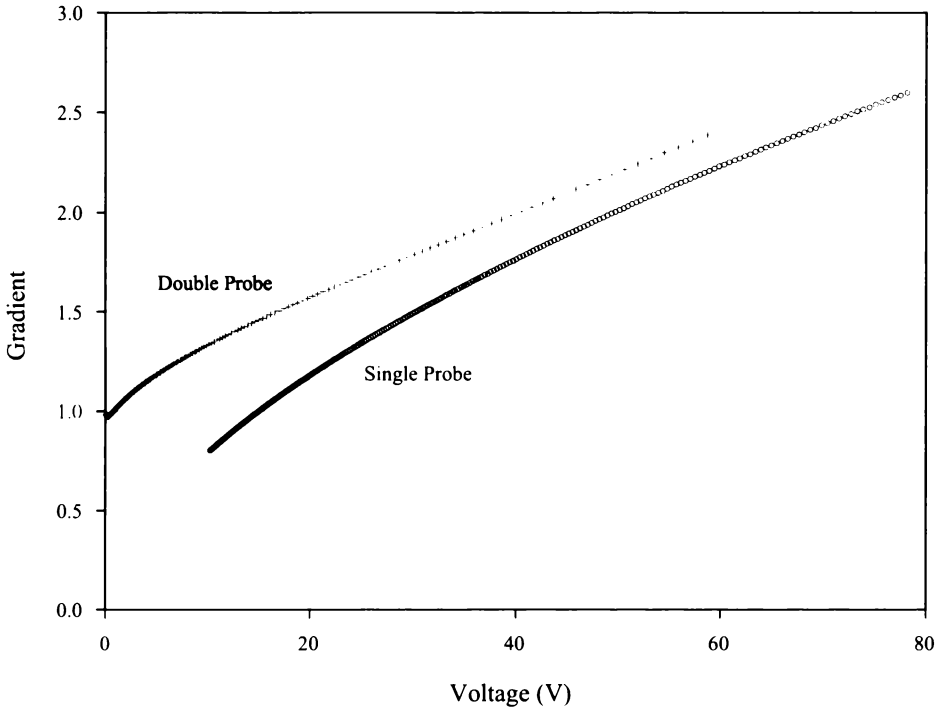

Figure 7.28 : The gradient of the single and double probe ion saturation currents plotted against the normalised applied voltage to the probe for the discharge conditions 200 V, 1.0 A. The data is normalised to the space potential.

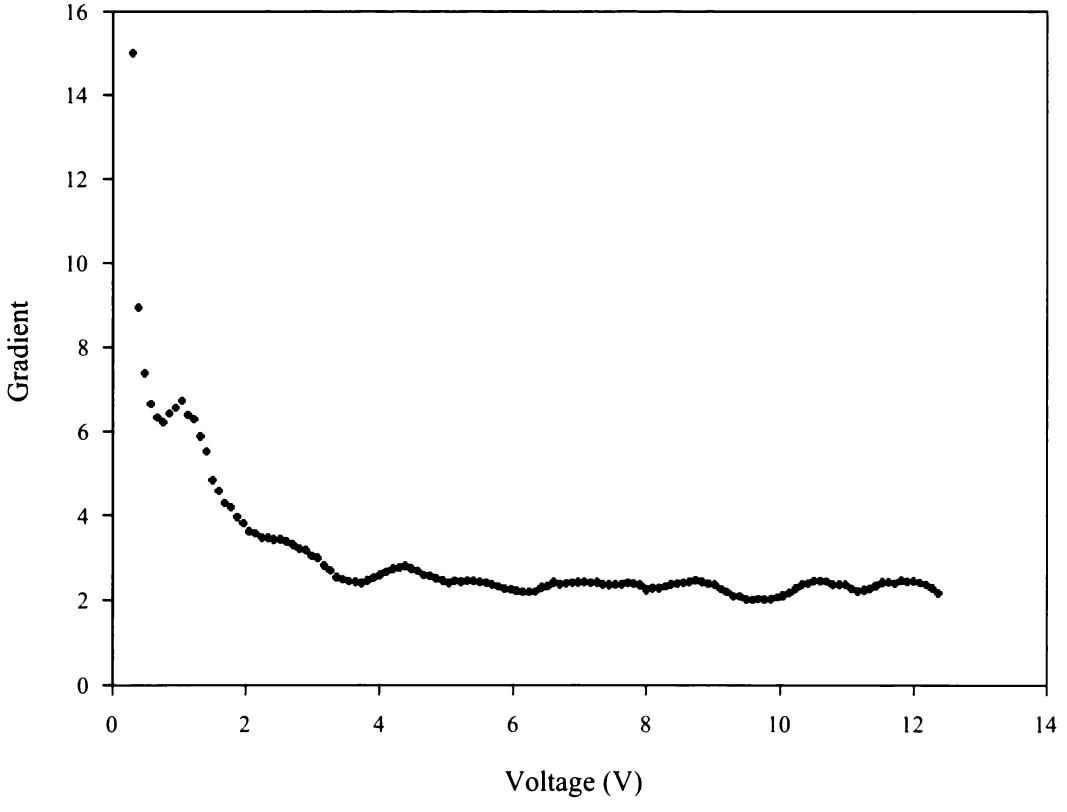

Figure 7.29 : The change in gradient for a single probe electron saturation current for the discharge conditions 200 V, 1.0 A normalised to the space potential.

Similarly for the single probe data "OML" is obtained at -50 V where the gradient passes two.

In a similar manner to the ion current gradient analysis we can calculate the dependence of the electron saturation current on the applied potential to see if OML is followed. As for the ions, a slope of two is expected but there is no radial theory available for comparison since it is for ions only. From figure 7.29 it can be seen that the gradient of the electron saturation current falls to, and maintains an approximate value of two as theory predicts, indicating that the OML theory is followed.

Thus, contrary to previous analysis, the ions *do not* follow either the radial or OML theories and hence their densities are incorrect. For both theories, the calculated density is higher than it would be if the theories were followed, a fact confirmed in figure 7.26. The electrons do follow OML and hence return, within the bounds of the theory, the correct density. From simply observing figures 7.8 and 7.12 one cannot tell that the electrons follow OML while the ions do not.

7.3.6 Summary of Plasma Properties and Related Calculations

7.3.6.1 Temperature Determination

The previous sections illustrate the methods used for the analysis of the probe data. The plasma experiments were conducted at only two accelerating voltages. The reasons for this were that the plasma was unstable at higher accelerating voltages (> 300 V) where it could switch to an arc, and the inability of the plasma to sustain a sufficient discharge current under 200 V. Thus experiments were conducted at the 200 V and 300 V accelerating voltages. The discharge currents at these voltages were incremented in 0.5 A steps up to 3 A. Beyond this current, the O-ring seals of the vacuum system melted and in one case the glass Pyrex discharge tube became sufficiently fluid to allow the pressure gradient between the vacuum and the atmosphere to push a hole through the tube wall and cause catastrophic vacuum failure. Power levels over 1000 W were inclined to be destructive with respect to the experimental equipment in time frames under one hour, while those under 200 W did not produce plasma of sufficient temperature and uniform density.

Figure 7.30 shows the final calculated temperatures and their error ranges The plot shows the single probe low temperatures and the double probe values as the high temperatures. The high temperature single probe values are considered to be in error due to their sensitivity to the removal of the ion saturation current.

In light of the previous sections on the Langmuir probe analysis where it was found that a significant error source was the small variation in the plasma discharge

conditions, the error range has been calculated over the entire variation of the calculated temperatures. Each individual measurement is accurate to ±2% but the random error introduced by the discharge conditions pushed this out to a maximum of ±10% while the errors were on average ±5% when the highest and lowest temperatures were taken into account for a particular discharge condition. Even with this discharge variation the errors are still quite small. Considering figure 7.30 it can be seen that the 300 V discharge range produces temperatures that seem more consistent and follow a more steady progression as the plasma discharge current is raised.

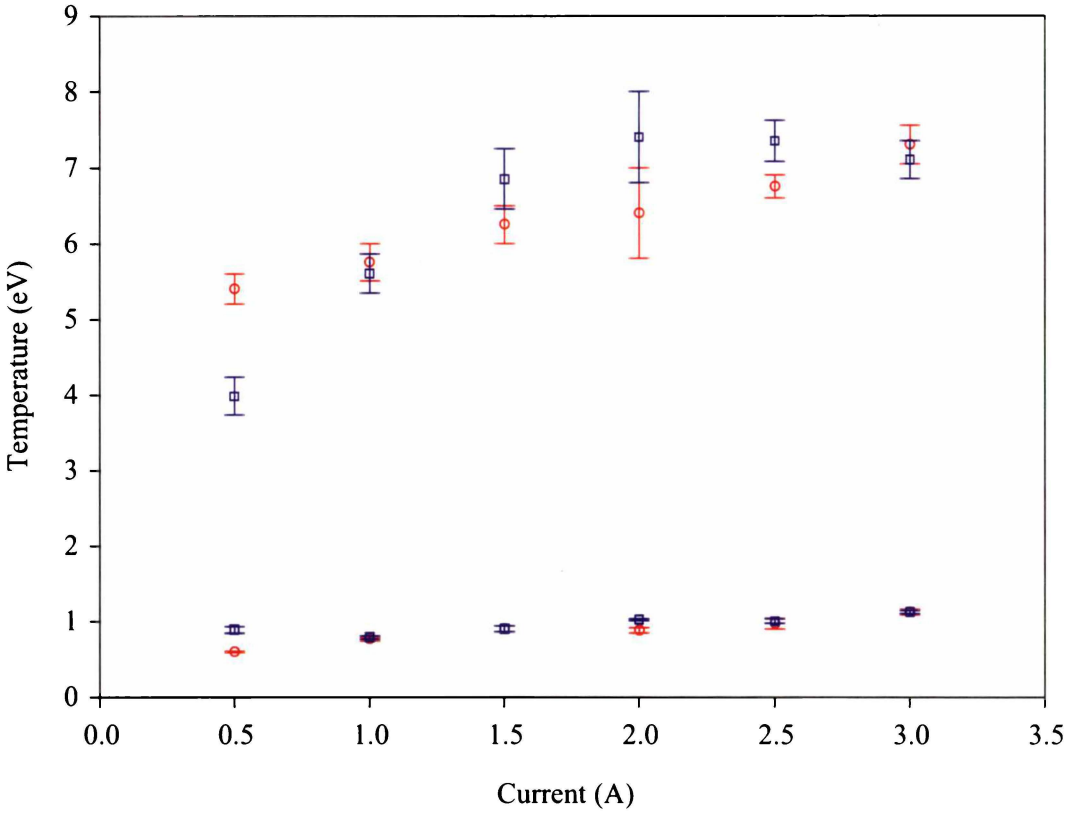

Figure 7.30 : Electron temperatures calculated (with errors) from the Langmuir probe data. The blue squares are the 200 V data while the red circles are the 300 V data.

The reason for this is that with a 300 V acceleration the electrons acquire energy faster from the electric field and hence can undergo more energetic collisions more frequently resulting in a more "Maxwellian" plasma distribution. A significant number of initially accelerated electrons will retain some of this energy and thus have a distribution temperature well above the mean electron temperature. Since we have not employed a transverse magnetic field, which would effectively increase the path length for electrons from the cathode to the anode, the number of collisions per electron is relatively low, and hence it is not surprising as shown in figures 7.6 and

7.7 the distribution functions are somewhat removed from Maxwellian. Simply put, the electrons do not suffer the number of collisions between the cathode and the anode necessary for equilibrium to be approached.

As noted earlier, the single probe data shows a dual electron temperature. One "temperature" increases from 4 eV to 7.5 eV over the range of discharge collisions and is for the non-equilibrium electrons, while the other "temperature" remains reasonably constant at 1 eV. The lower electron temperature is likely to be the "true" equilibrium value of the plasma, while the higher values are for the group of electrons that suffer fewer collisions. Alternatively it is possible that the lower temperature is representative of the electrons knocked out of the ion shells i.e., the electrons lost by the atoms and molecules upon ionisation, while the higher energy distribution consists of the electrons accelerated from the filaments which have generally not lost sufficient energy to reach an equilibrium temperature. It was observed in analysing the data across discharge conditions that the high electron distribution became more and more dominant so that an increasing portion of the semilog plot curve was from this distribution. The portions for each distribution can be seen in figure 7.23.

7.3.6.2 Density Determination

The calculation of the plasma density allows for both OML and radial motion theories to be used, enabling a comparison between the Langmuir equations, and the more elaborate calculations of Chen (1965). As seen in section 7.3.5 the densities, similar to the temperature calculations, are the most accurate and consistent from the single probe electron saturation regime using the OML theory. They are also self consistent with the theories mentioned above. Again the density values given for each discharge condition will be assigned an error so that the variation across the values calculated will fall into the error bands. The densities are shown in figure 7.31 where it can be seen that the density values are more consistent across the 300 V discharge potential, while the errors in general are approximately ±4 %.

The analysis of a nitrogen plasma across a variety of power levels was to determine a suitable choice of plasma voltage and current parameters for initial coating work. However, from manufacturing considerations and considering the power dissipation of the cooling system, higher currents simply caused faster breakdown of the O-ring seals around the filament areas. These had a typical life of a few hours. Heat dissipation from the AC current in the filaments caused this problem. Furthermore, voltages over 350 V created momentary transitions to a spark discharge before switching back to normal plasma discharges. Thus the initial choice for coating experiments was a voltage range of 300 V where the temperatures and

densities are most consistent while the current was chosen to be 1 A to avoid overheating problems. Thus the plasma discharge conditions chosen for the coating experiments were $T_e = 5.75 \pm 0.25$ eV, and $N_e = 2.4 \times 10^{10} \pm 0.2$ cm^{-3}.

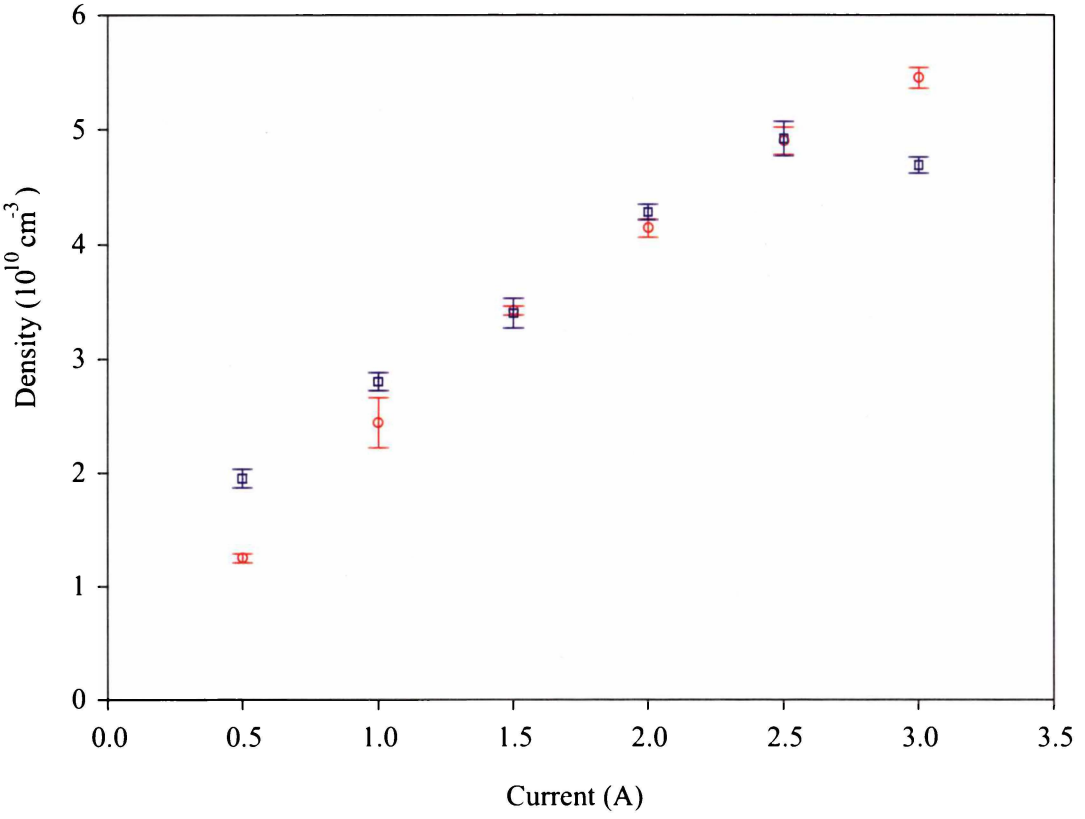

Figure 7.31 : The electron density of the plasma for various discharge conditions where the squares are the 200 V data and the circles the 300 V data.

7.3.6.3 Fundamental Parameters

With the electron temperature and the plasma density determined for a N_2 discharge, the Debye length, mean free paths, and volume throughput could be calculated. These parameters also relate to the following sections on the coating experiments since the temperatures and densities calculated for pure nitrogen plasma experiments are the same (see chapter eight) as those used in the coating experiments. We begin by calculating the mean free paths, which turn out to be similar for nitrogen and carbon monoxide.

Several types of "free path" can be obtained from theory presented in chapter three. These calculations require the dimensions of the molecule, a matter not considered until now. Since the nitrogen molecule is not spherical, the simple solid sphere model approximation is difficult to apply. Experimental averages have to be used for cross-sections and the like. At a pressure of 1 Pa (10^{-2} mbar) there are 2.45×10^{20} particles/m^3 while the gas temperature is approximately 500 K. From these data

and the equations in chapter three we find that we have a neutral-neutral mean free path of 1.9 cm, an electron-nitrogen MFP of 10.7 cm (equation 3.6), an elastic electron-neutral MFP of 1.3 cm (figure 3.11) and ionising mean free paths of 8 cm or 16 cm at an energy of 100 eV using data from figures 3.6 and 3.7 respectively. This larger value of 16 cm is likely to be more accurate since the ionising MFP should be greater than the total electron MFP of 10.7 cm. Further values of interest are that the ion-neutral MFP is 2.6 cm while the ion-ion MFP is 219 m. All of these values are the estimated minimum values for these plasma parameters as they correspond to the peak cross-sections. In other words, they are minimum mean free paths possible under the correct energy conditions. For the same conditions, the Debye lengths range from 0.16 mm to 0.07 mm. These figures indicate that gas collisions should play little part in the sheath dynamics due to their much larger mean free path, and that the sheath should be "collisionless". However, if ionised particles are trapped in orbits about the probe, the distance they travel within the sheath or pre-sheath area is greatly increased and then collisions are possible. From the Debye lengths we find that the probe radius to the Debye length ratio covers a range from 1.6 to 0.7.

The typical gas flow rates used were around 14 sccm (standard cubic centimetres per minute) which indicates that the plasma chamber is swept out about 4 times per second.

7.3.7 Radial Density Variations and Mobility

From sections 3.6 and 3.8 it was shown that the drift velocity of the ions is proportional to the density gradient across the plasma (equation 3.37). This implies that if the density gradient is low, the random velocity of the ions must be much greater than their drift velocity to the walls. The density gradient across the nitrogen plasma has been experimentally determined (300 V, 1.0 A) and is presented in figure 7.32 for the ion and electron density. The distance axis is measured from the chamber wall to the approximate centre of the chamber, 10 cm from the walls.

From Langmuir (1929) the potential drop between the centre of the plasma and the sheath edge is given by

$$V_m - V_s = 1.98 \times 10^{-4} T_e \log_{10}(1 + a/24\lambda_p) \tag{7.1}$$

where V_m - V_s is the potential difference, T_e is in degrees, a is the distance between the electrode sheaths, and λ_p is the mean free path of the ions. Using the data summarized in section 7.3.6 this potential drop is 2 V. Such a low voltage is expected since the electric field produced by this potential causes the density gradient. The calculated E/p_0 ratio is 26.6, for which the electron mobility, from von Engel (1965),

is approximately 9×10^4 ms^{-1}. The random electron velocity from equation 4.2 is 1.5 $\times 10^6$ ms^{-1} indicating that the random velocity is ~ 17 times the drift velocity. Thus diffusion plays a minor role in the movement of the ions and electrons, and confirms the radial plasma density variation shown in figure 7.32.

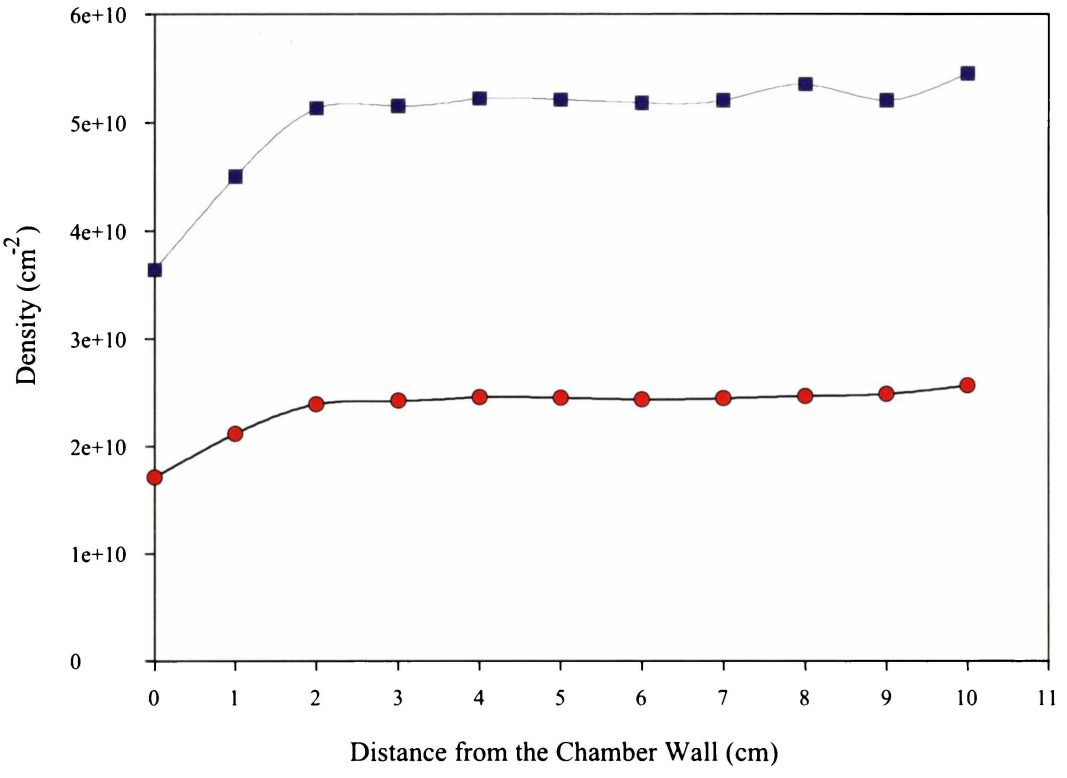

Figure 7.32 : A plot showing the electron and ion density across the horizontal chamber profile. The distance scale is referenced to the chamber wall so that 10 cm is approximately the centre of the plasma. The circles represent the electron density while the squares are the ion density.

7.4 Critical Literature Review

Since probe diagnostics are the easiest and most important technique to determine the density and temperature of a plasma, there have been a large number of papers published in this area, usually as part of a wider investigation into the particular plasma in question. Full coverage of such a broad area is not feasible, so comparisons will be made with those papers that concern automated systems such as the one presented and used for measurements in this thesis, as well as those that try to correlate the measured data with theory. Papers that simply present results with no theoretical comparison, or basis for accuracy, will be ignored.

The first direct comparison of any probe theory was by Tonks and Langmuir (1929A, 1929B) where it was found that the ion currents were much greater than theory (OML) predicted. From these experiments it was also common for the intercept of the curve fit to the I^2 - V plot at I = 0 not to pass close to the space potential.

After the theoretical formulations and solutions instigated by Allen, Boyd, and Renyolds (1957) (ABR) a comparison between the new theories and experiment was available. These comparisons are still ongoing ~50 years later since some researchers find one theory works while others don't. To facilitate these comparisons Sonin (1966) created a new form of plot where the comparison could be made independently of the plasma generation conditions. His interest was the analysis of flowing plasmas such as those surrounding rockets passing through the atmosphere rather than confined, stationary laboratory plasmas. The comparison was to take a value of the ion current at some normalised position, usually -10 or -15 kT_e/e, below the space potential and plot it against a normalised current to obtain a graph onto which the ion current theories are also plotted. The original plot is reproduced in figure 7.33 along with an equivalent plot calculated from the experiments of Annaratone *et al.* (1992).

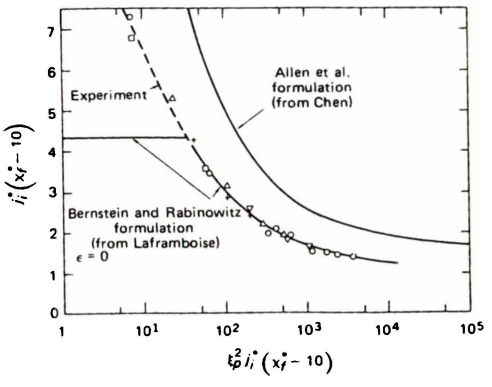

A) Sonin (1966)

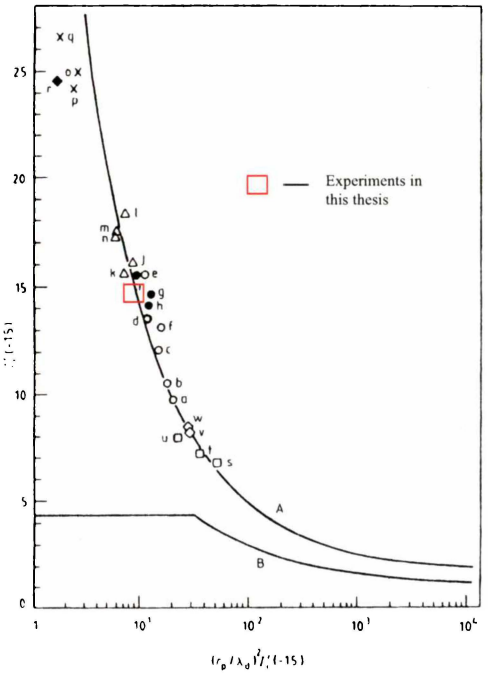

B) Annaratone *et al.* (1992)

Figure 7.33 : Two forms of the Sonin plots. Part A is the original plot devised by Sonin (1966) showing that although the data follows the Laframboise (1966) calculations, it continues past the theoretical limits of this theory. Part B shows the values obtained by Annaratone *et al.* (1992) where the data follows the ABR zero temperature ion theory. The position of the experimental data determined in this thesis is also shown.

Sonin (1966) originally found that the experimental data, while initially following the Maxwellian theory of Laframboise (1966), fails to match when OML is reached (the horizontal lines in figure 7.33). He conjectured that ion-ion collisions affected that data, and without this influence the experimental curve in part A of figure 7.33 should be shifted upwards to match the ABR formulation. Annaratone *et al.* (1992) found such a shifted curve for measurements in a RF generated argon plasma at a pressure of 5 Pa (5×10^{-2} mbar).

The conclusion made by these authors is that, although the theory of Laframboise (1966) is a better physical formulation (ions have a Maxwellian distribution) and should be more accurate, in practice it is not. It only matches the experimental data when collisions in the sheath occur, a process not accounted for in either theory. The lesser approximations (ions have zero initial energy) of the ABR theory inexplicably match the experimental results although they should not. This is the basis for the ambiguous choices of theory used to analyse Langmuir probe data. Superimposed on plot B of figure 7.33 are the calculated values obtained from probe measurements recorded during this research. It provides a contradictory view to that previously discussed where it was shown that the experiments, when analysed in terms of gradients, did not conform to the ABR theory.

Smith and Plumb (1973) recorded cylindrical Langmuir probe characteristics in the afterglow of noble gas plasmas at 0.1 Torr generated by RF pulses. The resulting data was analysed using OML theory. Ion densities always exceeded the electron densities, regardless of which noble gas was used. An empirical dependence of the ion density on the ion mass was proposed which matched the ion density increase across various noble gases correctly. The electron densities from the Langmuir probes were confirmed by microwave diagnostics in conjunction with other researchers, and were determined to be correct.

Hopkins and Graham (1986) published a comprehensive examination of experimental Langmuir probe data and compared them to the theories previously discussed in this chapter. The plasma generation method was similar to that described in this thesis except that permanent magnets were used to confine the plasma, allowing a lower pressure to be examined (0.13 to 1.3 Pa) to reduce the influence of ion collisions. They found that (in agreement with the results presented here) the ion density was consistently 1.2 to 1.6 times higher than the electron density regardless of the gas used (hydrogen and argon), the pressure, and even with the removal of the magnetic field. They conclude that, similar to Smith and Plumb (1973), the value of the electron density is correct and that a more detailed investigation was necessary to determine the discrepancies in the ion densities.

Chatterton *et al.* (1991) obtained cylindrical probe characteristics from an argon RF plasma using self-compensating probes. At pressures of 2.66 and 5.33 Pa they found that the ion density was approximately twice the electron density using OML theory. They state that these differences are "true for all other workers in this area" and provide several possible explanations. These include possible contamination of the plasma with particles that could form electronegative ions, and problems associated with the current ion collection theories.

Rodgers *et al.* (1992) recorded cylindrical Langmuir probe characteristics in the afterglow of a pulsed, unmagnetised plasma. The type of gas used was unspecified. An iterative fit using parameterized solutions calculated by Laframboise (1966) was applied to the data. This fit matched the raw data well and it was then assumed that the values obtained from this method were correct. As previously discussed in this section, this theory is generally not believed to represent the ion current at these densities (2.3×10^9 - 2×10^{10} cm^{-3}), and from the ion current analysis earlier in this chapter "good data fits" can be deceiving. Further methods such as OML and simple Langmuir probe theory were used to calculate the ion and electron densities which were in disagreement with the Laframboise analysis by values of up to 2.5 times. The authors note that $T_e >> T_i$ may not have been valid for the measurements and state that the ion current saturation is not a very reliable method of calculating the ion density. However, they conclude that the numerical calculations of Laframboise (1966) have been validated in the regime $0.5 < \xi < 5$ and even provide empirical correction factors for the other theoretical methods.

Sudit and Woods (1993) used a DC hollow cathode glow discharge utilising nitrogen as the discharge gas to obtain Langmuir probe data which were analysed for electron distribution functions. This paper was primarily to test a new discharge configuration and an automated data acquisition system. The negative glow and the positive column of the resulting plasma were analysed. For the negative glow, densities of 2.7, 2.3, and 1.9×10^{10} cm^{-3} were obtained for the ion density using Laframboise's theory, the OML electron density, and integration of the electron energy distribution function (EEDF) respectively. In the positive column, the EEDF integration yielded 8.35×10^{10} cm^{-3} while those from Laframboise's ion current analysis were an order of magnitude higher and were deemed to be incorrect.

In a more detailed paper, Sudit and Woods (1994) compared the electron and ion densities of helium and nitrogen using cylindrical and planar probes with microwave measurements. A variety of theories were used and the conclusions of the research determined that the OML electron densities matched those obtained from integration of the EEDF over the entire parameter space investigated and were in acceptable agreement with two non-probe density determinations. The ion currents

however, whether determined by OML, ABR or Laframboise theory exceeded the uncertainties in the non-probe densities. Differences up to an order of magnitude were found in some instances.

Batani *et al.* (1997) applied Langmuir probe analysis to a low density, low temperature toroidal plasma discharge plasma with a high magnetic field. The paper details that even the electron density can be erroneous in such a high magnetic field plasma. However, the cylindrical "probes" used are 1 mm in diameter and 2 mm long which invalidate the assumptions of the various probe theories used. Furthermore, no end effect corrections have been applied which would certainly be significant for a probe with these dimensions. Even the correction of the results to compensate for the data acquisition circuit significantly altered the probe characteristic.

Chen (2001) has analysed all the major ion current probe theories (OML, ABR and Laframboise) for their validity in high density ($> 10^{11}$ cm^{-3}) argon plasma. Extensive analysis routines for each of the three main theories were developed, as detailed in this paper, to minimise errors and provide an iterative least squares method until self-consistent results were obtained. These are now available from the author's laboratory home web page (http://www.ee.ucla.edu/~ltptl/presentations.htm). The resulting densities from these analyses were then compared to those obtained from microwave measurements where all theories were found to give erroneous results. After analysing this data, Chen *et al.* (2002), found a compromise that allowed the correct calculation of the ion density. This was to modify the ion current by raising it to the power of 4/3 (rather than 2 for OML) to provide an estimate of the ion saturation current which could then be used to correct the data and the density determined from the electron component of the I - V curve. The method is assumed to work by cancelling out two competing effects that are neglected, the cylindrical curvature in the sheath thickness calculations and the orbiting of ions about the probe.

7.4.1 Data Analysis Comparison

The analysis methods used by Chen (2001) include a raw I - V characteristic which can be analysed by the methods determined and used in this thesis. Figure 7.34 shows the gradient of the electron saturation regime where it can be seen that the OML gradient of two is not reached until the maximum applied voltage (16 V) is reached. In figure 7.29 for comparison, OML is attained at six volts above the space potential. Either OML is not followed at these densities, as Chen (2001) concluded, or an insufficient voltage was applied to satisfy the conditions of OML.

For the ion saturation current, the curve could not be differentiated directly and a curve fit to the data was differentiated instead. The data, by inspection, was

recorded via the voltage across a single current sensing resistor and hence the ion current resolution was low. The gradient of the ion saturation current is shown in figure 7.35 where the dependence on the applied voltage is different to the analyses of the data in this thesis. From figure 7.35 it can be seen that the gradient is approximately two, but does not follow OML from the analysis of Chen (2001). By analysing this curve, the nature of the collection can be inferred. For voltages below 22 V, the effect of the high energy electrons in the Maxwellian distribution can be seen. At 22 V a full ion sheath forms and all electrons are repelled. This voltage represents the maximum gradient and hence the sheath must be too thin for orbiting to occur. Beyond this voltage where the gradient falls and then subsequently rises, it can be assumed that orbiting does occur. The value of ξ for these data is 3.9, which from figure 4.13a indicates that no orbiting should occur. The indication that it does occur is clear and supports the conclusion of Chen (2001) that the theory does not match the experimental results.

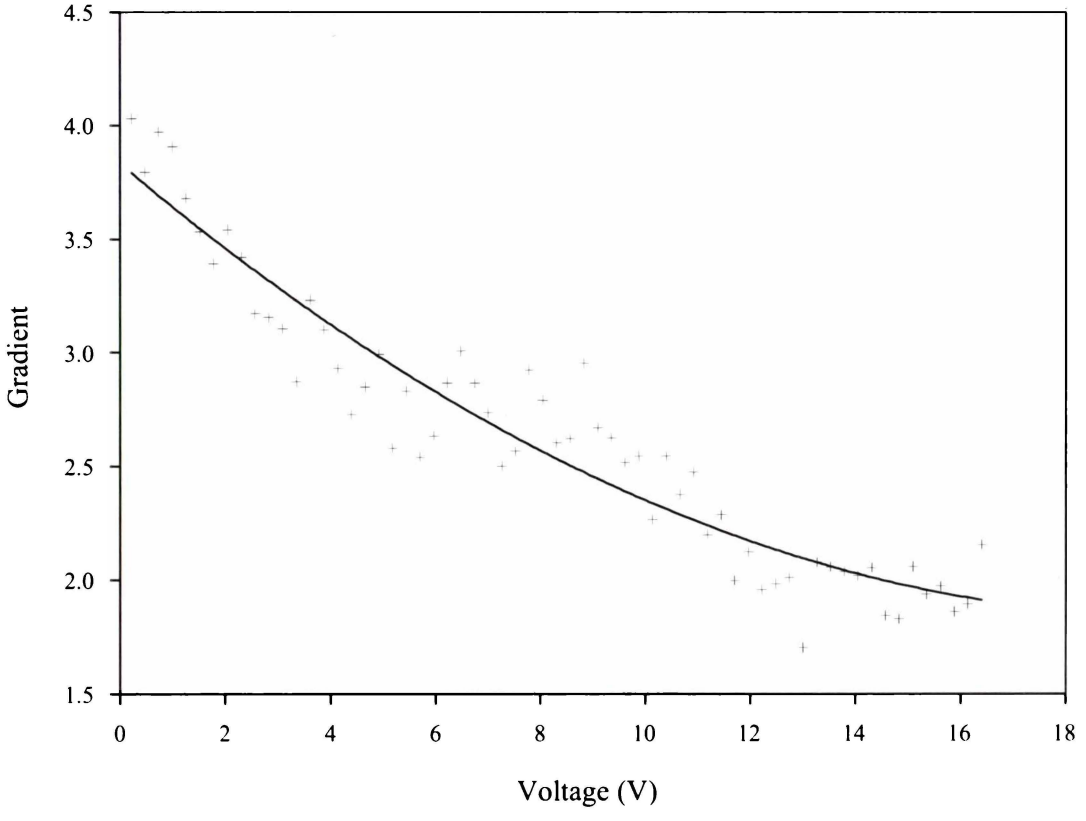

Figure 7.34 : The gradient of the electron saturation regime plotted against voltage, normalised to the space potential. A quadratic curve fit to the data has also been included to show the general trend. The data used is from Chen (2001), (http://www.ee.ucla.edu/~ltptl/presentations.htm).

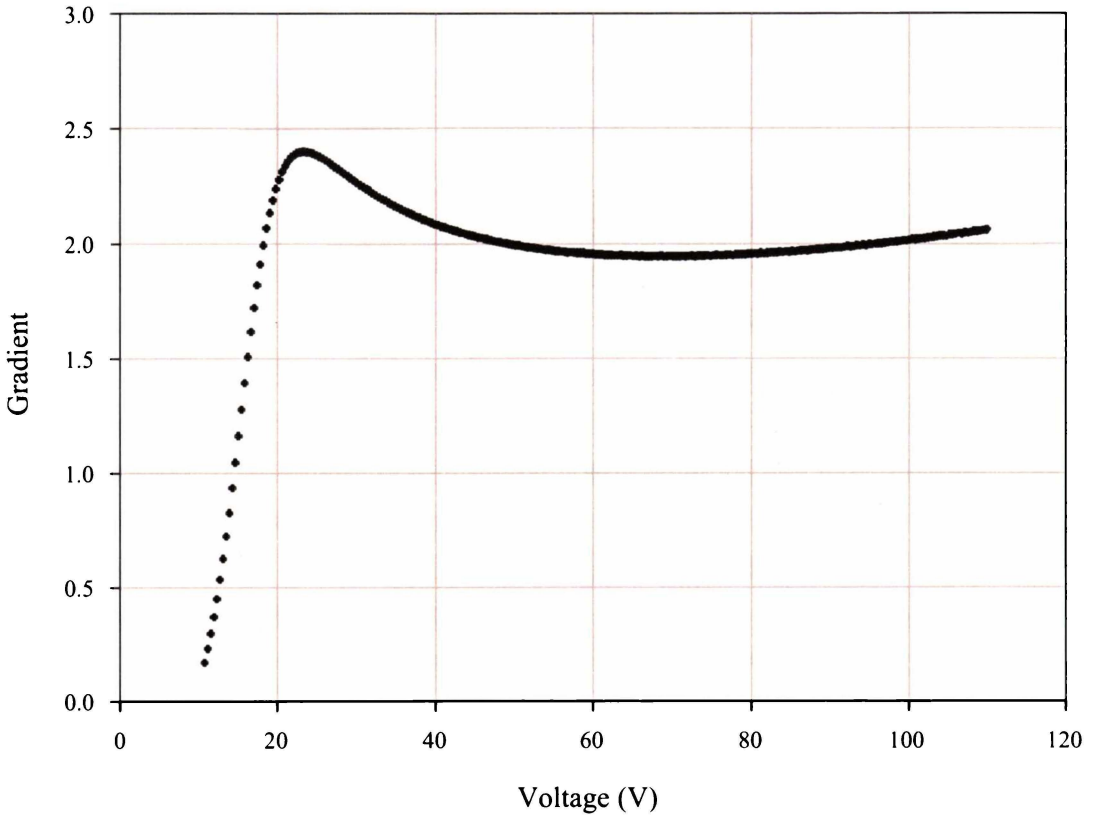

Figure 7.35 : The gradient of a curve fit to the ion saturation current, normalised to the space potential. The data used is from Chen (2001), (http://www.ee.ucla.edu/~ltptl/presentations.htm).

7.5 Summary

From the analysis of the Langmuir probe data in this chapter, it can be seen that data from both double and single probes needs to be collected to definitively determine the temperature, density, and distribution functions of the electrons and ions. It has been shown that by careful analysis of the data, the generally believed conditions for the application of radial or OML theories can be incorrect. The best method to test compliance of the experimental data to a particular theory is to determine the theoretical and experimental dependence of the observed current on the applied voltage for comparison. This method conclusively showed that the ion saturation regime neither follows OML nor radial motion and contradicted the generally held belief that a linear I^2 - V fit with an intercept at approximately T (eV) below the space potential is a sufficient condition for OML.

Experimentally it appears that the electrons have a sufficiently high velocity, and thus angular momentum, for OML to be followed. The ions do not have this feature. From chapter six it was determined that the ion temperature was almost room temperature so they have much lower random velocities than the electrons, after

taking the mass difference into account. This must provide them with a distribution of angular momentum that is too low for OML to be followed, but too high for the purely radial solution to apply. The angular momentum they do gain will be primarily from their transit through the presheath region where they must fulfil the Bohm criterion.

These results hold some difficulties for RF plasmas since a complicated setup is needed to acquire data from a double probe system. Furthermore, the entire set of Langmuir probe theories relies on the assumption that the positively charged species (the ions) all have the same charge, and the same mass. It is common in nitrogen discharge plasmas at low pressures to have significant amounts of N^+ ions as well as the normal positively charged molecules. This is of particular importance to RF nitriding processes (for instance Conrad *et al.* (1987) and Tang *et al.* (1993)) and high density plasmas where the input power is high, Chen (2001). If there is a significant dissociation of charged molecules into charged ions, the analysis of Langmuir probe data will be incorrect regardless of the approaches used since no theory has been developed to account for ions of different mass. This dissociation affects both the ion saturation current and the electron temperature since it was shown in this chapter that the ion subtraction process can drastically affect the calculated temperature. Chapter five in this thesis showed that no dissociation of nitrogen molecules into their constituent atoms occurred so the Langmuir probe theories presented in chapter four could be correctly applied.

In the review of Langmuir probe analyses by different researchers, it was seen that the difference between the ion and electron density, found in the research of this thesis, has been observed before. Collisions in the sheath and charge-transfer collisions, and secondary electron emission were, in general, proposed as the reason for these discrepancies. In these papers, although OML appeared to be followed, no analysis like that presented here was completed to confirm or deny this postulation. For similar density plasmas generated in this thesis, no evidence of ion orbiting was found since no minima occurred in the gradients of the ion saturation currents.

Using the analysis methods described in this thesis, it has been shown by the analysis of the data from Chen (2001), that for high density plasmas, orbiting does occur.

7.6 References

Allen, J. E., R. L. F. Boyd, P. Renyolds, 1957, Proc. Phys. Soc. (London), **70**, p 297.

Annaratone, B. M., M. W. Allen, J. E. Allen, 1992, J. Phys. D: Appl. Phys., **25**, p 417.

Batani, D., S. Alba, P. Lombardi, and A. Galassi, 1997, Rev. Sci. Instrum., **68**, 11, p 4043.

Bohm, D., 1949, *The Characteristics of Electrical Discharges in Magnetic Fields* (McGraw-Hill, New York).

Chatterton, P. A., J. A. Rees, W. L. Wu, and K. Al-Assadi, 1991, Vacuum, **42**, 7, p 489.

Chen, F. F., 1965, J.Nuc. Ener.C., **7**, p 47.

Chen, F. F., 2001, Physics of Plasmas, **8**, 6, p 3029.

Chen, F. F., J. D. Evans, and D. Arnush, 2002, Physics of Plasmas, **9**, 4, 1449.

Conrad J.R., J. L. Radtke, R. A. Dodd, F. J. Worzala, N. C. Tran, 1987, J. Appl. Phys., **62**, 11, p 4591.

Hopkins, M. B., and W. G. Graham, 1986, Rev. Sci. Instrum., **57**, 9, p 2210.

Laframboise, J. G., 1966, *Fourth symposium on Rarefied Gas Dynamics*, edited by J.H. De Leeuw (Academic Press, New York), **Vol II**, p 22.

Langmuir, I., 1929, Phys. Rev., **33**, p 954.

Rodgers, J. H., J. S. De Groot, and D. Q. Hwang, 1992, Rev. Sci. Instrum., **63**, 1, p 31.

Smith, D., and I. C. Plumb, 1973, J. Phys. D: Appl. Phys., **6**, 2, p 196.

Sonin, A. A., 1966, A. I. A. A. J., **4**, p 1588.

Sudit, I. D., and R. C. Woods, 1993, Rev. Sci. Instrum., **64**, 9, p 2440.

Sudit, I. D., and R. C. Woods, 1994, J. Appl. Phys., **74**, 8, p 4488.

Tang, B. Y. , R. P. Fetherston, M. Shamin, R. A. Breun, A. Chen, J. R. Conrad, 1993, J. Appl. Phys., **73**, 9, p 4176.

Tonks, L., and I. Langmuir, 1929A, Phys. Rev., **34**, p 876.

Tonks, L., and I. Langmuir, 1929B, Phys. Rev., **33**, p 195.

Chapter 8 Coating Experiments and Analysis

8.1 Introduction

Alternative methods to electroplating, as discussed in section 2.4.2, are becoming increasingly important due to the stringent requirements on health, safety, and the disposal of contaminants and waste products from these methods. Consequences of these new requirements are driving up the cost of electrodeposition, and it is becoming increasingly attractive to search for alternative chromium deposition methods.

The purpose of these coating experiments was to attempt to form chromium films onto stainless steel substrates through the plasma deposition of chromium hexacarbonyl. The author considered this a likely plasma deposition precursor since it would easily break down under plasma conditions to its constituent parts. Carbonyl compounds are weakly bonded with the π backbonding to the vacant d orbitals stabilising the molecules. The literature indicates that a few researchers had attempted such a deposition procedure. These papers were reviewed in section 2.6.1 where the deposition processes include UV photolytic, electron beam, laser photolysis, pyrolytic, low and high pressure RF, and CVD methods. After examining these papers, it was found that the main containments in the metallic films were carbon and oxygen. A reasonable conclusion was that either the carbon monoxide molecules, released by the breakdown of the carbonyl molecule, were being dissociated and the resulting atoms incorporated into the films or that the ionised carbon monoxide molecule itself was being incorporated. The dissociation could either occur in the deposition process (due to the acceleration of the carbon monoxide ions onto growing film), or in the plasma itself. Regardless of the transport process of the carbon and oxygen to the film surface, the carbon monoxide atoms appeared to receive sufficient energy to dissociate in the plasma since the reported atomic compositions of these two elements were often different. A DC plasma system, detailed in chapter five, was chosen to conduct the coating experiments in.

8.2 Preliminary Carbonyl Plasma Analysis

Before deposition experiments were attempted, an investigation of the discharge formation and properties of chromium hexacarbonyl in plasma conditions were investigated. It was found that a small surface area (5 - 10 cm^{-2}) of the solid powder was sufficient to sublime the carbonyl into the vacuum system resulting in a pressure of 0.5×10^{-2} mbar. This was sufficient to produce and maintain a discharge which was blue-violet in colour. After running this discharge for over an hour, it was observed that the inside of the discharge chamber was covered with carbon. This was attributed to the transport of ionised carbon monoxide, through diffusion, to the boundary walls where some of the particles must have gained sufficient energy to dissociate. This process has been seen before by other researchers and is referred to as "sooting", and manifests itself in two forms. Either sooting occurs on the sample, or at the chamber walls. In ion plating, Mattox (1998) found that sooting occurred preferentially at the chamber walls when high rates of vaporisation were used, but was only a problem for system maintenance. He notes that sooting of the samples did not occur since the vapour phase of the condensed particles became negatively charged and hence were repelled from the negatively biased sample. Samples without a negative bias could suffer from the inclusion of the sooting products into the growing film.

From the experiments in a nitrogen atmosphere, detailed in chapters six and seven, it was seen that the optimum operating conditions were a pressure of 1×10^{-2} mbar with the discharge settings of 300 V and 1 A for the DC bias and current respectively. It was decided to use two different carrier gases to raise the pressure in the chamber so a 50:50 mix ratio of the carbonyl vapour and carrier gas would bring the total to the chosen pressure of 10^{-2} mbar. Nitrogen and argon were chosen as these gases for the following reasons:

Firstly nitrogen, as detailed in chapters three and six, behaves almost identically to carbon monoxide when the discharge phenomena is the 1st positive band. This is the dominant band structure found in the discharge as detailed in chapter six. The emission lines are within a few angstroms of each other and for a mix of carbon monoxide and nitrogen, the band structures could barely separated with the monochromator resolution employed in this thesis. It was thus expected that a 50:50 ratio of CO and N_2 would be virtually indistinguishable from a 100% CO or N_2 discharge. Spectroscopic evidence of this is shown in figure 8.1 where it can be seen that the peaks from the carbonyl-nitrogen mix superimpose directly on the pure nitrogen plasma peaks. From this figure it can be seen that there is a lack of carbon and oxygen emission lines indicating that, like the response of nitrogen to this discharge configuration (see figure 6.18), no dissociation of carbon monoxide occurs.

There are also no chromium lines. The strong lines from Cr II are just over 2000 Å which is outside the detectable range of the monochromator while the Cr I lines fall at positions where the band structures of CO/N_2 occur and would be swamped by them.

Secondly, it was possible, as per papers reviewed in chapter two, that carbon and oxygen could still be incorporated into the films by dissociation of carbon monoxide atoms. To reduce this possibility, a stable and non-reactive monoatomic gas, argon, was also chosen to be added, if needed, to the carbonyl vapour. The rationale was that molecular gases can store considerable energy in their rotational and vibrational states. Collisions with other molecules do not reduce this internal energy, it simply transfers it from one molecule to the other depending on the nature and type of the collision. From chapter six it was determined that the ion temperature was very low, hence the random velocities of the ions were low and thus a significant portion of the total molecular energy could be contained in vibrational and rotational states.

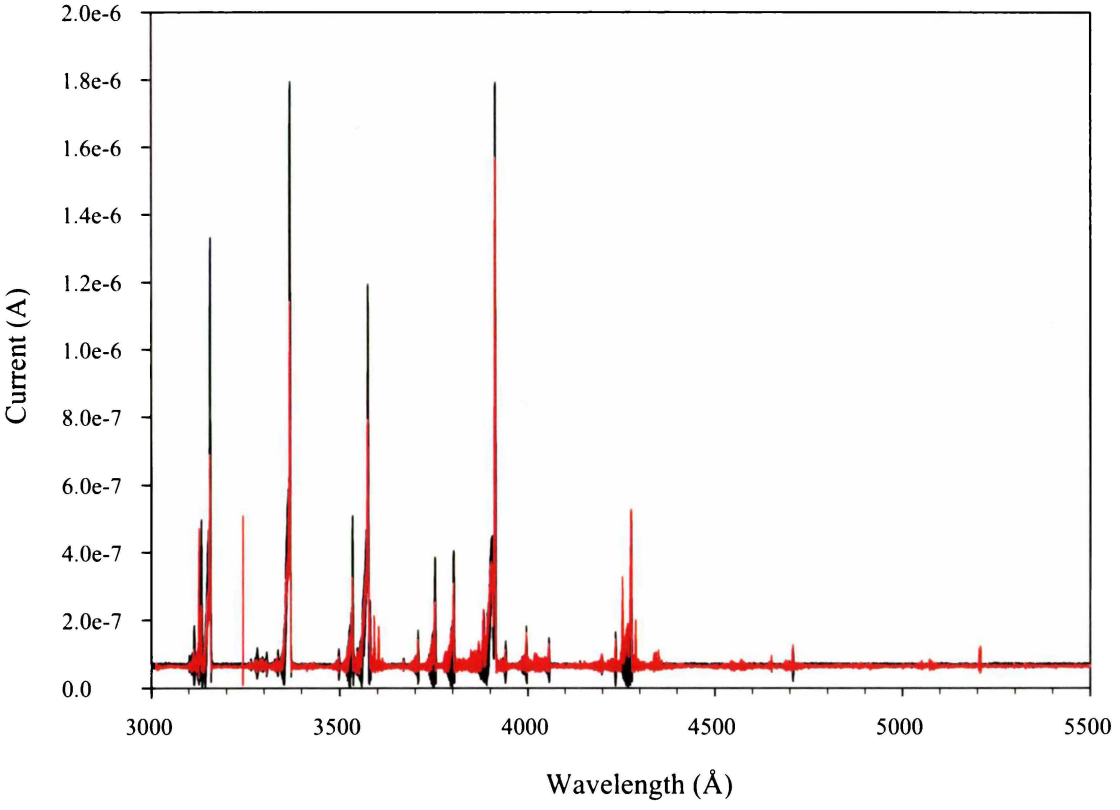

Figure 8.1 : The superimposition of a 50:50 mixture $Cr(CO)_6$ - N_2 plasma spectroscopic scan (red) over that recorded from a pure N_2 plasma (black) with the discharge conditions, 300 V DC and 1 A current.

Collisions between heavier atoms and lighter molecules would, in general, lower the energy in the vibrational and rotational states of the molecules since energy would be transferred to the atom from the molecule. Argon has a molecular weight of 40 while carbon monoxide is 28. Thus argon atoms are slower moving than carbon monoxide molecules and therefore collisions between them would drain energy from

the latter. This would leave the carbon monoxide molecules with a lower average total energy and hence would be less susceptible to dissociation. Some evidence for this can be seen in figure 8.1 where it can be seen that the peak intensities with Cr atoms in the discharge are lower than they are for the pure nitrogen discharge.

Argon can also be used as a bombardment gas, similar to the ion plating methods if the need arose. It was initially decided to not use accelerating potentials on the samples since bombardment by carbon monoxide atoms, at voltages below those used in ion plating, may still result in the ions gaining sufficient energy to dissociate on impact with the sample. This would result in unwanted impurities of carbon and oxygen in the chromium film, the contamination that we wished to avoid.

8.2.1 Langmuir Probe Analysis

After the initial observations were complete, Langmuir probe data was acquired from the carbonyl mixtures. The data acquisition and analysis was difficult to accomplish since the probes were subject to a greater degree of contamination in these gas mixtures. Hysteresis measurement checks on the probe were necessary for every scan to determine whether the probes had been contaminated. Hysteresis tests the validity of the probe data by determining if the current drawn to the probe is the same when the voltage is rising or falling. The application of a triangular waveform rather than a linear ramp to the Langmuir probes facilitated this verification. The results did indicate that contamination was a problem and great care had to be taken in the acquisition of the data. Furthermore, the probes had to be cleaned by ion bombardment after every acquisition cycle. An example of this hysteresis effect is shown in figure 8.2.

In general, the experimental Langmuir probe densities and temperatures matched those determined in chapter seven for a pure nitrogen discharge. There were exceptions however, but they occurred when the discharge fields were distorted by the bias applied to the sample. For example, sample 1 had a bias of +200 V applied to it, and the electron density obtained from OML theory was 1.63×10^{10} cm $^{-2}$. Since there is only 300 V applied between the filaments (cathode) and the ground ring (see figure 5.2) it is likely that the density difference occurred from this intrusive electric field.

Similarly for samples 7 and 8, when -30 and -200 V were applied to the sample, the densities obtained were 2.82 and 3.94×10^{10} cm^{-2} respectively. The density expected from a nitrogen discharge with a 300 V potential and a 1 A current is between 2.23 and 2.87×10^{10} cm $^{-2}$. Other coating experiments, where the sample was left floating, or was grounded, yielded densities of 2.47 and 2.73×10^{10} cm^{-2}, well within the range found for a nitrogen discharge. These density values for the coating

experiments (and the temperatures) matched those found for the equivalent nitrogen discharge when the sample bias was below that necessary to change the discharge configuration, i.e. the transition from a diode to a triode discharge. This potential was found to be approximately ±50 V, or under 20% of the discharge voltage. The variation of measured density vs. applied bias is shown in figure 8.3.

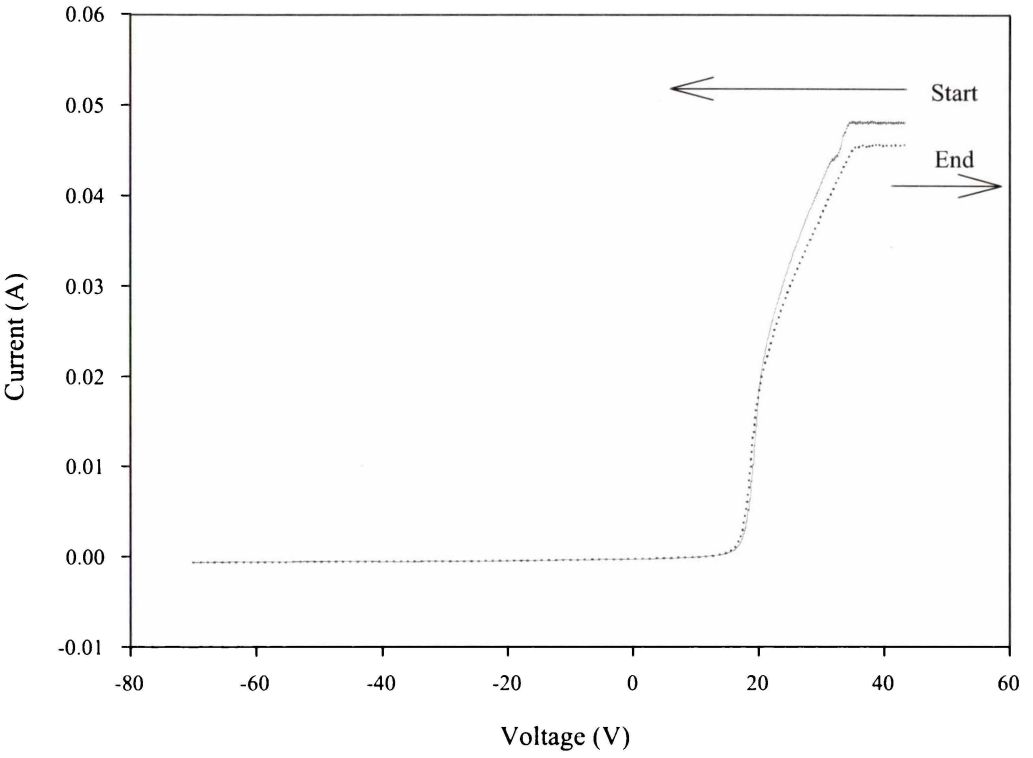

Figure 8.2 : An example of the hysteresis effect indicating contamination on the probe surface.

Every metallic object immersed in a plasma will act as a Langmuir probe, the samples being no exception. The presheath from the sample either created an electron deficient, or electron rich region around the sample, which ultimately affected the plasma conditions around the Langmuir probes since they were placed close to the samples. A negative bias will decrease the electron density surrounding the sample resulting in a higher electron density immediately outside the presheath (due to the reflection of electrons from the presheath boundary, i.e. the electrons cross this region of space twice). Any probe in the vicinity of this region will collect an increased electron saturation current resulting in a steeper gradient in the corresponding I^2 - V plot and hence an increased density. Similarly for a positive bias, the region outside the presheath is electron deficient since the electrons are accelerated into the sample sheath. This causes a constant drain on the plasma, causing an increased electron velocity in the region of the probe resulting in lower collection rates. Thus the measured density is lower than it would otherwise be expected.

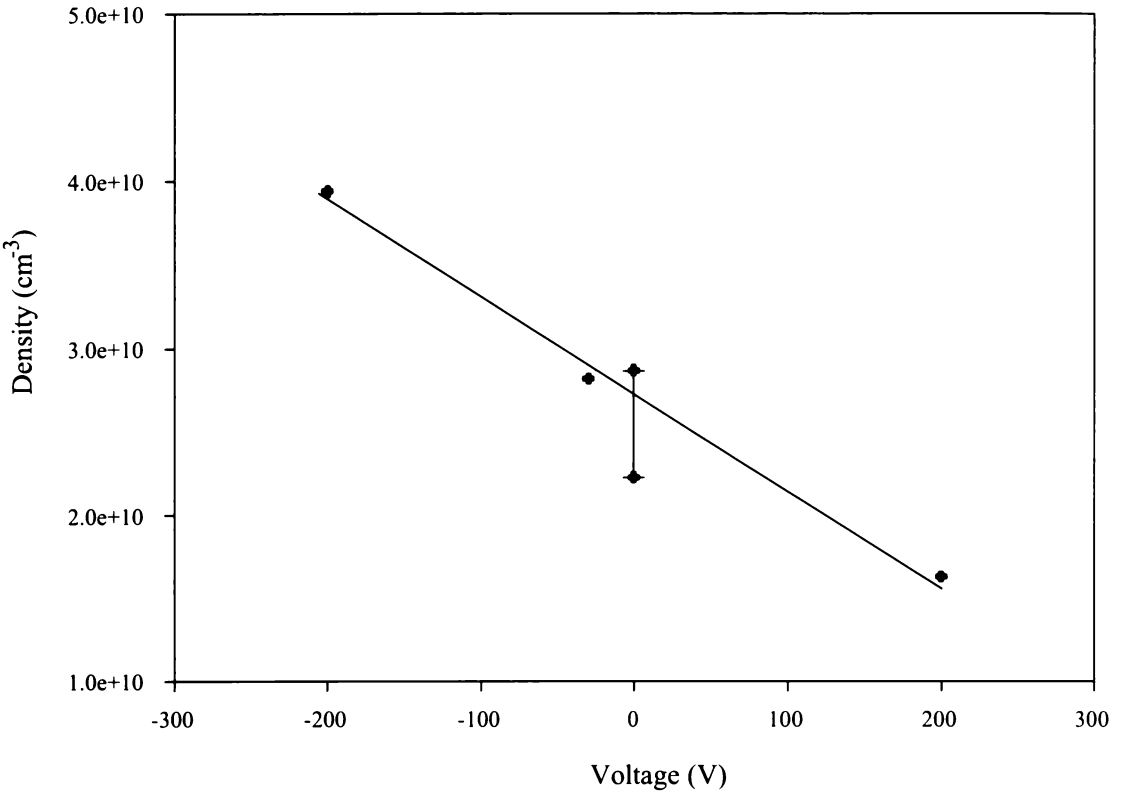

Figure 8.3 : The variation of OML electron density plotted against the bias applied to samples 1, 7 and 8. The two data points with error bars represent the high and low density values obtained in chapter seven for a nitrogen discharge.

8.2.2 Sample Preparation and Mounting

It was decided to attempt to coat chromium onto stainless steel rather than non-conductive materials since a bias could then be applied. Samples and a holder were designed to fit into a vacuum feed-through on one of the chamber side-arms shown in figure 5.1. The holder and the sample dimensions are shown in figure 8.4. The aluminium rod used as the vacuum feed-through is contained well within the area of the side-arm of the vacuum chamber so as not to disturb the plasma.

Preparation of the substrates involved polishing the surface with finer and finer grit paper until the final stage when 1 μm diamond paste was used for the final polish. This gave the surface a mirror finish. Before immersion into the plasma, the samples were thoroughly cleaned with acids, bases, and degreasing solvents. They were then washed clean of any residual chemicals with double distilled water and dried. Before any coating in the plasma commenced, the surface of the sample was bombarded with

the carrier gas (nitrogen or argon) in the same manner as the probes were to remove any contaminates and the oxide layer that is bound on the surface.

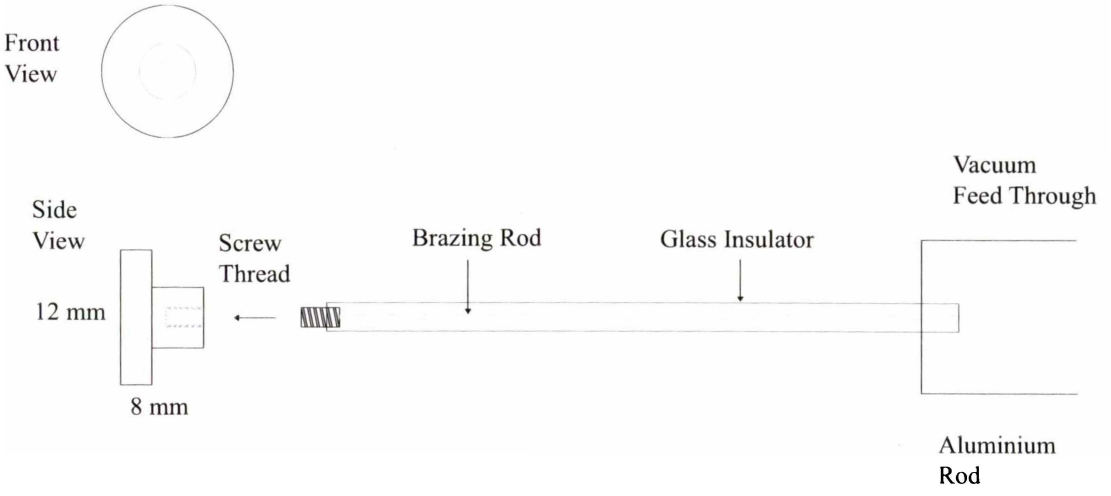

Figure 8.4 : A pictorial representation of the sample and its vacuum feed through.

There was a compromise in choosing the sample size as there is in any discharge configuration. The choice is simply between the surface area of the sample (and hence a restriction on the tests able to be performed) and the distortion to the plasma from the effective collection area. Any conducting body in a plasma will distort the plasma electric fields which is why Langmuir probes are constructed with such a thin wire to minimize these effects. The effective distortion is a combination of the applied bias (previously discussed) and the current drawn to the foreign object. If either is a significant draw or perturbation on the plasma, distortions will occur as can be seen in figure 8.3.

8.3 Initial Experimental Work

A series of eight experiments were initially conducted to determine the deposition mechanism of the chromium coatings and the effects varying the substrate bias had on the sample, and on the plasma.

From the previous sections, it was seen that no ionised chromium, or indeed any neutral chromium could be identified on the spectral scans. This lead to three possibilities, either there is no ionisation, no chromium atoms were present at all (if the carbonyl molecules didn't fully dissociate), or the emission lines were masked. As discussed, the main ionized peaks chromium occur at spectral wavelengths below those able to be measured and the neutral state could well be masked by the nitrogen/carbon monoxide band system intensities. It was determined to resolve this issue first, since if no ionized chromium is present, any film containing chromium

must be a CVD process. To test the deposition process, the first sample had a bias of +200 V. This was sufficient to repel all positively ionized species while leaving the neutral particles unaffected. Thus if the deposition process was CVD, a chromium coating would form which would be similar to others deposited at zero or negative voltages.

These eight samples were tested under varying bias conditions and carrier gases before analysis of the films formed was undertaken to determine their composition and surface structure. The samples could be observed *in situ* through a quartz window to observe the film growth. The films were black in colour and could easily be differentiated from the steel substrate during the experiments. The samples were coated for approximately one hour under the conditions shown in table 8.1 where the current to the sample is the normal definition (electron current is negative). This is contrary to the Langmuir probe analysis where the electron current is positive by convention.

Sample 1 formed a very poor quality film which delaminated almost immediately on removal from the vacuum system. Compared to later samples, the film was further determined to be very thin indicating that electron bombardment and the positive bias of the sample significantly slowed the film growth. Sample 4 was the only other experiment where a positive bias was applied to the sample. A better quality film than sample 1 was formed, and was able to be examined. At this sample bias, no ions should reach the sample and hence the film formed indicates that the coating (later confirmed to have a high chromium content) formation did contain a CVD component. The remaining 4 samples were used to determine the effect of the microstructure of the films from ion bombardment by allowing the samples to be grounded and floating for nitrogen and argon carrier gases respectively.

Contrary to sample 1, samples 7 and 8 had a negative bias applied to them to facilitate the bombardment of the film, which should, according to the ion plating method, result in a higher quality film. The advantages of ion plating (discussed in chapter two) were not particularly beneficial in these experiments. In the literature review detailed in chapter two, it was seen that previous attempts to deposit chromium films from chromium hexacarbonyl resulted in contamination of the samples by carbon and oxygen when high bias potentials such as those used in ion plating were applied. For our deposition process, the etching rate at potentials such as that applied to sample 8, was nearly as high as the deposition rate. A film, or a pseudo-film was grown on the sample. For a -200 V bias (sample 8) the film under observation to the eye appeared to be a light dusting on the surface substrate. The reflection from the mirror finish of the steel substrate was easily observable through the film and the film surface was uneven. The uneven coating was caused by the concentration of the electric field

lines at the sharp edges of the sample where an increased bombardment rate occurred. The film that was present was easily broken down after contact with the atmosphere and disintegrated almost as quickly as sample 1. Sample 7, with a -30 V bias did produce a more stable film than sample 8 although the film was more brittle and subject to delamination more readily than films grown with no, or a lesser, substrate bias. This can be seen in the results of Moh's hardness tests presented later in this chapter.

Sample Number	Sample Status	Gas Mixture	Gas Pressure	Coating Duration	Grain Size
1	+200 V DC -10 mA	50% Nitrogen	7×10^{-3} mbar	75 mins	
2	Floating, 8-12 V DC 0 mA	50% Nitrogen	1×10^{-2} mbar	60 mins	0.4 μm
3	Grounded, 0 V DC 15 mA (1.2 mA)	60% Nitrogen	1×10^{-2} mbar	60 mins	0.1 μm
4	+40 V DC -250 mA (-3.5 mA)	60% Nitrogen	1×10^{-2} mbar	65 mins	0.2 μm
5	Floating, 8-10 V DC 0 mA	50% Argon	1×10^{-2} mbar	55 mins	1 μm
6	Grounded, 0 V DC 200 mA (2 mA)	50% Argon	1×10^{-2} mbar	65 mins	0.05 μm
7	-30 V, 5 mA (3.0 mA)	50% Argon	1×10^{-2} mbar	60 mins	-
8	-200V 10 mA	50% argon	1×10^{-2} mbar	57 mins	-

Table 8.1 : A summary of the plasma conditions for the first six coating experiments. The rest of the gas mixture in column 3 is $Cr(CO)_6$ while the grain size is that determined from photographs taken while the samples were being examined with a scanning electron microscope.

After the initial experiments were complete, it was subsequently determined that the currents drawn to the probe were inaccurate. Some of the current values in table 8.1 were recorded from the current meter on the 0 - 500 V DC power supply which was used to apply the voltage to the sample. This inaccuracy is highlighted in the contradictory currents drawn by the samples 1 and 4. In later experiments, a separate current meter was placed in the circuit which correctly determined the current drawn to the sample. From later experiments in table 8.2, for example, a grounded sample in either nitrogen or argon drew 1.0 - 2.0 mA while at -50 V a current of 2.0 -

4.0 mA was drawn. The initial conditions of experiments 1 - 8 were repeated and the current draw to the sample was re-measured accurately. These measurements are given in brackets after the original, and incorrect current for these samples is given.

8.3.1 Initial Analysis

After these initial eight experiments, analysis of the films was undertaken with a scanning electron microscope (SEM) to determine the film composition and the surface morphology. Snapshots of the sample surface were taken which allowed examination of the surface structure of the film. The SEM has an "EDAX" (Energy Dispersive X-ray Spectrometer) unit attached to it which allowed elemental analysis to be conducted. This analysis was capable of determining whether the films were in fact chromium or not. However, for lighter elements such as carbon, nitrogen, and oxygen, the detection resolution of the EDAX system is low due to the ever decreasing atomic excitation cross-sections of lighter elements. This made it difficult and inaccurate to determine the impurity elements in the films. Different analysis techniques were subsequently used to resolve this issue.

Examination of the film surface indicated that for a positive bias, or for a floating sample, there was a difference in the grain/cluster size of the films for the argon carrier gas. For nitrogen, the grain size is approximately the same for all three potentials (+40 V, +12 V, 0 V). The cluster sizes for both carrier gases were approximately the same for all films when the samples were grounded. This indicates that the ion bombardment of the film has a much larger effect for an argon carrier gas. Representative pictures of samples 2 - 6 are shown in figure 8.5.

Figure 8.6 shows the elemental analysis of samples 3, 6, and a blank uncoated sample determined with the same EDAX conditions. Both samples were grounded and subject to the plasma conditions for approximately the same time but sample 3 used nitrogen as the carrier gas while sample 6 used argon. Examination of figure 8.6 shows several features. Firstly, the films for both cases have strong chromium emission signatures indicating that the films formed with both carrier gases are primarily chromium. Secondly, the chromium film produced in the nitrogen atmosphere appears thicker implying growth rate is faster. This can be determined by the iron peaks showing through in the spectra of sample 6. These peaks are from the steel substrate and are absent in the sample 3 scan, indicating that the film thickness is greater than the skin depth of the x-rays. This is not the case for the film grown in the argon atmosphere. Both samples appear to contain oxygen and possibly some carbon. Sample 3 contains no tungsten but sample 6 may. The blank sample analysis in figure

8.6 shows that the chromium peaks in samples 3 and 6 are from the coating and not from the steel substrate since the iron peaks are significantly reduced.

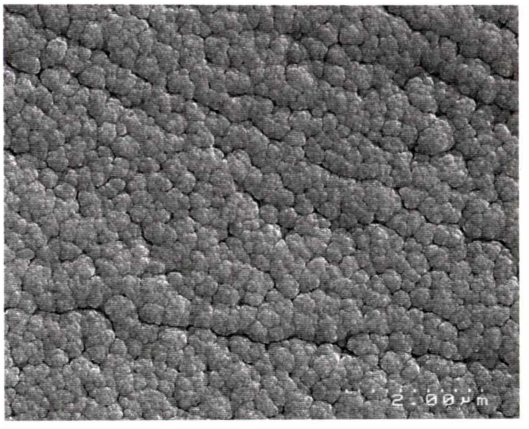

Sample 2

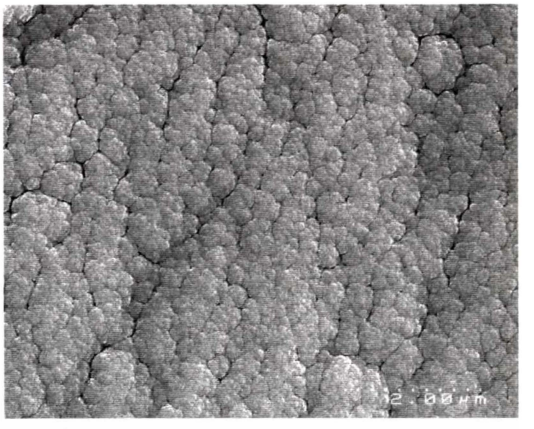

Sample 3

Sample 4

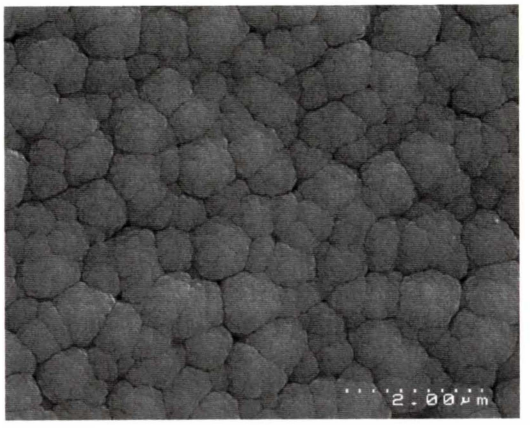

Sample 5

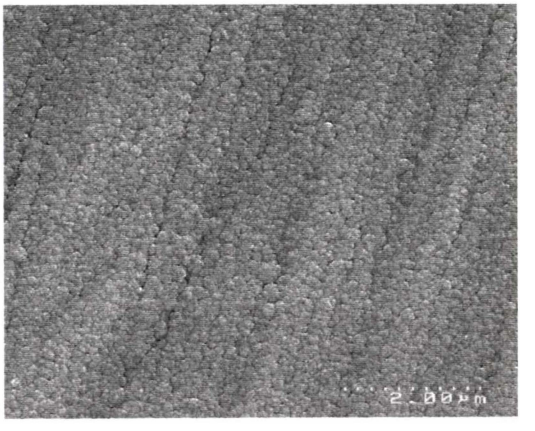

Sample 6

Figure 8.5 : SEM pictures of samples 2 to 6 showing the surface morphology.

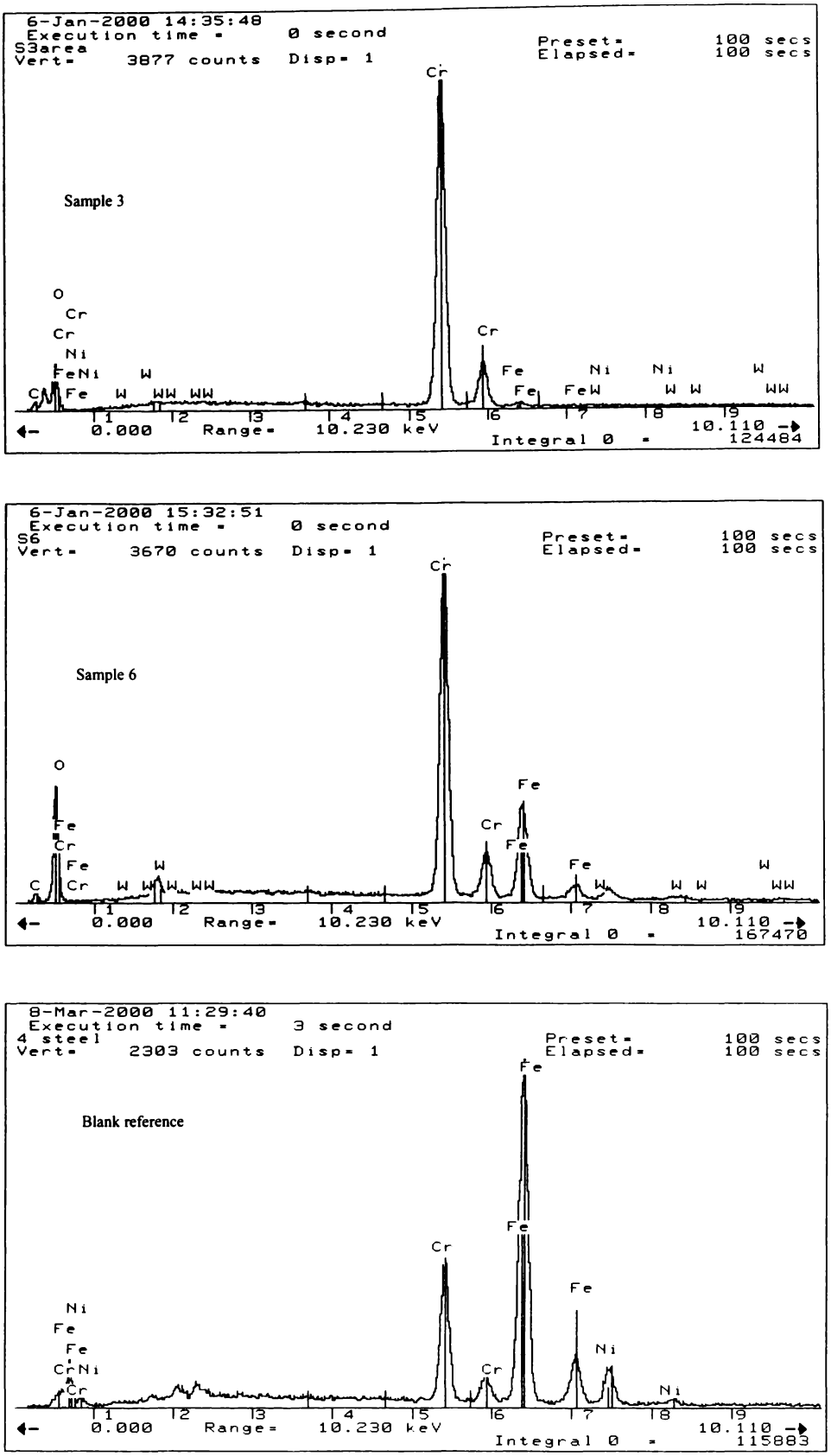

Figure 8.6 : SEM EDAX spectra (20 keV acceleration voltage) of the grounded nitrogen and argon carrier gas samples (samples 3 and 6) and a blank uncoated sample showing the elemental composition.

On further examination of the spectra from sample 6, the tungsten peaks positioned at just over 17 and 18 keV correspond to nickel which is present in the steel substrate, but not marked on figure 8.6. Similarly, the peak at approximately 1.8 keV could be from silicon, an impurity in this steel. However, it is possible that some tungsten sputtered from the filaments could have been incorporated into the films. The evidence against its incorporation stems from the fact that the face of the sample has no direct line of sight to the filaments and that two tungsten peaks are present, but most are absent in figure 8.6. One would expect all the tungsten spectral fingerprints marked to show some form of peak on sample 6, not just a couple, and to also be present in sample 3. Oxygen and possibly carbon seem to be present in both samples. It is difficult to definitively state this from these EDAX scans since iron has a peak at roughly the same position as oxygen. Elemental analysis using Rutherford back-scattering (RBS) will be presented in the next section which determined the impurity content in the films, and resolved these questions.

8.4 Subsequent Experiments and Film Characterisation

In the previous section it has been shown that the films are primarily composed of chromium. These preliminary tests were unable to accurately determine the impurity content but did demonstrate that it was possible to deposit chromium from the $Cr(CO)_6$ precursor. The remaining questions involve the levels of impurities, film structure, morphology, adhesion, and quality of the films.

A further 14 film samples on the same stainless steel substrate were grown with the varying conditions of substrate bias and gas composition to observe the effects these variables had on the impurity content, structure and elemental composition of the films. As will be seen in the next section, these new samples were coated for four hours (rather than the one hour previously used) to increase the film thickness in order to facilitate further analysis tests and to avoid delamination of the films. The experimental details, similar to those in table 8.1 are presented in table 8.2. Some of the later samples were repeats of previous experiments, which were necessary to retest the deposited films that were destructively tested.

A series of sections will now be presented which will discuss various tests of the films from mechanical to chemical composition.

Sample Number	Sample Status	Gas Mixture	Gas Pressure	Coating Duration
9	Grounded 15 mA (1.2 mA)	50% Nitrogen	1×10^{-2} mbar	250 mins
10	Grounded 12 mA (1.3 mA)	50% Argon	1×10^{-2} mbar	235 mins
11	Grounded 1.1 mA	50% Nitrogen	1×10^{-2} mbar	235 mins
12	Grounded 0.9 mA	50% Argon	7.5×10^{-3} mbar	240 mins
13	-50 V 2.1 mA	50% Nitrogen	7.5×10^{-3} mbar	250 mins
14	-30 V 2.2 mA	50% Nitrogen	5×10^{-2} mbar	240 mins
15	Grounded (200 V, 2A) 2.8 mA	50% Argon	5×10^{-2} mbar	250 mins
16	Grounded 1.2 mA	50% Argon	1×10^{-2} mbar	165 mins lost vacuum
17	-30 V 2.4 mA	50% Argon	1×10^{-2} mbar	210 mins lost vacuum
18	Grounded 1.3 mA	50% Argon	1×10^{-2} mbar	225 mins
19	Grounded 1.2 mA	50% Nitrogen	1×10^{-2} mbar	60 mins Filaments burnt out
20	Grounded 1.15 mA	50% Nitrogen	1×10^{-2} mbar	150 mins lost vacuum
21	-50 V 2.0 mA	50% Nitrogen	1×10^{-2} mbar	240 mins
22	Grounded 1.3 mA	50% Nitrogen	1×10^{-2} mbar	240 mins

Table 8.2 : A summary of the plasma conditions for the last 14 coating experiments. All samples were coated at plasma conditions of 300 V, 1 A unless otherwise specified (sample 15). Those experiments that had difficulties are noted in the column, coating duration (sample 16, 17, and 19).

8.4.1 Growth Rates - Etching vs. Deposition

8.4.1.1 Growth Rates

From the EDAX analysis of the initial samples it was seen that the films had approximately the same composition, while from observation of the surface morphology, the argon carrier gas produced similar features to nitrogen when the samples were grounded. Two samples, both from a nitrogen carrier gas, were chosen for cross-sectional analysis to determine the film thickness. These samples were numbers 4 and 9.

In order to determine the film growth rates, a measurement of the film thickness was required. It was necessary to cross-section the samples which required regrinding and polishing one side of the coated sample. To facilitate this, the sample was immersed and hardened in a resin which was easier to handle and subsequently mount for further SEM observation. This resin was ground back on grinding wheels with varying grit sizes, using the same procedure for substrate preparation, until sufficient depth through the side of the substrate had been obtained. The resin block was then gold-coated, as the resin is non-conductive (a requirement of SEM analysis is to have conductive samples). The samples were then examined in the SEM for film width and again for atomic composition across the film width using spot analysis. No changes were detected in the film composition, but the process described above delaminated the film from sample 4. This delamination was common for films in the preliminary coating experiments with a 1 hour deposition time. Conversely, sample 9 suffered no delamination and remained fully bonded to the substrate along the entire interface examined in the SEM. This implies that the delamination in sample 4 did not occur in the grinding process, but was the result of the resin shrinking as it dried. The film surface was more strongly bound to the resin that it was to the substrate.

SEM pictures of both samples are shown in figure 8.7 where the boundary between the film and the substrate is clearly defined. At the ion energies used in these experiments, no boundary mixing was expected, nor did it occur.

8.4.1.2 The Effect of Bias.

As previously described in section 8.3, initial attempts to apply a bias potential approaching those used in ion plating were unsuccessful in producing a coating. The initial tests involved samples 7 and 8. Although these thinner films were less adherent to the samples, it was found in subsequent experiments that a negative bias of -50 V for a nitrogen atmosphere was the maximum that could be applied and still produce a

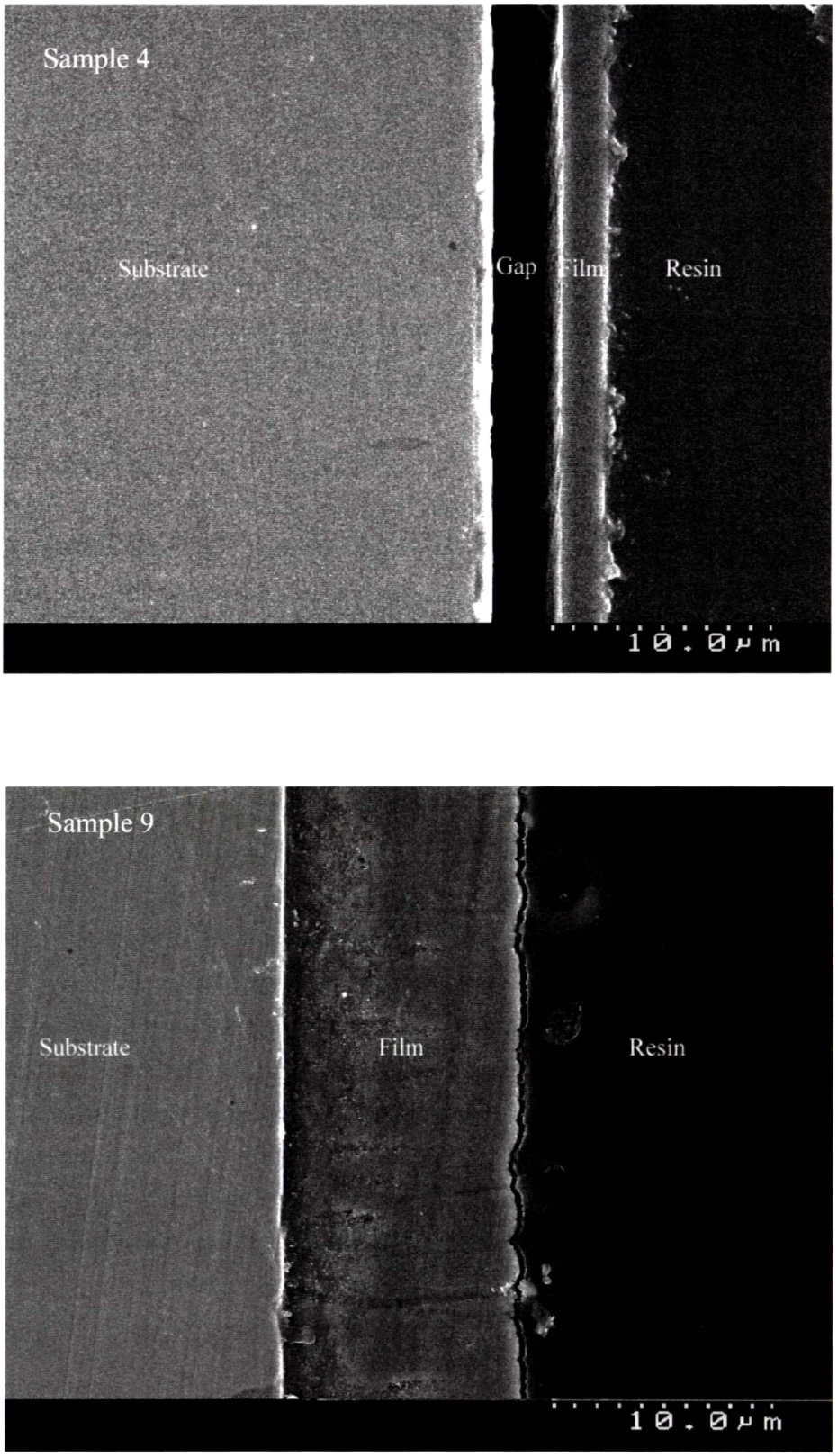

Figure 8.7 : SEM photographs showing the cross-sections of samples 4 and 9. Sample 4, coated for 1 hour delaminated in the resin while sample 9, with a 4 hour deposition process did not. The film growth for both samples is approximately the same at 2.5 - 3 $\mu m\ hr^{-1}$.

film. For an argon carrier gas, -30 V was found to be the maximum applied potential. This bias, or even grounding the sample rather than leaving it floating, decreased the cluster size of the film, especially for argon. This can be seen in the photographs of samples 5 and 6 in figure 8.5. This reduction did not increase when more negative biases were applied to the samples, such as the -50 V applied to sample 21 shown in figure 8.8.

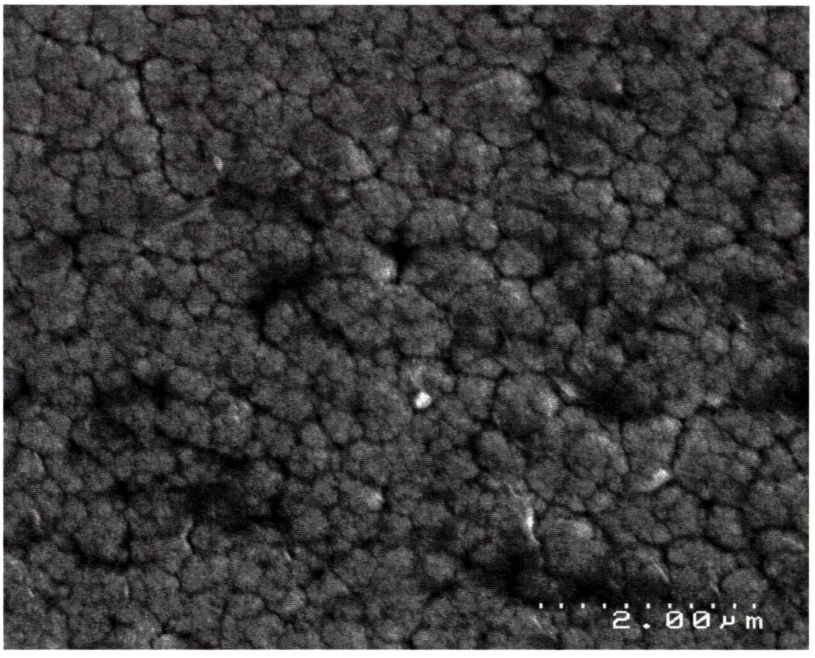

Figure 8.8 : A surface picture of sample 21 taken in the SEM.

8.4.2 Film Composition

A variety of tests were performed on different samples to conclusively determine the elemental content and the structure of the films. It will be beneficial to start with the elemental composition to aid in the interpretation of the remaining tests such as x-ray diffraction.

8.4.2.1 RBS and NRA Analysis

Two samples, numbers 10 (argon) and 22 (nitrogen), grown under the same plasma conditions and bias potential, were sent to the Institute of Geological and Nuclear Sciences in New Zealand for Rutherford backscattering (RBS) analysis. These spectra were cross checked with nuclear reaction analysis (NRA) (for C, N and O), and particle induced x-ray emission (PIXE) (for Cr). The RBS beam consisted of deuterium atoms directed normal to the film surface with a 920 keV energy, while the

detector was set at a 165° backward angle with a collection resolution of 18 keV. The depth resolution at the surface was 10 nm.

For sample 10, oxidation occurred in the first 500 nm of the film coating which represents the first 5% of the film thickness. The remainder of the sample contained 3 ± 1% nitrogen and 97 ± 1% chromium. The RBS spectrum of sample 10 is shown in figure 8.9.

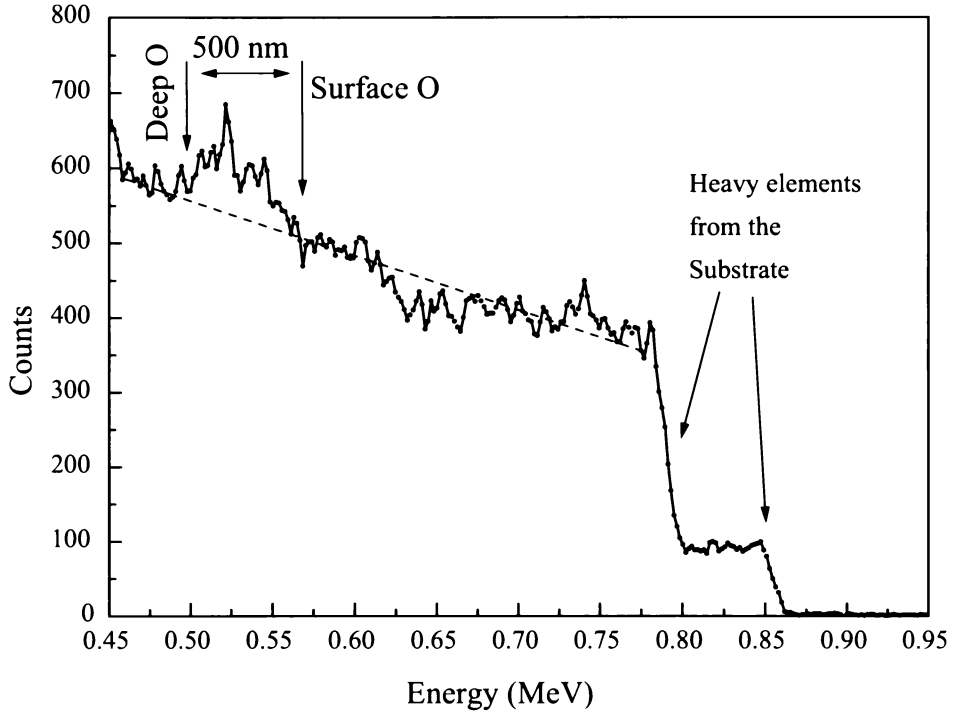

Figure 8.9 : A RBS scan of sample 10.

Sample 22 was analysed with the same procedure and the same instrument settings as sample 10. Approximately the same level of oxygen was found in the first 500 nm of the film surface as was found for an argon carrier gas. The lack of carbon in the films (none was detected), and the surface layer composition indicates that the oxygen originates from exposure to the atmosphere rather than being incorporated into the growing film by dissociation of carbon monoxide. This confirms that the original assumptions, design, and plasma parameters chosen to minimise the dissociation of molecules are justified.

The rest of the elemental composition of sample 22 was somewhat different, nitrogen levels of 62 - 72 atomic (at.) % were detected in the film structure. This was an interesting result since it gave a Cr/N ratio of 0.36 - 0.37. To put this in perspective, there were three nitrogen atoms per chromium atom, while the lowest ratio found in the review in chapter two was 0.73. For nitrogen bonded into the crystal

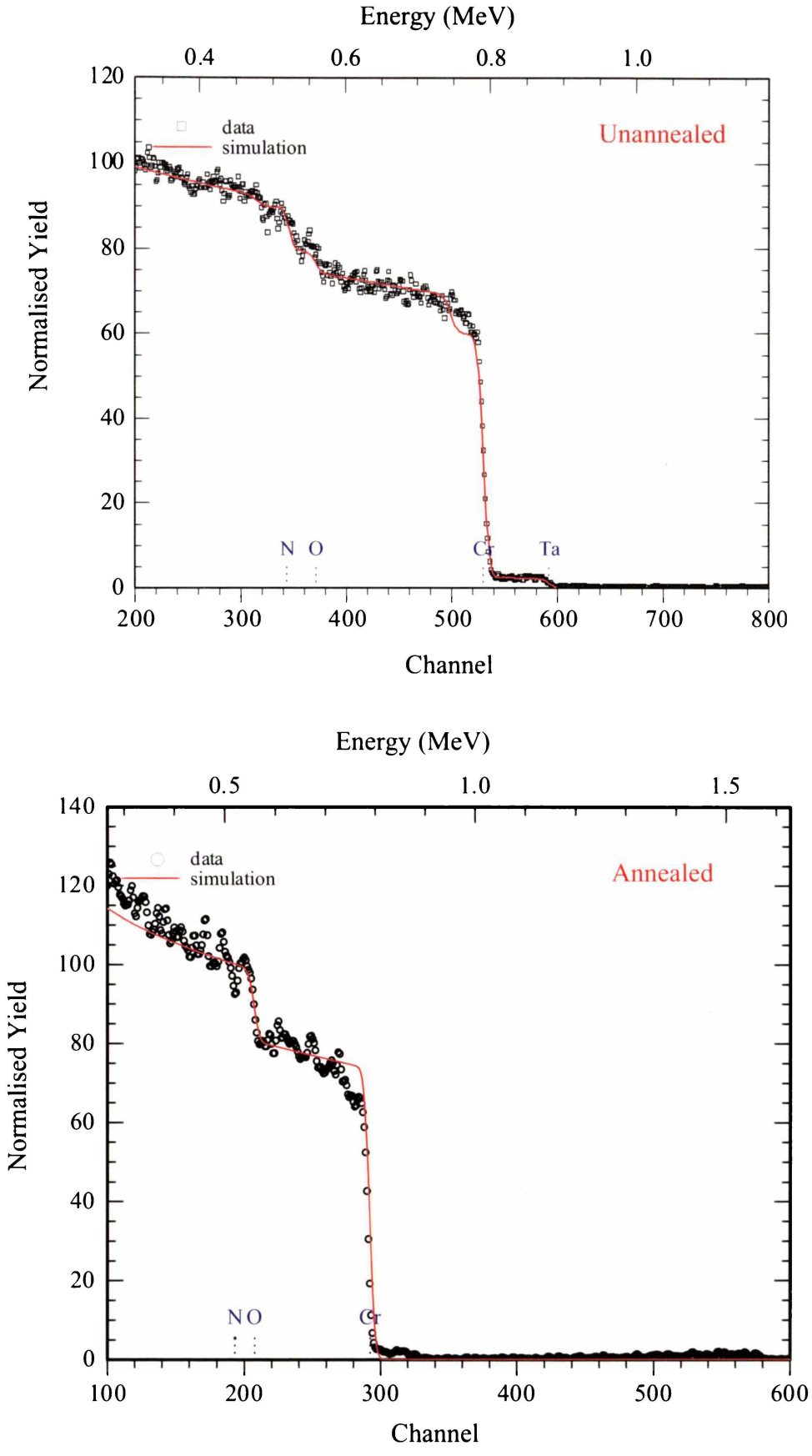

Figure 8.10 : The RBS spectra of the annealed and unannealed sample 22.

structure of chromium, Cr/N ratios of 2 and 1 are expected for Cr_2N and CrN respectively. Even if CrN was formed, there must be a significant amount of interstitial nitrogen contained in the films. Considering the low energies used in the deposition process of this thesis, it was speculated that most, if not all of the nitrogen may be trapped as N_2 gas within the film during deposition. To test this hypothesis, the sample was vacuum annealed at 380 °C and tested again. The same RBS test was then run on the annealed sample where it was found that only 3 at. % nitrogen remained. The sample now contained a uniform amount of oxygen throughout the film which was unexpected for vacuum annealing. It was later discovered the sample had been placed in the furnace while it was still at 240 °C, and then the evacuation process started. This would allow ample time for atmospheric oxygen to attack the film, but would not have affected the loss of nitrogen from the film. The RBS results for sample 22 are shown in figure 8.10 while the compositional analysis for both samples is given in table 8.3.

	Argon (sample 10)		Nitrogen (sample 22)		
	Unannealed		Unannealed		Annealed
	Layer 1 (at surface)	Layer 2	Layer 1 (at surface)	Layer 2	Layer 1
Thickness (μm)	0.2 ± 0.01	> 2.1	0.2 ± 0.01	> 2.1	> 2.1
Cr (at.%)	64 ± 1	97 ± 1	22 ± 1	27 ± 1	30 ± 1
O (at.%)	31 ± 1	-	15 ± 1	< 2	67 < 2
N (at.%)	3 ± 1	3 ± 1	62 ± 1	72 ± 1	3 ± 1
Ta (at.%)	-	-	0.1 ± 0.05	0.1 ± 0.05	0.1 ± 0.05
Cr/N			0.36	0.37	10

Table 8.3 : A summary of the compositional analysis using RBS of the argon and nitrogen atmosphere chromium films.

Several conclusions can be draw from these results. Firstly, no chromium nitride was formed since annealing the sample effectively removed all the nitrogen.

Secondly, interstitial nitrogen may have been present, but if it was, it was weakly bound and the annealing temperature and pressure differential in the vacuum provided sufficient energy for it to escape the film.

Thirdly, two forms of the film were able to be created from a nitrogen and an argon carrier gas respectively. Argon provided a 97% chromium film, while nitrogen appeared to produce a similar film with significant quantities of trapped nitrogen gas.

Fourthly, no carbon monoxide was trapped in either film since carbon wasn't detected. The plasma conditions for sample 10 contained no nitrogen, yet it was found in the RBS analysis of the film. There are three possible explanations for its presence

in the film, either it was incorporated from exposure to the air, it was bound into the film during deposition, or the RBS technique cannot distinguish between 0% nitrogen and 3% nitrogen. None of these explanations are satisfactory. If incorporation was from exposure to air, it would be present in the surface layer like oxygen was. The background vacuum was 3 orders of magnitude lower than the pressure the experiments were conducted at, so a theoretical maximum of 0.1% nitrogen could be present. Finally, the RBS results cannot be incorrect since the impurity content (C, N and O) was verified using NRA. Therefore, the most likely conclusion from these options is that the nitrogen in sample 10 arose from background contamination of the vacuum. There is one last possibility, and this is that the "nitrogen and oxygen free" argon gas bottle was not nitrogen free.

Fifthly, it seems apparent that these particular chromium films have a high affinity to nitrogen and some form of stabilisation or bonding may occur to retain the high levels observed in sample 22. Furthermore, it appears to be specific to nitrogen since, as discussed, no carbon monoxide was trapped. Carbon monoxide may well have been incorporated into the film, but lost just as easily.

Sixthly, since the nitrogen was easily lost from sample 22, the density of the films must be substantially lower than those found in chromium metal. Although no density measurements were conducted, it will be seen that the x-ray diffraction (XRD) measurements showed that no uniform crystal structure could be detected.

8.4.2.2 Transmission Electron Microscopy

Transmission electron microscopy (TEM) tests were conducted on samples 19 and 20 at the Department of Mechanical Engineering at Hong Kong University. TEM samples are required to be thin (200 - 500 nm), and extensive milling processes are employed to remove the substrate and to obtain the required film thickness. Since the films sent for analysis had a thickness in excess of the minimum requirements, a portion of the film itself was removed by milling so that the first 200 - 500 nm of the film was prepared for analysis. A high resolution transmission electron micrograph (HRTEM) is shown in figure 8.11. The overall film composition was amorphous, but did contain embedded nano-crystallite particles, some of which are marked on the image. Elemental analysis of the film was determined using energy dispersive x-ray analysis (EDX) and confirms, in general, the results obtained from RBS. The elemental analysis for various area scans are presented in table 8.4. The reference scan on the substrate shows significant levels of chromium, nickel and oxygen present in the steel. This confirms the earlier EDAX analysis from the SEM of the film where these elements were present. The EDX analysis did show that the oxygen content in

the film is higher than those recorded from RBS. To correlate these differences, further oxidisation of the film must have occurred so that the preparation process needs to be examined. The milling of the film occurred in two stages. These were mechanical grinding of the substrate to a particular width after which ion beam milling is used to remove the remaining material to the required thickness. A typical temperature rise for these processes is 100 °C. Considering the milling time (typically two weeks) the additional oxidisation of the film could have occurred in the mechanical grinding process.

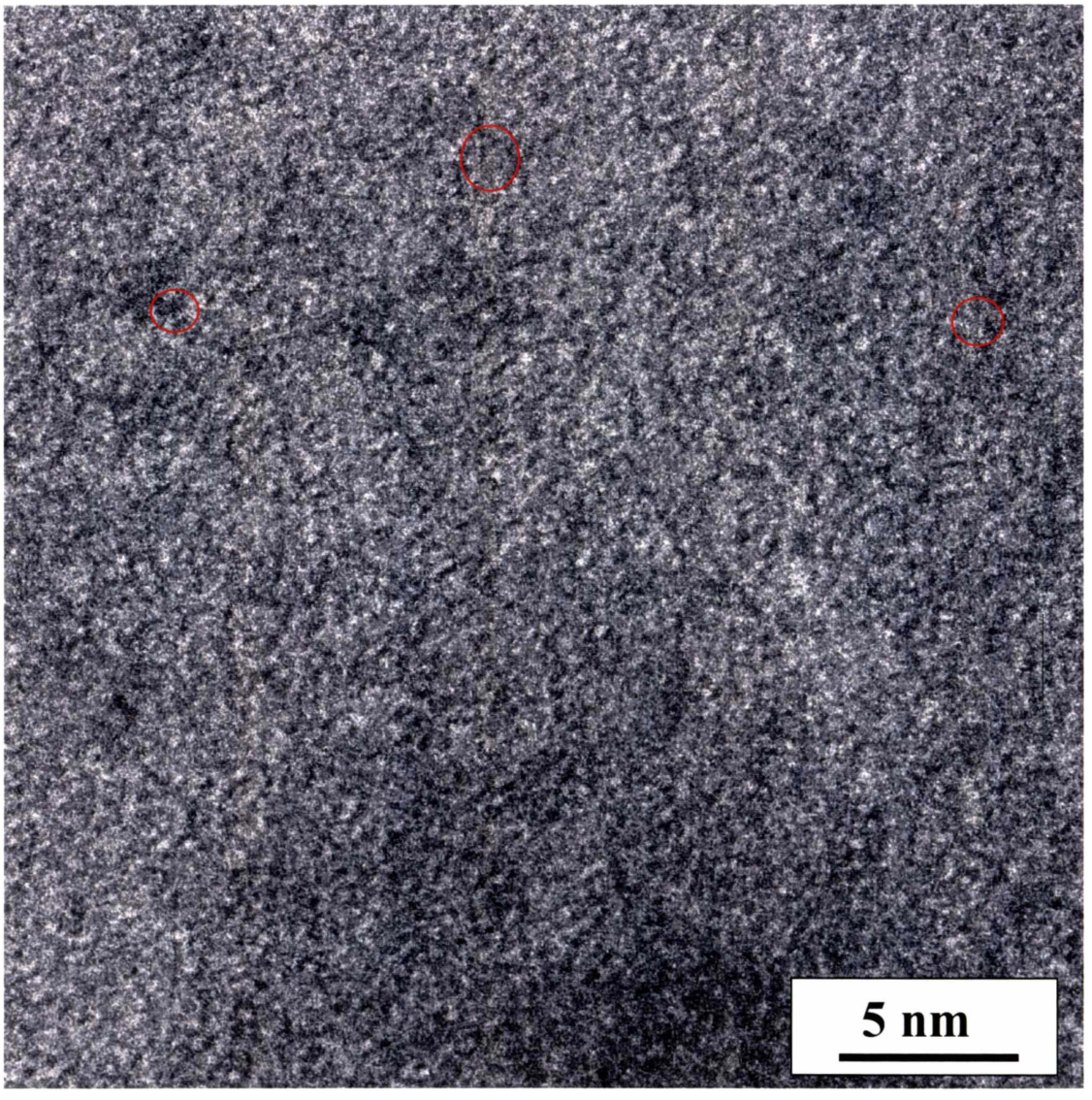

Figure 8.11 : A HRTEM image showing the detailed surface morphology. Examples of the nano-crystallites visible in the film are circled in red.

Element	Substrate	EDX 1	EDX 2	EDX 3	EDX 4
N at. %	-	28.27	23.68	26.28	12.59
O at. %	11.14	45.96	58.98	56.57	24.75
Cr at. %	20.00	25.77	17.34	17.16	62.67
Fe at. %	60.55	-	-	-	-
Ni at. %	8.31	-	-	-	-

Table 8.4 : A summary of the TEM compositional analysis of the argon and nitrogen atmosphere chromium films.

The nano-crystallites highlighted in figure 8.11 were subjected to x-ray diffraction in order to determine their composition and structure. The crystals were identified to be chromium nitride in the stoichiometric ratio of 1:1 (CrN). The diffraction pattern of the crystals is shown in figure 8.12.

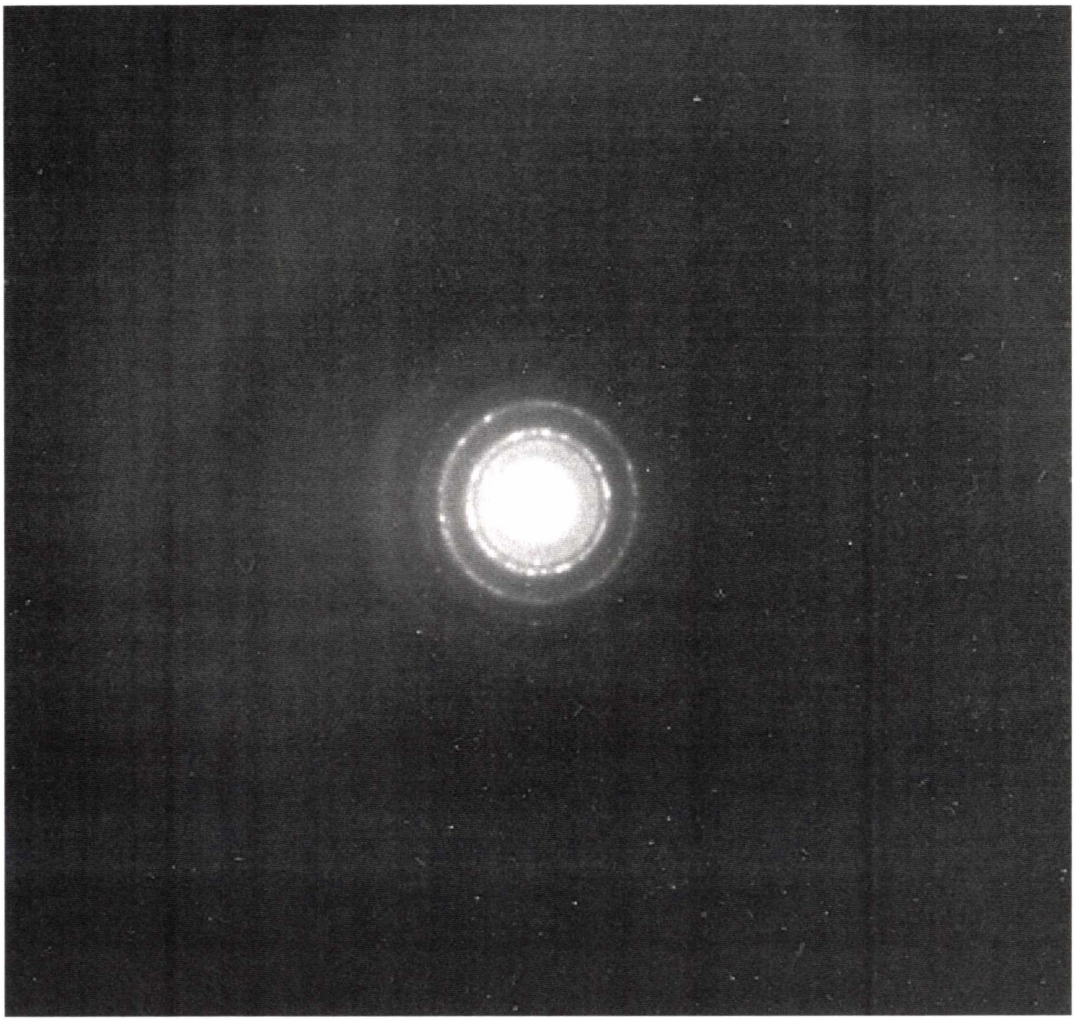

Figure 8.12 : A TEM diffraction spectra of the nano-crystallite particles found in figure 8.11.

From figure 8.12, four diffraction rings are observable which have the diameters 12.2, 14.3, 20.0, and 24 mm respectively (on the scale of the photograph). Thus the ratios

$r_1^2 : r_2^2 : r_3^2 : r_4^2 \approx 3:4:8:11$ indicates a FCC lattice structure while the diffraction rings were indexed to be from the {111}, {200}, {220} and {113} planes respectively. CrN has the b1 FCC structure of NaCl while Cr_2N is HCP, Goldschmidt (1967A). All the stable oxides of chromium are non-FCC, Goldschmidt (1967B), so the pattern was tentatively identified as CrN. According to the relation $L\lambda = rd$, where camera length, L, is 580 mm, electron wavelength, λ, is 0.00251 nm (200 keV), and $d = a_0/\sqrt{h^2+k^2+l^2}$, a_0 was calculated to be 0.413 nm using r_{111} (r_1) and d_{111}, which is consistent with the reported value of 0.415 nm for CrN.

8.4.2.3 X-ray Diffraction and Raman Spectroscopy

Films grown in both the carrier gas atmospheres were analysed before and after annealing using XRD both at the University of Waikato and (for sample 10) at the ANSTO Materials and Engineering testing facilities in Australia. At ANSTO, the tests were performed using a Siemens D500 diffractometer with a cobalt source (λ = 1.789 Å), while at the University of Waikato, a Philips X'pert instrument with a copper source (λ = 1.5405 Å) was operated in a low angle mode (0.3 - 5°).

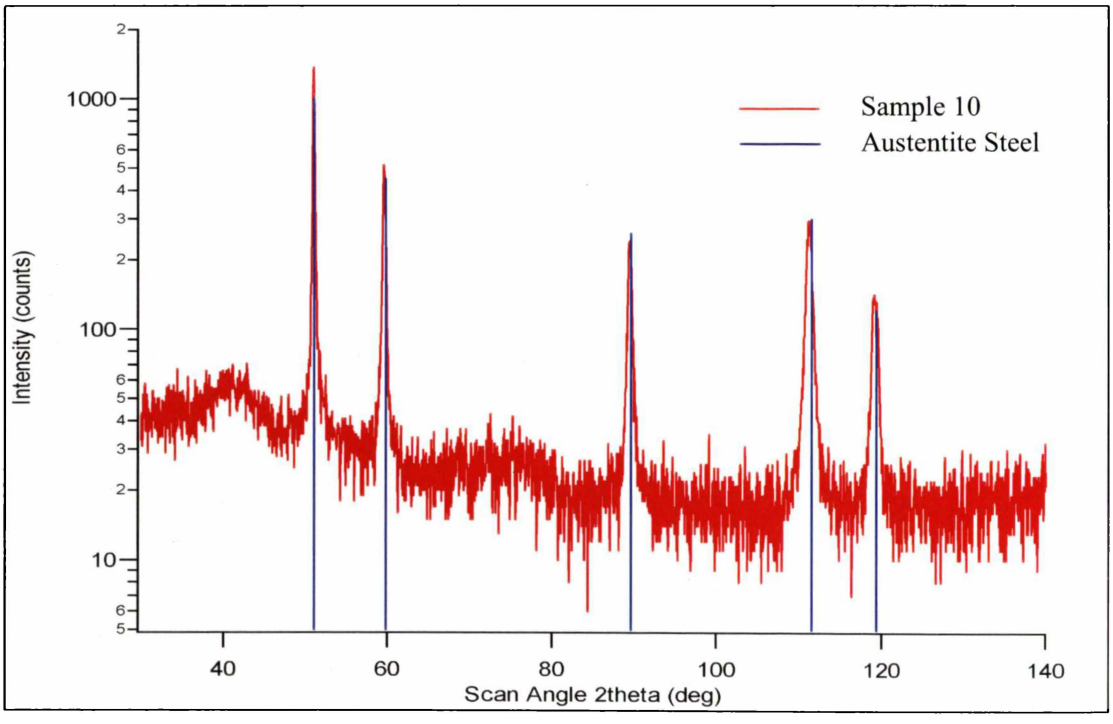

Figure 8.13 : An XRD scan recorded at ANSTO showing the sample response and the expected peak positions for austenite steel.

Figure 8.13 shows the normal XRD scan of sample 10 recorded at ANSTO. The results show that the penetration of the film was significant and the peaks

recorded were typical of stainless steel but the intensity was lower, indicating an absorbing, non-diffracting layer was present on the sample surface. This result matches the identification of the film morphology determined from TEM.

Figure 8.14 shows the unannealed, low angle scan, XRD profiles of samples 11 (nitrogen) and 16 (argon). Samples 11, 14, 15, and 16 were chosen for XRD analysis and the spectra were recorded. The samples were then annealed at 700° C for one hour and allowed to slowly cool. Only samples 11 and 16 survived this process so only the results for these two samples will be discussed since their unannealed scans were almost identical to those in figure 8.14.

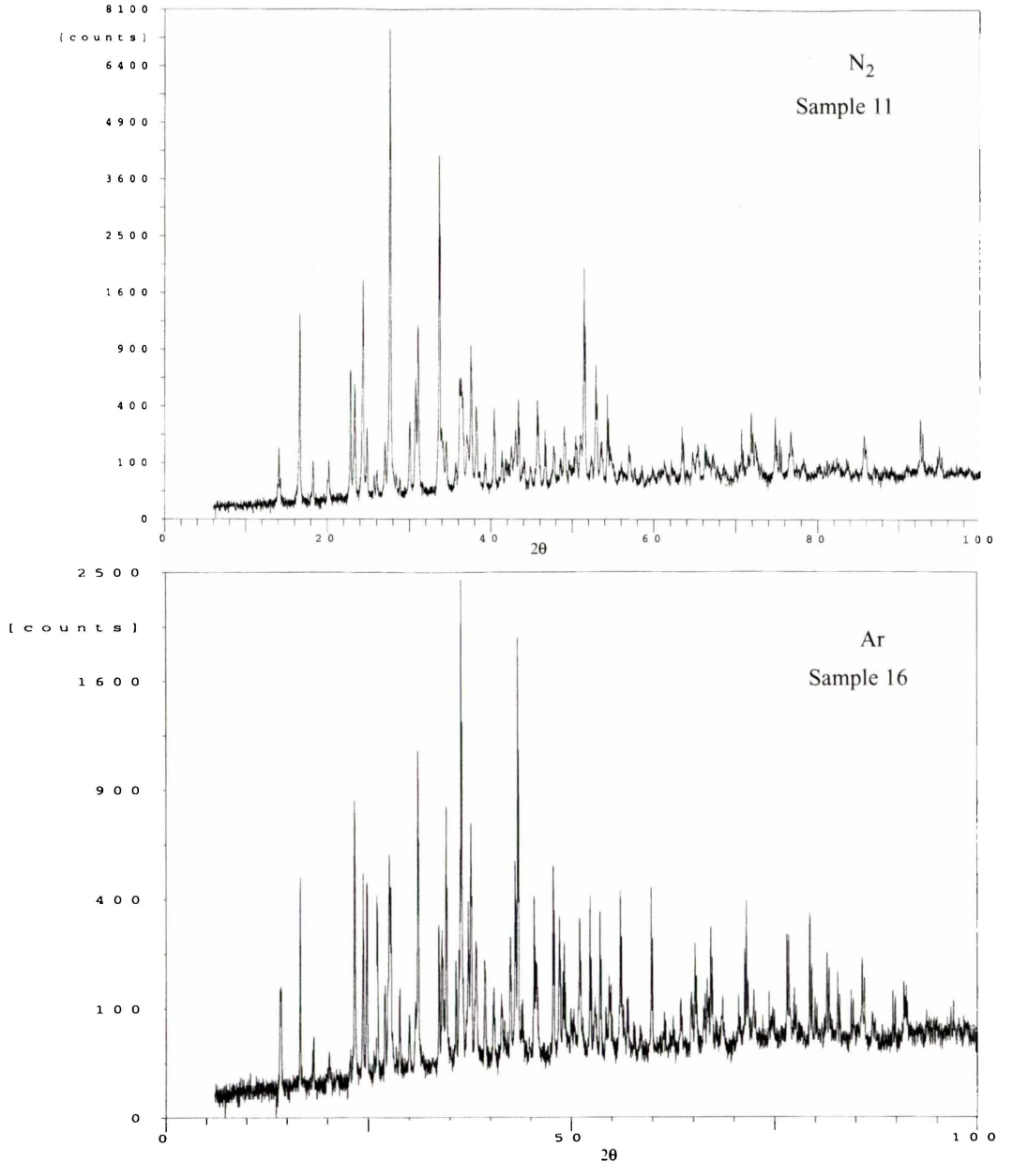

Figure 8.14 : Low angle XRD scans recorded for an unannealed nitrogen and argon sample. The argon scan has been scaled to match the 2θ angle of the nitrogen scan.

Identification of the peaks shown in figure 8.14 by the automated analysis program, chose compositions such as $Cr_{0.19}Fe_{0.7}Ni_{0.11}$, FeC, FeNi, $Fe_{0.98}O$, $Cr_{23}C_6$. The spectra after annealing were smoother and contained fewer peaks but the same identification process was even less helpful. Compounds containing aluminium, molybdenum, copper, and cobalt were identified. Clearly this identification is incorrect. What is important, is that the XRD fingerprint for chromium was not detected, nor did the scans match the profiles of the chromium nitrides. The conclusion to be drawn is that the films did not contain a regular crystal structure and were semi-crystalline or amorphous, confirming the overall TEM analysis. Figure 8.15 shows the XRD fingerprints of samples 11 and 16 in their post annealed state.

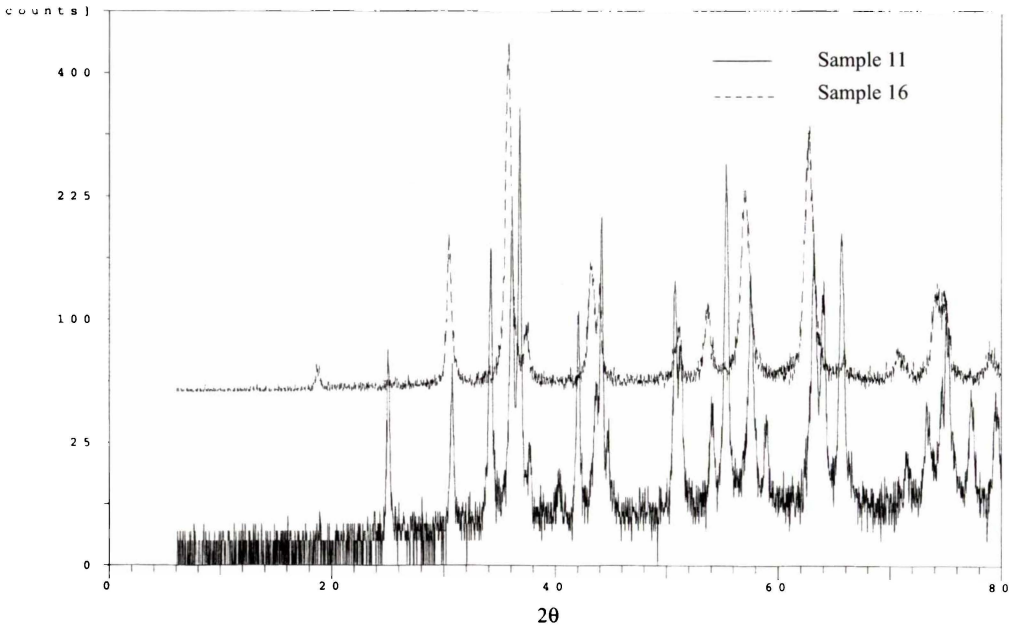

Figure 8.15 : Low angle XRD scans recorded for sample 11 and 16 post annealing.

One sample, number 10, was analysed using Raman spectroscopy to determine whether the oxygen contained in the surface layer of the chromium films was bonded or not. The result of this analysis is presented in figure 8.16 where the data from the film are offset from the comparative baseline stainless steel sample. A minor peak containing Cr_2O_3 was detected indicating that the atmospheric attack of the film surface resulted in a normal oxidisation process of the chromium film.

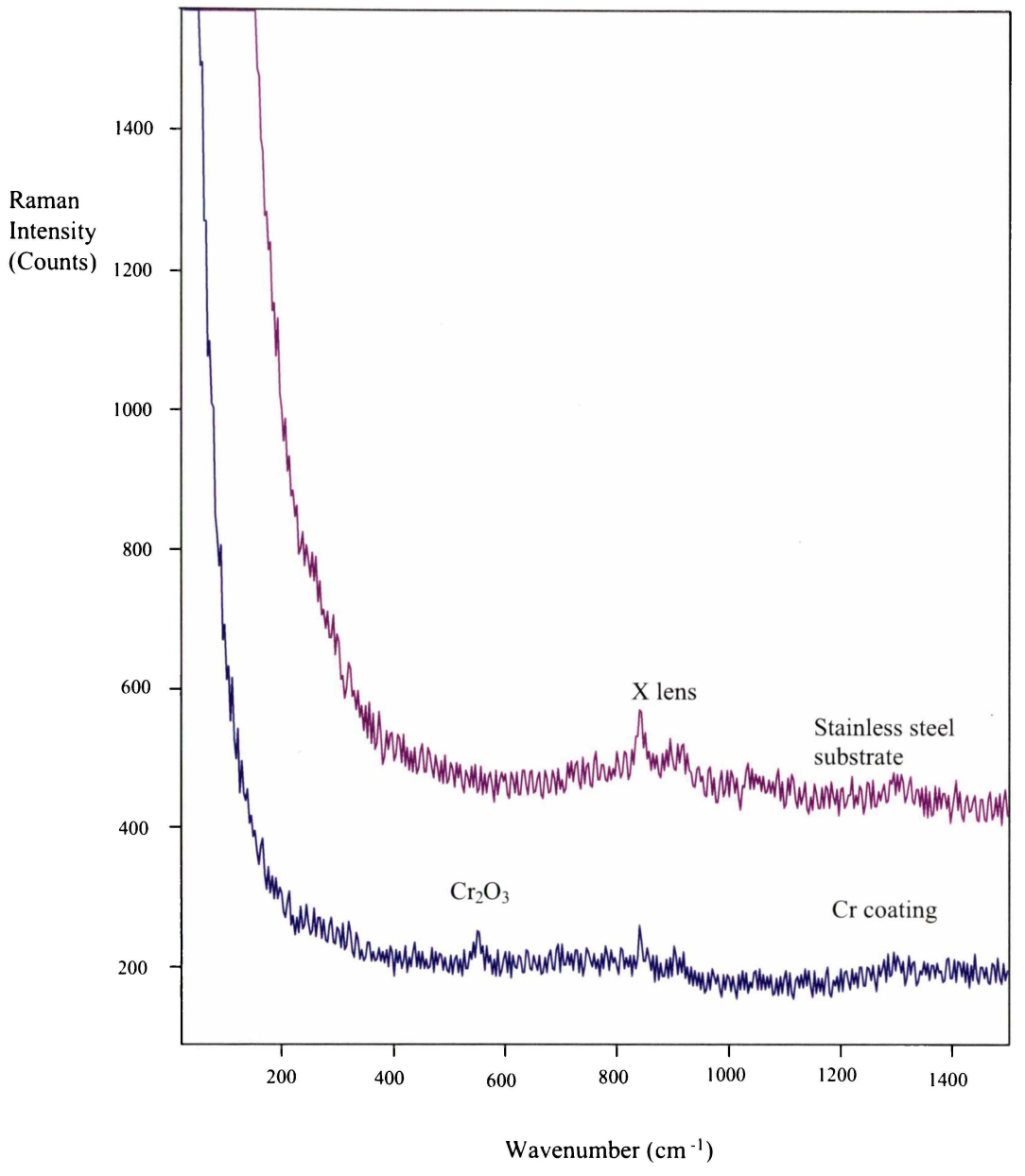

Figure 8.16 : The Raman spectrum of sample 10.

8.4.2.4 Hardness and Adhesion

The films were subject to two types of mechanical hardness tests. Firstly they were subject to scratch testing using crystals of different hardness (Moh's hardness test as detailed in the *Metals Handbook* (1982)). The samples were then observed after each test to determine the level of damage to the film structure. A blank, polished stainless steel substrate was used as a comparative baseline measurement. The crystals ranged from 1 to 5 (out of a possible 10), and corresponded to Talc, Gypsum, Calcite, Fluorite, and Apatite in order of hardness respectively. This test, although not ideal, does allow some measure of the film hardness to be determined. The results for

samples 2 to 7 are presented in table 8.5. The values from this table for all samples are well below the quoted chromium value of 9 from Weast and Astle (1979). This indicates that the properties of the film are different from bulk chromium, and correlates well with the lack of crystal structure determined by TEM and XRD analyses.

Sample Number	Hardness level	
2	Talc	No scratching
	Gypsum	No scratching
	Calcite	Scratches
3	Talc	No scratching
	Gypsum	No scratching
	Calcite	No scratching
	Fluorite	No scratching
	Apatite	Scratches
4	Talc	No scratching
	Gypsum	No scratching
	Calcite	No scratching
	Fluorite	Tiny scratches
	Apatite	Scratches easily
5	Talc	No scratching
	Gypsum	No scratching
	Calcite	Tiny scratches
	Fluorite	Scratches well
6	Talc	No scratching
	Gypsum	No scratching
	Calcite	No scratching
	Fluorite	Scratches most times
7	Talc	No scratching
	Gypsum	No scratching
	Calcite	Tiny scratches
	Fluorite	Scratches well
Blank Stainless Steel	Talc	No scratching
	Gypsum	No scratching
	Calcite	Tiny scratches
	Fluorite	Scratches well

Table 8.5 : Hardness testing on samples 2 to 7, including a blank, uncoated sample.

Secondly, sample 10, while it was at ANSTO, was subject to hardness testing using a NanoInstruments IIs indentation system. This test used a triangular diamond as an indenter that deformed rather than penetrated the film surface giving a measure of restorative force. Indent loads of 50, 250, and 1000 mN were applied to the film surface resulting in hardness values of 6.2, 5.2 and 4.1 GPa respectively. The indentation at the maximum load was ~ 3.5 μm, which is ~30% of the film thickness. These values are represented graphically in figure 8.17.

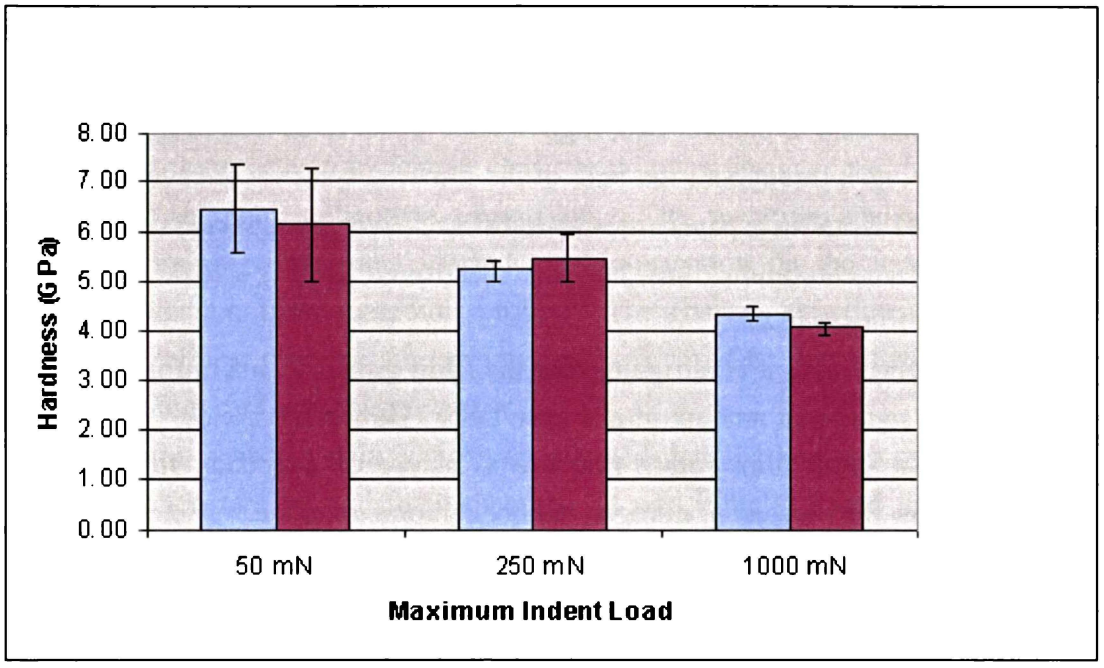

Figure 8.17 : Hardness tests of sample 10 for three different loads.

The hardness values shown in figure 8.17 are equivalent to work hardened stainless steel. Sartwell *et al.* (1998), found that electrodeposited chromium films have hardness values around 10.1 GPa. The indentation depth for this test was 2.1 μm and is directly comparable to the tests in figure 8.17 which indicates that the chromium films produced in this work are, at best, 60% as hard as electrodeposited chromium films. Values lower than electrodeposited chromium were expected since a uniform crystal structure is lacking

8.5 Summary

From the tests conducted on the film substrate, it is apparent that the method used in this thesis to coat chromium films has not provided a replacement for electrodeposition methods. This can be deduced by the lower hardness values, the tendency of the films to delaminate, the lack of a regular crystal structure for either

chromium or its nitrides, and the inferred lower density of the films. However, the objectives of the experiments have been met. Chromium films have been grown that contain no carbon or oxygen in the bulk of the film using $Cr(CO)_6$ as a precursor. Referring back to chapter two, a comprehensive literature review has found no evidence that this been achieved by any other researchers, even though it is still being attempted from the recent publication dates.

Although ion bombardment of the growing film could be used to increase the film density and hence its physical properties, it was not successful due to the high etching rates of the deposited film. The discharge configuration did not readily lend itself to this deposition method, nor was it intended to by design. As stated earlier in this chapter and also in chapter two, high bombardment rates lead to incorporation of carbon and oxygen throughout the bulk of the film, the issue researchers appear to be trying to avoid from their paper titles and abstracts. We have successfully deposited contaminant free chromium films, but have discovered there is a trade off in that the quality of the films is low.

On a final note, it is intriguing that the films grown with a nitrogen carrier gas retain such a significant amount of nitrogen, but no carbon monoxide. This raises the possibility that these films might find use as a type of molecular filter since they appear to allow the passage of nitrogen but not carbon monoxide.

8.6 References

Goldschmidt, H. J., 1967A, *Interstitial Alloys*, (Butterworth and Co., London) p 220.

Goldschmidt, H. J., 1967B, *Interstitial Alloys*, (Butterworth and Co., London) p 359.

Mattox, D. M., 1998, *Handbook of Physical Vapour Deposition (PVD) Processing*, (William Andres Publishing/Noyes Publications, New York).

Metals Handbook, 1982, Vol 8, (ASM International, Metals Park, Ohio).

Sartwell, B. D., P. M. Natishan, I. L. Singer, K. O. Legg, J. D. Schell, and J. P. Sauer, 1998, AESF Plating Forum, (Hard Chrome Replacement Team, March 1998, http://www.hcat.org/Pub_and_pres.htm).

Weast, R. C., and M. J. Astle, 1979, Eds., *CRC Handbook of Chemistry and Physics* (59^{th} edition, CRC, Boca Raton, Florida).

Chapter 9 Summary and Conclusion

9.1 Results

9.1.1 Langmuir Probe Analysis

The objectives of this thesis were to design, build, analyse, and conduct diagnostic and coating experiments in a thermionically enhanced DC discharge. A new high resolution electronic circuit configuration was designed and implemented for automated Langmuir probe data acquisition. The resulting analysis of the data obtained from this instrument yielded new information on the nature of ion and electron collection from Langmuir probes. The coating experiments conclusively showed that almost pure metallic chromium films could be deposited in a plasma by using chromium carbonyl as a precursor.

Results from the data acquisition allowed detailed analyses of the Langmuir probe characteristics by two main theories. It was initially found that the electron saturation current obeyed orbital motion theory, while the ions in the converse saturation regime followed both the orbital and radial motion theories. The application of these theories to the ions and electrons yielded different densities which were contradictory. There was also a paradox in that the collected ions could not be collected by the probe from radial and orbital trajectories simultaneously.

These problems have been reported by previous researchers but no solution to untangle this paradox, nor to determine which density was correct had been achieved through the use of Langmuir probes. The determination of the correct density had previously been resolved by other researchers through the use of non-probe diagnostics, such as microwaves, where it was found that the electron density was the correct value.

We chose to analyse the theories in depth to resolve this paradox. In this investigation it was found that the solutions of the pure radial ion collection theory allowed orbital motion to occur when the Debye length was greater than the probe radius. From the initial analysis it was seen that this transition was on the boundary of our experimentally determined values. Thus, *there was no paradox* since *both* theories allow orbital motion of the ions to occur in the saturation regimes found in the work of this thesis. This change from orbital to radial trajectories of the ions was determined by calculating the dependence of the current on the applied voltage to the probe for various numerical solutions of the appropriate equations. Other researchers have

shown that in general, for the Debye length to probe radius ratios found in this thesis the dependence of the ion current on the applied potential for the radial and orbital theories is approximately the same. The results presented in this thesis demonstrate this to be correct and definitively determine what the theoretical dependence actually is for a wide range of ratios. The recorded Langmuir probe data could also be analysed using this method because of the high sensitivity, resolution, and accuracy of the multiple current sensing resistors used in the data acquisition circuitry. The dependence of the ion current on the applied probe voltage was shown to *neither* match the radial nor orbital motion predictions. The conclusion to be drawn from this analysis was that the ion current densities obtained by application of these theories were incorrect. Application of the same procedure to the electron saturation confirmed the previous analysis that the electrons were following the orbital motion rigorously and that the electron density was correct. This new treatment of the Langmuir probe data, experimentally and theoretically, confirms what previous researchers speculated. It was further shown that even if the square of the ion saturation current is apparently linear, and the intercept with the voltage axis passed close to the space potential, this is not sufficient to prove that the ions obey the orbital motion theory.

The evaluation of the electron temperature from the Langmuir probes was shown to have a greater dependence on the removal of the ion current than was previously reported in published works where the subtraction process is normally given a cursory and brief mention. This caused difficulties with the plasma system used in this thesis since a two-temperature distribution was found and the resulting high temperature values varied significantly. To aid in the temperature evaluation, a theoretical Langmuir probe characteristic was analysed and the change in the evaluated temperature was found by the variation method, applied to the saturation current. It was also shown that the "correct" ion current to be removed could be determined by this method when there is only one electron distribution, i.e. one temperature. This is achieved by subtracting increasingly larger ion saturation currents until the slope of ln(I) vs. V gains a point of inflection. The correct ion current is therefore the largest current subtracted which does not lead to this point of inflection. This method is preferential to the existing procedure of fitting a straight line to the ion saturation curve and measuring the ion current value where the line intercepts the space potential. Using this method allows greater accuracy in the determination of the electron energy distribution function's high energy tail, calculated from the corrected data. The problem with the straight line fit method is that the ion current does not saturate and hence over what saturation range a fit is made is an arbitrary decision. It was shown that not only does the ion saturation current not saturate, but that its dependence on

the applied voltage rises with increasing voltage bias to the probe, both experimentally and theoretically for radial motion.

9.1.2 Coating Experiments

The experiments designed to deposit chromium metal from a plasma containing the chromium carbonyl precursor provided successful and interesting results. These experiments were conducted after the plasma conditions had been determined by extensive Langmuir probe and spectroscopic investigations. It was shown from these measurements that the carbonyl/nitrogen combination plasma behaved similarly to a pure nitrogen discharge. This allowed (and was confirmed) the plasma parameters to be determined more efficiently, which was a significant advantage since the Langmuir probes were easily contaminated in the carbonyl vapour.

Two different forms of chromium films were deposited with the two different carrier gases used. When the gas mixture was nitrogen/carbonyl, chromium films were deposited that contained significant levels of nitrogen. The Cr/N ratios for these films were ~0.26 indicating that there were 3 nitrogen atoms for every chromium atom. Post annealing, this sample lost virtually all its nitrogen indicating that the gas was trapped rather than bound into the film. For an argon/carbonyl mixture almost pure (97%) chromium could be deposited. The remainder of this film was nitrogen. Nitrogen was an unexpected impurity in this discharge but no carbon monoxide was detected in the film even though its concentration would have been many orders of magnitude greater. The surface of the films for both carrier gases contained significant levels of oxygen which occurred by prolonged exposure of the films to the atmosphere.

Coating experiments were conducted with different biases applied to the sample in both gas combinations. It was discovered that an ion plating discharge configuration with a bias as low as -50 V resulted in the etching rate (via ion bombardment), being almost the same as the deposition rate. This meant that the film properties could not be improved by this process. The discharge configuration was not designed for ion plating which, in general, requires short physical distances between the anode and the cathode.

Testing of the samples were conducted by different procedures which determined the film properties. Initial SEM analysis confirmed that the films were predominantly chromium while RBS analysis accurately determined the film composition before and after annealing. The XRD spectra, before and after sample annealing showed no chromium or chromium nitride peaks for either carrier gas. There were a variety of peaks that were misidentified by the automated analysis

routine, most of which related to the substrate, even for low angle scans. In summary, XRD could only show what was not there.

The samples were also analysed using a TEM which showed the amorphous and semi-crystalline nature of the films. The compositional analysis confirmed the RBS spectral results, but much higher levels of oxygen were found in the films. There were two reasons for this, firstly the first 200 - 500 nm of the film was analysed which contained an oxygen surface layer. Secondly, heating of the samples in the milling process accelerated the attack on the film by atmospheric oxygen resulting in increased oxygen levels. This heating would also have induced the nitrogen incorporated in the film structure to outgas. Several compositional analyses on different regions of the film surface gave rise to different levels of each element.

The nano-crystallites found in the film surface were conclusively identified to be chromium nitride, with the CrN structure. This is a novel result since from chapter two, chromium nitride formation generally requires either high energy implantation or equivalent ion plating biases on the samples. Furthermore the chromium source used in these reviewed papers was "pure", from sputtered or previously deposit chromium.

Raman spectra were also attempted as an identification method. This procedure is useful to identify chemical compounds through their characteristic bonding structure. Only small amounts of chromium oxide (Cr_2O_3) were discovered in the film surface. This indicated that atmospheric oxygen was oxidising the film surface.

Mechanical testing of the samples using a micro-indenter indicated that the film hardness was, at best, 60% of the hardness of electrodeposited chromium. Moh's hardness test produced approximately the same results. In this test, chromium has a hardness value of 9, while the sample coatings generated in this thesis had values between 4 and 5.

9.2 Contributions to Original Research

This thesis has made several contributions to original research in two areas, Langmuir probe analysis and the plasma deposition of chromium films from a chromium hexacarbonyl precursor.

- The Langmuir probe data acquisition design involved modifications to those published by other researchers. These earlier devices were of two designs where either the power supply was grounded or it was allowed to float. Both of these methods had deficiencies in their operation since the raw data obtained required correction for the voltage drop over the current sensing resistor. Furthermore they commonly used only one sensing resistor which limits the

resolution of the ion saturation regime, creating difficulties for accurate and detailed analyses in this region. Both deficiencies were overcome through the use of a transimpedance amplifier and a real-time switching system so that different sensing resistors could be chosen depending on the resolution required.

- Through theoretical and experimental measurements, a precise method to determine the correct ion saturation current (for zero temperature ions) was identified. This was shown to be the maximum value obtained before a point of inflection occurs in the semilog plot of current vs. voltage.
- We have presented evidence that the zero temperature radial motion theory allows orbital motion. It has been speculated that this may occur by other researchers, but never demonstrated. The transition from orbital to radial motion was shown to occur at an ξ value between one and two. Furthermore, it was also shown that *all* numerical solutions for the zero temperature radial motion theory tend to two when either the current or applied voltage tends to zero (the thin sheath limit).
- Exact calculations of the current dependence of the zero temperature radial motion solutions were presented as a gradient x (where $I^x \propto V$). This showed that for $\xi < 3$ the current dependence is similar to orbital motion theory. To distinguish between these two theories, the resolution of the ion current needs to be greater than that allowed by a single current sensing resistor (if the raw data rather than a curve fit to the raw data are to be differentiated).
- For Langmuir probes it was shown that the ion saturation current, although passing the currently accepted tests for validity of the orbital and radial motion theories, did not follow either theory correctly. This determined, through the use of Langmuir probes, that only the electron saturation current allowed the correct density calculation. This has been concluded previously by other researchers but only for non-probe methods.
- The Langmuir probe data acquisition system design and subsequent testing, showing the resolution of the instrument, was presented at the fifth Electronics New Zealand Conference (ENZCon) in 1998 and was later published in the Review of Scientific Instruments (2003).
- At least two further papers are in the process of being submitted for publication. These will detail the experimental and theoretical Langmuir probe analysis (Pilling and Carnegie), and the film properties and deposition process (Pilling, Carnegie, and Chen).

- Pure chromium films were deposited from an argon/chromium hexacarbonyl plasma. Many attempts to do so by other researchers contained unacceptable levels of impurities.
- Chromium films with a high nitrogen content could be deposited from a nitrogen/chromium carbonyl gas mixture. The N/Cr ratios of the samples in this thesis were far higher than those seen in the literature review. It was determined by RBS analysis that after annealing almost all the nitrogen content of the film was lost.
- TEM analysis showed that the unannealed nano-crystallites found in the surface of the films, grown in a nitrogen atmosphere, corresponded to CrN. Nitrides of chromium have not been found by other researchers using nitrogen based carrier gases such as ammonia with a chromium hexacarbonyl precursor.

9.3 Future Work

Although this thesis has been successful in its objectives, several areas of the research warrant further investigation.

One of these is the replacement of the reed relays in the Langmuir probe circuits. These relays were a bottleneck for the sampling rate due to the time needed for them to switch when changing gain levels. They can be replaced with a more sophisticated electronic device allowing switching rates up to the maximum sampling rate of the DAQ board. This modification would allow many sets of 12 bit resolution I - V characteristics to be recorded each second using the gain system developed. This would open up the application of this device to transient plasmas and significantly reduce the time the probes are subject to contamination.

Further research on the Langmuir probe analysis developed in this thesis for different discharge methods, such as: RF, a wider range of densities and temperatures, and different discharge gases is warranted. The analysis of the Langmuir probe response in terms of its gradients allows a simple determination of whether the saturation regimes follow theory. For plasmas with a Maxwellian distribution, solutions of the radial motion theory which assumes a Maxwellian distribution for the ions are necessary, but is presently uncalculated. This would allow a comparison of the probe data against all the main theories. High density plasmas analysed by this method clearly show the effects of orbital motion. Further investigation of such behaviour would allow a greater understanding of the plasma dynamics involved in such processes.

Now that impurity free chromium coatings can be generated from a chromium hexacarbonyl precursor, a wider range of investigation to determine what conditions

lead to the incorporation of impurities found by other researchers is warranted. The discharge configuration presented in this thesis is not suited to this investigation since it is not designed to be compatible with ion plating. There may be a regime where bombardment of the growing film results in a high quality coating without impurities being incorporated into the film.

The affinity of the films coated in this thesis to absorb nitrogen, but not carbon monoxide, would also be interesting to investigate and raises the possibility of their use as diffusion barrier coatings.

Investigations into chromium deposition of chromium hexacarbonyl with a nitrogen carrier gas through the control of the substrate temperature could lead to a alternative method of chromium nitride deposition. The phase diagram of this compound and the review of chromium nitride film deposition presented in chapter two, shows that a high temperature is needed to deposit the CrN crystal structure. In the literature review the only source of chromium for chromium nitride films grown *in situ* was from sputtering. No chromium nitride film deposition from two gaseous precursors (one containing chromium, one containing nitrogen) was found.

There is also the possibility to deposit other metals from their carbonyls either as a pure metal, or as a nitride. Films of metals such as cobalt, iridium, iron, nickel, niobium, osmium, rhenium, rhodium, ruthenium, tantalum and technetium as well as other transition elements could be deposited.

9.4 Summary

The importance of precisely measuring the Langmuir probe characteristics has been highlighted through the results in this thesis where it has been shown that high accuracy is needed for a theoretical comparison. Conditions commonly accepted as proving a match to the theory have been shown to be incorrect. Previously this lead to speculation about charge-transfer collisions and secondary electron emission effects by previous researchers which has now been shown to be erroneous for low density discharges.

In summary, all the objectives of this thesis have been met. New data acquisition equipment was built to analyse the plasma and almost pure chromium films successfully deposited with an argon carrier gas. Changing the carrier gas to nitrogen resulted in chromium films with a high nitrogen content which could subsequently be removed by annealing. However, there was chromium nitride formation which exclusively contained the CrN crystal structure.

Appendix A Relevant Spectroscopic Transitions

A1 Transitions of Carbon Monoxide

State	B_e (cm^{-1})	r_e (10^{-8} cm)	Observed Transitions	
			Designation	ν_{00} (Å)
$c\ ^3\Sigma^+$	1.9563	1.1210	$c \rightarrow a$	2293.5
e			$e \rightarrow a$	2414.5
$b\ ^3\Sigma^+$	2.075	1.088	$b \rightarrow a$	2828.2
			$b \leftrightarrow X$	1192.9
$d\ ^3\Pi_i$	1.2615	1.3960	$d \rightarrow a$	7512.8
$a'\ ^3\Sigma^+$	1.331	1.359	$a' \rightarrow a$	14380.2
			$a' \leftarrow X$	1805.7
$a\ ^3\Pi_r$	1.6810	1.2093	$a \leftrightarrow X$	2063.0
T			$T \leftarrow X$	647.8
S			$S \leftarrow X$	690.9
R			$R \leftarrow X$	776.0
Q			$Q \leftarrow X$	776.8
P			$P \leftarrow X$	791.1
$G\ (^1\Pi)$			$G \leftarrow X$	950.0
$F\ (^1\Pi)$			$F \leftarrow X$	1002.7
$E\ ^1\Sigma^+$			$E \leftrightarrow X$	1076.2
$C\ ^1\Sigma^+$	1.9422	1.1250	$C \rightarrow A$	3680.0
			$C \leftrightarrow X$	1087.9
$B\ ^1\Sigma^+$	1.961	1.120	$B \rightarrow A$	4510.3
			$B \leftrightarrow X$	1150.5
$A\ ^1\Pi$	1.6116	1.2351	$A \leftrightarrow X$	1544.5
$X\ ^1\Sigma^+$	1.9313	1.1281		
CO^+				
$B\ ^2\Sigma^+$	1.7999	1.1686	$B \rightarrow X$	2191.4
$A\ ^2\Pi_i$	1.5894	1.2436	$B \rightarrow A$	3964.2
$X\ ^2\Sigma^+$	1.9772	1.1150	$A \rightarrow X$	4900.2

A2 Transitions of Nitrogen

State	B_e (cm^{-1})	r_e (10^{-8} cm)	Observed Transitions	
			Designation	ν_{00} (Å)
$D\ ^3\Sigma_u^+$	1.961	1.108	D → B	2349.7
C'			C' → B	2613.0
E			E → A	2173.3
$C\ ^3\Pi_u$	1.8259	1.1482	C → B	3370.3
$B\ ^3\Pi_g$	1.6380	1.2123	B → A	10463.5
$A\ ^3\Sigma_u^+$	1.440	1.293	A → X	2009.8
$y\ (^1\Pi_g)$	1.80	1.16	y → a'	2154.2
$x\ (^1\Sigma_g^-)$	1.74	1.18	x → a'	2199.6
w			y → w	2355.1
$a'\ (^1\Sigma_u^-)$	1.48	1.28		
v			v ← X	824.8
$u\ ^1\Sigma_u^+$	1.07	1.50	u ← X	829.3
t	1.16	1.44	t ← X	844.0
s	1.11	1.47	s ← X	857
e			e → a	2145.4
			e ← X	865.3
$h\ ^1\Sigma_u^+$	1.63	1.22	h → a	2282.2
			h ↔ X	886.7
$r\ ^1\Sigma_u^+$	1.07	1.50	r ← X	901.4
$s'\ ^1\Sigma_u^+$	1.58	1.23	s' → a	2397.8
f			f → X	907.5
$q\ ^1\Sigma_u^+$	1.13	1.46	q ← X	910.5
g			g → X	917.9
$p\ ^1\Pi_u$	1.21	1.40	p ← X	922.7
o			o ← X	928.9
$r'\ ^1\Sigma_u^+$	1.67	1.20	r' → a	2672.6
$m\ ^1\Pi_u$	1.36	1.32	m → a	2747.7
			m ← X	949.2
d			d → a	2796.3
$p'\ ^1\Sigma_u^+$	1.93	1.12	p' → a	2827.2
			p' ← X	958.5
$b'\ ^1\Sigma_u^+$	1.145	1.45	b' ↔ X	964.5
$b\ ^1\Pi_u$	1.41	1.31	b ↔ X	985.6

j $^1\Sigma_u^+$	1.46	1.28	j ← X	991.9
i			i ← X	1015.4
a $^1\Pi_g$	1.637	1.213	a ↔ X	1450.2
X $^1\Sigma_g^+$	2.010	1.094		
N_2^+				
C $^2\Sigma^+$	1.65	1.21	C → X	1549.3
B $^2\Sigma_u^+$	2.083	1.075	B → X	3911.4
X $^2\Sigma_g^+$	1.932	1.116		

A3 Strong Chromium Lines

Wavelength (Å)	Intensity	Spectrum	Notation
2055.52	19000	II	$a\ ^6S_{5/2}$ - $z\ ^4P^\circ_{7/2}$
2061.49	14000	II	$a\ ^6S_{5/2}$ - $z\ ^4P^\circ_{5/2}$
2065.42	8900	II	$a\ ^6S_{5/2}$ - $z\ ^4P^\circ_{3/2}$
2677.16	1800	II	$a\ ^6D_{7/2}$ - $z\ ^6D^\circ_{7/2}$ $a\ ^6D_{9/2}$ - $z\ ^6D^\circ_{9/2}$
2835.63	2500	II	$a\ ^6D_{9/2}$ - $z\ ^6F^\circ_{11/2}$
2843.25	1700	II	$a\ ^6D_{7/2}$ - $z\ ^6F^\circ_{9/2}$
2849.84	1200	II	$a\ ^6D_{7/2}$ - $z\ ^6F^\circ_{7/2}$
2986.00	1500	I	$a\ ^5D_3$ - $y\ ^5D^\circ_3$
2986.47	2100	I	$a\ ^5D_4$ - $y\ ^5D^\circ_4$
3000.89	1100	I	$a\ ^5D_3$ - $y\ ^5D^\circ_2$
3014.92	1400	I	$a\ ^5D_2$ - $y\ ^5F^\circ_3$
3017.57	2800	I	$a\ ^5D_3$ - $y\ ^5F^\circ_4$
3021.56	2800	I	$a\ ^5D_4$ - $y\ ^5F^\circ_5$
3024.35	1100	I	$a\ ^5D_2$ - $x\ ^5P^\circ_2$
3578.69	19000	I	$a\ ^7S_3$ - $y\ ^7P^\circ_4$
3593.49	17000	I	$a\ ^7S_3$ - $y\ ^7P^\circ_3$
3605.33	13000	I	$a\ ^7S_3$ - $y\ ^7P^\circ_2$

3919.16	1900	I	$a\ ^5D_4$ - $z\ D^\circ_4$
3963.69	1900	I	$a\ ^5G_6$- $y\ ^5H^\circ_7$
3969.75	1600	I	$a\ ^5G_{4\ or\ 5}$- $y\ ^5H^\circ_6$
3976.66	1600	I	$a\ ^5G_{4\ or\ 5}$ – $y\ ^5H^\circ_5$
4254.35	20000	I	$a\ ^7S_3$ - $z\ ^7P^\circ_4$
4274.80	16000	I	$a\ ^7S_3$ - $z\ ^7P^\circ_3$
4289.72	10000	I	$a\ ^7S_3$ - $z\ ^7P^\circ_2$
4339.45	1100	I	$a\ ^5D_2$ - $z\ ^5F^\circ_3$
4344.51	1900	I	$a\ ^5D_3$ - $z\ ^5F^\circ_4$
4351.77	2300	I	$a\ ^5D_4$ - $z\ ^5F^\circ_5$
4646.17	1600	I	$a\ ^5D_4$ - $y\ ^5P^\circ_3$
5204.52	5300	I	$a\ ^5S_2$ - $y\ ^7P^\circ_1$
5206.04	8400	I	$a\ ^5S_2$ - $y\ ^7P^\circ_1$
5208.44	11000	I	$a\ ^5S_2$ - $y\ ^7P^\circ_3$
5409.79	1400	I	$a\ ^5D_4$ - $z\ ^5P^\circ_3$